ATL-GEN-2005-001
13 January 2005

Estimation of Radiation Background, Impact on Detectors, Activation and Shielding Optimization in ATLAS

Atlas Radiation Background Task Force Summary Document

Reported by

S.Baranov[1], M.Bosman[2], I.Dawson[3], V.Hedberg[4], A.Nisati[5] and M.Shupe[6]

[1] Albert-Ludwigs-Universität Freiburg
[2] Institut de Física d'Altes Energies (IFAE Barcelona)
[3] University of Sheffield
[4] University of Lund
[5] Università di Roma I "La Sapienza"
[6] University of Arizona

List of participants

S. Baranov
I. Bedajanek
M. Bosman
C. Buttar
I. Dawson
D. Fournier
F. Luering
V. Hedberg
M. Huhtinen
D. Lissauer
G. Mikenberg
A. Moraes
M. Morev
M. Nessi
A. Nisati
P. Norton
S. Pospĭsil
M. Price
M. Shupe
S. Stapnes
I. Štekl
R. Veness
M.Virchaux
W. Witzeling

Index

Executive summary

This document summarizes the work carried out by the ATLAS Radiation Task Force (RTF) since it was formed in the summer of the year 2000 until the publication of this report at the end of 2004. The RTF was created by T. Akesson and the ATLAS management, with the charge to certify the radiation background simulations being done by the ATLAS Radiation Working Group, and to identify and quantify the effects of these backgrounds on the detector performance and to human safety. (The full charge is given in Appendix I).
Throughout its operation, the RTF has been convened by Martine Bosman (IFAE-Barcelona). The Summary Document is reported by M.B., S.Baranov (University of Freiburg), I.Dawson (University of Sheffield), V.Hedberg (University of Lund), A.Nisati (University of Roma-I) and M.Shupe (University of Arizona). The complete list of participants is given on page 2. In addition, there have been a number of standalone analyses, whose results appear in this document. I.Štekl, S.Pospišil, and other Prague collaborators, have participated in shielding engineering design, and done independent measurements and simulations on cladding design. M.Morev (MEPhI) and co-workers have done extensive activation calculations. M.Mokhov (Fermilab) collaborated in the MonteCarlo comparison studies. The Radiation Task Force has also received assistance from subsystem experts which have provided dimensions and materials for the simulations. G.Mikenberg (Weizmann) has participated in the work of the Task Force and has provided many insights into the workings of the Muon Spectrometer. M.Huhtinen (CERN), who provides the radiation simulations for CMS, has shared his extensive knowledge and has participated in the Task Force meetings. Similarly, P.Norton (RAL) has provided his expertise and knowledge of the ATLAS shielding design.

Background Radiation Effects and Their Estimators

The deleterious effects of the background radiation fall into a number of general categories:

(1) Increased detector occupancy. In tracking detectors this can lead to inefficiencies, worsened resolutions, and fake tracks. In calorimeters, the increased pileup fluctuations degrade energy resolution.
(2) If the backgrounds consist of penetrating tracks, the rates of spurious triggers can increase. Also, increased occupancies can increase the rates of random triggers.
(3) Radiation damage of silicon detectors and electronics. For example, bulk damage gives rise to increased leakage currents. This effect is parameterized using 1MeV-neutron equivalent fluences which are obtained by convolving predicted energy spectra with displacement-damage functions. Other damage estimators require dose, for example radiation damage to MOS electronics.
(4) Interactions leading to anomalous deposits of local radiation can disrupt electronic signals (single event upsets), or destroy components (single event damage.)
(5) Wire detectors can experience “aging” (reduced efficiency) due to polymerised deposits on the wires caused by radiation interacting with organic additives in the detector gas.
(6) Nuclear interactions in dense materials lead to the creation of residual radionuclides. The resulting dose rates from such material radioactivation will lead to radiological hazards that impact access and maintenance scenarios.

The basic measure leading to quantification of these effects is particle “fluence”, a “directionless” quantity defined as the number of particles corssing a hypotetical sphere of unit cross section area. Throughout this document the quantity flux is also used, which is equivalent to the fluence rate. The majority of the effects listed above can be related directly to the fluxes of

incoming particles of one, or several, species. A number of them are scaled to quantities derived from flux, for example the bulk damage in silicon mentioned above. A complete description of the estimators used in this document is given in section 5.1.

ATLAS Regions That Most Critically Affect Radiation Levels

At the LHC the dominant primary source of background radiation is collisions at the interaction point. Beam halo particles and beam gas interactions are negligible by comparison. In the inner detector, charged hadron secondaries from inelastic proton-proton interactions dominate the radiation backgrounds at small radii, but further out the effects of other backgrounds, such as neutrons, become more important.

In ATLAS, most of the energy from primaries is dumped into two regions, the TAS collimator and the forward calorimeter, that are then strong sources of secondary radiation. These two sources are somewhat self shielding, and since they are compact they may be further shielded with layers of dense material and cladding. The beam vacuum system spans on the other hand the length of the experiment and is in the forward region a major source of radiation backgrounds. Primary particles from the I.P. strike the beam pipe at very shallow angles – so the projected material depth is large – and by this mechanism the beam pipe becomes an extended line source illuminating the interior of the forward cavity. Studies have shown that the beamline material contributes more than half of the radiation backgrounds in the muon system. Unfortunately extra shielding in this region is not possible due to access constraints as discussed below.

If we look at the ATLAS detector with a global view (see Fig. 1 and Fig. 2), it becomes clear that there are several regions where the shielding is particularly weak. The calorimeters themselves are the primary shield protecting the muon system. But between the barrel and endcap there is a channel approximately 50 cm in width running radially to the outside, filled with lightweight cryostat structures, electronics, and services. In simulations of the mid-1990's this electronics "gap" appeared to put a serious "plume" of radiation into the barrel muon system. But as engineering proceeded, and the gap material could be modeled more realistically, it turned out that the effects of the plume (which can now be seen only in energetic hadrons) are small compared to the backwash of radiation in the barrel region, originating from the forward region.

Another potential weak area was the endcap calorimeter, particularly in the "corner" where the CSC muon detectors are placed. For this reason, three shielding "plugs" of copper alloy have been placed inside and at the back of each endcap cryostat to increase the total absorption lengths through the EMEC/HEC and FCAL calorimeter sections. Shielding in front of the CSC has been carefully optimized. The net effect of all these shielding improvements is that the overall rates in the CSC/TGC region behind the endcap calorimeter are acceptable for muon system operation. In fact, the background fluxes passing through the CSC's from upstream (except for muons), are smaller than those coming from downstream.

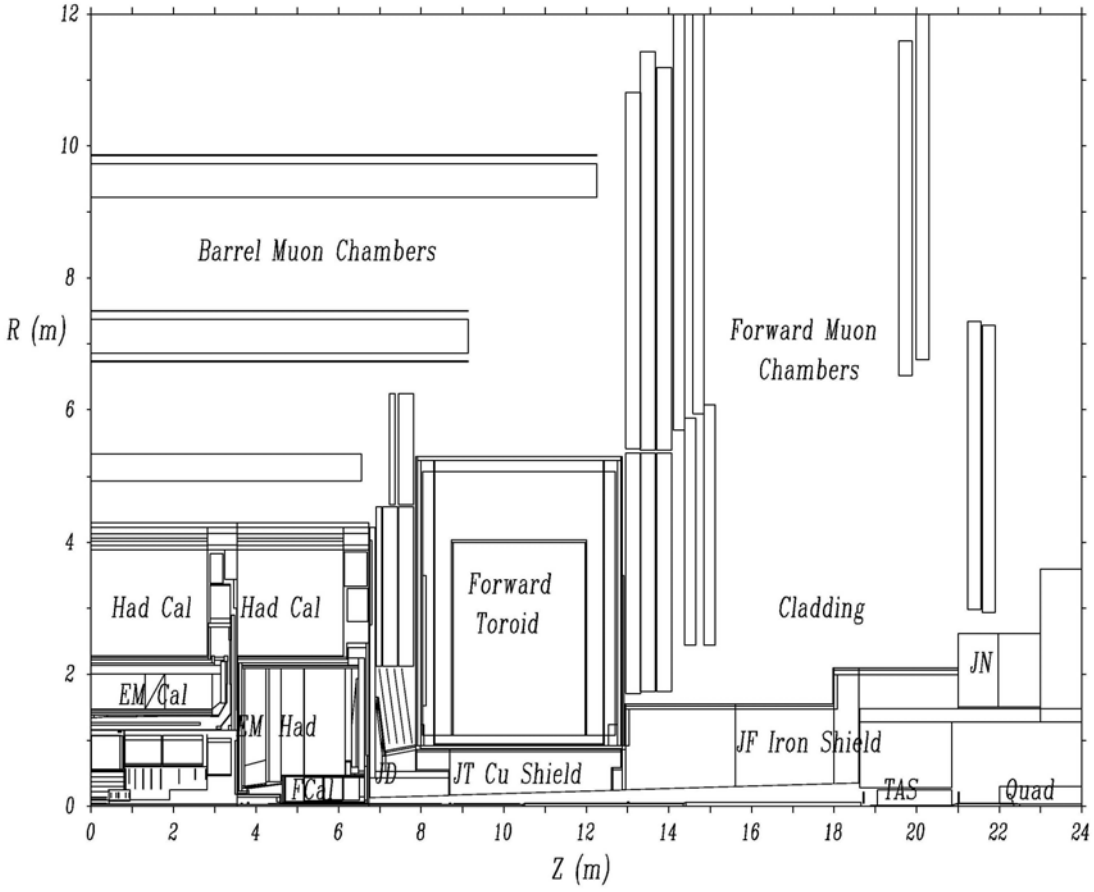

Fig. 1 A full quadrant of the ATLAS Jan03 layout as modelled with GCALOR.

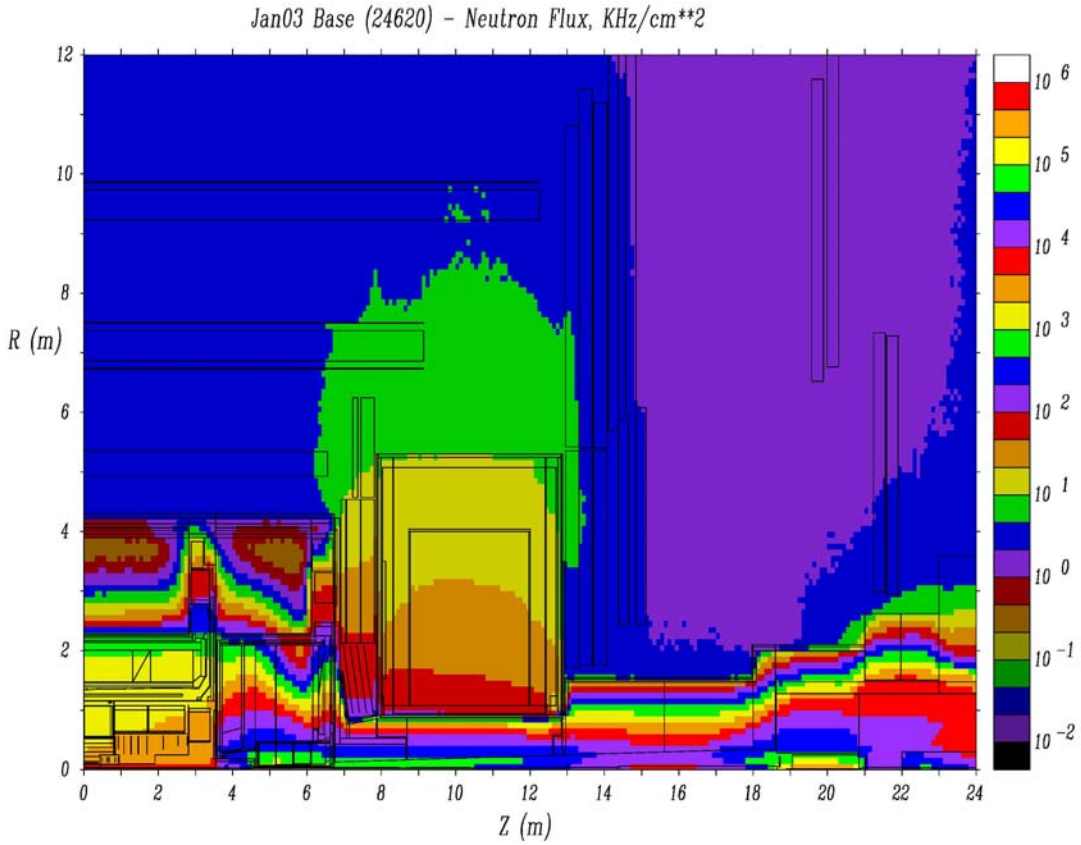

Fig. 2 The neutron flux in the GCALOR Jan03 baseline geometry.

The reason for this last effect is that, taking all factors into account, the thinnest part of the ATLAS shield is the core of the forward toroid, while there is ample space to shield the TAS collimator and adequate space to shield the FCAL. The volume where shielding can be placed in the toroid core is restricted at the outer (cylindrical) boundary by the inner radius of the toroid coils, and at the inner (conical) boundary, by clearances needed when the toroid is fully retracted for access to the ATLAS inner detector. This is also the reason for a cylindrical beam pipe design. In order to reduce backgrounds in the muon system to acceptable levels, the toroid core shield must be reinforced by additional moderator "rings" at the front and back of the toroid support tube, and by moderator facings integrated with the front and back walls of the toroid.

Tasks Initiated and Completed By the Radiation Task Force

Critical review of simulation tools

One of the major concerns of the Task Force has been to validate the geometry and material description used by the simulation programs. The sub-detectors representatives provided dimensions and materials for the various detectors. Information was collected for the beampipe and the associated vacuum equipment; the toroids, the shielding elements envelopes and material were revised. The collected information was then implemented in the detector description in GCALOR and FLUKA. For all major changes of the design, the geometries in FLUKA and GCALOR were brought into as much correspondence as possible, and run as cross checks of each other. Section 4.2.3 describes the changes to geometry since 1998 and engineering realism has caused a substantial increase of rates. A "plume" has developed in the endcap toroid region. Much effort has been dedicated, as described further on, to optimize the shielding within these new boundary conditions. On the other hand, in the inner detector cavity, the predicted rates are similar or somewhat lower than in 1998.

Secondaries from the proton-proton inelastic collisions are responsible for the bulk of the radiation backgrounds. Two different proton-proton minimum-bias event generators, PHOJET1.12 and PYTHIA6.2, were used together with the FLUKA2001 transport code to cascade the particles through the detector material. Comparison of energy-integrated particle fluences, in all regions, show that differences in the two sets of predictions are typically less than 20% (see section 7.3). This can be compared to the 30% currently assumed by ATLAS and CMS as an estimate of event-generator uncertainty. Larger differences (~50%) were observed for pions, kaons and muons for energies greater than several GeV; however these particles give only a small contribution to the total fluence and in most cases will have little consequence for the ATLAS experiment.

In order to investigate transport-code differences, simple but well-defined cross-comparisons were made of FLUKA2001 with MARS14(2002) and GCALOR (see section 7.2). The FLUKA versus MARS study investigated the lateral development of particle fluxes up to large radii for various combinations of a wide range of materials including iron, copper, concrete and a borated polyethylene cladding layer. Good agreement is observed for energy-integrated neutron, photon and e^+e^- fluxes as well as energy-deposition as a function of the cylinder radius; typically within 50%. The agreement for charged-hadrons is not as good, but differences are always within a factor 2.5. The largest differences were seen for some of the minor components of the radiation field (very energetic photons with energy above 10 MeV and muons) at large radii, giving motivation for further investigation. The relative importance of the muon component in terms of impacting a detector system is unlikely to be significant compared to the muons from heavy flavor decays. However the very energetic photon component may be of relevance for the muon

trigger rate since it has a small probability of fulfilling trigger coincidences. This is discussed in details in Section 6.2.3.

The FLUKA versus GCALOR study investigated differences in predictions for identical simplified versions of the ATLAS shielding. Of particular interest are the comparisons in the outer-detector regions, where the muon-tracking system is located and differences in the flux predictions are likely to be greatest. Energy-integrated neutron and photon fluences were always within factors 1.3 in all regions in the case where all material consists of pure iron except the concrete cavern walls. Good agreement, within a factor 1.4, is also seen in the "hybrid" case where elements are made of iron, copper, cast iron and borated polyethylene similar to the real ATLAS situation. The corresponding comparisons for the "copper" simulation were not as good, but always within a factor 1.9. Significant discrepancies were observed for photons in the 10 to 20MeV energy range in the outer-detector regions, and for high-energy neutrons on the outer face of the barrel calorimeter. Charged particle fluxes in the outer-detector regions are dominated by protons, muons and e^+e^- and the corresponding comparisons, while not as good as for the neutrons and photons, are reasonable. Differences were always less than factor of 1.8 for the protons and 2.5 for the e^+e^- and muons.

It can be concluded that the predictions of FLUKA, MARS and GCALOR are in good agreement for neutron and photon fluxes, especially for material environments dominated by iron. At large radii, or in outer-detector regions, neutrons and photons are usually the most important components of the radiation background and the consistency of the Monte Carlo predictions gives confidence in their predictions. For the iron dominated simulations, no discrepancy has been seen greater than a factor of 1.5. Also encouraging are results of the charged-hadron comparisons, dominated by protons at large radii or in the outer-detector regions; always within a factor 2.5.

It should be noted that the Monte Carlos simulation codes are continually evolving. For example, a significant improvement of the neutral kaon transport was introduced in 2000 in FLUKA which resulted in a factor 2 to 8 fewer muons and reduced charged pions fluences down to negligible levels (in GCALOR the K^0_L transport has since then been handled by GHEISHA). Some of the observed discrepancies may disappear in future versions.

Comparisons of the full ATLAS simulations between FLUKA and GCALOR (using similar but not identical geometry and material descriptions) showed levels of agreement not too dissimilar from the simplified geometry study. This is encouraging as it suggests that the uncertainties due to geometry, material and magnetic field differences are no larger than the uncertainties in the transport models.

SPS benchmarking data of neutron and photon fluxes emerging from a thick (11-14 λ_{abs}) iron absorber were reproduced by FLUKA with an accuracy of ~20%. This suggests that a lower safety-factor than 2.5 could be used for neutron and photons in iron dominated material environments (see section 7.4.1). The relative merits of cladding layers of different compositions, polyethylene and boron or lithium doped polyethylene, have been benchmarked at the PS. They are well reproduced by Monte Carlo simulations based on GEANT coupled to GAMLIB (see section 7.4.2).

One can conclude that no discrepancies have been observed which exceed the safety-factor of 2.5 used by ATLAS as an estimate of transport-code uncertainties in the outer-detector regions except for the very energetic photon component. The predicted photon fluences with energies above 10 MeV present larger uncertainties (factor 10) and its impact on the muon trigger should be investigated in more details.

Predicted radiation levels in ATLAS

A large effort has been made by the Radiation Task Force to calculate the fluence of particles in different parts of the ATLAS experiment. The result of this work is presented in chapter 5 of this report and Table - 1 gives a list of figures and tables that give the actual rates. The fluences of the most important particle types in the muon spectrometer are summarized in Fig. 3. A web site [1] has also been set up with a complete set of contour plots as well as tables of different particle rates and dose rates.

The fluencies predicted by FLUKA in the inner detector region have been compared with those predicted by GCALOR although the scoring regions used with the two programs were not identical. No overall trend was seen with one program predicting more of one particle type everywhere. The difference in photon flux for example, varied from one scoring region where GCALOR gave a 54% higher result than FLUKA to another scoring region where FLUKA predicted 48% more than GCALOR. For neutrons one could in the same way find one scoring region where GCALOR predicted 30% more than FLUKA to another where FLUKA gave 55% more. For a majority of the scoring regions the difference between the two programs was less than 20%.

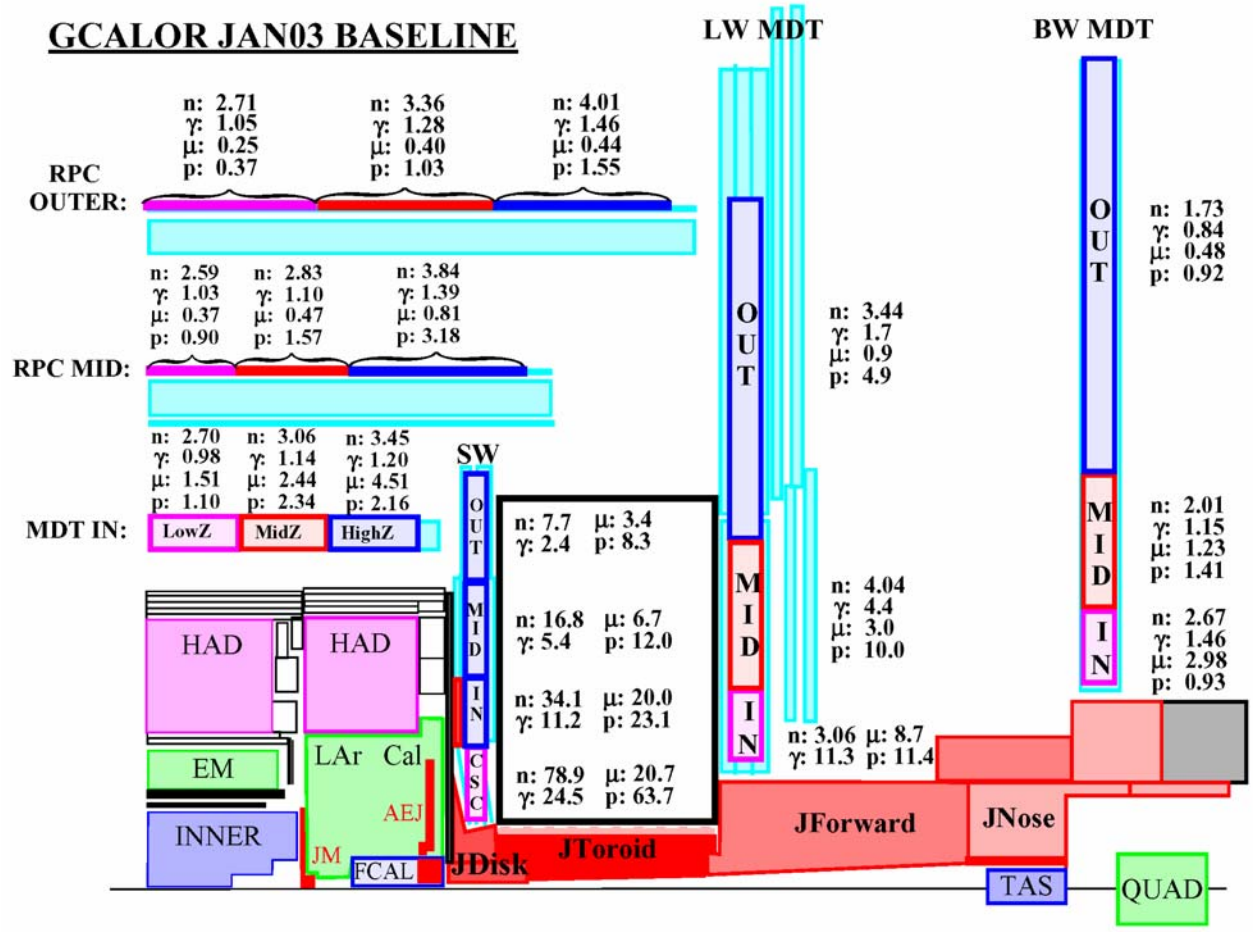

Fig. 3 Fluences in the muon chamber locations at high luminosity (10^{34} $cm^{-2}s^{-1}$) as predicted by GCALOR for the Jan03 layout. The n and γ fluences are in units of kHz/cm^2 and the μ and p fluences in Hz/cm^2.

The rates with the most recent simulation geometry in FLUKA (AV16) was also compared with the one used at the time of the Inner Detector Technical Design Report (TP44). The predicted neutron flux has gone down since the TDR with an average of 27% while the photon flux has gone down with an average of 29%.

The particle fluencies in the muon spectrometer predicted by GCALOR and FLUKA were also compared to those predicted at the time of the Muon Detector Technical Design Report. Neutron fluxes have typically increased with a factor of two while the photon flux has typically gone up with a factor of two in the barrel and a factor of three in the forward region.

INNER DETECTOR		
Type of fluence	**FLUKA**	**GCALOR**
Hadrons	Figure 5.1 & Figure 5.4 & Table 5.2	Table 5.5
Neutrons	Figure 5.2 & Table 5.1	Table 5.5
Photons	Figure 5.5 & Table 5.2	Table 5.5
Muons	Table 5.2	Table 5.5
Electrons	Table 5.2	Table 5.5
Ionisation Dose	Figure 5.6 & Table 5.2	Table 5.5
1 MeV neutron equiv.	Figure 5.7 & Table 5.1	-
MUON SPECTROMETER		
Type of fluence	**GCALOR**	**FLUKA**
Hadrons	Fig. 5.10 & Fig. 5.11 & Fig. 5.15 & Table 5.8	Table 5.10
Neutrons	Fig. 5.8 & Fig. 5.12 & Fig. 5.15 & Table 5.8	Table 5.10
Photons	Fig. 5.9 & Fig. 5.13 & Fig 5.15 & Table 5.8	Table 5.10
Muons	Figure 5.15 & Table 5.8	Table 5.10 & Figure 5.17
Electrons	Figure 5.15 & Table 5.8	Table 5.10
Ionisation Dose	Table 5.7 & Table 5.9	-
1 MeV neutron equiv.	Table 5.7 & Table 5.9	-
Single Event Effects	Table 5.7 & Table 5.9	-

Table - 1 A list of figures and tables that give the fluence of different types of particles in ATLAS as calculated by the FLUKA and GCALOR programs.

Muon system detector response and trigger rates

The impact of radiation background on the muon system has been systematically reviewed (see section 6.2). Single plane efficiency as well as the probability to fulfill the various level-1 trigger coincidences have been calculated with GEANT3. The detailed geometry description of the muon chamber setup in the cavern has been used. Energy dependent efficiency curves have been estimated for neutrons, photons and electrons. Calculations have been done for the various chamber types taking into account the angular distribution of the particles at the chamber locations. Fluxes tend to be isotropic in the barrel, while in the endcap a substantial fraction of the particles comes from the interaction region or from the main local source of radiation. Single plane efficiency curves have been compared with existing experimental data and simulation and show good agreement. Observed differences can be explained in terms of the differences in geometry or gas composition.

Average single plane chamber efficiencies have been obtained by folding efficiency curves with the energy spectra predicted at each chamber location. Uncertainties due to the shape of the energy spectrum, the angular distribution or the surrounding material have been studied and are compatible with the factor 1.5 uncertainty used previously.

Single plane counting rates have been calculated according to the formula:

$$\text{Single plane counting rate} = \mathbf{n}\times\varepsilon_n + \gamma\times\varepsilon_\gamma + \boldsymbol{p} + \boldsymbol{\pi} + \boldsymbol{\mu} + \mathbf{f_e}\times\boldsymbol{e}$$

where "**n**" and "**γ**" stand for neutron and photon particle fluences, and ε_n and ε_γ are the respective neutron and photon efficiencies for firing a single plane. Fluence is proportional to particle track length and is the relevant radiation estimator to be used for neutral particles that produce hits via an interaction. Relatively energetic charged particles traverse the chambers, ionize the gas and produce a hit with 100% probability. In that case the relevant radiation estimator is current which is proprotional to the number of particles crossing a surface (see Appendix II): "***p***", "$\boldsymbol{\pi}$", "$\boldsymbol{\mu}$" and "***e***" stand for proton, charged pion, muon and electron currents. Electron current is multiplied by a factor $\mathbf{f_e}$, that is the fraction of the electron fluence which is not produced locally by photons and thus already accounted for in the photon efficiency; the value of $\mathbf{f_e}$ has also been reviewed. Table 6.11 summarizes all chamber efficiencies. Fluences are taken from GCALOR Jan03 predictions of Table 5.8. Charged particle currents are obtained from the GCALOR fluences by multiplying with the ratio of current to fluence calculated by FLUKA for the various particle species and chamber locations (Table 5.11). The predicted counting rates are shown in Fig. 4 together with the rates quoted in the muon spectrometer TDR.

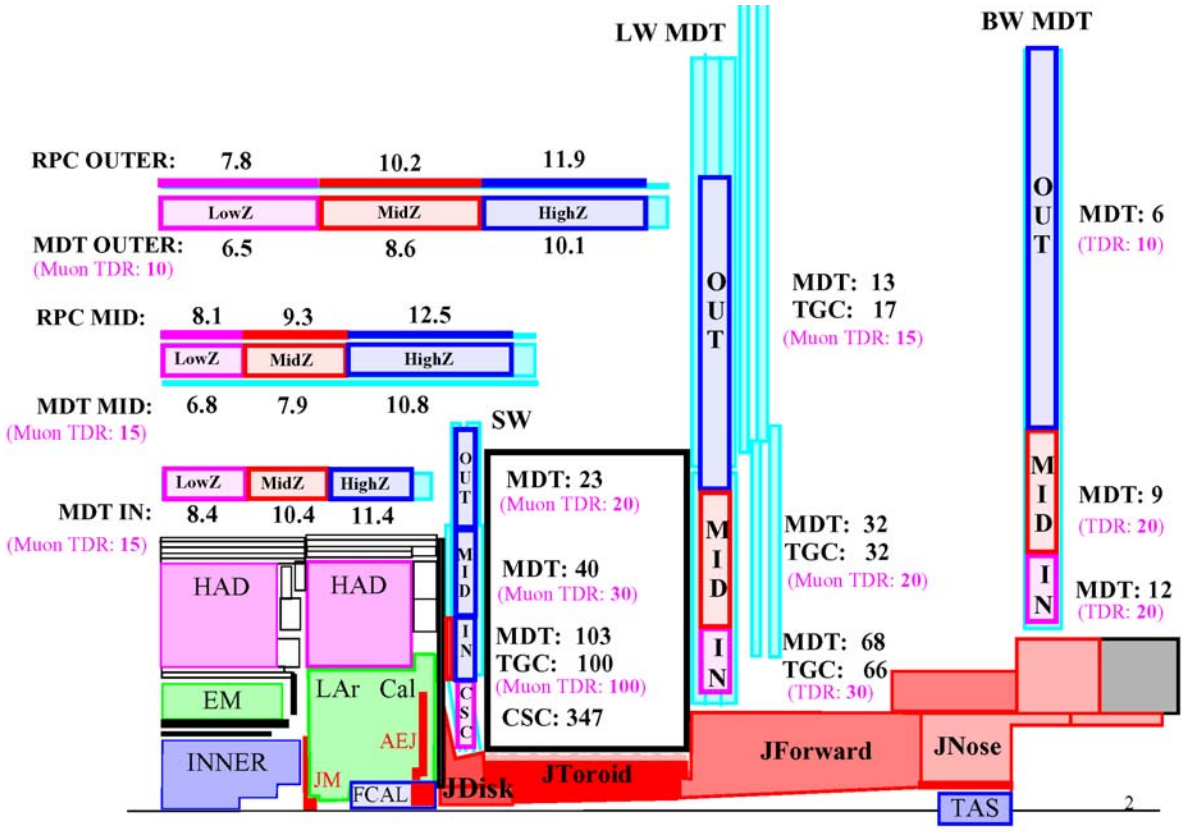

Fig. 4 Average single plane counting rate (Hz/cm2) at 10^{34} $cm^{-2}s^{-1}$ in various scoring regions. Values in parenthesis indicate the rates estimated at the time of the muon spectrometer TDR.

Counting rates in the barrel are of the order of 10-12 Hz/cm^2 both for MDTs and RPCs. They are dominated by the photon contribution (~80%) followed by neutron and protons (~10% each). In the inner barrel, the contribution from punchthrough muons raises to about 15% and from pions to a few %. In the forward region, photons contribute somewhat less to the counting rate. In the CSC for example, photons account for about half of the rate while muons account for 30% and protons for 10%. In the barrel, rates are in general similar or slightly lower than the rates quoted in the muon spectrometer TDR. Although photon fluences have roughly increased by a factor 2, the new average photon efficiencies are about 40% lower and muon and pion punchthrough contributions have decreased due to the improvements in the neutral kaon transport. In the endcap, the counting rates have doubled in the large wheel and they reach 70 Hz/cm^2 at high rapidity. However the highest rate is still the 100 Hz/cm^2 in the small wheel closest to the beam, the same level that was predicted at the time of the muon spectrometer TDR. Chambers have been designed to handle 5 times that level, in line with the overall factor of 5 uncertainty that was estimated at the time of the TDR as the result of a conservative linear superposition of a factor 1.3 on the p-p cross-section, a factor 2.5 on fluences and 1.5 on single plane efficiencies. All our studies and comparisons with available experimental data have confirmed that this is still valid. The predicted rates in the CSC are also within the specifications.

The rate of penetrating particles that generate a coincidence in a pair of RPCs or TGCs, is evaluated as follows:

$$\text{Penetrating counting rate} = \mathbf{f_p}\ \boldsymbol{\gamma} * \varepsilon_\gamma + \boldsymbol{p} + \boldsymbol{\pi} + \boldsymbol{\mu} + \mathbf{f_e} * \boldsymbol{e}$$

where $\mathbf{f_p}$ is the fraction of the photon fluence that produces a coincidence. The value used so far for $\mathbf{f_p}$ was 10%. It has now been calculated for the various chambers and regions and is found to be in the range 4 to 8%. The penetrating particle rates are given in Table 6.12. Photons and protons account for about 70% of the rate while muons and electrons share the remaining 30%, pions are negligible. The uncertainty on $\mathbf{f_p}$ is of the order of a factor 2, because "penetrating" photons are energetic and there is a relatively larger uncertainty associated to that part of the photon spectrum. However this larger uncertainty only applies to 30% of the rate.

A new effect, capable of fulfilling the 3-out-4 logic in a pair of RPC or TGC doublet, has been identified: "Double-Compton photon scattering". An energetic photon produces first a Compton electron that generates a signal in the first doublet. The photon continues, unhampered by the magnetic field, and produces a Compton in the second doublet. This new contribution to the low-p_T trigger rate has been quantified. In case of the RPC, the trigger logic window sizes in the simulation were adjusted to the real size. For the TGC, the probably for photons to fire 3 out of 4 planes of a set of TGC doublets, 2 out of 3 planes of a TGC triplet and of fulfilling the full endcap trigger logic have been calculated. However, in this case, the trigger logic window sizes were wider than the nominal size. Hence, the predictions in the endcap should be considered as an upper limit. The uncertainty on these rates, associated to the increasingly higher energy part of the spectrum, is of the order of a factor 3.

A new trigger rate estimate has been done based on the GCALOR Jan03 fluences and the complete set of new efficiciencies. Figure 6.35 shows the trigger rate estimates for the low-p_T trigger. Both in the barrel and in the endcap, rates of accidentals are low and at the same level as at the time of the muon spectrometer TDR. Applying a factor 5 overall uncertainty still lead to rates well below prompt muon rates. In the barrel, Double-Compton is of the same order as the accidentals. After applying uncertainty factors, the rates are still below prompt muons. In the endcap, Double-Compton dominates over accidentals. Applying the uncertainty factor to that rate brings it close to that of the prompt muons. However, as mentioned above, this is an upper

limit. It is thus recommended to make a more precise estimate of that effect, although applying the correct trigger window sizes will likely bring it to an acceptable level. On the other hand, the contribution of protons to the low-p_T trigger, based on an old proton efficiency estimate, is of the order of the prompt muons in the barrel and higher in the endcap. It is thus important to try to have a much more precise simulation of the proton trigger efficiency. In the case that it would be confirmed that protons may be responsible for high trigger rates, more robust trigger schemes can be implemented as described in detail in [66]. It has been shown that, with the described schemes, the trigger rate induced by the background can be reduced below the physics rate, although at the price of a somewhat lower muon trigger efficiency.

The high-p_T trigger is shown in Figure 6.36. Rates of accidentals are low, at the same level as at the time of the muons spectrometer TDR. They are acceptable, even when applying a very conservative factor 10 uncertainty. In the endcap, the probability for photons to fulfill the high p_T trigger logic has been evaluated although, as mentioned above, this was done with wider coincidence windows. This leads to an upper limit on trigger rates of the order of 1-3 kHz. The photons at the origin of these triggers have energies of the order of 100 MeV. The uncertainty on the predicted flux in that case is higher (a factor 5-10). It is recommended to make a more precise evaluation of these efficiencies, with the correct coincidence window sizes, in order to assess the associated expected trigger rate.

Shielding optimization

The shielding strategy extensively used in ATLAS consists of using dense materials wherever possible to develop hadronic and electromagnetic showers, and to range out their particles. Ideally, the material should be thick enough to absorb all charged particles. The remnants of the cascade, mostly neutrons, are moderated, either “in the shower” (for example by carbon in cast iron), or “at the end of the shower” in a cladding layer, and then captured. Fast neutrons are effectively moderated in polyethylene by elastic scattering on Hydrogen and partially absorbed by $^1H(n,\gamma)^2H$ capture. However, the neutron capture by H is responsible for a copious production of high energy gammas of 2.2 MeV. If polyethylene is doped with boron (BPE) or lithium (LiPE), the neutrons are absorbed predominantly by these nuclei due to their high neutron capture cross-section. Consequently, the absorption of neutrons by H is suppressed. In the case of BPE, production of 478 keV photons will take place instead. However these relatively low-energy gammas can be shielded by only 3 cm of iron or more effectively by lead.

There is not always sufficient space to accommodate an “ideal shielding” and it became apparent that the global optimization of the shielding involves, as the term implies, tradeoffs of one radiation effect against another. For example, in any given region there are usually bad effects coming from both low energy and high energy neutrons. But shielding design in a limited space will involve judgments about the relative seriousness of these effects from the two components, and within some margin the shield design can be tuned accordingly. The critical fluxes that have been monitored are neutrons (below and above 100 keV), photons, hadrons (above 20 MeV), pions and 1 MeV Equivalent Neutron Flux in the inner detector or counting rate and penetrating particle rates in the muon chambers.

Hundreds of geometry options were simulated using GCALOR, and consuming the majority of the CPU cycles at the ATLAS Brookhaven Computing Center from 2000 through mid-2003, and at the same time FLUKA, run at CERN and Sheffield was used for confirming highlights of each region. They are briefly summarized here. More details can be found in Chapter 8.

The inner part of the JM had to be redesigned to facilitate access to the pixel detector services

and to support it from the cryostat rather than the beampipe. The lining of the FCAL alcove has also been simplified. These changes brought only very minor increases of rates.

Optimisation of the JD shielding properties has involved simulation of a large number of design variants, where materials (and some dimensions) of the core, cone, hub, and cladding have been changed. In many cases, especially if the fractional changes are small, the effects are noticeable only in the CSC's, inner TGC's, and inner-forward MDT's. The large disk must be iron to return the magnetic flux effectively and support the inner TGC chambers. A stainless steel tube is attached to the disk and serves as a support for the copper shielding inside and the shielding "hub" outside. Some of the most important conclusions are: the cone filling the space in front of the CSC is necessary; the material should be copper, not iron. The cladding is needed both in the cone and in the hub. Dimensions and composition have been optimized. Changing the inner core to tungsten improves radiation in many regions by 15 to 30%. Since the cost is very large, of the order of 1.5 MCHF, this option is kept as a possible upgrade.

The toroid region is composed of the JTT shield in the inner bore and the JTV consisting of the various moderator layers situated inside and outside of the endcap cryostat. The JTT relative absorber and cladding thickness and composition have been optimized to compensate as much as possible for reduction in space and the change from pure copper to copper alloy for cost reason. The moderator layer inside the forward toroid between the coils could not be retained for engineering reasons and instead moderator rings and a front wall inside the cryostat as well as a back wall outside of the cryostat have been studied and included in the design.

The massive forward shield between the back of the forward toroid and the front of the JN shield (TX1S) underwent major engineering revision. The previous design concept had filled the "maximum available envelope" of the muon acceptance and was conical with outer surfaces along $|\eta| = 2.7$ but was "overshielding". A new engineering concept for the structure and assembly sequence has allowed reducing significantly the mass without raising the background rates appreciably in the muon system detectors. The background rates are determined by the weakest points, i.e., the JT and to some extent the very front part of JF. Adding 1000 tons of iron to other parts is useless. The relative absorber and cladding thickness of the front part has been optimized. A staging option has also been proposed.

The JN region is the responsability of the LHC but the task force has collaborated in the optimization of the design. A series of cast iron "washers" slide on a central steel tube and a block surrounding the TAS is bolted inside the tube. Dimensions and composition have been checked.

A number of additional studies have been carried out: (1) varying the beam pipe parameters to better understand its background contribution and anticipate its eventual redesign, (2) checking the effects of increasing service gaps, and (3) exploring the effects of the cavern shape and wall composition.

Background rates in USA15

The USA15 cavern next to the ATLAS experimental cavern is going to contain most of the electronics in the experiment. When the wall between the USA15 cavern and the ATLAS cavern was designed it was required that the radiation levels in USA15 should not exceed those permitted for a simple controlled area, i.e., an area to which people can have an unlimited access as long as they are equipped with a filmbadge. Based on a study by Ferrari et al. in 1995 [2,3] it was decided that the wall thickness should be 2 meters since this would give a dose rate of at

most 3 μSv/h in USA15. Another study of the attenuation of radiation through passageways and duct was made in 1999 by Rollet, Potter and Stevenson [4]. It concluded that the attenuation was sufficient everywhere.

There are several reasons why the Radiation Task Force found it necessary to again study the problem of the radiation levels in USA15: (1) The radiation levels in the experimental cavern have increased by typically a factor 2-3 since the early studies; (2) The size of the ATLAS experimental cavern has on the other hand increased which will lower the amount of radiation reaching USA15; (3) The study by Rollet et al. did not include the final design of the trigger holes that penetrates the wall between the ATLAS cavern and USA15; (4) It is expected that the limits for a simple controlled area will be lowered in the future.

The Radiation Task Force made a coarse estimate in 2003 based on the change of high-energy neutron fluences that are driving the penetrating component through the wall while taking into account the increase of the distance between the wall and the interaction point. This gave an estimated dose of 5 μSv/h at the worse regions of USA15 which are in the "plume" of neutron radiation coming out of the endcap toroid magnets (see Fig. 5).

However, the effect of the new trigger cable ducts in the wall was not taken into account and the estimated dose was uncomfortably high. Hence, a new complete and more precise calculation has been carried out which is reported separately [5]. The results in the new study are consistent with the coarser estimates as can be seen in Fig. 5. This study also showed that the trigger holes are not expected to increase the radiation levels with a large amount and that it is the "plume" regions where the radiation will be the highest.

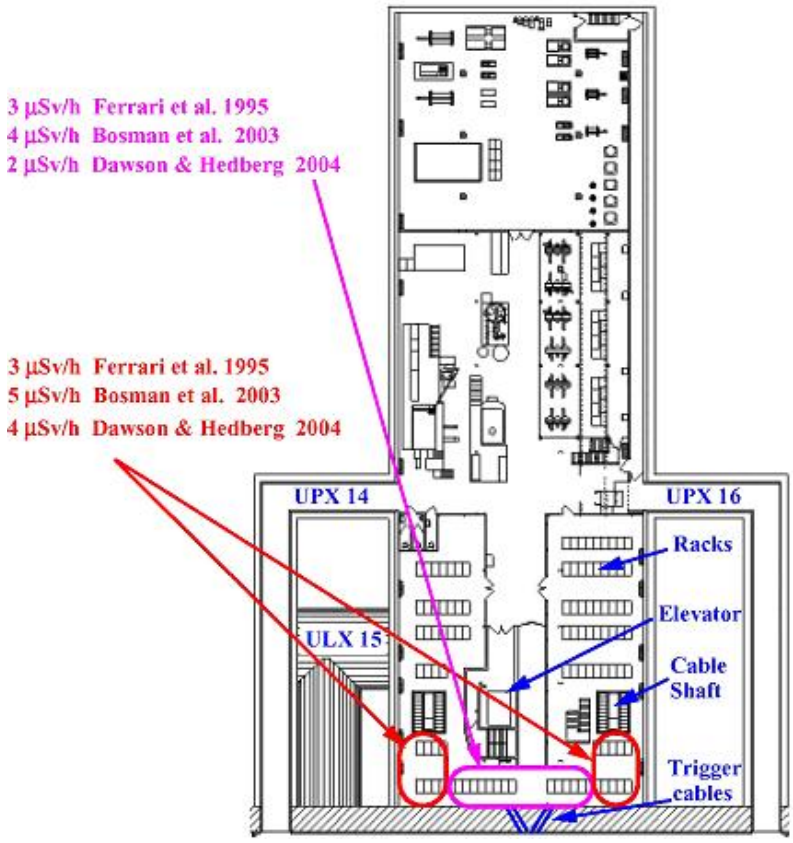

Fig. 5 Layout of the lowest floor in USA15. Two regions, close to the wall between USA15 and the ATLAS cavern, are indicated together with the expected dose rates in these regions during running at 10^{34} $cm^{-2}s^{-1}$.

Activation

Induced radioactivity will be a major problem at the LHC. Activation was not taken into account as a design criteria when ATLAS was designed and of the LHC experiments it is in ATLAS where one will encounter the highest levels of induced radiation. This is due to the small radius of the ATLAS beampipe, the small bore of the forward calorimeter and the shielding elements close to the beampipe.

A group of nuclear physicists lead by M. Morev at the Moscow Engineering Physics Institute has worked in close cooperation with members of the Radiation Task Force to calculate induced activity in ATLAS and the result is the most comprehensive study of induced radioactivity in any of the LHC experiments. There are now more than 600 radiation maps for different regions, running times and cooling-off times available on the ATLAS activation web-pages [109]. The calculations have been crosschecked with other calculations made in ATLAS and by the CMS collaboration and are in a good agreement with those.

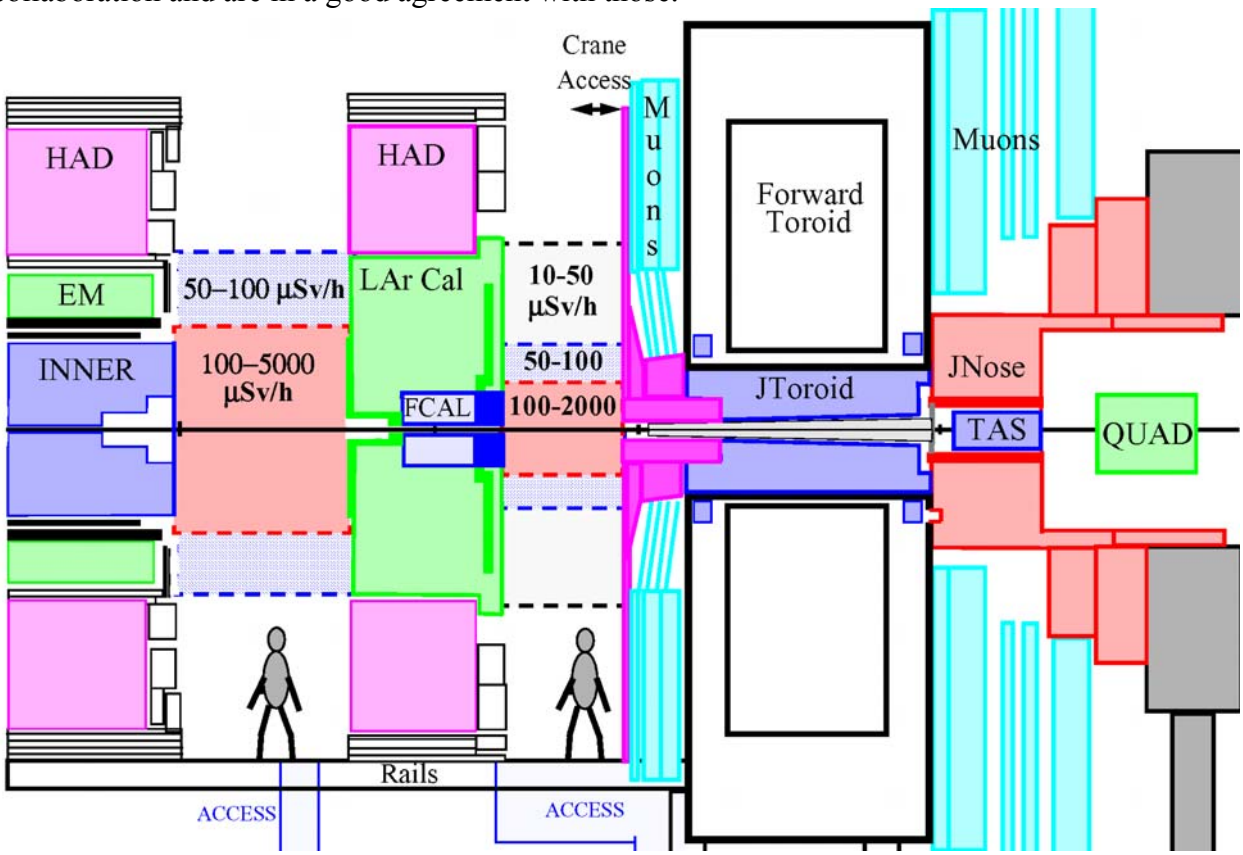

Fig. 6 One half of the inner region of the ATLAS experiment during standard access. The predicted dose rates in the two access areas are also shown. The calculation was done for one year of running at 10^{34} $cm^{-2}s^{-1}$ and five days of cooling off.

The basic conclusion of the study by Morev et al. is that the beampipe will be the major source of radiation in ATLAS. Fig. 6 shows the radiation levels in the two access areas during standard access. It is recommended that the area around the beampipe, out to a radius of about one meter, is fenced off by a cage-like structure. This will ensure that people working in ATLAS during standard access will not receive more than 0.1 mSv/h and that people thus will be able to work for at least 2-3 weeks before reaching their yearly dose-limit. The only detector that will be inside the cage is the inner detector and so only maintenance of the inner detector will be

severely limited during standard access. With the beampipe in place it will in any case be difficult to do extensive maintenance to the inner detector and so the limited availability of the inner detector might not be a problem.

ATLAS has a second access scenario which is called the Inner Detector access scenario. In this scenario all the beampipe sections except the one in the Inner Detector are removed as well as the small muon wheel and the endcap toroid. The final configuration is shown in Fig. 7. Also shown in the figure are the results of calculations of the dose rate by Morev et al. Two hotspots are clearly seen. One is due to the end piece of the Inner Detector beampipe which is made of aluminium (the rest of the beampipe is made of beryllium) and here the dose rate can reach 0.2 mSv/h. It is recommended that this relatively small area is temporary shielded with lead blocks during maintenance of the Inner Detector. The other hotspot is in front of the forward calorimeter where the dose rate is predicted to reach as much as 0.5 mSv/h. It is therefore recommended that also the front of the FCAL is temporary shielded with lead plates but it has to be made in such a way as not to limit the access of the crane. With these precautions it should be possible to work on Inner Detector maintenance for at least 5 weeks per person and year.

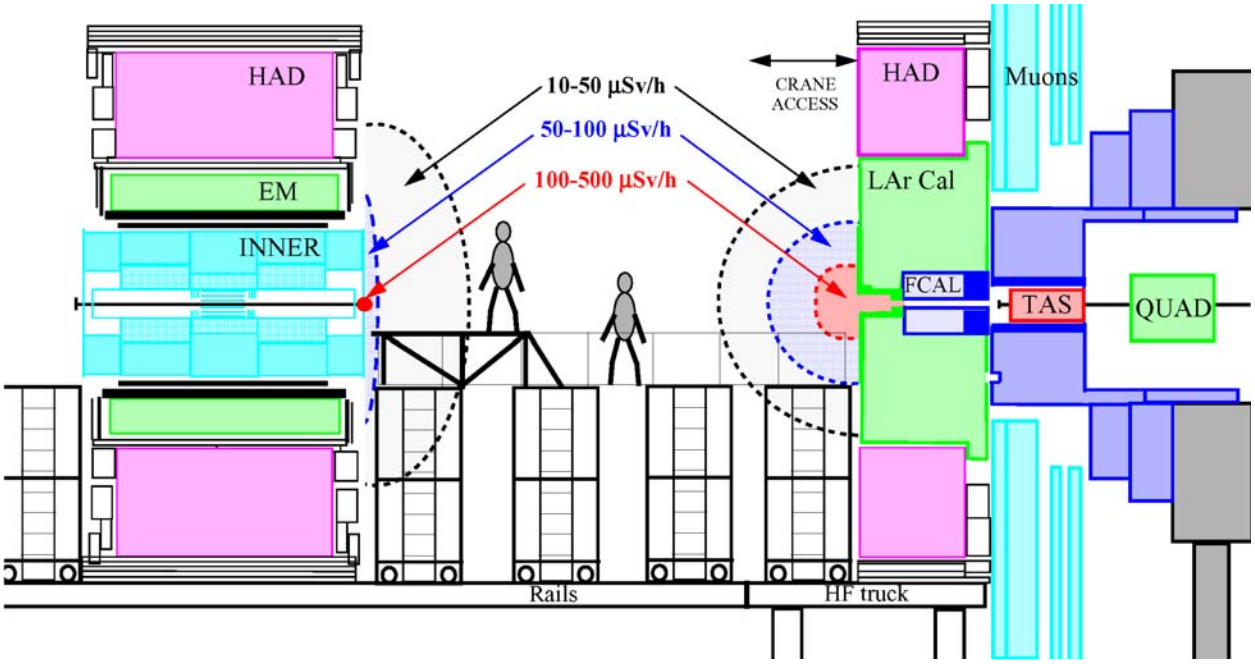

Fig. 7 The central part of the ATLAS experiment during Inner Detector access. The predicted dose rates close to the Inner Detector and the endcap calorimeter are also shown. The calculation was done for 10 years of running at 10^{34} $cm^{-2}s^{-1}$ and five days of cooling off.

One problem with the Inner Detector access is that the very radioactive beampipe has to be removed. This could give the vacuum technicians several mSv of integrated dose and since they will have to work on several LHC experiments this might become a serious problem. One way of reducing the dose to the vacuum people is to make the beampipe out of aluminium instead of stainless steel. This is expected to give a factor 10-50 in reduction of dose levels. If the beampipe material is instead changed to beryllium the dose rate would go down with a factor 100-1000 but this is a very expensive option.

.

High Luminosity Running

The LHC has asked the experiments to consider the possibility of running at higher than current design luminosity, perhaps as high as 10^{35} $cm^{-2}s^{-1}$. In this event, the beamline and shielding in ATLAS will need major redesign. A study of this was made in 2004 which is reported separately [6]. The basic conclusion of this study was that a change of the material of the beampipe from stainless steel to beryllium (at a cost of at least 2 MCHF) would lower the activation of the beampipe to almost nothing and reduce the background rates in the muon spectrometer with a factor 2-3. Even drastic changes to the shielding design could on the other hand not reduce the background rates in the muon spectrometer with much more than a factor of 2 and so the most effective way of reducing the background radiation is to eliminate the source of the background rather than to try to shield against it.

Conclusions

The ATLAS Radiation Task Force has met its charge, and done a number of investigations well beyond the scope of the original plan. This effort has taken two to three times longer than expected, and has required dedicated work of more people than might have been anticipated. But it has nicely bracketed the time when all the major decisions on the ATLAS forward shield were made. All shielding components are now completed, in fabrication, or have been committed to fabrication. We are all looking forward to the day in 2007 when collisions begin in ATLAS and, as peak luminosity is achieved, to seeing the radiation background levels created by the natural processes of particle physics, instead of by simulation.

1 Introduction

The high design luminosity and the high energy of the LHC beams generate important levels of secondary radiation in the detector and in the Atlas experimental hall. A large effort has been made since the early phase of the detector design to calculate the radiation background in the different areas of ATLAS and to design an effective shielding [7,12].

The taskforce was created in July 2000 to evaluate the understanding of the radiation levels in ATLAS. The taskforce mandate included looking into the geometry and material used in simulation, the physics models and the analysis methodologies used for evaluating the radiation background. The task force was also asked to evaluate the most critical areas, i.e. where small variations in physics, geometry and material have the strongest impact on the radiation levels. The charge of the taskforce was also to contact colleagues responsible for different parts of the apparatus to ensure that the corresponding geometry modeling in the background calculations corresponds to the set-up being built. The taskforce would analyse the levels predicted and their impact on ATLAS.

Radiation Backgrounds at the LHC

Particles from the proton-proton inelastic collisions are responsible for the bulk of the radiation background expected at ATLAS and CMS, as opposed to backgrounds originating from beam-gas and beam-losses [14]. In the inner detector, these particles can be the most serious radiation background. However we are also often concerned with radiation produced by particles interacting with the beam line system and structures near it, or creating showers in the calorimeters. In the final analysis, any source of secondary particles, no matter how strong, can be attenuated to a harmless level as long as there is sufficient space available for shielding materials. Much of the work of the taskforce has centered on the problem of shielding a number of background sources simultaneously in regions where the space for shielding materials is limited.

Atlas Detector Concept and Consequences for Background

The overall layout of the ATLAS detector is shown in Figure 1.1. ATLAS has an inner detector region with low-mass tracking detectors in a solenoidal magnetic field, surrounded by hermetic calorimetry. So does the CMS experiment. However their forward region and muon systems are substantially different. The CMS forward calorimeter stands by itself, beginning at 11 meters from the interaction point; whereas the ATLAS forward calorimeter is considerably smaller and integrated into the liquid argon endcap calorimeter, with its front face at z = 4.7 meters. The CMS muon system consists of magnetized iron blocks interleaved with tracking planes; whereas the ATLAS system has air core toroidal field coils and tracking chambers suspended together on open space frames. As a result, in CMS the forward region is “open” for a larger distance along the beamline than in ATLAS. But less shielding is required to protect the CMS muon system from forward calorimeter radiation, because it is much more self-shielding than the ATLAS muon system. Both experiments have collimators (TAS) at z = 19 meters to protect the final focus quadrupoles from radiation from the interaction point. But the beamline designs are different in several ways. The CMS beampipe is “flared” to larger radius in front of its forward calorimeter, and in two regions behind. Unfortunately, ATLAS access scenarios require a smaller, uniform-diameter, beampipe to large distances from the interaction point (see Figure

1.2). This small pipe presents target material in the region where there is a large high-momentum flux of primary particles, and the ATLAS beampipe creates a "line source" of secondary particles between the back of the forward calorimeter and the front of the TAS.

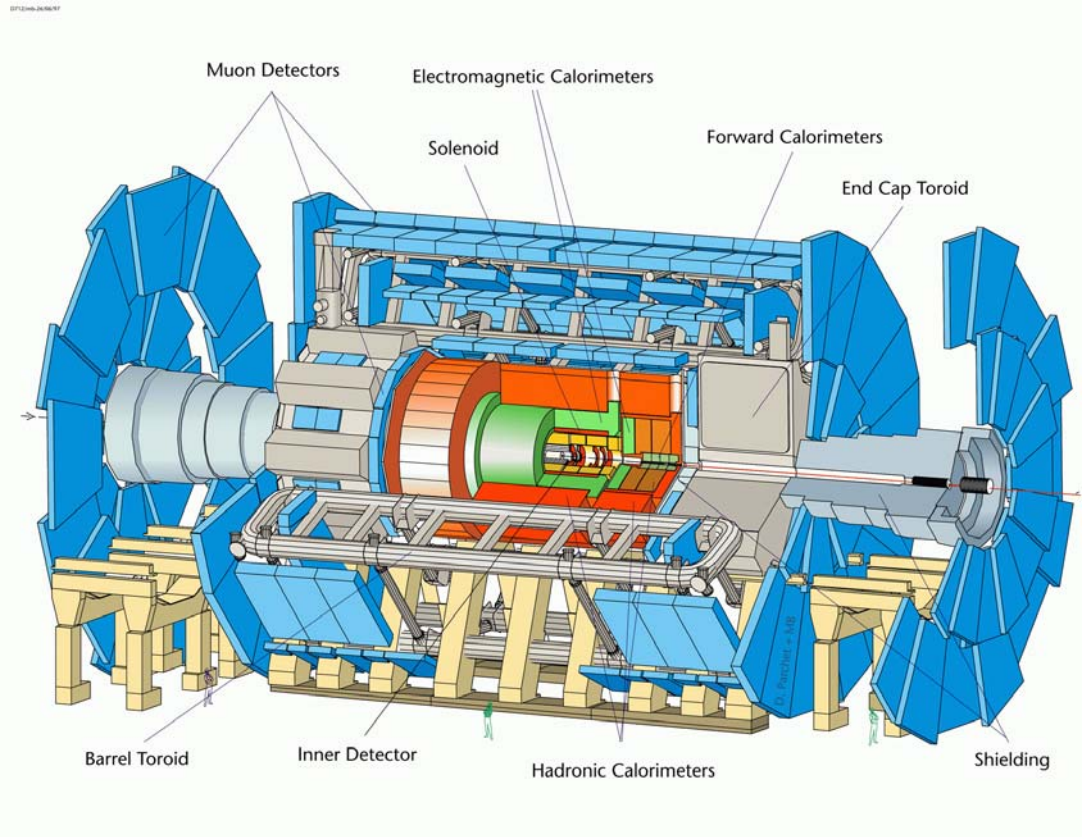

Figure 1.1 Overall layout of the ATLAS detector

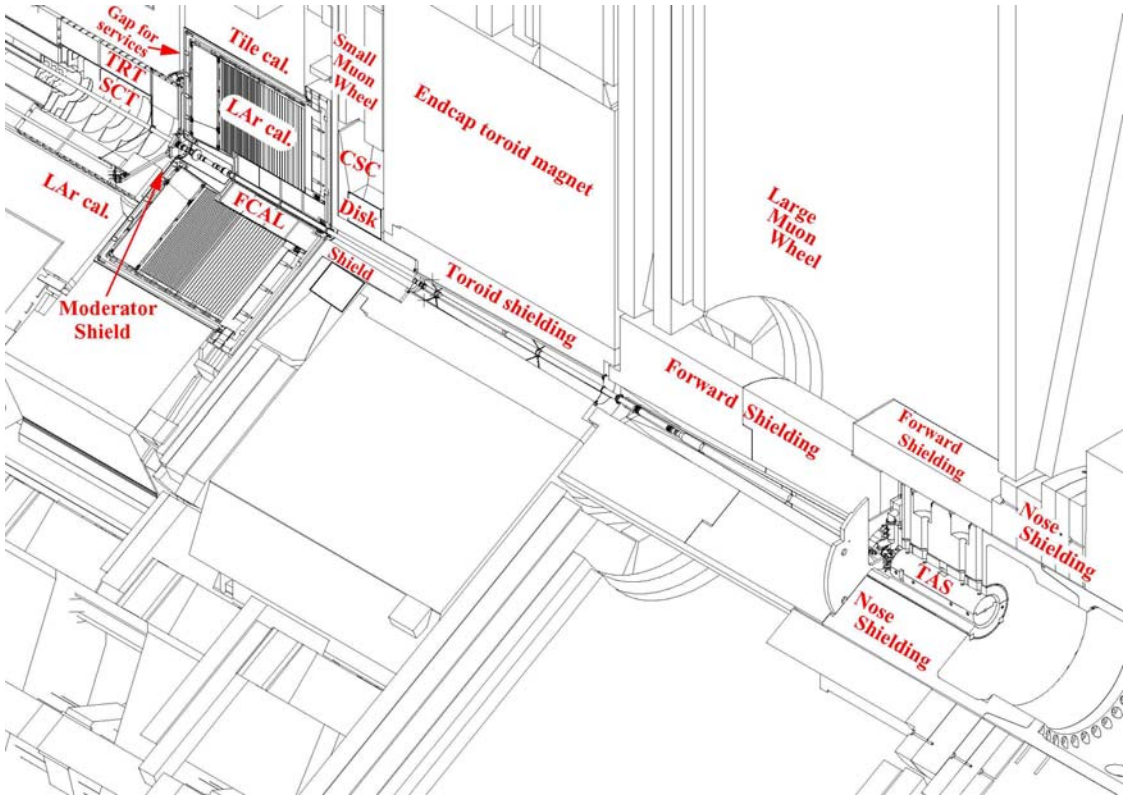

Figure 1.2 Beam line and nearby detector elements

Main sources of background

Inner Detector Cavity:

The inner detector sees the primary particle production coming from the interaction point, along with albedo particles with their largest number coming from the face of the endcap calorimeter. For primaries, the most serious background component is charged pions. Albedo particles are predominantly thermal and low energy neutrons. Hadrons above 10 MeV are less numerous, but are also important, as we shall discuss in more detail in section 5.2. The other feature of this region is the services gap between the barrel and endcap calorimeters, which can potentially allow radiation in the inner detector to escape into the barrel muon system.

Forward Region and the Muon System

One can understand the secondary sources leading to background radiation in the "outer" regions of the detector by first looking at the locations where the most energy is deposited by primary particles. The three hottest sources in order of importance are (1) the core of the TAS collimator at 19.5 meters, (2) the core of the forward calorimeter at 5.2 meters, and (3) the beamline, from 5.2 meters to about 14 meters. The energy deposited in each TAS collimator is of the order of 2.3 TeV [18]. Each FCAL calorimeter absorbs about 0.45 TeV while about 50 GeV are deposited in the beam pipe. However, the radiation background reaching the detectors due to these sources is, roughly speaking, in *opposite* order of importance. The TAS copper is somewhat self-shielding (flux containing), and is surrounded by massive shielding. The forward calorimeter is also self-shielding, but sits inside the endcap calorimeters, and is not far from the first forward muon station, where the CSC's are the nearest muon detectors. There is relatively little space for shielding in this "corner" of the detector, and many design iterations have been done to optimize the shielding shapes and materials in this region. Finally, as noted above, the beam pipe creates a long line source of secondary interactions and though it is low mass, it is not self-shielding. This source feeds secondary particles into the thinnest region of the forward shield, the core of the forward toroid magnet, which has also been the subject of exhaustive study and design iteration. Particles emerging from the thinnest sections of the forward region are not only the main backgrounds in the forward region; they also create most of the radiation background in the muon barrel with the services gap contribution being small by comparison.

History of radiation background simulation prior to task force

Beginning in the early 1990's, Alfredo Ferrari used the Standalone FLUKA package to provide background radiation calculations for the ATLAS experiment, as part of design and engineering for the experiment. By 1993 this effort was focusing on two major areas: the inner detector cavity, and the muon region (in effect, the two "open" regions of ATLAS). Ferrari, along with Paola Sala, worked closely with the Forward Integration Working Group, convened by Peter Norton. The main activity was to design shielding to protect the muon system from hot regions near the beamline, in particular, the TAS collimator region.

In 1994, there was a major revision of the ATLAS calorimeter design when the Calorimeter Review Panel, Chaired by John Dowell, rejected the original far-forward calorimeter design, with standalone calorimeter subsystems placed at 13.0 meters from the I.P., in favor of an integrated forward calorimeter design proposed by the University of Arizona. In the latter configuration, the forward calorimeters (a new small-gap design) are inside the endcap calorimeter vessel, with front faces at $z = \pm 4.5$ meters. This concept improves forward jet

resolution and more importantly for the muon system, bottles up much of the forward radiation inside the forward calorimeter modules. Moreover, flux escaping the beam hole in the forward calorimeter enters a space where the beamline can be heavily shielded without affecting either calorimeter or muon system acceptance in the "shadow" of the FCAL. The net result is a reduction of backgrounds in the muon system by approximately two orders of magnitude relative to the far-forward design.

Beginning in 1994, as part of the proposal process for the integrated FCAL design, Michael Shupe began simulating ATLAS radiation backgrounds using the GCALOR package written by Christian Zeitnitz for use in the design of SSC experiments. GCALOR is an interface between GEANT3 and CALOR, the neutron transport package developed at oak Ridge by Tony Gabriel. By early 1994, the new integrated FCAL geometry was being simulated in both FLUKA, and in GCALOR. This tradition of "dual" simulation has continued up to the present and has been crucial to the avoidance of mistakes and to the understanding of uncertainties.

Between 1995 and 1998, the majority of the ATLAS background calculations were done by Ferrari and Sala, using FLUKA, with periodic checks of the most current geometry by Shupe, using GCALOR. This changed in 1998, when Ferrari and Sala left for other experiments. In spring of that year, Shupe was appointed to convene the Radiation Backgrounds Working Group and at that point the bulk of the calculations shifted to GCALOR. That summer, the experiment entered a phase of intense final-engineering design in a number of the subsystems, including portions of the forward shield.

Fortunately, continuity was maintained through this transition period in late 1997 through 1998. Ferrari presented a design configuration with full rate calculations to an LHCC review in February of 1998. This design (TP43) was also simulated fully in GCALOR and remains as one of the benchmarks used for comparison with current rates. In addition, the Radiation and Shielding Working Group chaired by Marina Cobal had been working through 1997 and early 1998 to augment Ferrari's work. The work done in that context is summarized in a note [9].

Ian Dawson (University of Sheffield) joined the effort in mid-1998. He had already used the FLUKA program for several LHC machine design studies, agreed to take on the task of doing full simulations for ATLAS and liaised with Ferrari in order to become familiar with the ATLAS situation. Ferrari and Sala provided ongoing assistance to Dawson during this period. In return, Dawson's own persistance in understanding unstable behavior in the simulation of neutral kaons lead to improvements in FLUKA (provided by Ferrari and Sala) and ultimately, in GCALOR. From 1999 to the present, the Radiation Working Group had operated in this mode, using both transport codes for comparison in critical geometries and doing a large number of independent studies in the domains where each transport code excels.

In 1998, the focus of shielding development shifted to the Shielding Engineering Working Group, convened by Werner Witzeling. GCALOR and FLUKA have been used in tandem, often in specialized studies particularly suited to one or the other. At times where major shielding revisions were complete, "identical" full geometries were produced for both transport programs and run for comparison. Since this history spans more than a decade, it is necessarily oversimplified. During this same period there were important contributions to the understanding of ATLAS radiation backgrounds and activation from Alberto Fasso, Yuri Fisyak, Sue Willis, Vladimir Sirotenko, Marina Cobal, Andrei Ozunian, and Gianpaolo Benincasa. In particular, Ivan Štekl and collaborators, using GCALOR interfaced with a different photon sector, GAMLIB [26] contributed extensively to the radiation and shielding studies. The shielding design is also the result of the work of many dedicated engineers who have contributed to this

project, including Bertrand Nicquevert, Jean Pierre Corso, Ian Hooton, Jenda Palla, François Butin (TAS and JN region), Ed Towndrowe (forward toroid core), Leif Shaver (endcap plugs), Jaromir Sodomka (inner detector cladding and JM) and Ray Veness (beam vacuum system).

In 2000, the ATLAS management realized that the shielding simulation task, and its coordination with subsystems, had become too large for Shupe and Dawson, and the Radiation Backgrounds Taskforce was created, chaired by Martine Bosman. Bosman coordinated the collection and analysis of subsystem engineering data on materials and dimensions and initiated a number of crucial analyses of shielding effectiveness. In 2001, the convenorship of the Shielding Engineering Working Group turned over to Vincent Hedberg, who brought additional expertise on activation to the working group. A complete re-assesment of the shielding was made which resulted in the shielding being reduced by more than 1000 tons of different materials as described in this document. The engineering design of all parts of the shielding was also greatly simplified in order to reduce cost. Also in 2001, Sergei Baranov began new investigations of the response of muon system detector elements to background radiation, with detailed GEANT3 descriptions of each chamber type. Baranov, Leandro Nisati, and Martine Bosman have carried forward the analysis to understand muon system counting rates and trigger rates much more deeply, based on these simulations.

In sum, beginning in the early 1990's, ATLAS radiation background simulations have been done throughout the design, engineering, and production phases of the experiment, and have lead to simulation and analysis of the radiation effects on detector response, detector damage, trigger response, electronics damage, and safety during running and accesses. A number of ATLAS collaborators, both physicists and engineers, have contributed to this process, and the simulations themselves have been built on software developed over many years by physicists both inside and outside ATLAS.

2 Shielding Physics and Strategies

High energy particles from the interaction point initiate hadronic and electromagnetic showers, as they encounter the materials of the detector and its services. If the material is thick, these cascades will continue until most of the charged particles have been absorbed (with muons typically the exception). Hence, "inner" shielding material should be as dense as possible to shorten the showers and of sufficient depth to contain most of the deposited energy.

The remaining neutrals are mostly neutrons, which can travel long distances, losing their energy gradually. These remnant neutrons lead to further photon production. Gammas result from excited-state decays of spallation products and from fast neutron interaction with atomic nuclei. At the lowest energies, thermal neutrons result in production of gammas by the process of nuclear capture.

For shielding to be efficient, most of these neutrons and gammas should be confined to the shielding volume. This implies that an optimized "outer" shield should be a structure made of neutron and gamma absorbing materials, sometimes in the form of "cladding layers". These layers are selected and combined to increase moderation (slowing by elastic collisions) of unconfined fast neutrons and to attenuate gammas produced by the neutron interaction processes mentioned above.

Shower lengths will be determined by the material-dependent length scales, L: radiation lengths for electrons and photons, and hadronic interaction lengths for hadrons. The first interaction will occur at a vertex inside the material, following the usual $e^{-X/L}$ distribution, where X is in units of the length scale and shower maximum will occur a few L later. Shower lengths increase logarithmically with particle energy so, as the energy increases, shower maximum moves deeper into the material and leakage out the back of the shielding increases.

Material	**ρ (g/cm^3)**	**Λ_0 (cm)**	**X_0 (cm)**	**Comment**
Pure Cu	8.9	17.5	1.45	(expensive)
Cu Alloy	8.6-8.8	18.0-18.4	1.40-1.35	(machinable)
Pure Fe	7.9	19.1	1.8	(n resonances)
Steel	7.8	19.2	1.8	(low carbon)
Cast Fe	7.2	20.4	2.0	(3% carbon)
Pb	11.4	18.9	.56	(γ filter)
Pure W	19.3	10.3	.35	(elemental)
W Alloy	18.2	11.2	.38	(expensive)
Concrete	2.4	46.9	10.9	(walls)
C	2.3	50.0	18.8	(moderator)
Al	2.7	37.2	8.9	(structural)
Polyethylene	.94	92.4	47.0	(moderator)

Table 2.1 Radiation lengths and interaction lengths for the materials more commonly used in the shielding

Table 2.1 shows these length scales for the materials most commonly used in shielding. Since $\Lambda_0 >> X_0$ for the materials used for dense shielding, hadronic shower development sets the thickness scale for radiation shielding, and the logarithmic increase of shower length with energy implies

that shielding thickness must increase in regions where the average incoming flux has higher energy per particle. This is the case in ATLAS (see Figure 2.1), where the integrated shielding depth between the interaction point and the muon system increases with |η|, to follow the increase of particle energies with |η|.

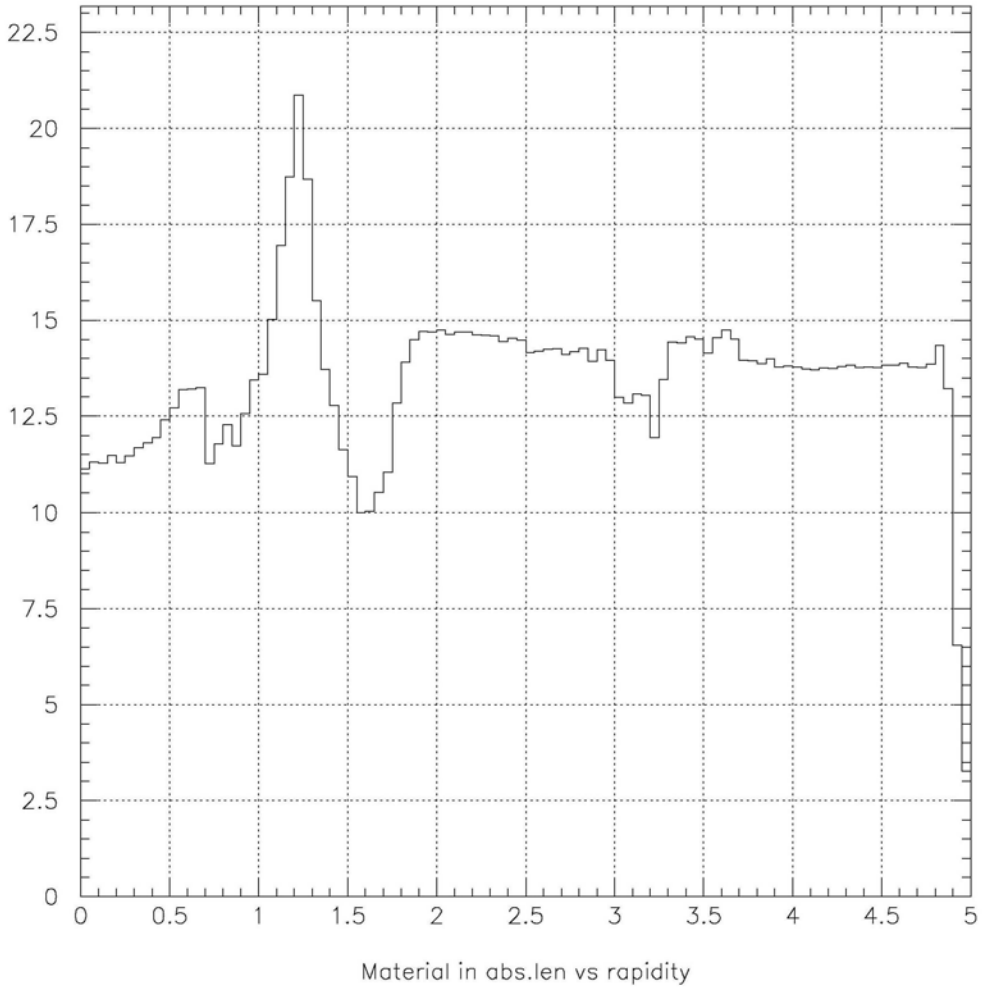

Figure 2.1 Total thickness of calorimeters and plugs in Absorption Length.

The parts of the ATLAS detector most relevant to shielding of radiation backgrounds in the muon system are the dense, massive structures of the calorimeter system. These in themselves are insufficient to protect the muon system and other components from background radiation, so additional structures must be added to shield these systems from radiation hot spots. In many locations, cladding layers must be used in addition to further attenuate low energy neutrons and photons.

Physical Processes Affecting Shielding Depths and Material Choices

Electromagnetic Showers

In dense shielding, we are most concerned with the formation of electromagnetic showers in the GeV range and beyond. Radiation lengths in dense material are typically in the centimeter range, and the p_T of the interactions is most often low. As a result, high energy electromagnetic showers have a characteristic tranverse dimension (Moliere radius), of order 1 centimeter and longitudinal dimensions of tens of centimeters. In contrast to hadronic showers, electromagnetic showers are

very uniform because (1) the particle statistics are large and (2) high momentum transfer interactions are rare (eg. from the tails of plural scattering).

Hadronic Shower Composition at High Energies

Through a variety of hadronic and nuclear processes the incident hadron will produce secondaries that are predominantly pions (π^+,π^-,π^0), followed in importance by nucleons (p,n), strange mesons and baryons (kaons, Λ^0,...), and photons.

The π^0 component is noteworthy, since their two-photon decays produce imbedded electromagnetic showers and irreversibly shift shower energy from the hadronic to the electromagnetic sector. The electromagnetic fraction of the total shower energy increases with incident energy because there are more generations of shower cascade, giving more opportunities for π^0 production.

Some muons will be produced in the shower due to charged pion decay, and will most often exit the calorimeter or shielding where they are produced. But in most cases these are greatly outnumbered by the muons resulting from charged pions from the interaction point, decaying in the inner detector. At the highest η in the inner forward muon system, these muons pass through the calorimeter and are comparable to other sources of radiation background in this region.

Charged Particle Energy Loss

Most energy loss for high energy charged particles is due to the atomic processes included in the Bethe-Bloch formula for dE/dX, often referred to as "ionizing energy loss". The cross sections for these atomic processes are so large that dE/dX energy loss accounts for "all" of the energy deposited in EM showers, and roughly 2/3 of the energy deposited in hadronic showers. This fraction has large fluctuations from shower to shower and evolves with energy. These large dE/dX cross sections imply that hadronic shower shape is determined primarily by the sequence of hadronic interactions, coupled to dE/dX loss of charged particles as they propagate in materials

Neutron Propagation

Lacking dE/dX loss, neutrons propogate "decoupled" from the rest of the shower, subject to elastic scattering and low energy nuclear interactions, and in most situations, considerably more penetrating than the charged component. Much of the complexity of GCALOR and FLUKA is associated with neutron transport, and we focus on this sector in upcoming sections.

Intermediate Energy Regime and Energy Loss

Hadrons above approximately 100 MeV can undergo nuclear reactions that lead ultimately to the creation of more neutrons. The most violent of these are spallation processes that may break the nucleus into a number of small or large fragments, accompanied by the direct release of neutrons and the possibility of additional neutrons evaporating from the fragments.

Since these fragments are ionized by the collision, and have large Z, they will stop quickly in dense materials by dE/dX energy loss, and may deposit sizeable quantities of ionization in very small regions. The local ionization densities from these types of events may be hundreds of times larger than those typical of minimum ionizing particles. When calculating the “total ionizing dose” (TID) in a given region, one must add these contributions to the usual dose calculated from the dE/dX loss of individual particles.

Nuclear Resonance Scattering

To complicate the neutron phenomenology further, the total cross section in some materials exhibits a rich resonance structure in the domain where incident neutrons are of the right energy to excite nuclear energy levels. A classic example of this in an often-used shielding material is pure iron, whose cross section exhibits a rich resonance structure beginning at around 1 keV and ending around 5 MeV, as shown in Figure 2.2. This region creates a problem because neutrons at the cross section peaks will be absorbed. However for neutrons with energies in the minima, the material will appear much more transparent and these neutrons may escape the shield. In many cases, cast iron can solve this problem because its carbon content causes a small moderation effect. Even this small effect helps, because it shifts neutrons at the minima into the peaks, where they interact.

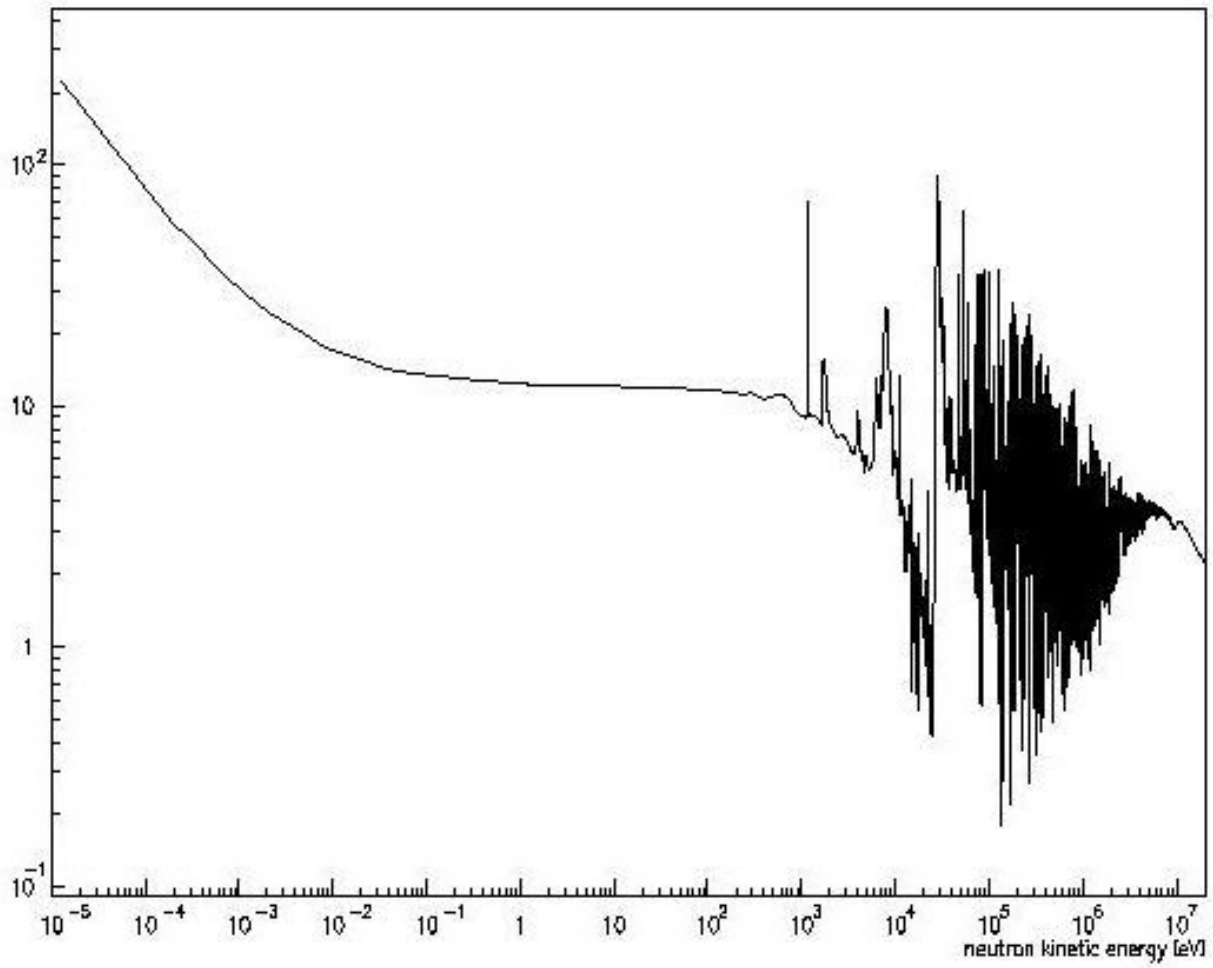

Figure 2.2 Neutron cross-section in pure Fe.

Neutron Elastic Scattering and Moderation

The neutron elastic scattering cross section on nuclei is large at all energies and leads to a useful tactic that is often employed in shielding applications to reduce neutron backgrounds. Kinematics dictates that the scattered neutron will give up energy in each elastic collision, especially if the target nucleus is light, and carries away a large fraction of the energy as it recoils. So hydrogen and light elements are most effective at reducing neutron kinetic energy. This process is called "moderation" and materials introduced to cause it are called "moderators". Hydrogen and carbon are the two most practical and commonly used moderators. In ATLAS,

polyethylene is employed as a hydrogenic moderator, and cast iron is used in place of steel where practical because of its (few-percent) carbon content.

What is gained by moderating neutrons if their numbers are not changed? There are two advantages:
(1) In most cases, high energy neutrons are a more serious radiation background than low energy neutrons because they can do more damage or cause electronic disruption. Moderation can drop their energies below damage thresholds.
(2) At low energies, neutrons can be stopped by additional materials with large capture cross sections.

Low Energy Regime: Thermal neutrons

Note that by the process of repeated elastic scattering, neutrons can be moderatd to the point where they reach equilibrium with the thermal velocity distributions of the materials in their environment. At this point they are termed "thermal neutrons", with energies typically as low as 10^{-5} eV.

Materials such as lithium, boron, and cadmium have large neutron capture cross sections, and may be used "as is" in some convenient compound, or added as dopants to moderators such as epoxy or polyethylene. This latter form is particularly efficient since the neutrons will be captured in the mixed material as soon as they are moderated to low energies.

The disadvantage of enhancing neutron capture with dopants is that capture gammas are radiated during the process, and if these are sufficiently high energy, they must be attenuated. As stated in the overview to this section, layered cladding is often used to provide moderation and capture in one layer, followed by photon attenuation in another.

Air Gaps and Chicanes

In the course of the engineering design at interfaces, air gaps may be introduced, that constitute potential channels for radiation backgrounds to penetrate shielding. But there are a number of effects that determine whether or not any particular gap is harmful. "Channeling" efficiency depends on particle type. When one considers all the interaction mechanisms such as dE/dX loss, pair production, bremsstrahlung, and hadronic interactions, most particles will fall into one of two classes:

1. Their interaction length scales are long compared to the depth of the material, and they will not "see" the channel, except as it reduces material geometrically along the particle path. Muons are the obvious example, but this also applies to any particle in the "thin shielding" regime where the material depth is sufficiently small. Note that in this regime the shielding material is not attenuating the flux, but may be reducing its energy by dE/dX loss.

2. Their interaction length scales are short, and they tend to be stopped upon first entry to walls of the channel. In this regime the channel geometry dominates the problem. The degree to which backgrounds penetrate the channel depends strongly on the aspect ratio (width/length) of the channel, as well as the entry angles of particles. A given channel will be harmless if it is sufficiently long compared to its width (solid angle seen by incoming flow is small) or if the bulk flow is at an angle to the channel.

However, special care must be taken with low energy neutrons in channels. Even if the surrounding material is in the "thick shielding" regime where (1.) does not apply, there can still

be a problem. Since neutrons do not undergo ionizing energy loss, their behavior at low energies is dominated by elastic scattering--the process that moderates them and eventually leads to thermalization. Thus, low energy neutrons readily scatter from the walls of a channel and reenter it, propagating down the channel in a series of reflections, much like photons along an optical fiber. On the other hand, the geometry of this effect implies that the neutron flow does not readily turn corners, and that "chicanes", or "kinks" may be effective in preventing neutrons (or other particle species) from reaching the end of an air channel. All of the above effects lead to a set of guidelines for estimating the effects of air channels and optimizing the shielding in their presence:

1. (Obvious.) Make the channels narrow by constructing them as closely as possible to nominal dimensions. The gains will be large in the case where the incoming flow is directed into the channel (because of solid angle reduction).

2. If the incoming flow is directional, angle the channel away from this direction whenever possible. In many cases, this means making the channel non-projective in phi or theta relative to a source, such as the interaction point, the beam line, or the TAS collimator.

3. If the two preceding steps are not sufficient, introduce a chicane or kink into the channel.

4. Determine if it is practical to fill the channel with some material following assembly. For example, if low energy neutrons are the primary problem, this could be a low density material containing hydrogen, carbon, or both, to moderate them.

Summary of Shielding Tactics

The physical processes described in the preceding section lead to shielding strategies that have been used extensively in ATLAS. Dense materials are used wherever possible to develop hadronic and electromagnetic showers, and to range out their particles. Ideally, the material should be thick enough to absorb all charged particles. The remnants of the cascade, mostly neutrons have to be moderated, either "in the shower" (for example by carbon in cast iron), or "at the end of the shower" in a cladding layer, and then captured. Fast neutrons are effectively moderated in polyethylene by elastic scattering on Hydrogen and partially absorbed by $^{1}H(n,\gamma)^{2}H$ capture. The photon production can be a problem, so that a final photon filter--in the form of a second cladding layer--is needed. Finally, gaps at shielding interfaces must be minimized, filled or made harmless by introducing chicanes.

3 Simulation Tools

Predictions of particle fluences and doses at hadron collider experiments rely heavily on Monte Carlo simulations. ATLAS uses the event generators PHOJET [32,33] (default) or PYTHIA [35] to simulate the proton-proton interactions, and the programs FLUKA [0] or GCALOR [8,45,48] to simulate the interactions and cascades of particles in the detector material. Both these Monte Carlos are well established in high-energy physics simulations.

3.1 The Event Generator

Secondaries from the proton-proton inelastic collisions are responsible for the bulk of the radiation backgrounds, as opposed to backgrounds originating from beam-gas and beam-losses. It is therefore necessary to simulate the proton-proton interactions and this is done using Monte Carlo "minimum-bias" event generators. Minimum-bias processes are dominated by soft interactions, but also contain contributions from harder (high-p_T) parton-parton scatterings. A good "minimum-bias event generator" should be able to describe both the soft and hard interactions. Although hard processes are well described by perturbative QCD, there is a wide variety of models with distinct theoretical concepts attempting to describe the properties observed in low-p_T interactions. The Monte Carlo event generator PHOJET [32,33] uses the Dual Parton Model [36] for particle production in low-p_T processes, and perturbative QCD for the hard interactions. PYTHIA [35] uses the leading order QCD matrix elements with a very low transverse momentum cut-off to model low-p_T non-diffractive physics, and has incorporated several different approaches for dealing with the corresponding divergences. The low-p_T models employed by PHOJET and PYTHIA, though different, allow a smooth transition between soft and hard processes which is another desirable feature when one is interested in generating minimum-bias events. Other well known Monte Carlo event generators such as ISAJET [37] and HERWIG [38] have not yet been fully developed for minimum-bias event generation, lacking more specific models to describe soft interactions as well as to connect smoothly the soft and hard processes [41].

Given in Table 3.1 are the cross-sections for the different interaction processes, as predicted by PHOJET1.12 and PYTHIA6.2, for a centre-of-mass energy of 14TeV.

Process	**Cross section (mb)**	
	PHOJET1.12	**PYTHIA6.2**
inelastic	84.5	79.3
(non-diff)	69.2	55.2
(single-diff)	11.2	14.3
(double-diff)	4.1	9.8
elastic	33.6	22.2
total	118.1	101.5

Table 3.1 Predicted proton-proton cross-sections at 14 TeV.

In order to better understand the impact of different event generator predictions on radiation backgrounds, a comparison study was performed. The results are presented in Section 7.3.

3.2 The Transport Programs

3.2.1 FLUKA

The standalone FLUKA code [0] is well-established for studies of hadronic and electromagnetic cascades induced by high-energy particles and can transport particles over a wide energy range, from thermal neutrons to cosmic rays. It is intrinsically an analogue code, but can be run in biased mode for a variety of deep penetration applications. FLUKA is under constant development and is being used for an increasing range of applications (high-energy experimental physics and engineering, shielding, detector and telescope design, cosmic-ray studies, dosimetry and medical physics). It should be noted that standalone-FLUKA is not the same as GEANT3-FLUKA, which uses the hadronic routines of the 1992 version of FLUKA. Details of the FLUKA code and its strategy for handling: inelastic hadron–nucleon and hadron–nucleus interactions; hadron elastic scattering; charged-hadron and muon transport; low-energy (<20 MeV) neutron transport; electron and photon transport; neutrino interactions; can be found in [0] and references therein.

The original FLUKA simulations for ATLAS were performed by Ferrari and Sala, until the geometry version "TP43h". Starting with this version, FLUKA simulations for ATLAS have been performed by I.Dawson. "TP43h" became "AV1" with just one difference that no boron was included in in the concrete of the cavern walls. FLUKA simulations during the period 1999-2001 were focussed on three areas: 1) implementing engineering realism into the detector, machine and shielding descriptions used in the simulations, 2) design and optimisation studies for the various shielding parts and 3) understanding level-1 muon backgrounds, in particular the so-called "100MeV muon problem", an ATLAS specific problem in which a background from muons having momentum ~100MeV was identified as being potentially problematic in terms of the induced Level-1 muon rate contribution. While FLUKA simulations during the period 2001-2002 have focussed more on studies to better understand uncertainties related to radiation background predictions.

An important improvement in the FLUKA version 2000 was a better treatment of low-energy neutral kaon transport. In previous FLUKA versions, $\overline{K}$ inelastic interactions were stopped at 50 MeV (elastic ones at 20 MeV) due to the lack of (reliable) cross sections and a decent low-energy $\overline{K}$ interaction model. K_L were made to decay within one interaction length computed at 50 MeV and this somewhat artificially increased their chances to survive and produce penetrating π to μ decays. For the FLUKA2000 version, the tabulations used for the KLOE experiments of $K/\overline{K}$ cross sections were implemented, and at the same time the PEANUT interaction model was extended to low-energy $\overline{K}$, implementing all relevant phase shift analysis (available up to 1.5 GeV/c) for all elastic, strangeness exchange, charge exchange etc. channels (they are plenty since many $\overline{K}N$ - Hyperon pion channels are open down to zero energy). These $\overline{K}$-N processes are then implemented in PEANUT in the standard FLUKA framework for intranuclear cascading etc, giving a hopefully meaningful model for $\overline{K}$ interactions at low energies. Hence the 50 MeV threshold has been substantially lowered (down to the physical threshold for inelastic excitation). Regeneration is still not treated in a fully satisfactory way due to the lack of interference in the way nuclear amplitudes are managed, however the authors plan to make further improvements on this point.

The effect of the improvement in the transport program is shown in Table 3.2 that shows the comparison of the results obtained with Fluka99 and Fluka2000 using same input files. The

consequences of the *new* neutral-kaon transport on ATLAS backgrounds are the following: no change in neutrals and protons but large reductions in muons due to fewer K_L decays. (Large reductions were also observed in charged pions, however the rates are much smaller than the other particle species.) As a consequence the muon background is reduced by a factor 2 to 8 and pions do not contribute significantly to the rates.

Position	Neutrons	Photons	Protons	Pions	Muons
Barrel					
1st, low-z	1.02	0.91	1.08	0.69	0.82
2nd, low-z	1.00	0.91	1.07	0.07	0.26
2nd, high-z	0.98	0.94	1.21	0.15	0.46
3rd, high-z	0.99	0.97	0.98	0.08	0.83
Forward					
1st, mid-eta	1.00	0.96	0.99	0.34	0.90
2nd, low-eta	0.98	0.97	0.99	0.02	0.13
2nd, mid-eta	0.98	0.97	1.09	0.11	0.42
2nd, high-eta	0.99	0.97	1.18	0.14	0.54
3rd, low-eta	0.99	0.95	0.95	0.02	0.19

Table 3.2 Ratios of FLUKA2000 to FLUKA99 for the AV11 geometry, showing effect of the changes in neutral kaon transport on the predicted fluences. Location of the scoring regions can be seen in Figure 4.18

3.2.2 GCALOR

The GCALOR package [8] contains the CALOR [48] simulation code (including the low-energy neutron code MICAP [103]) developed and maintained by the Oak Ridge National Laboratory (ORNL), and an interface to GEANT3 [45]. CALOR has been used extensively for analysing calorimeter systems for high-energy physics detectors, and was one of the recommended detector simulation codes used to support the development of detector designs for the Superconducting Super Collider project. The transport of electromagnetic interacting particles in GCALOR is performed by GEANT, as well as the tracking and the calculation of energy deposition.

For hadron inelastic interactions, GCALOR activates the same routines as GEANT-FLUKA for pions and nucleons with energies greater than 10 GeV (and for all other particles anyway). Below 2.5 GeV for pions and 3.5 GeV for nucleons, interactions are handled using the Nucleon Meson Transport Code (NMTC), which is based on the intranuclear cascade evaporation model as implemented by Bertinin [46]. Between these thresholds, a hybrid treatment is implemented in which a fraction of the interactions is performed as in GEANT-FLUKA and the remainder of the fraction is simulated by NMTC. The value of the fraction varies linearly going from 0 at the thresholds to 1 at 10 GeV. It should be noted that in the current ATLAS-GCALOR simulations, neutral-kaon transport is performed with the G3-GHEISHA routines [47].

Two improvements were made to GCALOR since 1998. First, the neutron cross sections in the input file xsneut.dat were updated from ENDF/B distributions in 2000 by Christian Zeitnitz, as part of standard upgrades to GCALOR.

The other improvement was actually in the GEANT3 sector, where it was discovered that the neutral kaon transport has a problem in the FLUKA sector of the standard version. It appears that K_S and K_L from the primary interaction (introduced through KINE) decay and interact correctly, as do K_S produced as secondaries—but that K_L secondaries produced within the code are non-interacting, and only decay, making them penetrate the detector until they decay. The provisional solution introduced in the summer of 2000 was to return K_L's to Gheisha for transport, via a patch in the routine FLDIST [48]. With this patch, all neutral kaon transport appears "reasonable" during tracking, though it does not contain an accurate physical model of the neutral kaon sector.

3.3 Comparison of FLUKA/GCALOR Models

Electromagnetic Interactions

Electromagnetic interactions are well understood at the most fundamental level, and may be simulated with high reliability using a combination of methods such as (1) precalculation of material-specific cross section tables from QED-based formulas or (2) parameterizations that have been determined "once and for all" and are contained in the simulation code. The two transport codes used in ATLAS simulations have very different electromagnetic sectors. The GEANT3/GCALOR package calls the electromagnetic sector of GEANT3, which relies on parameterizations and in situ calculations, requiring no external cross section tables. The Standalone FLUKA package has a highly developed precision EM sector, which originally evolved from EGS4, but now contains a large number of unique routines to improve, especially, the calculation of low energy EM processes. Like EGS4, FLUKA also employs cross section input files, precalculated for each material.

Hadronic Particle Production

The energy regime above about 5 GeV is considered the "high energy" regime in particle production calculations, where hadrons interact with target nuclei treated as ensembles of independent nucleons. The incoming hadron and target nucleons are described at parton level as collections of valence quarks, valence diquarks, and sea quark pairs. But because simulations must include all possible interactions contributing to formation of the hadronic shower, the non-perturbative parts of the total cross section dominate. For this reason, event generator and particle transport codes at these energies must include both (1) high p_T perturbative interactions based on QCD $2 \rightarrow 2$ crossections and (2) non-perturbative descriptions of parton interactions.

In GCALOR (with GEANT FLUKA), and standalone FLUKA, the non-perturbative behaviour is handled via the Dual Parton Model (DPM), where the exchange particles, instead of being gluons, are Pomerons or Reggeons (quasi-particles) modelling the whole QCD interaction [32]. Each hadron splits into two colored partons, which combine to form back-to-back jets. The model tracks the colour flow from the original collision through recombination to the production of colour-neutral "chains" that constitute the final state hadrons. In effect, the parton level description conserves quantum numbers, such as colour, while the exchanged quasi-particles provide the dynamics.

Because the "independent" target nucleons are actually constituents of a nucleus, the Gribov-Glauber approximation is used in the DPM to model the full nuclear interaction. In this approximation, the inelastic interaction with individual nucleons is used to build up the description of the interaction with the full nucleus, where the target nucleus is assumed to be in the ground state. The full inelastic interaction results from the interaction with N target nucleons, binomially distributed as a function of impact parameter, b, according to a profile function that folds the nuclear density with scattering profiles along the path at b. The Glauber-Gribov description also includes Fermi motion of the nucleons within the nucleus, leading to smearing of the p_T distributions of outgoing particles.

In GCALOR (using GEANT3 with FLUKA option), and standalone FLUKA, the high energy transport sector is essentially the same (of common origin in the distant past) and follows the DPM scheme described above [32].

Modelling of Intermediate Energy Processes

The above discussion of spallation greatly understates the complexity of nuclear processes in the intermediate energy regime. Neutron transport codes must treat this energy range in much more detail to get the correct yields for neutrons and photons. Between approximately 100 MeV and several GeV, we are in the region where the characteristic momentum transfer and the incident hadron wavelength are comparable to the size of individual nucleons—smaller than a nuclei, but larger than the partonic level used in the Dual Parton Model. For this reason, most neutron transport codes treat the first stage of the hadron-nucleus reaction as an intranuclear cascade (INC), where the incoming hadron collides with one or more individual nucleons, which in turn collide with other nucleons in the same nucleus, creating a cascade. This description is essentially classical, and relies on having accurate nucleon-nucleon and pion-nucleon cross sections as input. The original INC code was written by Bertini, and there are more recent versions such a ISABEL, by Yariv (used in LAHET).

After the nucleus has been excited by the INC, the standard approach is to let the nucleus undergo "evaporation" (EVAP), to shed neutrons, protons, and light nuclei. This picture is based on work originally done by Weisskopf, Hauser, and Feshbach, with most simulation packages using code developed by Dresner. This evaporation process assumes that the nucleus has attained thermal equilibrium at an energy scale less than the nuclear potential depth of about 40 MeV. Unfortunately there is an energy gap between this scale and the INC scale, which some codes, such as standalone FLUKA, fill in with a "pre-equilibrium" stage, to cover energies below about 100-150 MeV. In these codes, quasi-particle excitations of the nuclear Fermi gas are evolved by means of a master equation, and these states are characterized by particle escape probabilities and damping widths. Generally, fission is incorporated into the PREEQ and EVAP stages.

The pre-equilibrium stage is clearly a quantum mechanical model (following a classical INC stage), and this whole sequence of INC/PREEQ/EVAP should probably be seen as a "brave attempt" at modeling nuclear processes in this energy range. More realistically, it is a complex parameterization that can be tuned reasonably well to experimental data [34].

In this intermediate energy regime, a number of processes will contribute to "invisible energy" in calorimeters. This is sometimes called "nuclear binding loss energy", and fluctuations in this component from shower to shower are the primary determiner of hadronic calorimeter energy resolution.

Energy Loss Mechanisms

There is an important distinction between the ways that energy loss is reported in each transport step in GCALOR and FLUKA. In GCALOR, based on GEANT3, the dE/dX loss is reported for each step. But if energy is also carried away by interactions, this will not be accounted for unless the resulting secondaries are also tracked or stopped. For example, in GCALOR, recoil nuclei are not tracked by default, and losses due to nuclear excitation will never appear. By contrast, FLUKA reports the total energy loss in each step, and is thus an "energy conserving" calculation. This issue comes into play when calculating quantities such as "total ionizing does", TID, and "non-ionizing energy loss", NIEL, in the two programs, and will be discussed in more detail in following sections.

4 The ATLAS Geometry

Detailed descriptions of the ATLAS experiment geometry and of its subsystems exist on the World Wide Web [94], in the ATLAS Technical Proposal [15], and in a series of Technical Design Reports [16]. In this section, we visit each detector region in some detail, describing the geometry of ATLAS as it exists now in June of 2004 after more than a decade of design evolution. During this time it has been optimized for physics capabilities, engineering integrity at reasonable cost, and shielding power; subject to geometric constraints such as design envelopes and clearance zones, and the need for support structures and detector services.

The first section of the chapter describes the present ATLAS geometry and focuses on the issues relevant to shielding while the following sections describe how this detailed geometry was translated into FLUKA and GCALOR simulation geometries.

4.1 Description of the present ATLAS geometry

4.1.1 The Beamline Vacuum System

Figure 4.1 shows the ATLAS beamline vacuum system. The beampipe in the inner detector region is made of beryllium and runs from the interaction region to about z = ± 355 cm. The wall of this beampipe is 0.8 mm thick, and it has an inner radius of 29 mm. The interior of the beampipe is coated with getter alloy to act as an integrated non-evaporable getter (NEG) pump. A thermal insulation jacket made of 4 mm thick aerogel is used to protect the silicon B layer during the periods when the NEG is heated to restore its pumping efficiency. The beam line structure in the inner detector is designed to minimize material while retaining good pumping efficiency for beam vacuum contaminants such as methane. Since the radiation backgrounds in the inner detector region in the first tens of centimeters near the beam line are dominated by particles from the interaction point, minimizing beam pipe material helps assure that it does not become a major source of secondary background radiation.

At z = ± 355 cm, there is a short 10 cm long aluminum section. The beampipe material then changes to stainless steel, and the pipe still has an inner radius of 29 mm and a thickness of 0.8 mm. This small beampipe radius is needed through the narrow FCAL bore to allow space for thermal insulation and for calorimeter bore misalignment relative to the beampipe. The pipe remains this dimension until z = ± 1046.5 cm, where it flares to an inner radius of 40 mm (thickness 1 mm) by z = ± 1050.7 cm. It remains this dimension until a second flare at z = ± 1434.2 cm, where it expands to an inner radius of 60 mm (thickness 1.5 mm), by z = ± 1441.6 cm. The pipe stays this dimension until it nears the front of the TAS absorber, at z = ± 1865 cm. The beampipe must be flared in this stepwise fashion to allow for retraction of the FCAL over the smallest section, and the endcap toroid over the next section, during short accesses—without breaking the beam vacuum.

There are a number of flanges, pumps, and pump-associated structures in the beamline throughout this region. Working our way from the I.P. outward, the position at z = ± 354 cm is at the front of the endcap calorimeter cryostat, at the entrance to the alcove that ends at the front of the forward calorimeter (FCAL). In this alcove there is a stainless steel ion pump at z = ± 380 cm that provides the main pumping power for the inner detector region. It is low mass (2 kg) and uses the magnetic field near the end of the inner detector solenoidal magnet as its operating

field. There are also low mass flanges at z = ± 365 cm to couple the beryllium pipe after the short aluminum section to the stainless steel pipe. The emphasis on low mass structures in this region is twofold: (1) to reduce albedo background radiation into the inner detector from beamline structures and (2) to prevent preshowering of photons far in front of the FCAL that would degrade its jet resolution.

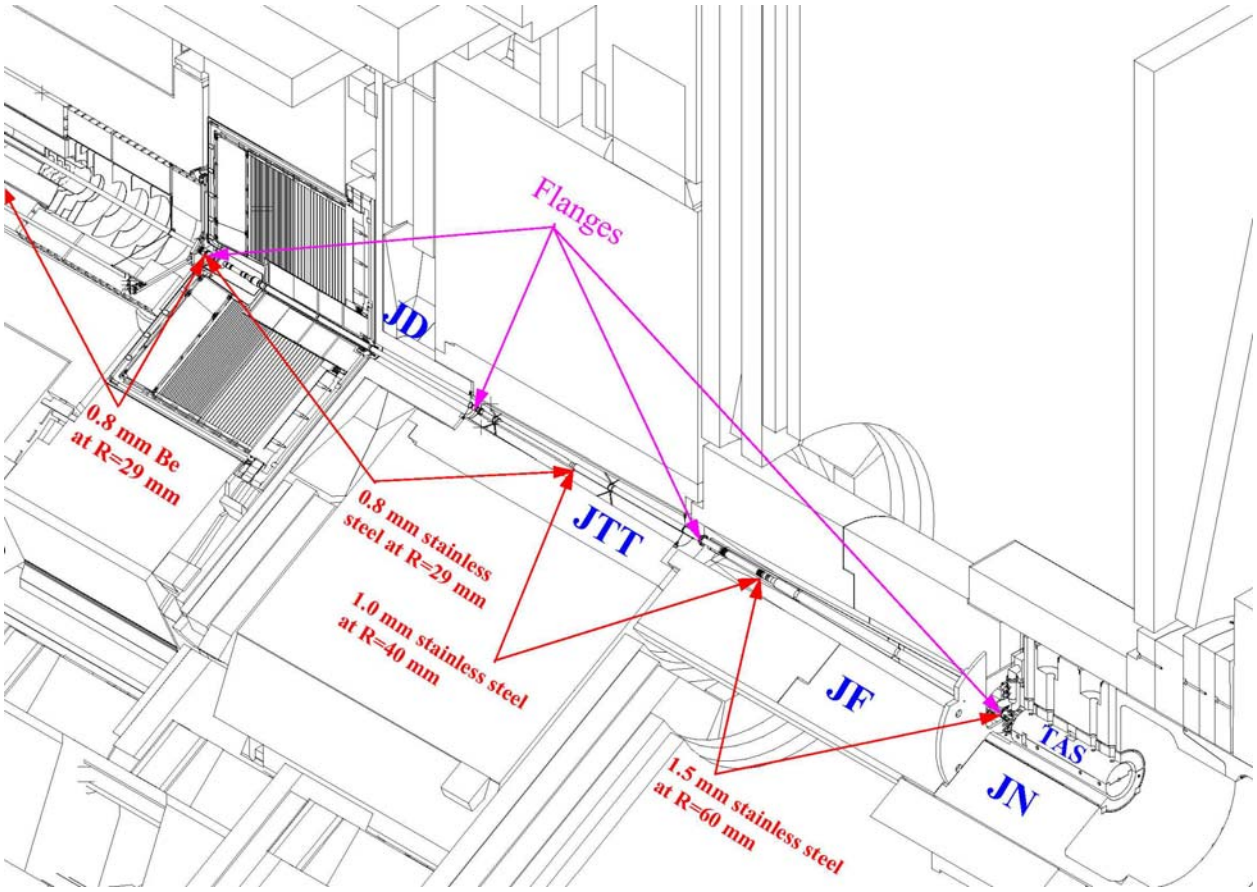

Figure 4.1 The beam line and its various elements.

In the FCAL region, the vacuum pipe includes a NEG pump coated on the pipe inner surface. Behind the FCAL there are flanges at z = ± 870 cm and ± 1300 cm, to allow for assembly and disassembly of the beamline. There are more NEG pump sections in the beampipe in the bore of the endcap toroid and in the beampipe inside the forward shielding. The entire ATLAS beampipe will have to be heated up (baked-out) prior to LHC operations and the beampipe is therefore surrounded by thin electrical heaters and an isolation jacket. This jacket consists of 4 mm of aerogel.

To pass through the small hole in the TAS collimator, by z = ± 1888 cm the beampipe reduces (unflared) to an inner radius of 17 mm, with a wall thickness of 13 mm, and makes a transition to copper (roughly the same material as the TAS collimator itself). The outer diameter of the beampipe fits perfectly in the hole in the TAS, creating a collimator unit with inner radius 17 mm. Detailed design of this transition region, which includes an ion pump, is not yet complete, but changes in this small region will have negligible effect on any background radiation levels that reach the detector.

There is another large ion pump at z = ± 2094 cm, behind the TAS collimator. The concern here is whether or not this might present a secondary source that would irradiate the region inside the support tube behind the JN monoblock. This pump is, however, well shielded from I.P flux by the TAS collimator itself, and is not a problem. The beam pipe flares behind the TAS, and proceeds through the final focus quadrupoles, but has no effect on background radiation levels in the ATLAS detector.

4.1.2 The Inner Detector Region and the Moderator Shield (JM)

The inner detector cavity is filled to a large extent by tracking detectors and their services (support, electronic and cooling). The only spaces available for shielding are on the face of the endcap calorimeter cryostat, and in parts of the "alcove" in front of the forward calorimeter (see Figure 4.2). These spaces are filled with polyethylene (doped with boron) to moderate the albedo neutrons, and capture them. The inner detector is low mass, and nothing can be done to attenuate the flux of prompt particles (especially charged pions) from the interaction point.

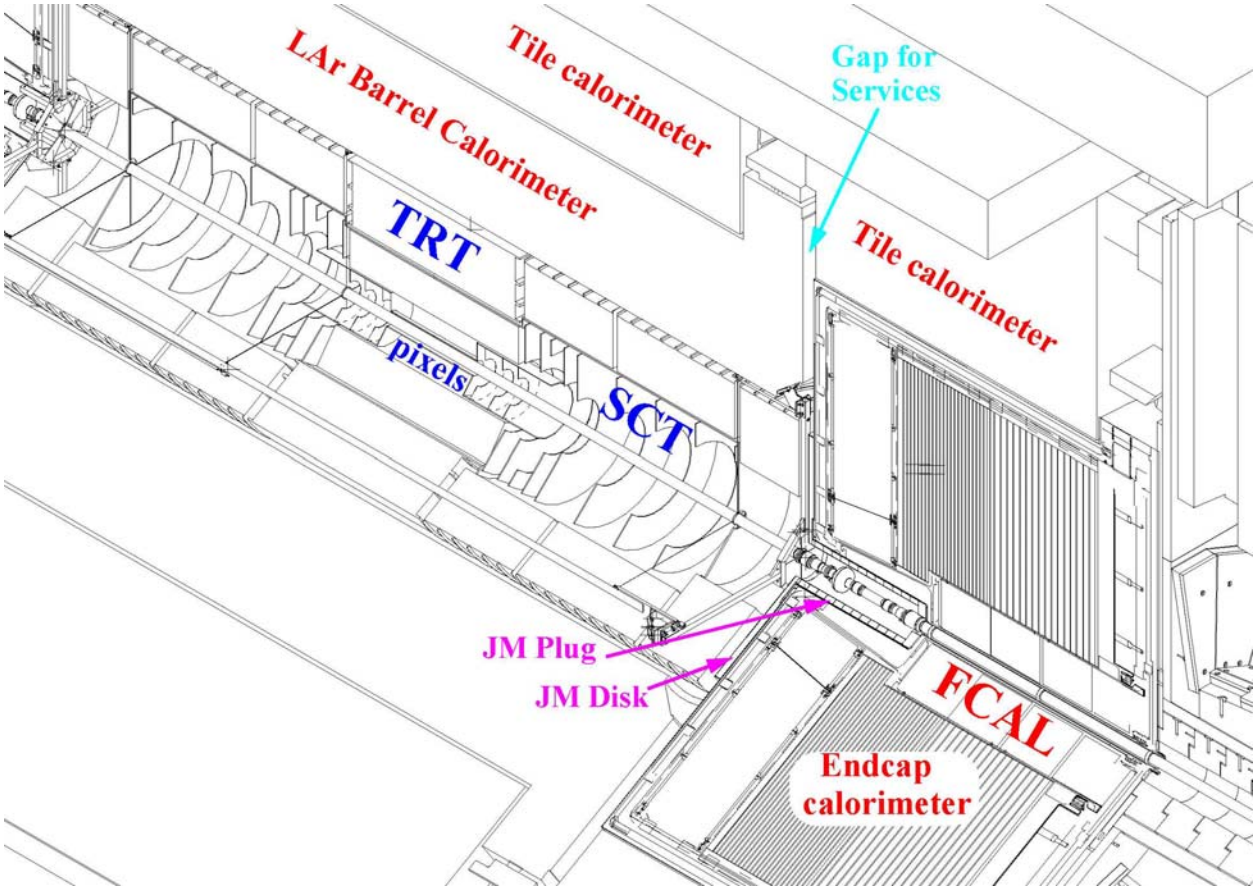

Figure 4.2 The region of the inner detector and the JM moderator shield.

The moderator (JM) on the face of the endcap calorimeter is a disk of polyethylene, doped with boroncarbide B_4C (5% boron by weight). The inner part of the disk, from a radius of 13.8 cm to 35 cm, is 4 cm thick while the remaining disk out to a radius of 98.2 cm is 5 cm thick. It covers

the whole face of the endcap calorimeter exposed to the inner detector cavity. The alcove in front of the FCAL is moderated by a cylinder that lines the bore of the warm wall, and by a disk on the face of the FCAL warm wall. The former has an inner radius of 14 cm and an outer radius of 18 cm, for a thickness of approximately 4 cm, and the latter is 8 cm thick, starting at an inner radius of 7.5 cm and connecting to the cylinder at its outer radius. Both of these pieces are polyboron (5% boron by weight in the form of B_4C). This alcove geometry seems to be effective both to reduce albedo from the FCAL, but, more importantly, to moderate neutrons spraying inward from shower development in the exposed edge of the EMEC and entering the alcove almost isotropically.

4.1.3 The Barrel Calorimeter

The barrel calorimeter (Figure 4.3) is completely filled with presampler and calorimeter modules, cables and services. Unlike the endcap cryostat, there are no space where additional shielding might be placed. Fortunately, the calorimeter depth is sufficient to shield the barrel muon system behind it.

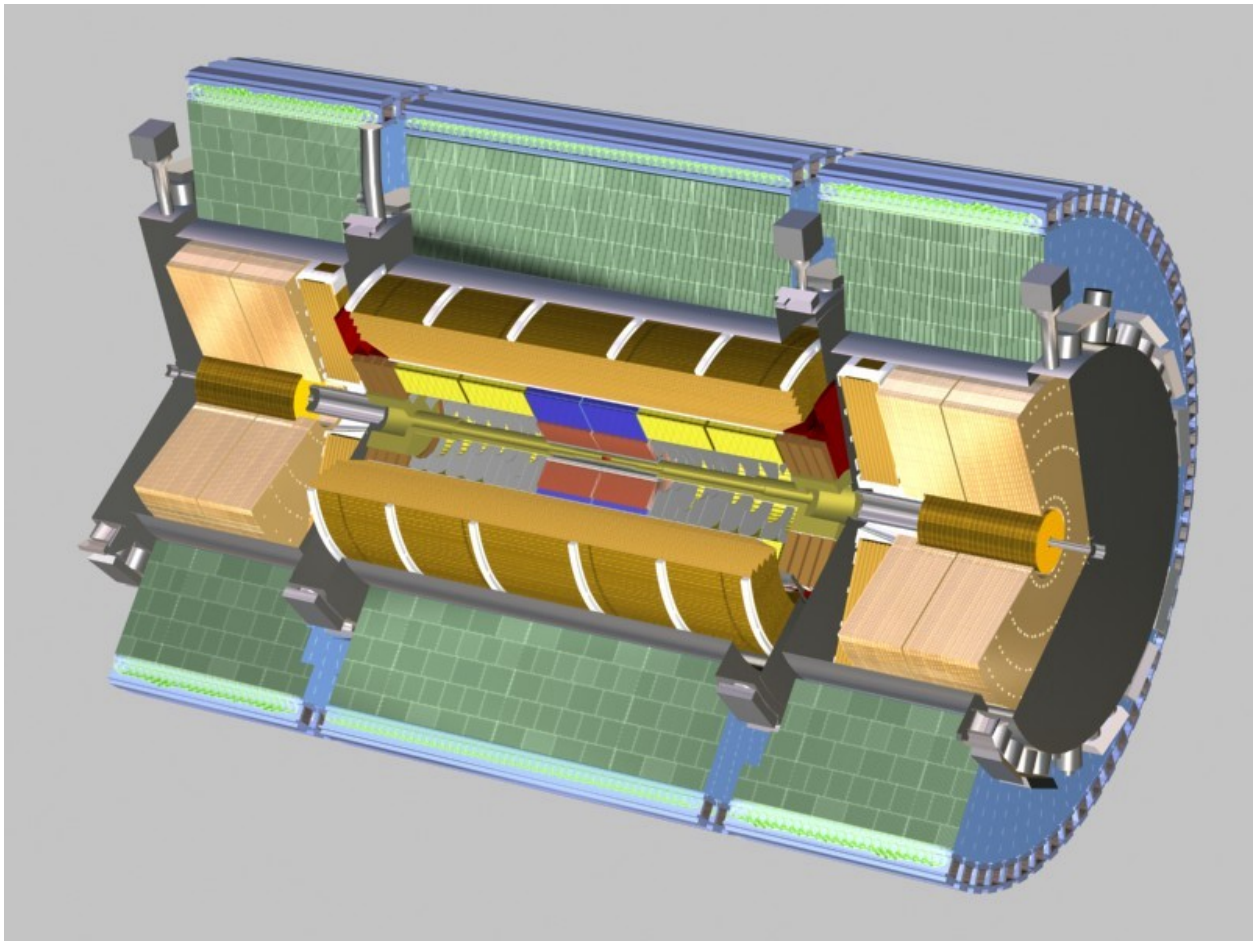

Figure 4.3 Artist view of the Atlas calorimeters.

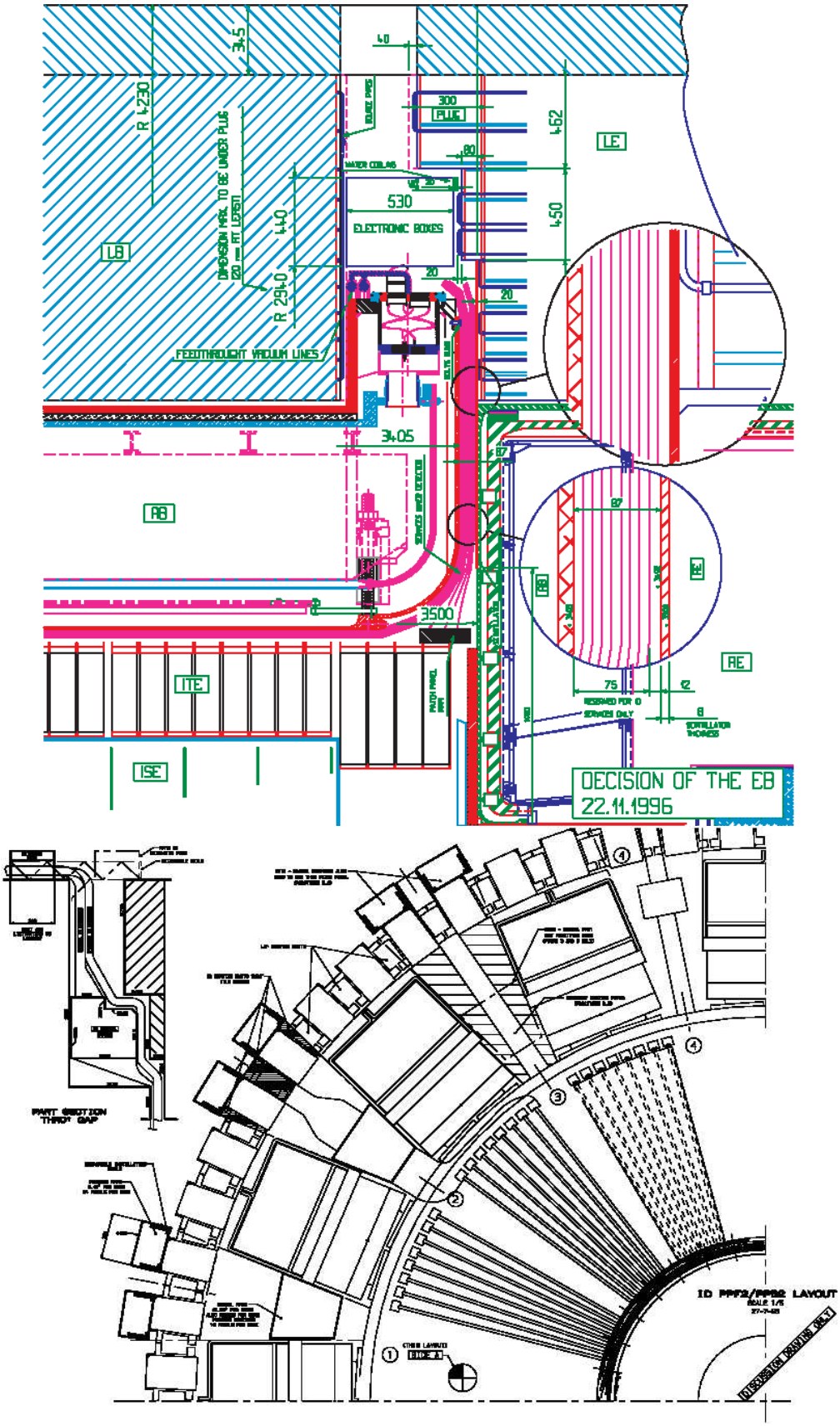

Figure 4.4 The gap region between the barrel and the endcap calorimeters in (r,z) view top and (r,ϕ) view bottom which shows the Inner Detector cables, the feedthrough and the Lar electronics crates. These figures are given for illustration, they do no correspond to the final configuration.

4.1.4 The Barrel-Endcap Services Gap

There are no "obvious" spaces to put shielding in the services gap between the barrel and endcap calorimeters (Figure 4.4). The space is populated with large electronics crates, cryogenic and cooling services, and cables (signal and power supply). These components are woven together in a complex 3d pattern that has been understood only with the help of a maquette, with material fill factors that vary greatly from place to place. The shielding plan for this area is to be opportunistic, and put neutron moderator in any interstitial regions that can accommodate it.

There is an important observation about this area that appeared in the course of simulation. In the region between the cryostats, the effective gap size is much wider than the distance between the cryostats. Its width for the more penetrating backgrounds is better approximated as the span between the barrel EM accordion and the ECEM accordion. This is because the cryostat walls, liquid argon, cryostat cabling, and vacuum spaces between the cold and warm walls present low density material compared to the modules themselves, creating a channel approximately ½ m wide that is more transparent than the calorimeter modules on either side to backgrounds from the inner detector. Thus, geometry has big effect on the shielding power of the gap region. Note however that, overall, the barrel and endcap calorimeters are very effective shields because of their large depths in radiation and interaction lengths. The calorimeter mass and hermiticity provide much of the shielding for the muon system.

4.1.5 The Barrel and Forward Muon Systems

An overview of the muon system is shown in Figure 4.5. The barrel muon system does not have locations for placement of shielding without interfering with the muon acceptance. This is also true of the forward muon system up to its acceptance boundary at $\eta = 2.7$. Because these systems are air core toroids, they are designed as an "open geometry" with as little mass as possible in the detectors and support structure in order to reduce multiple scattering of muons.

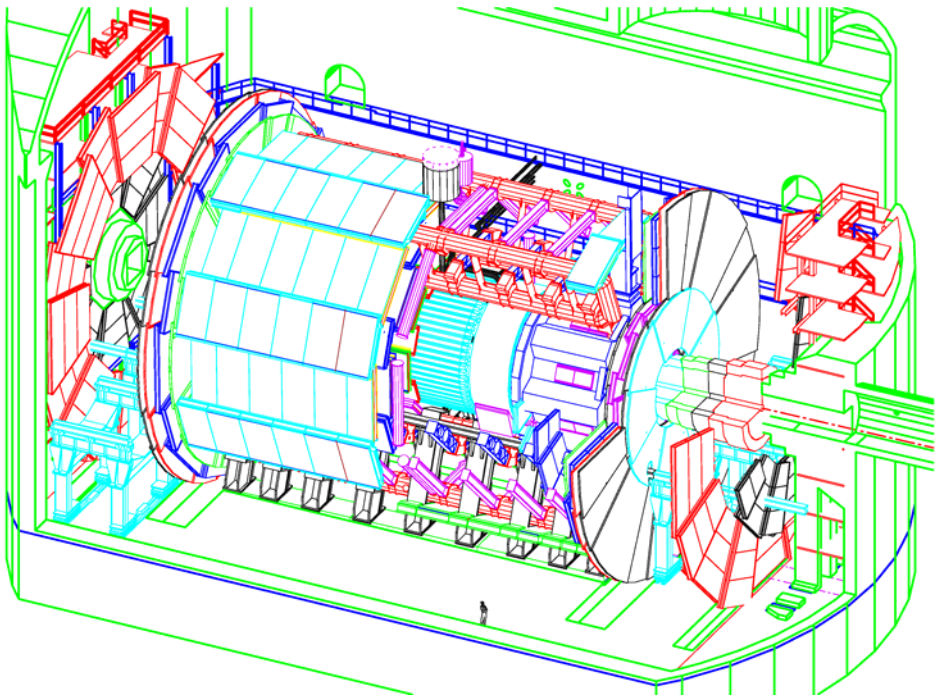

Figure 4.5 Three-dimensional view of the ATLAS detector. Some muon chambers and parts of the barrel toroid are removed to show the inner structure of the detector.

4.1.6 The Endcap Cryostat and Shields (Plugs)

The endcap cryostat is filled, beginning at the front face, with the EMEC calorimeter, followed by the HEC modules. Inside these structures is the FCAL support tube, with the first forward calorimeter module, FEM, inside the first HEC modules, followed by the FCAL hadronic modules. Even after accounting for the space needed at the back of the HEC for services, there is free space behind the last HEC modules and last FCAL modules, between these modules and the cryostat cold wall. Instead of leaving this free space filled with liquid argon, it was decided to install copper plugs in this space to increase the total depth (radiation lengths and interaction lengths) of the cryostat (Figure 4.6). The geometrical constraints in this region are the shapes of the available free spaces. For example, at the outer radius of plug 1, the convergence of services on the outer back "corner" requires thinning the plug in this region. The shielding power in the calorimeters is most evident in the FCAL, which is the second "hottest" spot in the experiment, after the TAS collimator.

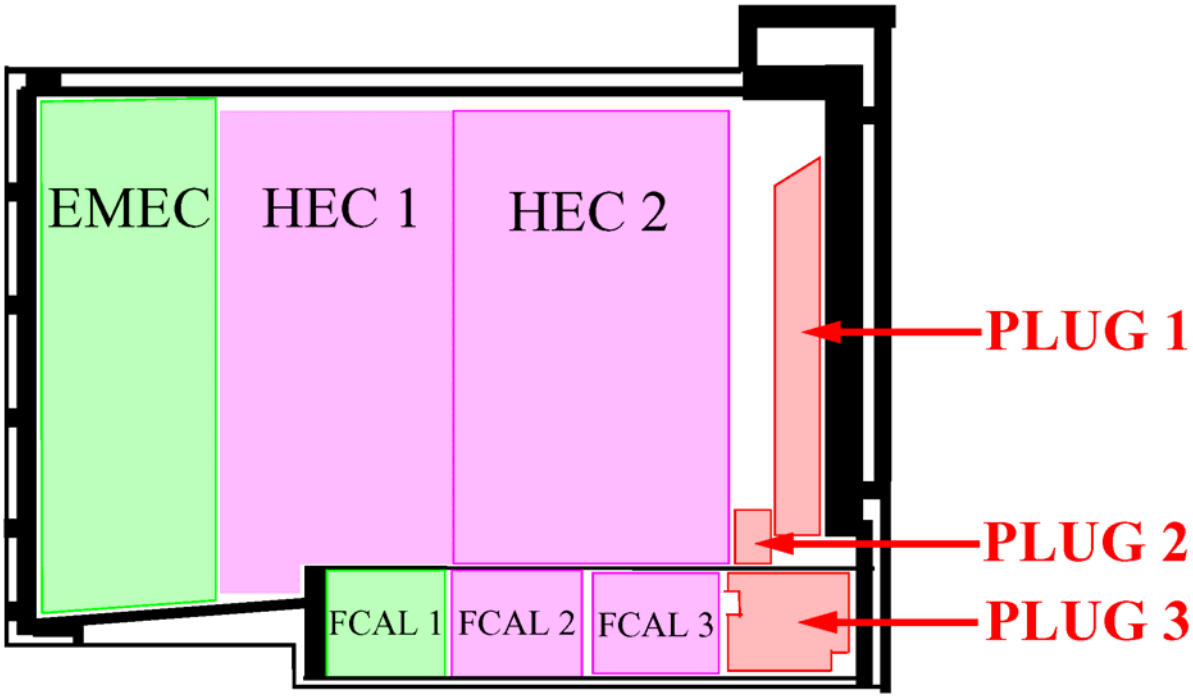

Figure 4.6 Schematic side view of the location of the three copper shielding plugs in one half of the endcap calorimeter.

4.1.7 The Flux Return Disk and Shield (JD)

The largest structural element in the JD region is the flux return disk (Figure 4.7), a steel plate sitting immediately behind the endcap calorimeter with an inner radius of 54 cm, an outer radius of 436 cm, and a thickness of 13 cm over most of its area, with some sections thinned to 8 cm outside the outer radius of the endcap calorimeter (to allow for electronic crate and cable positioning). This disk is intended to return and contain the flux from the inner detector solenoid, but it also serves as additional radiation shielding for the forward muon system. At the

center of the JD disk is bolted a stainless steel support tube: a cylinder roughly 1.8 m in length, with a wall thickness of 10 cm, extending from the front of the disk and serving three purposes: (1) the carrier for the dense "plug" shielding in this region near the beamline, (2) the support for a sliding "hub" that in turn carries the CSC and inner forward MDT detector systems, and (3) the inner part of the chicane interfacing to the front of the JTT.

The dense shielding in the core of the support tube is copper alloy in the baseline detector, and the tube design allows the option of replacing the core in the future with tungsten, should additional shielding power be needed. This core fills the support tube, up to mechanical tolerance limits, and its inner surface is projective along the line $\eta = \pm 4.65$. Because the CSC's are tilted to face the I.P., there is a space between the CSC's and the flux return plate that appears triangular in a Y-Z projection, and this space has been filled with the same copper alloy as the core. This structure is called the "cone". The sliding "hub" mentioned above is also made of the same alloy.

This corner of the shielding surrounding the CSC's is one of the “thinner” parts of the shield, and the use of cladding has yielded large reductions in neutron and photon background rates. The cladding occupies space where dense shielding material could be instead, but little or no increase is seen in high energy backgrounds, such as hadrons above 10 MeV, when cladding is introduced. The cladding in this region covers the surfaces of the cone and hub facing the CSC's and consists of a 5 cm (Cone) and 7 cm (Hub) inner layer of polyethylene doped with borontrioxide B_2O_3 (5% boron by weight) and an outer layer of 3 cm of lead. These components are relatively small and non-structural, but they have a large effect on radiation backgrounds in the first forward muon system.

The geometrical constraints on shielding space in this region are as follows. On the outer surface of the hub, it is the η=2.7 muon acceptance line. On the inner surface, the inner radius must be large enough to clear beam line components as the small wheel is moved away from the I.P. during access. The other geometrical constraints in this region come at the interface to the shielding in the bore of the endcap toroid (see the JT section below). A chicane is needed at this interface, with adequate clearance to allow for mechanical and alignment tolerances, and for motion of the endcap toroid as the coils are energized (since the JTT shield is carried by the toroid in a central support tube, and not supported on the main rails).

4.1.8 The Endcap Toroid and Its Shield (JT)

The endcap toroid magnet is a complex structure consisting of eight superconducting coils arranged to create a toroidal magnetic field, with its symmetry axis centered on the beamline. The coils themselves are approximately rectangular, so that the toroidal volume is also rectangular in cross section. Since the coils are superconducting, each is enclosed in its own cryostat extending 4.7 m along the beamline, 4.0 m in the radial direction, and 26.8 cm thick (dense part of coils). Most of the coil support structure is aluminum plate of 4 cm thickness with ("cheek plates") anchored near the front and back of the coil boxes, and outer support plates at about 4 m from the beamline. In addition, there are aluminum thermal shield plates of 2.0 cm thickness to enclose the coil region and reduce the cooling power needed for the cryogenics. Finally, there are 7.5 cm thick aluminum front and back plates, and a 7.0 cm thick outer plate to enclose the whole structure. The endcap toroid has eightfold symmetry about the beam axis, and the coils and their structural supports lead ultimately to a complex castelated shape for the outer envelope.

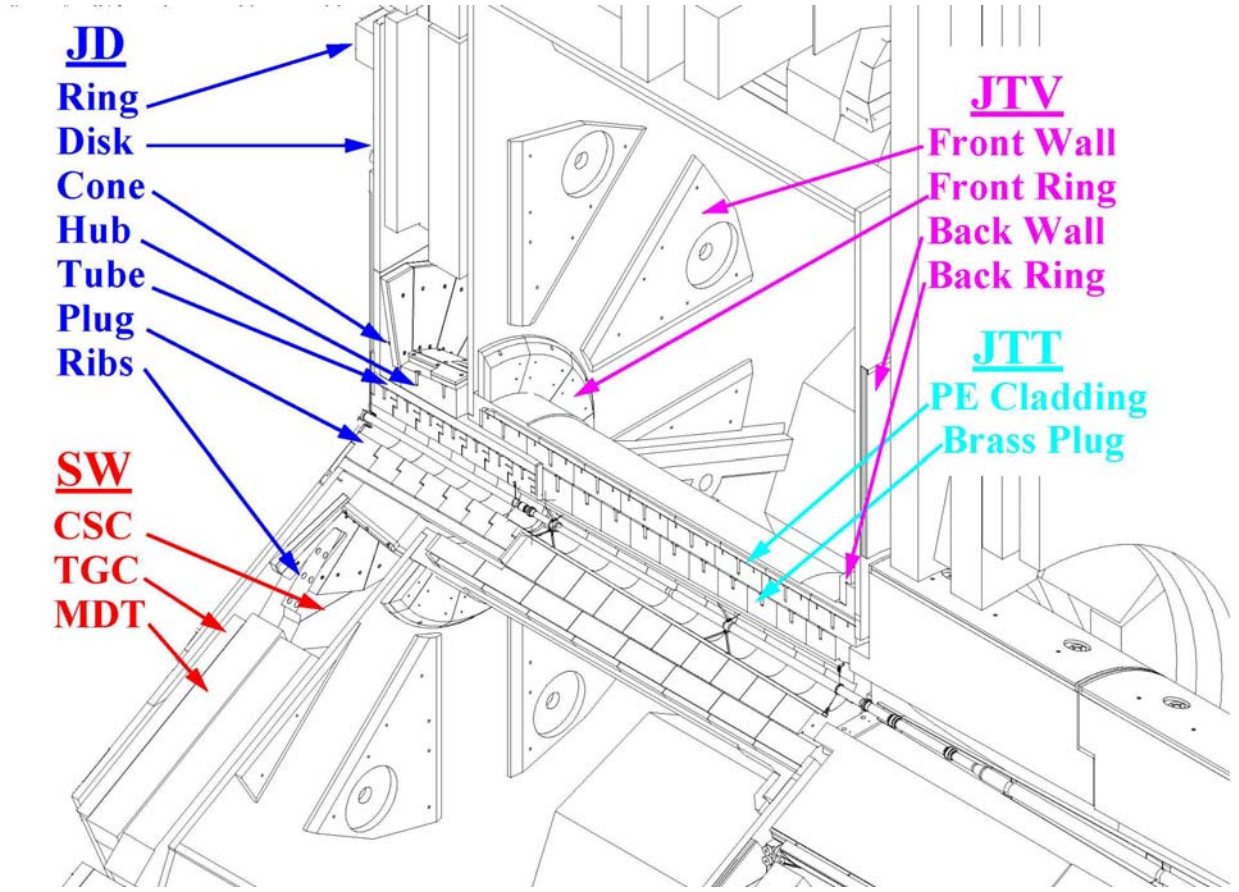

Figure 4.7 The drawings shows the location of the various pieces of the disk shield (JD) and toroid shield (JTT and JTV). The location of the different types of muon chambers in the Small Wheel (SW) is also indicated.

The fiducial region for muon acceptance in the most forward direction, as determined by the endcap toroid magnet, comes at its inner radius very close to the $\eta = 2.7$ boundary. In order to achieve this, the toroid coils and their cases must extend to smaller radius (non-projectively, with the inner edges parallel to the beam line). This greatly reduces the outer radius of the shielding in this region. The mechanical realization of the shield also reduces the total space available within the coil cases. In sum, the JT region is effectively the thinnest shielding region in ATLAS, and allows the passage of background fluxes that dominate much of the volume of the muon system.

A central bore tube of stainless steel with 4 cm wall thickness is suspended within the coils by large tie rods from the main endcap toroid structure. The inner radius of this tube is 87.25 cm and this determines the outer radius of the shielding. The bore tube is filled with nested copper alloy cylinders to create as monolithic shielding as possible (the "JTT brass plug" in Figure 4.7). The inner surface of this copper shield is projective along the line $\eta = \pm 4.65$. The transverse thickness of the copper core is therefore only 54 cm at the downstream end, which makes it extremely marginal for shielding the secondary flux from the line source of the beam vacuum system.

There is a chicane where the JT interfaces to the JD at the front end, and there is a similar chicane at the back where it interfaces to the JF shield. The radial clearance in the chicane between the JD tube and the JTT plug is 7 cm to allow primarily for positioning tolerances of the

disk shield and the endcap toroid but these gaps may be conservatively oversized, and are the subject of study, with the intention to make them narrower if possible.

The last 5.5 cm inside the bore tube are filled with borated polyethylene (5% by weight) in place of copper alloy (the "JTT PE cladding" in Figure 4.7). This causes a large reduction in neutron and photon fluxes outside the tube, with moderate and acceptable increases in the hadron flux above 20 MeV. This polyethylene layer is completely analogous to the inner cladding layer on the JD cone and hub, but in this JT location there is no need for a Pb outer layer because the stainless steel bore tube and the aluminum structures of the endcap toroid serve adequately as photon filters, both for the general photon flux and for the capture gammas generated in the boron.

Even with the doped polyethylene layer around the core, the background flux through it is so large that one cannot afford to stop with this neutron shielding. At the front and back ends of the bore tube, just outside the tube, are rings of borated polyethylene (5% B_4C) to attenuate JT neutron background flowing upstream into the CSC region in the "Small Muon wheel" and downstream into the middle forward MDT region in the "Big Muon wheel". These JTV rings are 49 cm (Front ring) and 38 cm (Back ring) in radial extend and are 16 cm (Front ring) and 8 cm (Back ring) in depth parallel to the beam axis. (JT shielding structures outside the bore tube go by the designation "JTV".)

Finally, it is proposed that the back face of the endcap toroid is covered with an 8 cm thick layer of polyethylene doped with LiF (2.7% by weight) covering the region from the forward shielding to an outer radius of 3.5 m. Lithium is used as a dopant here since it produces less capture photons than boron and a photon filter made of lead or steel would introduce multiple scattering in the muon measurements. This polyethylene layer provides the final neutron attenuation needed to assure comfortable operation of the muon detectors in the Big Muon wheel. This shielding is called the JTV "back wall". There is a reasonably large gap for this shielding layer between the back of the endcap toroid and the front wall of the MDT's in the Big Muon wheel. The space constraints at the front wall of the endcap toroid that faces the Small Muon wheel are too severe to attempt a similar solution there and so a layer of 8 cm thick polyethylene will be installed between the coils inside the endcap toroid structure (the "JTV Front wall"). These polyethylene pieces are doped with 5% B_4C.

4.1.9 The Massive Forward Shield (JF)

The forward shield region, JF, extends from the back of the endcap toroid at $z = \pm 13$ m to just beyond the back of the JN monoblock at $z = \pm 21$ m. Up to 18.6 meters from the I.P., the JF shield has nothing inside it except the beampipe, but beginning at the JN monobloc it surrounds this structure to provide additional shielding of the TAS collimator (Figure 4.8). The dual role of the JF shielding is to contain the flux from the beamline over its span of z, and at the highest z to add to the shielding thickness surrounding the TAS. The geometrical constraints in this region are, for the most part, not a problem. In contrast to the JT region, the full outer envelope from about $\eta = 2.7$ can be used for shielding. The studies reported in this document showed that earlier design concepts with conical outer surfaces running close to the 2.7 boundaries were "over shielded". As a result of these studies, large reductions in cost and complexity have been realized by going to a "stepped cylindrical" design lying well within this outer envelope.

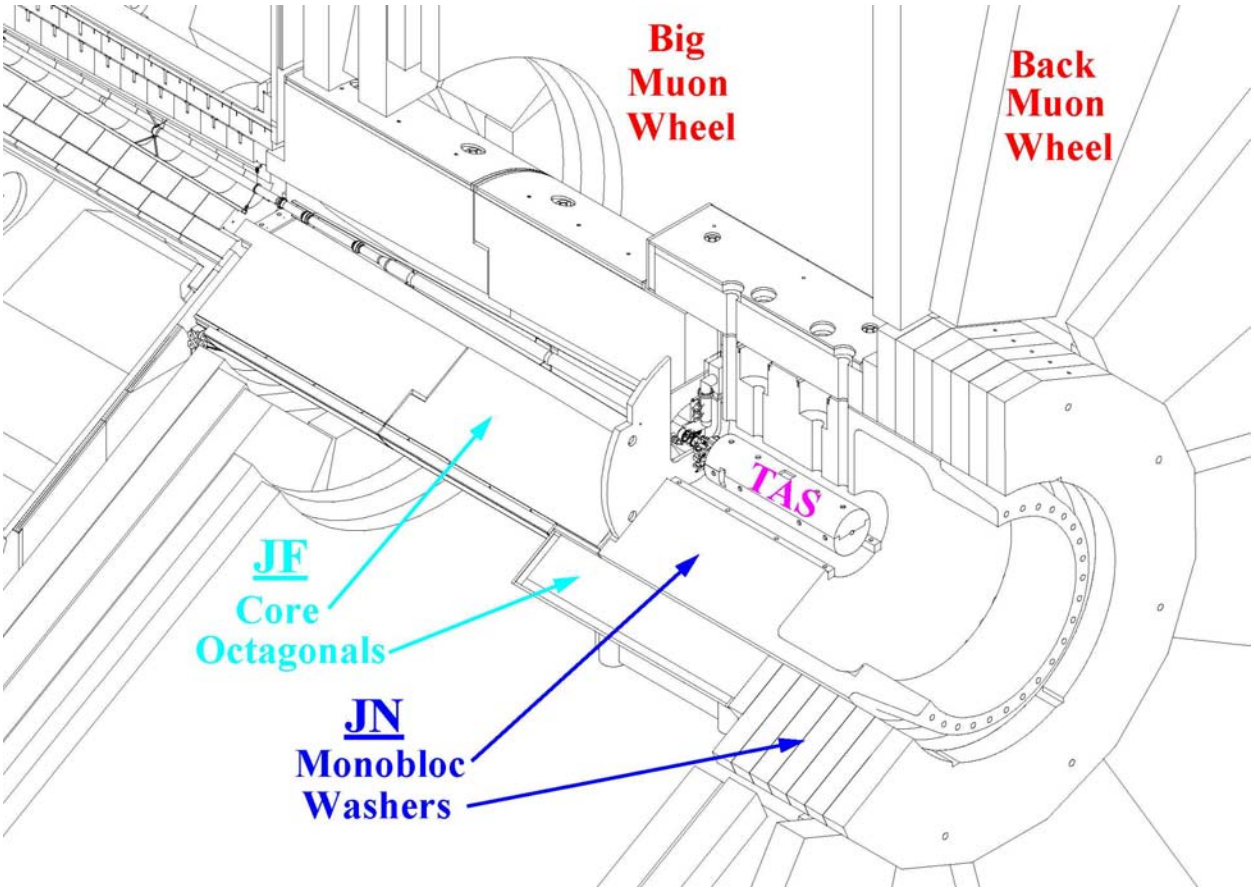

Figure 4.8 The massive shielding in the forward region (JF and JN) and the collimator (TAS).

The first part of the shielding ("the core") has a cylindrical shape while the second part that surrounds the JN monobloc and the TAS has an octagonal shape. The cylindrical core is made of cast ductile iron and consists of a bottom piece called the bridge and two top pieces (Figure 4.9). The boundaries in phi between the top and bottom pieces are made such as to not point towards the beamline in order to avoid streaming of backgrounds particles through the cracks. The inner boundary of the core section lies roughly along the line $\eta = 4.65$, continuing the inner surface line of the plug in the toroid shielding, and the outer radius of the cast iron cylinder is at 147 cm. The core cylinder interfaces at its front end, $z = \pm 13$ m, in a chicane with the JTT. At its back end near $z = \pm 18.6$ m, it abuts to the front face of the monobloc, where no chicane is needed since the core is here surrounded by the JF octagonal pieces. These pieces have an inner radius of 150 cm while the closest distance from the beamline to the outer flat surfaces of the cast ductile iron is 199 cm.

Cast iron is less dense than copper or steel, but it is much cheaper than copper. Due to its carbon content it is more effective than steel in the regime where there is a large neutron flux to moderate. Even though the forward cast shielding is massive, the neutron and photon fluxes coming through this shield can be reduced further through the use of cladding. At the front end, inside the middle forward muon detectors (the "big wheel") the shielding outer radius is restricted by the muon support structure to a maximum of 155 cm ($\eta = 2.82$). One is in the situation here found in other parts of ATLAS, where cladding is beneficial even when traded off against dense material. So on the outer surface of the 147 cm cast iron cylinder, there is a 5 cm layer of borated polyethylene (5% of boron by weight in the form of H_3BO_3), followed by a 3 cm layer of steel, bringing the outer radius to 155 cm. Steel was chosen in this region because, even though it is somewhat less effective as a photon filter it gives off less neutron radiation. Steel is also much cheaper and more structural than lead. The octagonal pieces also have cladding and

since there are not the same space limitations from the muon system in this region as in the big wheel, the borated polyethylene is here 8 cm thick, followed by a 3 cm thick photon filter made of steel. The closest distance from the beamline to the outside of the steel layer is therefore 210 cm (the most protruding corner on the front of the octagonal section is at $\eta = 2.77$).

Figure 4.9 The three cast iron pieces of the JF core section during manufacturing at the Skoda factory.

The octagonal pieces are foreseen to be upgraded and they have been made such that 25 cm thick steel plates can easily be added on top of the cladding. In this way the thickness of these shielding pieces can be increased from 60 to 85 cm if this turn out to be required at high luminosity running.

4.1.10 The Forward Nose Region (JN) and the TAS collimator

The nose region, JN, or TX1S as it is also called, is the domain of the LHC machine and constitutes the boundary where the ATLAS experiment envelope ends. This part of the shielding is permanently attached to the concrete wall of the cavern and it cannot (as the JF shielding) be removed during access. The primary task in this region is to complete the shielding of radiation from the TAS collimator and the beam-line structures extending into the final focus quadrupole (Figure 4.8).

Protruding from the endwall of the ATLAS cavern is a large, self-supported concrete structure to support the final focus quadrupoles. The face of this concrete is at $z = \pm 23$ m, and imbedded in this concrete, and protruding from it, is a large steel support tube of 20 cm thickness and outer radius 148.5 cm, see Figure 4.10. Attached to the end of the support tube is the JN monobloc. This massive piece made of ductile cast iron has an outer radius of 147.5 cm and a center hole

with a radius of 46 cm. The TAS collimator and the so-called cradle that surrounds it are located in this hole (Figure 4.11). TAS has an inner radius of 3 cm and an outer radius of 25 cm and is made of copper. The purpose of this collimator is to protect the first quadropoles from the particles coming from the interaction point in ATLAS, but in so doing it is creating a very strong radiation field in all directions. It is because of this radiation field that the JF octagonal pieces and the JN shielding have to be so massive.

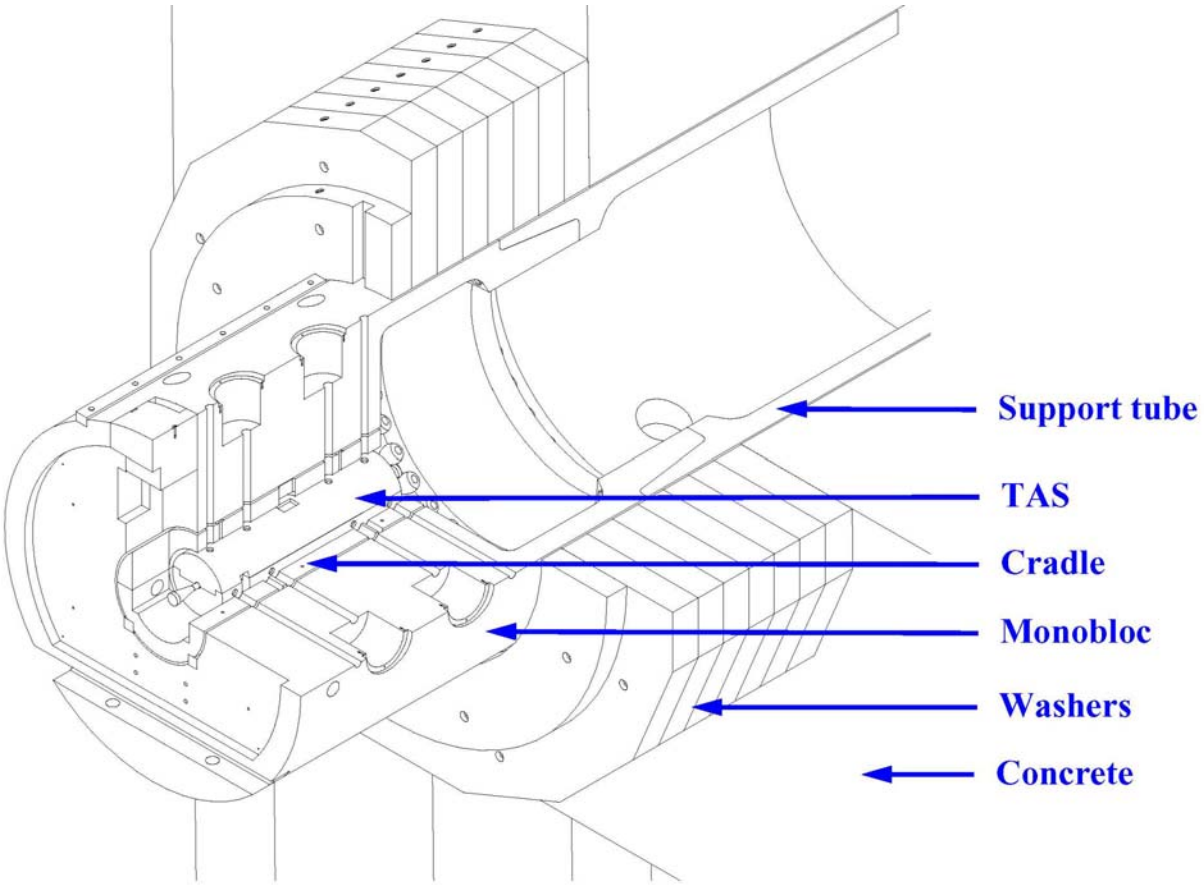

Figure 4.10 The various parts of the JN (TX1S) shielding.

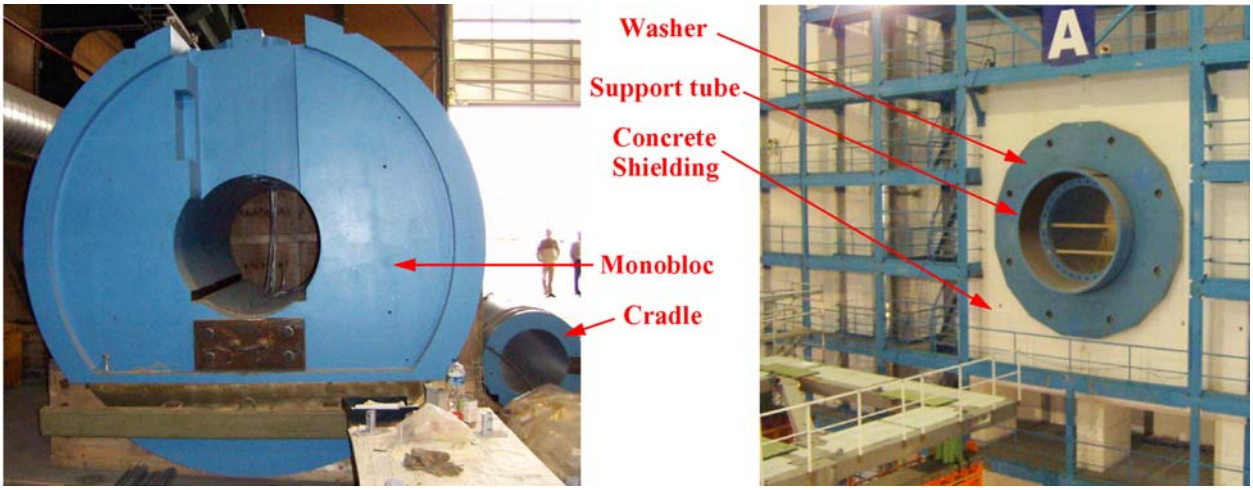

Figure 4.11 Photos of some of the JN parts.

A stack of large cast ductile iron disks surrounds the support tube and these disks ("the washers") are pinned against the face of the concrete. The first of these washers is cylindrical and has an outer radius of 216 cm while the rest of the washers have a hexadecagonal (16-sided) shape with a closest distance from the beamline to the outer surface of 262 cm. The first washer has a reduced outer radius in order to give space to the big wheel when it is moved into its garage position during access. There is no need for polyethylene cladding on the washers since they are made of ductile iron and the predicted absolute background rates in the back muon wheel are much lower than in the big wheel. The hexadecagonal shape makes it, however, possible to add a layer of cladding as an upgrade if that would become necessary during high luminosity running.

4.2 Geometry and Material Modeling in GCALOR and FLUKA

The ATLAS geometry has been implemented in the FLUKA and GCALOR programs in order to be able to estimate the background rates in the inner detector and the muon system. In this section is described how the specification of materials and geometry in this implementation was developed. One of the first concerns of the Task Force has been to validate the geometry and material description used by the simulation programs. The sub-detectors representatives provided dimensions and materials for the various detectors. Information was collected for the beampipe and the associated vacuum equipment; the toroids and the shielding elements and material were revised. The collected information [42] was then implemented in the detector description in GCALOR and FLUKA. For all major changes of design, the geometries in FLUKA and GCALOR were brought into as much correspondence as possible, and run as cross checks of each other. Simplified geometries were also calculated to isolate the origins of differences in predicted rates or spectra coming from the two transport codes.

4.2.1 Material Implementation

The materials specifications for FLUKA and GCALOR are sufficiently similar that it has been possible to maintain identical (parallel) material lists for the two types of simulation. For each material, elemental abundances may be specified by weight fractions or by atomic fractions, with the overall density as an additional input parameter. These material lists were updated over the years as engineering materials were chosen and the precise compositions, along with impurities, became better known. In most cases, the materials are specific elements, compounds, or alloys. But there are also “mixture” materials that represent the homogenized components of detector elements, such as calorimeter modules or silicon detectors.

4.2.2 Implementation of the Geometry in the Simulation

The methods to specify the geometry differ greatly in FLUKA and GCALOR.

The “combinatorial geometry” used by FLUKA is a modification of the package developed at ORNL for the neutron and gamma-ray transport program MORSE [38]. Two concepts are fundamental in combinatorial geometry: bodies and regions. Originally, MORSE bodies were defined as convex solid bodies (finite portions of space completely delimited by surfaces of first or second degree, i.e. planes or quadrics). FLUKA has extended this definition to include infinite cylinders (circular and elliptical) and planes (half-spaces). Use of such “infinite bodies” is encouraged since it makes input preparation and modification much easier and less error-prone. They also provide a more accurate and faster tracking. Regions are defined as combinations of bodies obtained by boolean operations: Union, Substraction and Intersection. The ATLAS

geometry and material description used in the FLUKA simulations contains some ~1500 regions and ~100 material definitions (elements, compounds and mixtures). The ALIFE editor and parser [44] is used to prepare the FLUKA input files. Where possible the geometry and magnetic-field description are simplified and described symmetrically in phi. (Fringe fields are not included.) Material regions associated with operation at cryogenic temperatures (e.g. liquid argon calorimeters at 87K) have associated to them low-energy neutron cross section data sets generated at that temperature.

GCALOR, on the other hand, running within GEANT3, uses a hierarchical, or tree structured geometry specification, wherein the fundamental geometrical quantities are volume shapes (boxes, solid cylinders, truncated cones, etc.). It is easier to specify complex geometries by this method, and this has made it possible to explore many configurations in the course of the process of the shielding optimization. The position and orientation angles of a given volume are specified in the reference frame of the volume in which it is placed: its "mothervolume". Each volume definition consists of a shape type, with all arguments needed to specify its dimensions (specific to the type), position and rotation information, and a pointer to the material from which it is made. Because most of the geometry description of ATLAS used in these simulations is phi symmetric, many of the volumes are "TUBE's" (cylindrical solids) or "CONE's" (solids with inner and outer coaxial cones) from the library of GEANT3 shapes. Most phi asymmetric shapes are "BOX's" (rectangular solids), placed at specified radii and phi orientations. Some of the materials are pure elements, but there are also many "mixtures" that represent compounds, alloys, doped materials, and materials with impurities. In addition, there are mixtures to represent the average composition and density of "homogenized" structures such as calorimeter modules. The magnetic field map used for all GCALOR simulations is the same 'bmag2' version used in DICE simulations, including realistic solenoidal, toroidal, and fringe fields.

The main energy flow of neutrons and photons coming out of the shield is not sensitive to the details of the geometry, so larger "average" volumes can be defined in which the emphasis is on achieving a good material description with the correct number of interaction and radiation lengths. However, there are exceptions in some critical regions, like the complex shielding and toroid structures in the forward region where in both simulations care has been taken to implement realistic engineering descriptions.

4.2.3 The history and evolution of the simulated geometry

Since 1998, when intensive engineering design began on ATLAS shielding, more than 500 geometry simulations (baselines and their options) have been done using GCALOR, with each simulation requiring approximately 2400 CPU hours on machines in the 450-850 MHz range, producing approximately 60 k events simulated per option. The bulk of this simulation has been done at the USATLAS Tier 1 Computing Center at Brookhaven, keeping roughly 50 of its CPU's busy with a duty factor of 75% since it came online. During this same period, many independent studies and comparison simulations were done with FLUKA on machines at CERN and Sheffield. Reporting the geometry evolution represented by these hundreds of simulation runs in any detail would be excessive, so this section seeks to telescope the description into the consideration of three crucial geometries: (1) TP43/44, the 1997/1998 geometry appearing in the muon system TDR, (2) the ATLAS shielding geometry at the end of 1998, and (3) the current geometry. The discussion will fill in the major steps in design evolution between these geometries.

The integrated forward calorimeter design was proposed to ATLAS in 1994 by the University of Arizona—to be installed in the endcap calorimeter cryostat at about 4.5 m from the I.P, instead

of a standalone device at 13 m. One of the primary features of the design was to make the calorimeter a uniform container of the flux from the interaction point up to $\eta = 5.0$, and to allow the calorimeter interaction lengths to provide much of the shielding depth needed to protect the open, low mass, muon system from background radiation. It also allowed for massive shielding to be placed behind the FCAL, extending to the shielding around the TAS collimator. Finally, it allowed for the FCAL bore itself to be designed to act as a large aperture collimator, restricting the forward streaming particles to flow toward the TAS shield, and reducing the flux heading for the inner and middle forward muon detectors (small and large "wheels", respectively).

In 1994 and 1995, studies were made periodically to see if the JT copper shield would be more effective if its inner radius were smaller. But it turns out that the $\eta = 4.65$ line is at the bottom of a broad minimum in rates extending from roughly 4.55 to 4.80. The effect is that as the shielding thickness is increased by moving the inner boundary to smaller radii, this material intercepts more flux streaming from the exit bore of the forward calorimeter. So what is gained in shielding thickness is overbalanced by increased intensity at the inner surface of the JT shield.

From 1992 to 1998, the majority of the radiation background calculations for ATLAS were done by Alfredo Ferrari and Paola Sala using Milan FLUKA (now known as standalone FLUKA). There were periodic comparison calculations done by Michael Shupe at the University of Arizona, using GEANT3/GCALOR. During this era, Ferrari worked closely with Peter Norton, of Rutherford Laboratory, to optimize the forward region shielding design given the requirements to maintain the muon acceptance and accommodate the mechanical structures of the endcap toroid, while minimizing the radiation backgrounds. By early 1998 that design exercise lead to the design depicted in Figure 4.12 and Figure 4.13**.**

The ATLAS shielding in the JD region is relatively thin, in the sense that small adjustments to the dimensions or materials can have a large effect on background fluxes, particularly in the CSC's. Ferrari discovered that neutron and photon fluxes improved greatly if PolyLiF and Pb cladding layers were used on the surface which we now refer to as the "hub" (Figure 4.7), and the layers can be seen in Figure 4.13 on the surface of the hub.

Similarly, the JT Cu Shield is thin, and neutron and photon backgrounds can be reduced if moderator is placed in the body of the endcap toroid, outside its support tube. Ferrari and Norton proposed blocks of LiF loaded epoxy be placed between the 8 coils of the endcap toroid magnet at small radius, and that other small blocks be placed near the front and back ends of the support tube. Unfortunately, the structure of the toroid prevents continuous layers from being placed within it, so one is forced to a lumped-moderator approach in this region with unshielded regions where the coils are situated.

The JF shield was designed to fill all the available volume between the JT and the TAS shield, in the range $\eta = 2.7$ to 4.65. The core of the JF was steel, for density and structure, followed by cast iron (for moderation by its carbon) followed by cladding layers of poly-LiF and Pb, to reduce low energy neutrons and photons.

The JM moderator was envisioned to be a poly-LiF sheet on the front face of the endcap calorimeter, accompanied by a plug block around the beamline. This moderator lowered neutron background rates in the inner detector, by moderating them in the polyethylene and capturing them in the LiF.

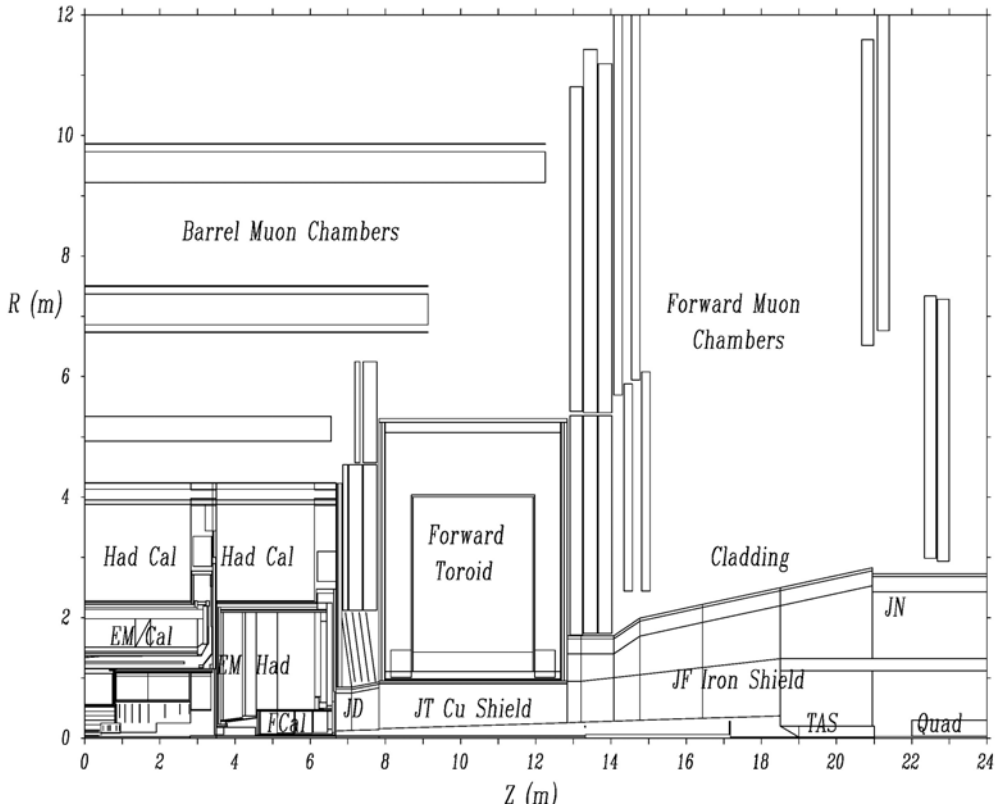

Figure 4.12 GCALOR TP43 geometry.

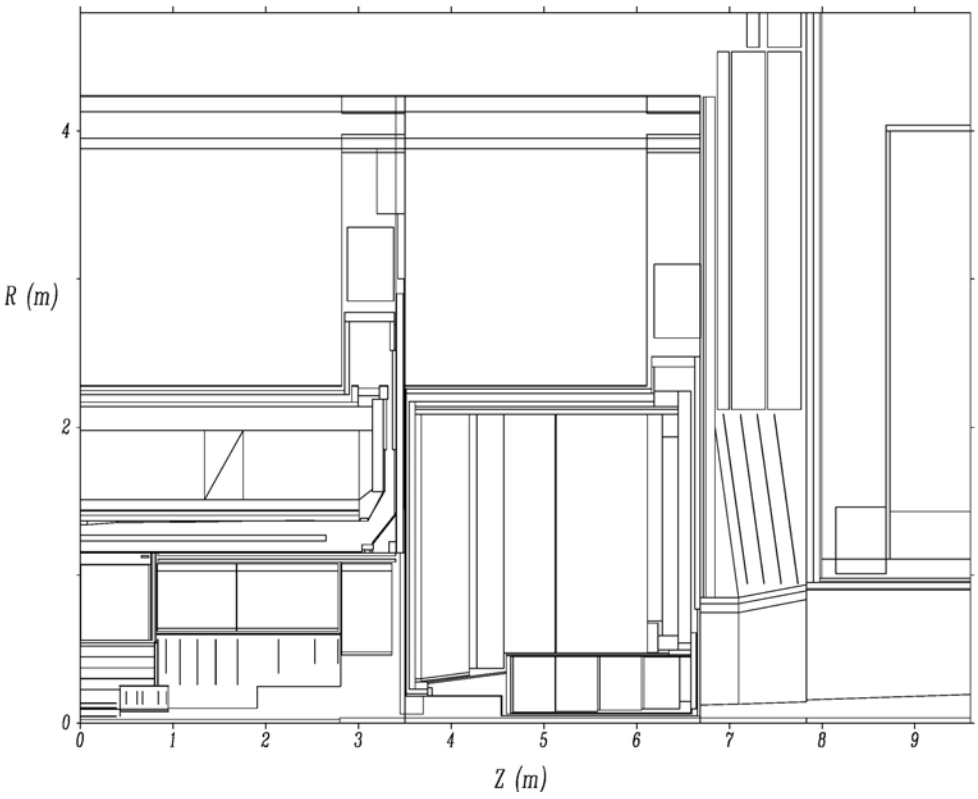

Figure 4.13 GCALOR TP43 geometry: calorimeter region.

Finally, copper alloy plugs were introduced inside the liquid argon of the endcap calorimeter, behind the HEC and FCAL sections, to increase the interaction lengths and provide additional shielding depth for the muon system. The design of these plugs has changed little from 1998 to the present day. They have been fabricated in Australia, in a three-way design collaboration with Arizona and CERN.

In the summer of 1998, Ian Dawson, from the University of Sheffield, took over FLUKA simulations for ATLAS. He worked closely with Alfredo Ferrari and Paula Sala during the transition period, and also introduced new front end geometry code (ALIFE, written by A.Morsch [44] for ALICE fluka simulations) to the ATLAS FLUKA package. Dawson discovered the problem with cross sections in the FLUKA neutral kaon sector, and provided information to Ferrari during the revision phase.

The engineering design of the JM, JD, JT, JF, and JN shields did not get well under way until the summer of 1998, with the formation of the Shielding Engineering Group, chaired by Werner Witzeling. The designs up to that time used practical materials, and were based on sound shielding knowledge; but they were still at a conceptual level.

The initial phase of engineering development went fairly rapidly, and could be characterized as "engineering the conceptual design of early 1998". By late fall of 1998 a new geometry had evolved, as shown below in Figure 4.14 and Figure 4.15. As might be expected, the engineered geometry had background rates considerably higher than those of TP43, due the effects of engineering realism. We will give a short list of the effects here, with brief discussion about their relative seriousness.

The TP43 design had one mechanical design flaw in the JD region that required serious rethinking of the shielding strategy there. In TP43, the cladding extended through the center of the large JD disk (flux return plate). Since the disk is supported from its rim, the JD hub must be joined to the disk firmly and, given the large masses involved, soft cladding cannot intrude into this joint. Since about 40% of the cladding would be lost, it was assumed best to try a different approach: to remove the cladding and make the core of the hub denser, with tungsten. In actuality, a long list of options was tried: (a) Cu hub, no cladding, (b) Cu hub, 60% clad, (c) Cu hub, W core, no cladding, (d) Cu hub, W core, 60% clad. None of these solutions was as good as TP43, and the tungsten needed was, ultimately, too expensive. Finally, it was decided to make the hub and cone copper (no W), and to clad BOTH surfaces, with some loss of Cu in the cone. This has turned out to be the best solution, though still not as good as the "imbedded cladding" design of TP43. In Figure 4.15, this region is shown as a monolithic block of copper.

The vacuum group was developing the beamline design in the spring of 1998, and the TP43 design was too simple. TP43 had a large ion pump at 17m, but the vacuum group design had pumps at 4.2 m, 13.2 m, and 18.3 m, as well as a number of flanges. The worst flange was at 3.5 m, just at the front of the endcap calorimeter. It created a secondary source illuminating the barrel/endcap services gap and raising the backgrounds near the ends of the inner detector volume.

A clearance gap of 3 cm had to be introduced between the JD disk and the back of the endcap cryostat (visible in the zoomed picture). This allows additional radiation to stream outward radially in front of the JD disk. As shown in the pictures, chicanes were introduced at the upstream and downstream ends of the JTT shield, and at two places in the JF shield. With

realistic mechanical tolerance gaps, the increase in rates due to these chicanes was negligible compared to other effects.

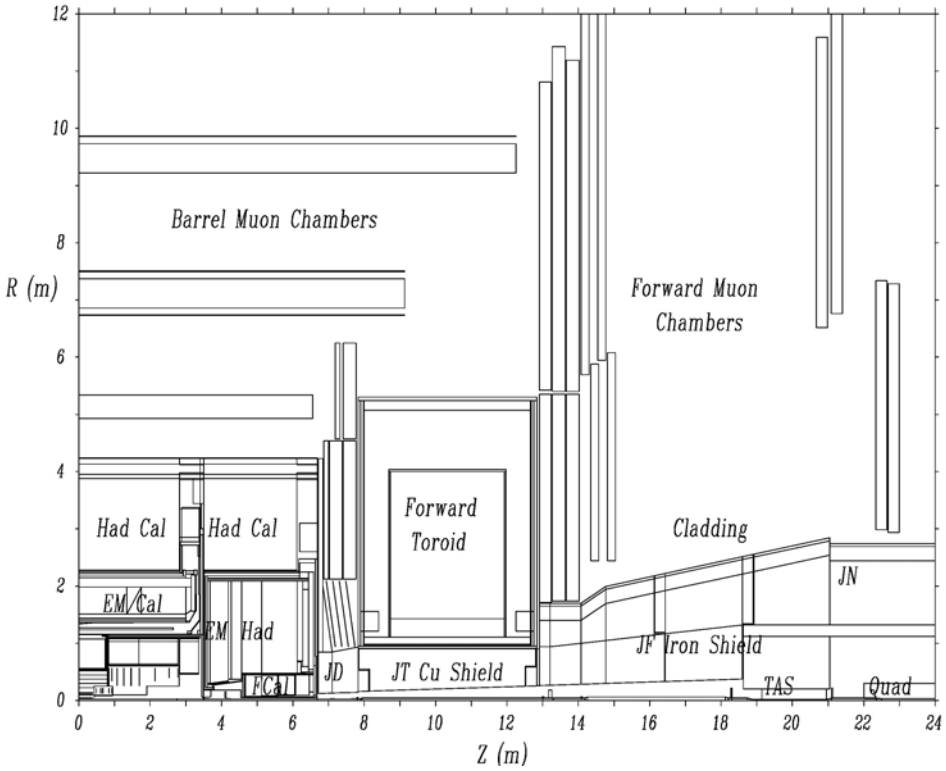

Figure 4.14 GCALOR September 1998 layout.

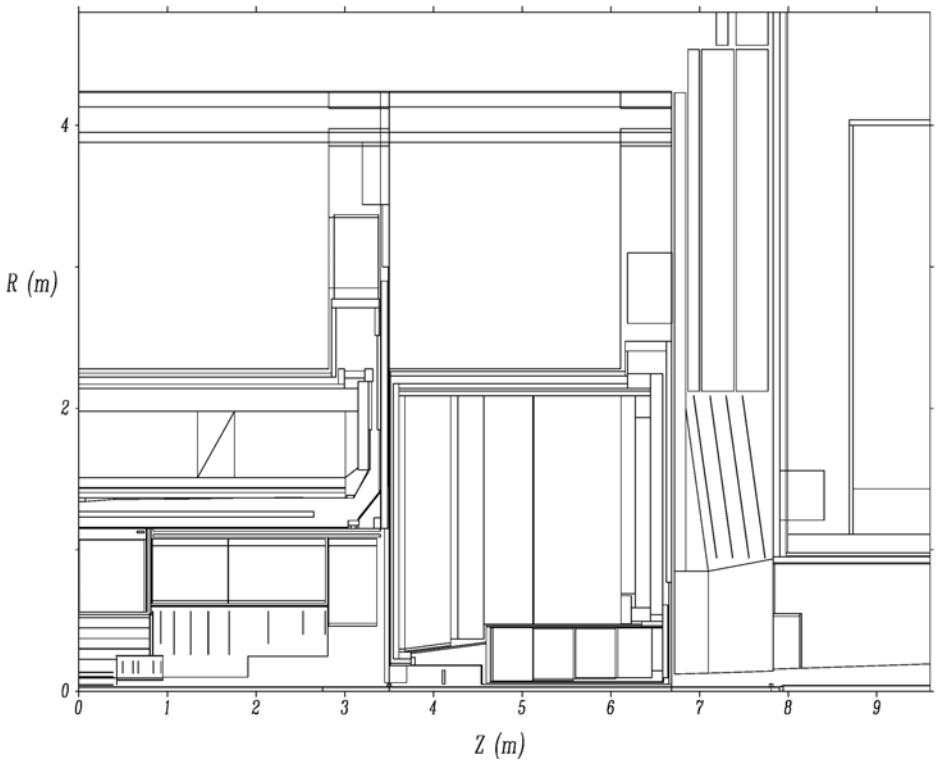

Figure 4.15 GCALOR September 1998 layout: calorimeter region.

Some of the dense materials specified in TP43, especially the cast iron in the JF, were too dense, and the copper composition was not realistic. The more realistic materials worsened rates in the 10-20% range in some locations.

The small epoxy blocks near the front and back of the JT had to be made smaller, and moved outward, which also worsened rates.

The combination of all these effects made background rates increase by factors in the range 1.5 to about 3 relative to TP43, depending on the region and particle species involved. It was clear that ongoing engineering would continue to make things worse, and that new approaches were needed.

From 1998 to 2000, shielding engineering was carried forward at CERN by Werner Witzeling, (envelopes engineer), Francois Butin, J.P. Corso, Peter Norton and Ed Towndrow (RAL), Stanislav Pospišil and Jaromir Sodomka (Prague), supported by background calculations from Ian Dawson, Michael Shupe, and Ivan Štekl (Prague). Ray Veness provided beamline designs during this era, and has continued to the present day.

In 2000, the Radiation Taskforce was formed, chaired by Martine Bosman. Werner Witzeling retired as chair of Shielding Engineering, to be replaced by Vincent Hedberg, from Lund University, to direct the engineering effort and bring in new expertise in the area of activation. Ian Hooton has been the primary ATLAS engineer on the shielding project since 2000. At the same time, we were joined in the simulation efforts by Mikhael Morev, on activation, and Sergei Baranov, on detailed simulation of muon chamber response. Leandro Nisati and Georges Mikenberg provided also input for the muon system.

Much progress had already been made by 2000, but these personnel changes brought renewed energy and focus to both the simulation and engineering work on ATLAS shielding and beampipe design. The period between year 2000 and 2003 therefore led to many design changes:

Beamline

The beryllium pipe in the inner detector lengthened from 2.8 m (halflength) to 3.6 m in order to lower background rates due to secondaries produced in the pipe, and became double-walled to provide a vacuum jacket for NEG pumping. The mass of the flange at 3.6 m was reduced. The ion pump in front of the FCAL underwent design development, and moved from 4.2 m to 3.8 m, for mechanical reasons. The pipe downstream to the TAS remained stainless steel, with some changes in flanges and transition locations, and two NEG pump jackets were added—inside the FCAL and inside the endcap toroid. The NEG jackets have raised radiation levels in the muon system, and are an ongoing target of study. A large ion pump at 13.2 m was removed from the design, and this improved rates in the Big Wheel and the Back Wall detectors since it was a secondary source for radiation from the I.P.

JM Region

The JM moderator underwent redesign in 2001/2002, especially in the FCAL alcove. The doped polyethylene moderator disk on the front of the endcap became somewhat smaller, to accommodate services at the outer radius. In the alcove, instead of a moderator block mounted on the beamline from 3.5 to 3.7 m, moderator now lined the alcove surface, and was mounted on the cryostat. This design was preferred for engineering reasons. The rates in the inner detector did not change, even though the ion pump at 3.8 m was now visible from the inner detector. This is because (1) the backward going albedo from this pump is very small in comparison with other

sources, such as the face of the endcap calorimeter, and (2) the new alcove design is very efficient because the moderator lining the alcove intercepts flux both from the beamline, and from inside the calorimeter. This is one of locations in the detector where the background rates are reduced "bidirectionally" by a moderator layer.

JD Region

A comparison of the pictures for late 1998 with the 2002 design shows that the JD has undergone substantial engineering development during this period. Some of options tried were discussed above: cladding vs. no-cladding, dense W core vs. Cu core, etc. The main conclusions from dozens of option studies were as follows: (a) A few centimeters of cladding—doped poly followed by photon absorber—were of great benefit, *even when replacing dense Cu at the outer radius,* and (b) given this cladding, a tungsten core gave only small improvements in backgrounds, in the 10% to 30% range, at great expense (and that the same money applied elsewhere would yield greater reduction in rates).

The other major developments in the JD design were mechanical—to develop a sliding hub system that allows the Small Wheel to be retracted from the back of the JD flux return disk, so that the fronts of the CSC and TGC detectors may be accessed. The 2002 design had (starting from small radius), a long Cu alloy core extending from 6.8 to 8.7 m, held by a 10 cm thick steel tube that joins to the JD disk at its front end and supports the Cu core. This tube also supports the Cu alloy sliding hub, and it constitutes the inner part of the long chicane at the front end of the JTT. The outer part of this hub, and the face of the Cu alloy cone mounted on the JD disk, were clad with borated poly and Pb, to complete the shielding.

JT Region

The endcap toroid region also underwent many changes since 1998. The JT Cu Shield simulated in 1998 had too large an outer radius. The JT support tube had to be made smaller to allow for JT coil clearance, and an additional 1 cm clearance gap was introduced inside the tube, to allow for clearance of the copper. The combination of these effects is quite apparent when comparing the pictures of the JT shield in the 1998 geometry with the current design, and this loss of dense material is serious because the JT is one of the thinnest parts of the shield to begin with, "illuminating" much of the forward and barrel muon system with its radiation leakage.

Between 1998 and 2000, the strategy was to put as much copper alloy shield inside the JT support tube as possible, and then moderate neutrons outside the support tube. This was done by placing epoxy loaded with LiF wherever feasible inside the endcap toroid, among its coils at small radius, and outside the support tube at small radius, both front and back. Starting in summer of 2000, two alternate tactics were employed: (a) putting a thin layer of borated polyethylene *just inside* the support tube, in place of copper, and (b) putting moderator on or near the front and back faces of the toroid outer wall, instead of inside, among the coils. Using these two tactics together has greatly reduced the cost and complexity of the shield, and at the same time lead to a better overall optimization of the background rates. Both of these moderator configurations, (a) and (b), are more hermetic than the "lumped element" configuration used up to mid-2000, and give a better result for muon counting and trigger rates, even though the dense material is being reduced.

In the picture of the 1998 geometry, one can see the epoxy blocks inside the toroid at small radius, and other blocks front and back, near it. In the 2002 design there is a 4 cm polyboron layer around the Cu plug, rings at the front and back of the support tube, and polyLiF on the back face of the JT outer wall to a radius of 3.5 m.

JF Region
From 1998 to 2000, the design of this region consisted of a "layered" geometry, with a steel core for high density, a middle layer of cast iron (lower density) to moderate neutrons with its carbon content, and two cladding layers--PolyLiF followed by Pb--on the outside. Beginning in early 2000, a large number of studies were done to vary the materials in ALL of these layers, and a number of patterns emerged:

(1) In regions where cladding is needed, there are cladding combinations which are more effective in removing both neutrons and photons than PolyLiF and Pb.

(2) With a cast iron middle layer, it is more effective if the core is also cast iron instead of steel. What is lost in density (7.8 becomes 7.2) is more than offset by neutron moderation due to carbon in the cast iron.

(3) For the same reasons, the original steel shield surrounding the TAS may also be cast iron. It is in effect the "core" section of shield in this area, so this result is not surprising. This study lead to the current design, where the TAS shield is a complex casting, referred to as the 'monobloc'.

In the 2000/2001 era, there were a number of insights leading to major redesign of the JF. The "classical" conical outer envelope of the 1998 design had been retained in the spirit of filling all available space with shielding material. But by 2001, it had become clear that this region was *overshielded* in the sense that there was a lot of tonnage of dense material that was making very little difference to rates in the muon chambers, especially in the zone from roughly z = 15 m to 21 m, where the JN begins. In looking at the flux maps and the rates in the middle (Big Wheel) and back (Back Wall) regions, it became clear that one could remove a lot of dense material (cast iron) at large radius, and thin the cladding to about half its earlier thickness, without increasing rates in the Big Wheel chambers. At the same time, the rates in the Back Wall chambers would increase somewhat, but still be roughly *one order of magnitude below* the rates in the Big Wheel chambers.

JN Region
The JN region surrounds the beginning of the final focus quadrupole. The nearest high intensity secondary source is the TAS collimator which is 25 cm shorter in the current design than in 1998, to allow space for quadrupole services and maintenance. The main structural feature in this region is the large support tube imbedded in the cavern end wall, supporting the quad magnet front end, and ending at 21 m. The TAS cast iron monoblock is bolted to the end of this support tube. The JN shielding pieces outside the support tube are cast iron in the region from Z = 21 m to 23 m, where concrete JN shielding begins. There is currently no provision for cladding in this region, although there is room to add it if needed.

The responsibility for the JN region is with the LHC machine, and not the ATLAS experiment, so development on this region has relied on close collaboration with Francois Butin, who moved to LHC engineering in 2000.

In all, there is less shielding depth in the JN region in the current design than in 1998, but the effect on Back Wall chamber rates is still well within acceptable levels, for the reasons noted in the JF region discussion.

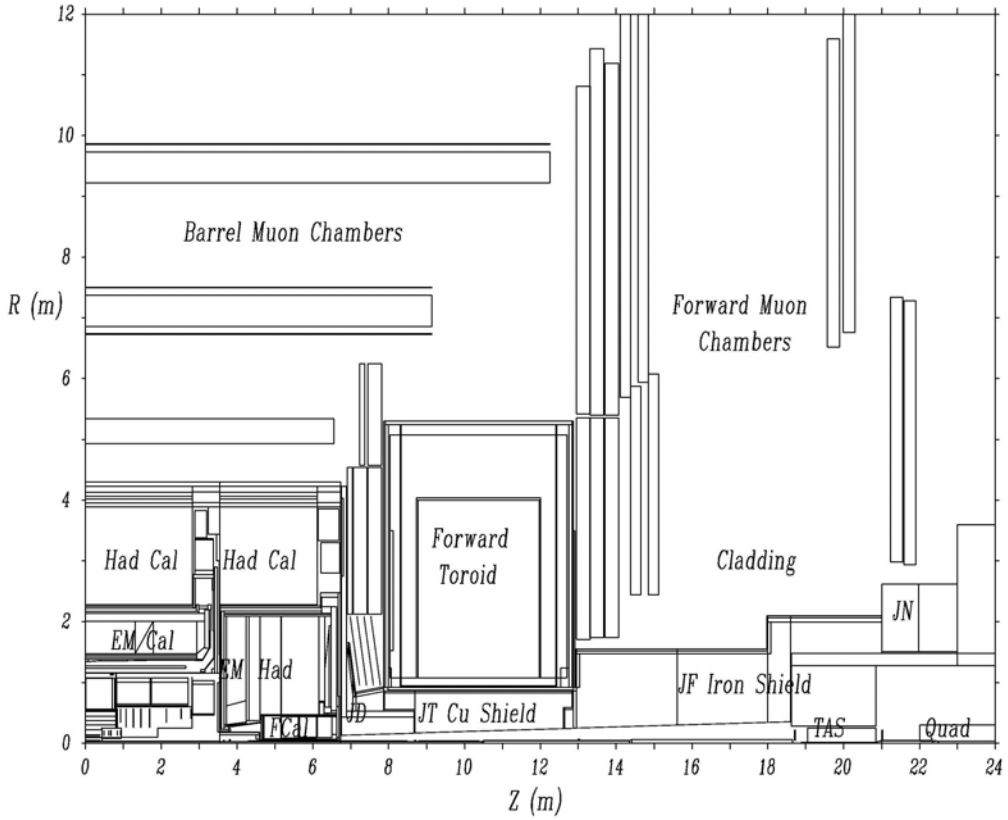

Figure 4.16 A full quadrant of the Atlas "Jan03" geometry layout as modeled with GCALOR. The picture shows all structures in phi projected into one plane. The old muon chambers positions have been kept for backward compatibility with earlier versions.

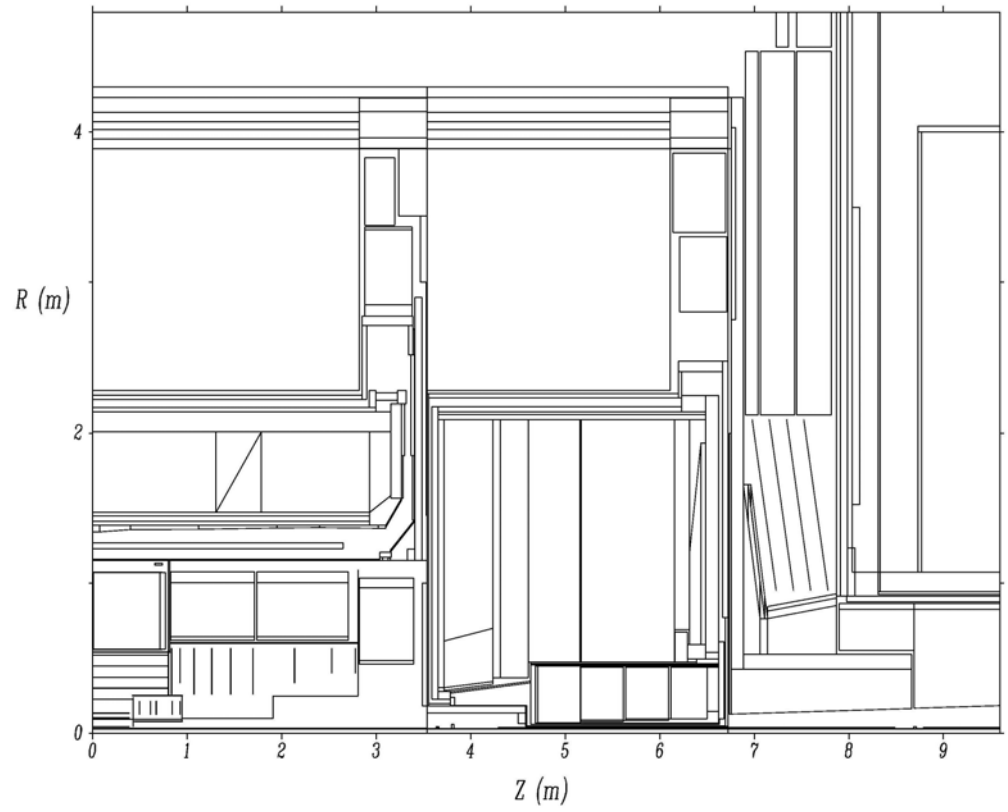

Figure 4.17 Zoomed view to the calorimeter region in GCALOR "Jan03" layout.

4.2.4 The latest version of the simulated geometry

The simulated baseline geometry used to calculate the radiation levels presented in this report are discussed in this section. The ATLAS geometry has, however, continued to evolve and in the next section the difference between the simulated baseline geometry and the present one will be discussed. The "final" baseline geometry used in GCALOR is called "Jan03" and it is shown in Figure 4.16 and Figure 4.17. The volumes and their dimensions for the GCALOR "Jan03" geometry, as well as the corresponding materials, are available in Appendix III and Appendix IV.

The most up-to-date geometry version in FLUKA used in this report, "AV16", is depicted in Figure 4.18 and Figure 4.20. It is a geometry layout similar to the "Aug01" in GCALOR, with the old conical JF concept.

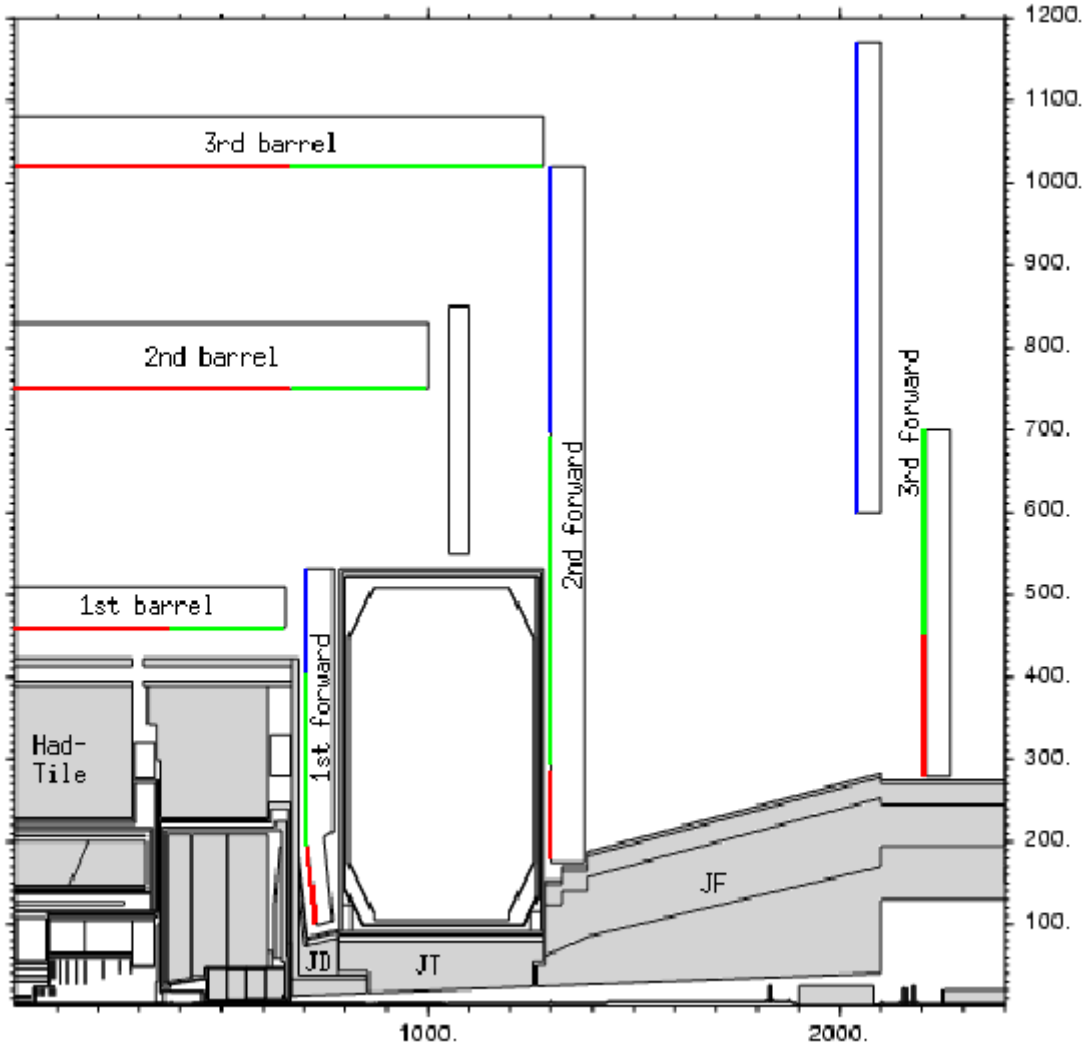

Figure 4.18 The Atlas geometry in the FLUKA AV16 configuration, similar to "Aug01" GCALOR layout with previous JF concept: the picture represents a simple slice at a fixed phi angle. Horizontal axis gives Z in cm and the vertical axis R in cm. The old muon chambers positions have been kept for backward compatibility with earlier estimates.

Beamline Vacuum System: The beamline model in GCALOR and FLUKA was based on the official LHC-vacuum-group drawings of December 2000 (Ray Veness et al). Most beamline components are made of pure metals or metal alloys, and are phi symmetric. Most shapes are solid cylinders, with cones where the beamline flares or unflares. Since the beamline is subject to particles emerging directly from the I.P., it must be modeled in detail, at least through the back of the TAS collimator.

The beam pipe in the inner detector region was assumed to be double-walled beryllium running from the interaction region to about z = ± 354 cm. Both walls of the pipe were 0.8 mm thick, with inner radii of 29 and 33.8 mm.

At z = ± 354 cm, the beampipe material changed to stainless steel, with an inner radius of 29 mm and a thickness of 0.8 mm. The pipe remained this dimension until z = ± 1046.5 cm, where it flared to an inner radius of 39 mm, with a thickness of 1 mm by z = ±1050.7 cm. It remained this dimension until a second flare at z = ± 1434.2 cm, where it expanded to an inner radius of 60 mm, with a thickness of 1.5 mm, by z = ± 1441.6 cm. The pipe stayed this dimension until it reached the front of the TAS absorber, at z = ±1865.0 cm. In order to provide isolation during bake-out a second stainless steel pipe ran from z = ± 429 cm to z = ± 849 cm, with an inner radius of 39 mm and a thickness of 1 mm. A second doubled wall pipe was located inside the front part of the bore of the forward toroid, running from z = ±878.5 cm to z = ± 1039.3 cm, with a second stainless steel pipe of the same inner and outer radii as the first.

To pass through the ion pump at z = ± 1870 cm, and then through the small hole in the TAS collimator, by z = ± 1888 cm the beampipe reduces (unflared) to an inner radius of 17 mm, with a wall thickness of 13 mm, and makes a transition to copper (Figure 4.19). The outer diameter of the pipe fits perfectly in the center hole in the TAS collimator.

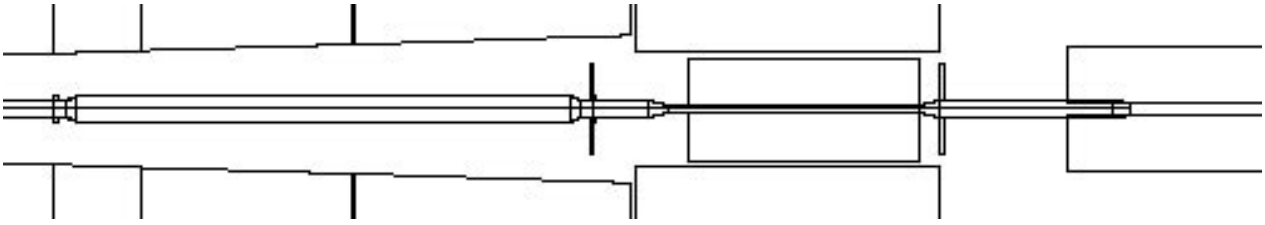

Figure 4.19 A zoomed view of the region of the TAS in GCALOR.

Included in the simulation is a low mass (2 kg) stainless steel ion pump at z = ± 380 cm that provides the main pumping power for the inner detector region. There is also a large ion pump at z = ± 1870 cm, in front of the TAS absorber. A third large ion pump at z = ± 2094 cm is located behind the TAS collimator.

Inner Detector and JM shield: All detector subsystems in the inner detector, along with their supports and services, are modeled as solid cylinders made of homogenized mixtures (see Figure 4.20). They include barrel and disk pixels, silicon tracker barrels and wheels (SCT's), transition radiation tracker barrel and endcap volumes (TRT's), along with support tubes, insulation and thermal shields, patch panels, and service layers. The dimensions and mixture specifications for each component were provided by Jo Pater and Fred Luehring of the ATLAS inner detector group, specifically for incorporation into the simulation geometries in GCALOR, FLUKA, and portions of DICE, based on the inner detector layout of fall, 2001.

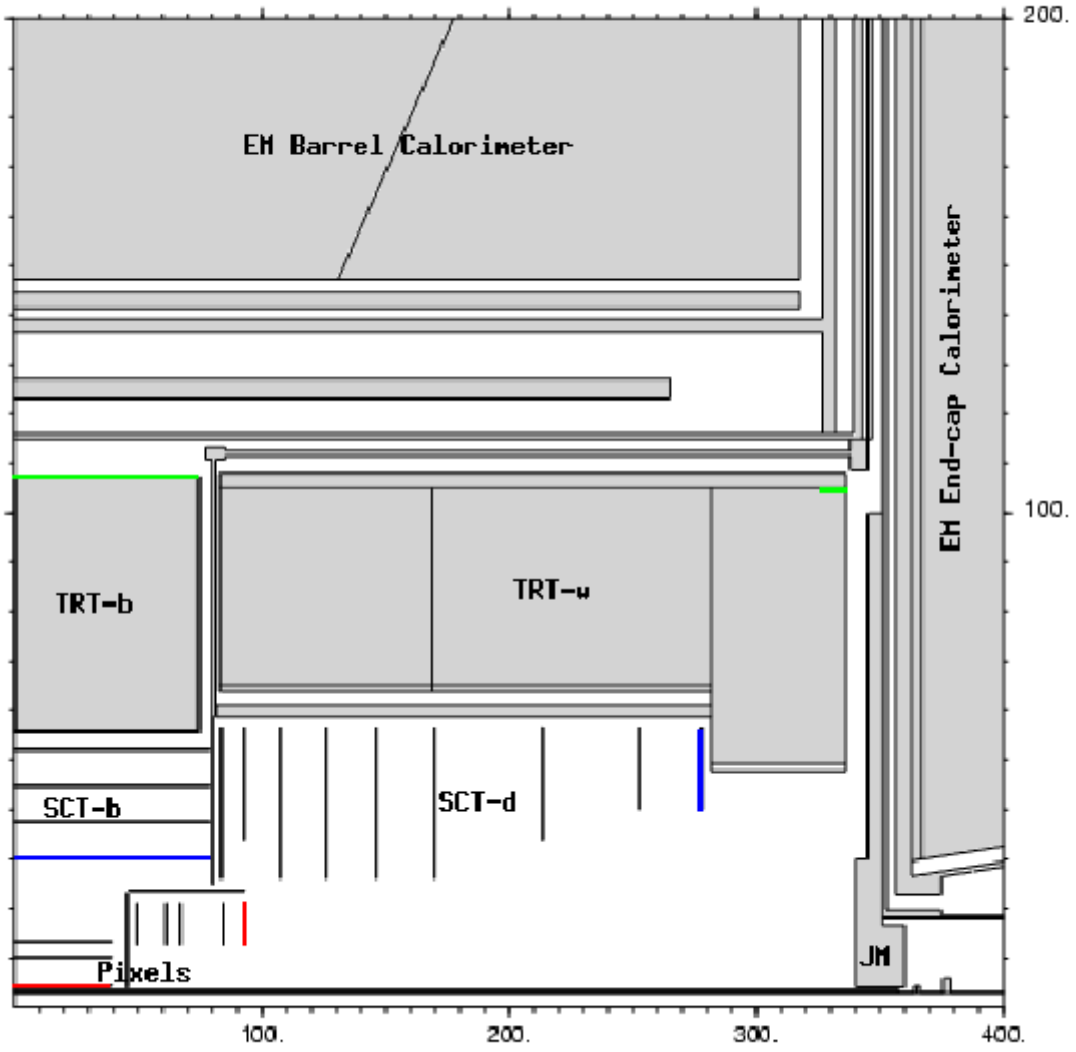

Figure 4.20 Zoom to the Inner detector region of the Fluka AV16 configuration.

The moderator on the face of the endcap calorimeter (JM) was simulated as a 5 cm thick polylithium disk with a radius from 18.3 cm to 100 cm. The alcove in front of the FCAL is moderated in the simulation by a cylinder that lines the bore of the warm wall. This cylinder, which is also made of polyboron, has an inner radius of 13.5 cm and an outer radius of 18.3 cm. On the front face of the FCAL, the inner radius of the cylinder goes down to 6.6 cm and forms the 8 cm thick so-called "JM plug".

Liquid Argon Barrel Calorimeter: The densest parts of the liquid argon calorimeters are the modules themselves, and even the modules with the coarsest segmentation—the hadronic endcap (HEC) modules, are sufficiently uniform as "shielding" components that they may be simulated as homogeneous mixtures within their own envelopes. In the barrel, the EM accordion is 'seamless', and is modeled as two phi-symmetric compartments with different mixtures, connecting along the $\eta = \pm .8$ surface, where the sampling fraction changes. In DICE simulations, the EM accordion is described in full detail, with thousands of volumes, and this GCALOR description is at the opposite pole in terms of the level of detail. However, for many pieces of the LAr barrel calorimeter, the two descriptions are as identical as it is practical to

make them. In the GCALOR description, the dimensions and materials for the solenoid, cryostat walls, and feedthroughs were taken from AGE scripts used in the DICE simulation. The remaining parts that are simulated as homogenized materials are (1) the preshower detector, and (2) the volumes inside the cold wall filled with mixtures of services and liquid argon. The information has been provided by D. Fournier. The reason for taking care in the modeling of the cryostat structures and services is that they face the barrel/endcap services gap, and constitute part of a lower-density channel that is more transparent to background radiation.

Liquid Argon Endcap Calorimeter and Plugs: The modeling of the liquid argon endcap is very similar to that used in the barrel: homogeneous, phi symmetric calorimeter modules, combined with detailed description of cryostat elements and other structures critical to the flow of background fluxes. Specifically, the EMEC is modeled in two compartments, inner and outer, with mixtures of slightly different composition and density. This is an approximation, since in reality the composition varies continuously as a function of radius within each compartment, but the effect on the integrated depth of the calorimeter, and the simulated background rates, is negligible. The HEC and FCAL modules are modeled as phi symmetric solid cylinders, each with the correct mixture. To simulate the radial gaps in the HEC region, BOX shapes filled with liquid argon are inserted into these compartments in the GCALOR geometry. For the endcap cryostat, all structures, dimensions and materials were taken directly from engineering drawings, instead of the DICE/AGE description. This is because for many years the DICE description was not sufficiently detailed, especially near the beamline, since this was not necessary for physics simulation. Likewise, all calorimeter and services mixture materials were calculated from information provided directly by collaborators in the EMEC, HEC , and FCAL teams, or gotten from subsystem TDR's. Finally, description of the shielding plugs (1, 2, and 3) behind the HEC and FCAL (Figure 4.6) has been updated many times during design development at Arizona and CERN, in the same spirit as the external shielding. This information has also been incorporated in the FLUKA simulation.

Tile Calorimeter: The barrel and extended tile calorimeters (TileCal's) are almost monolithic structures that, in backgrounds simulations, can be modeled as solid cylinders made of a uniform mixture of primarily steel and scintillator. This is also true of the ring of small modules at large radius attached to the front face of the extended TileCal in the barrel/endcap services gap. The inter-cryostat scintillators are also positioned on this face of the TileCal at smaller radii. However, the surfaces of the tile calorimeters at large radius consist of "girder" structures containing "drawers" that house the readout photomultiplier tubes and electronics. Also, in the same radial zone, in the barrel/endcap gap, steel 'fingers' form a bridge between the barrel and endcap girder structures, for services routing and to provide a flux return path for the inner detector solenoidal field. These structures are 64-fold symmetric, and are modeled with rectangular solid volumes. All of these girder, drawer, and finger structures must be simulated in some detail for two reasons: (1) the fingers provide partial shielding for the barrel muon system, and (2) electronics, power supplies, and other services in the drawer and finger regions are susceptible to single event upsets and damage, so the radiation background rates must be accurately known in these regions. All of the model dimensions and material mixtures for the girder and finger region (structures and services) have been provided by the TileCal group, and our primary contact has been Marzio Nessi.

Barrel/Endcap Gap: This region is difficult to model because it is filled with complex structures such as cryostat feedthroughs and services, electronics crates and services, and inner detector cooling and electronic services. None of these structures is phi symmetric. In the GCALOR description (see Figure 4.21), a compromise has been struck, with massive elements such as the electronics crates modeled as rectangular solids with all internal parts combined into

a homogeneous mixture filling the solid. This "lumped element" description is an attempt to get the total material budget correct (as in all regions of the ATLAS model), and to get the "fill factor" of the major masses correct. There are 16 of these crates in each gap, spread evenly in phi, in this model. There are small blocks of polyethylene moderator in the vicinity of these crates—with a relatively low fill factor—to anticipate some shielding material in this region. The services in the region outside the electronics crate and inside the fingers have been modeled as a solid ring of homogenized material (mix provided by TileCal group), but there are gaps around this ring (in the spirit of the DICE model) to simulate the effect of voids in the real design. At small radius, between the cryostat warm walls, the services channels have been modeled as 32 boxes of the proper cross sectional dimensions placed radially in the crack, filled with a mix that accounts for the sum of all services emerging from the inner detector. The separation between cryostats includes the 4 cm added in 2001 to increase the gap size for services routing. All objects filling the gap region, beginning at the inner detector and ending at the outside of the TileCal, reduce the backgrounds in the barrel muon system. The reduction, as the gap fill factor grows, is less than one might expect because the barrel and endcap cryostat structures create a "low density path" from the inside to the outside roughly ½ m in width, consisting of aluminum, liquid argon, and vacuum. It is not worthwhile trying to plug all paths to the muon system, especially inside the electronics crates, because of this wide, low-density channel.

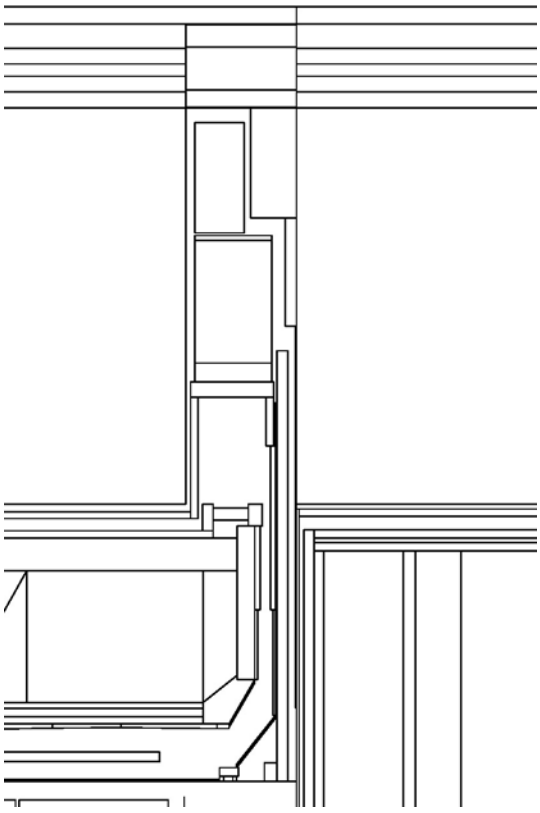

Figure 4.21 Zoomed view of the gap between the Barrel and the Endcap

Flux Return Disk and the JD Shield: It has been possible to model the flux return disk and JD shield fairly realistically since many of the pieces in this area are solid cylinders or cones, or close approximations to them. The model includes the steel, copper alloy, and cladding pieces as described in the baseline geometry, with realistic materials and clearance gaps. However, for simplicity the penetrations of the hub cladding by the supports of the small wheel are omitted.

Also, hub and cone surfaces are actually a series of "flats", of minimum radius equal to that use for shape dimensions in the simulation. Experience with detailed studies at other positions in the shield shows that these simplifications were safe, and our approach to the treatments of flats was in the conservative direction.

Endcap toroid and JT Shield: The endcap toroid models in GCALOR and FLUKA are complex, and as realistic as they can be made, and as similar as possible. The FLUKA description evolved during years of collaboration between Alfredo Ferrari and Peter Norton, and later between Ian Dawson and Steve Carr (July 2001). As noted in the description of the baseline geometry, the toroid is structured with eightfold symmetry in phi has large density variations due to the coils and their cryostats. It is also sufficiently massive to be an important element in the shielding of the muon system, and therefore cannot be modeled as a solid cylinder filled with mixed material. The coils and cryostats are modeled as rectangular solids with the corners beveled. Support plates for the coils, thermal shield plates, and front and back plates, all of aluminum, are included; as is the stainless steel bore tube. Tie rods to the bore tube, and other support structures, are not in the model. The bore tube contains the JTT copper alloy shielding core with 4 cm polyboron cladding and clearance gaps, as specified in the baseline geometry. The copper core will be fabricated in sections, but with sufficiently small (~2 mm) gaps to make them unobservable, so these gaps are not modeled. Chicanes of the correct dimensions are included at the front and back of the JTT copper core, where it interfaces with the JD and JF regions. The toroid shielding external to the bore tube, JTV, includes the polyboron rings at the front and back of the bore tube, and 8 cm of polylithium on the back plate of the endcap toroid.

JF Shield, the TAS Collimator and the JN Shield: Many options were simulated, and what emerged is seen in the picture of the current design, discussed in great detail in other sections of this report. Essentially, the outer boundary between 13m and 18 m is now cylindrical, and from 18 m to 21 m it is octagonal, with both of these surfaces being well within the previous envelope (muon acceptance boundary) of $\eta = 2.7$. The octagonal pieces were, however, simulated with a cylindrical shape with a diameter corresponding to the minimum distance between the flat surfaces. This representation is conservative since it underestimates the shielding and the rates.

The JN shield is modeled as a solid cylinder (of cast iron) since previous studies of the actual JN "disks and gaps" design showed no leakage through the gaps. The cast iron monobloc and the TAS steel carriage ("the cradle") have access holes for alignment. These have been modeled and studied in the past, and no important effects were seen because (a) these holes are narrow compared to their length and (b) the JF shield outside the monobloc blocks these holes and (c) the holes are in the region between the middle and outer MDT's, and not near either station.

Note also that the TAS shield (now in the monoblock), is 25 cm shorter in the current design than in 1998, to allow space for quadrupole services and maintenance.

ATLAS Cavern: The ATLAS experimental hall in GCALOR is modeled as a cylinder of radius 12 m, and half-length 24 m to each end, with concrete walls, and filled with air. The actual cavern is approximately rectangular in cross section, with the horizontal near wall at 13.3 m and the far wall at 16.7 m. Also, the ceiling and end walls are vaulted well beyond the surfaces used in the simulation. These simplifications allow the simulation to run faster, but some of the calculated rates will be higher since the GCALOR cavern size is undersized. In particular, backgrounds near the walls, with appreciable flow from the walls, such as thermal neutrons and capture gammas, will be higher in the simulation than in reality. There are results reported below on simulation runs performed with a more realistic cavern.

4.2.5 Changes of the beamline and shielding design since the 2003 baseline

Since the simulations presented in this report were made the design of the beamline and the shielding have continued to change. This is partly due to conclusions made as a result of these studies and partly due to "engineering realism" which have continued to impose changes on the conceptual design available in 2002. In this section we will go through some of these changes so that future simulation studies can take them into account.

As a result of the studies presented in this report it was decided to change the double-walled beampipe to a single-walled one with aerogel isolation. Table 4.1 gives the geometry of the simulated and present beampipe designs.

JAN 2003 SIMULATION DESIGN		
Z	**beampipe**	**isolation jacket**
0-354 cm	0.8 mm Be at R=29 mm	0.8 mm Be at R=33.8 mm
354-428.9 cm	0.8 mm SS at R=29 mm	nothing
428.9-849 cm	0.8 mm SS at R=29 mm	1 mm SS at R=39 mm
849-878.5 cm	0.8 mm SS at R=29 mm	nothing
878.5-1039.3 cm	0.8 mm SS at R=29 mm	1 mm SS at R=39 mm
1039.3-1050.7 cm	0.8 mm SS at R=29 mm	nothing
1050.7-1441.6 cm	1.0 mm SS at R=40 mm	nothing
1441.6-1888.3 cm	1.5 mm SS at R=60 mm	nothing
1888.3-2085 cm	2.0 mm Cu at R=17 mm	nothing

BEAMPIPE DESIGN IN JULY 2004		
Z	**beampipe**	**isolation jacket**
0-355 cm	0.8 mm Be at R=29 mm	4.4 mm aerogel + heater
355-365 cm	1.0 mm Al at R=29 mm	4.4 mm aerogel + heater
365-1050.7 cm	0.8 mm SS at R=29 mm	4.4 mm aerogel + heater
1050.7-1300.7 cm	1.0 mm SS at R=40 mm	4.4 mm aerogel + heater
1300.7-1441.6 cm	1.0 mm SS at R=40 mm	4.4 mm aerogel + heater
1441.6-1865 cm	1.5 mm SS at R=60 mm	4.4 mm aerogel + heater
1865-2094 cm	13 mm Cu at R=17 mm	nothing

Table 4.1 The beampipe in the simulation baseline "Jan2003" and the beampipe design in the summer of 2004.

The disk of the moderator shield was in the simulation expected to be 5 cm thick everywhere. In the final design, the part of the disk closest to the beamline (from a radius of 13.8 cm to 35 cm) is only 4 cm thick. While the disk was doped with lithium in the simulation it is doped with 5% boron in the real experiment (the expected effect of this change is presented in section 8.2.2). The thickness of the cylinder has also been reduced to 3.85 cm from 4.8 cm. The inner radius of the JM plug has been increased to 7.45 cm from the 6.6 cm used in the simulation. It is now also known that both the disk and the cylinder in front of the FCAL will be doped with B_4C giving a 5% (by weight) boron content in the polyethylene.

The inner 13 cm thick part of the JD disk goes to a radius of 275 cm in the simulation but only to 270 cm in real life. The radial thickness of the JD brass plug and hub has gone down with 1.0 cm and 1.2 cm respectively. The reason for this decrease is that the polyethylene layer on the hub is

now going to be 7 cm thick and not 5 cm thick as assumed in the simulation. The polyethylene will in the JD shield be doped with 5% B_2O_3. The density of the brass was assumed to be 8.83 g/cm^3 in the simulation and is now predicted to come out at only 8.35 g/cm^3.

The back part of the JD stainless steel tube sticks into the front part of the JTT brass shielding in order to create a chicane. Unfortunately the uncertainties in the positioning of the JD and the JTT have greatly increased the required clearance gap between the JD and the JTT and it is now 7 cm (2.6 cm in the simulation). The outer radius of the brass in the JTT has also decreased with the result that the total thickness of the brass in the JD-JTT overlap region has gone down with 9.3 cm since the Jan2003 simulations. The radial thickness of the brass has in the rest of the JTT decreased with between 3.9 and 5.5 cm. This is a significant change of the shielding in the most critical region and it is made worse by the fact that the density of the brass is, as in the JD, lower. While the JTT brass shielding is thinner than the simulation, the thickness of the JTT polyethylene layer has been increased to 5.5 cm from 4 cm.

The JTV rings inside the toroid are somewhat larger in the real world than in the simulation. The simulation assumed a radial coverage of 91.5-123.5 cm for each ring and a thickness of the front/back ring of 8/22 cm. The manufactured front ring will cover 93 to 142 cm in radius and be 16 cm thick while the back ring will cover 96.5-134.3 cm in radius and have a thickness of 8 cm.

The cylindrical JF core is assumed to be phi-symmetric in the simulation. This is not perfectly true in the final design where the top pieces have a different inner radius to the bottom piece ("the bridge"). Top pieces: The inner radius at the front is 1.2 cm larger and it is 6.7 cm smaller at the back compared to the simulation. Bottom piece: The inner radius is 3.1 cm larger at the front and the same as the simulation at the back.

The TAS collimator in the simulation is identical to the latest design but the radial gap between the TAS and the JN cradle is 0.6 cm larger in the real world and the 2.75 cm gap between the cradle and the monobloc is missing in the simulation. There is also a difference for the JN washers with the first 20 cm thick one having a radial thickness of only 65.5 cm (compared to 111.5 cm for the rest of the washers) and this reduced washer is not incorporated in the simulation.

4.2.6 The evolution of the FLUKA geometry since the Muon Technical Design Report

We show in Table 4.2 the updates in the geometry implemented in FLUKA. AV1 is the first geometry that I.Dawson simulated for ATLAS. It is equal to TP43h, the geometry used for the radiation studies presented in the Muon Spectrometer TDR [55], but without boron in the cavern walls.

	Evolution of ATLAS FLUKA geometry
av1	original atltp43h geometry and cavern description (February 1999)
av2	update geometry to include a new description of the vacuum chamber, collimator and moderator shielding JM
av3	update av2 to include latest engineering details for shieldings JD, JT, JF and JN. Change cavern concrete to an agreed "standard" CERN concrete.
av4	update to include a new description of Inner Detector and services layout. Also included for the first time in the gap between the barrel and end-cap cryostats are the LAr electronic boxes and ID patch-panel (PPB2/F2).
av5	include tungsten insert into JD shielding
av6	change JF shielding material assignment to: " steel + cast iron + polyLiF + lead " (new definitions for steel and castiron)
av7	put back poly-LiF/Pb outer layers in JD shielding and update inner JD + JT
av8	put in 20cm steel tube inside JF (July 2000)
av9	Copper $\rightarrow$ brass for JD, JT and LAr-shielding plugs (April 2001)
av10	update JD according to drawing ATLJD_26 and change: poly-LiF $\rightarrow$ poly-boron. Removed "extra" Cu between inner CSCs (May 2001)
av11	Had.-FCAL density 17.3 $\rightarrow$ 14.35 (May 2001)
av12	new beamline according to Veness drawings of Dec 2000 (June 2001)
av13	change JD tungsten insert to copper alloy (June 2001)
av14	remove epoxy shielding blocks from endcap toroids and implement JTT modifications etc (July 2001)
av15	change LAr EM Barrel and End-Caps according to D.Fournier's taskforce response. Make FCAL "almost" same as M.Shupe's (July 2001)
av16	improve and complete tile-cal description. Include shimming disk between EC and JD (September 2001)

Table 4.2 Evolution of Atlas geometry in FLUKA.

5 Predicted Radiation Background Levels

In this chapter we present the predicted radiation background levels in the different regions of ATLAS. In Section 5.1 we describe the radiation estimators used and their presentation. Section 5.2 reviews the predictions in the inner detector region, Section 5.3 in the calorimeters, Section 5.4 in the muon system.

5.1 Radiation estimators and their presentation

The "primary" estimators obtained directly from transport codes are fluence, energy deposition and inelastic collision (star) density. These quantites are determined by the tracking and physics models of the transport code and are rarely modified by the user. Estimators derived from these quantities, such as 1MeV neutron equivalent fluences, counting rates, single event upset rates, remnant dose, etc., can be considered "secondary" quantities which are obtained in the user "post processing" step by multiplying or convolving the primary quantities with conversion factors (often energy dependent).

The following is a brief summary of the radiation estimators used in this report to quantify the radiation backgrounds.

Particle fluence

The fluence can be defined as the number of particles crossing a hypothetical sphere of unit cross section area. Another useful and equivalent definition is the tracklength per unit volume. Fluence is the time integral of fluence rate, or flux (both terms are used interchangably thoughout this report). Fluence and fluence energy spectra can be obtained for most particle species, but in practice the dominant components of a typical radiation field are: neutrons, protons, pions, photons, muons and electrons. Particle fluxes are usually presented in this report in units of kHz/cm^2. (Note, the use of Hz should not be misunderstood to imply periodically occuring events, the background fluence rates will follow a Poisson distribution.)

Particle current

Whereas fluence "counts" the particles irrespective of their direction, current is a measure of the net number of particles crossing a surface with a well defined orientation. In a directed radiation field fluence and current are the same only for normal incidence to the surface. At all other angles the fluence is higher by a factor of $1/\cos\theta$ (see Appendix II). Charged particle current is the preferred estimator of the level one muon trigger group for obtaining "hit rates" from charged particles. Currents are usually presented in this report in units of Hz/cm^2.

Dose, Ionising dose

Absorbed dose is the mean energy imparted to matter per unit mass, taking into account all energy loss mechanisms (but corrected for rest mass effects) [51]. The dominant energy loss mechanism is usually ionisation, but non-ionising energy loss (NIEL) is important for understanding detector and electronic damage effects. Ionising dose is defined in this report to mean the dE/dx energy loss in matter from charged particles, but does not include ionisation energy loss from nuclear recoils. Ionising dose is responsible for surface or interface effects in

silicon devices, as well as inducing gas detector aging effects. Predictions are usually presented in units of Grays/Year.

1 MeV neutron equivalent fluence

The equivalent 1 MeV neutron fluence is obtained by convolving the various particle fluence energy spectra with Silicon displacement-damage functions, normalised to the value of the damage function for 1 MeV neutrons. Redefining the particle fluences in terms of the damage produced by 1 MeV neutrons allows comparison of damage effects for different radiation fields, so that damage studies can be performed at various irradiation facilities. The theory of displacement-damage is based on the Non Ionising Energy Loss (NIEL) scaling hypothesis, which is discussed in Section 6.1. Results are usually presented as the fluence obtained in one "high-luminosity" year (see below).

Single event effect fluence

Single event effects (SEE) include Single Event Upsets in electronic circuits (SEU), which are recoverable and Single Event Damage (SED), which may lead to the destruction of electronic components. In this document, the SEE rate is calculated by summing the rates of charged hadrons and neutrons with kinetic energies greater than 20MeV. This estimator is also used by the CMS experiment. These effects are discussed in more detail in Section 6.1. Results are usually presented as the fluence obtained in one "high-luminosity" year.

Muon single plane counting rate (kHz/cm^2)

Estimator for the rate at which Muon Drift Tubes and similar detectors in the muon system will count in response to the background particle rates. Defined and discussed in Section 6.2.

Muon penetrating particle rate (kHz/cm^2)

Estimator for the muon level-1 trigger rate from background particle rates. Defined and discussed in Section 6.2.

Star density (N/cm^3)

Density of hadronic inelastic interactions with energy above 50MeV. This quantity may be used as input to estimate activation and dose rates due to spallation.

The estimators listed above are usually averaged over time, so knowledge of the p-p interaction rates is required. Assumed is a p-p inelastic cross section of 80mb and a luminosity of $1x10^{34}cm^2s^{-1}$, corresponding to $8x10^8$ p-p collisions per second. For "annual predictions" 10^7 seconds per year is used.

Predictions are presented in various forms. Among the most commonly used forms are fluence or dose "maps", in colour or with contours, showing levels in slices through the simulation geometry, usually in the r-z or the x-y plane. Any estimator can be presented in such a map. An advantage of these maps is that in many cases the isoflux contours are an indication of the flow direction, and this can be helpful in shielding optimisation studies. Contour boundaries are a quick indicator if shielding is too thin, or if some regions are overshielded compare to others, or if a new shielding strategy is being effective.

Because colour maps are presented with a limited number of colours per log cycle, it is often the case that information cannot be read from them with sufficient accuracy. In these cases, it is more useful to present the exact predictions for specified regions, usually in the form of tables. The granularity of the maps in the GCALOR studies is 4cm x 4cm for the inner detector and

calorimeter regions, and 10cm x 10cm in the muon system. The corresponding granularity in the FLUKA studies is typically 2cm x 2cm and 15cm x 15cm respectively. However, in the FLUKA studies, fluences and currents were also obtained across region surfaces, especially for the tracking systems.

Furthermore, energy spectra may be required in specified regions or across region surfaces. These are especially useful when optimising shielding cladding design. Energy spectra are also needed, for example, for convolving with "damage functions" for producing the 1 MeV neutron equivalent fluences. In the GCALOR studies, tables were produced for specified regions in log divisions of energy, as 25 bin energy spectra. In the FLUKA studies, the number of energy bins ranged from 80 for charged particles, up to 250 for neutrons.

5.2 Prediction for the inner detector region

The inner detector regions of ATLAS have been the subject of several studies since the early 1990's [15,52]. All radiation issues are at play in the inner detector: occupancy, silicon damage, single event upsets, activation, etc.. In Section 5.2.1 we present the fluence and dose predictions of the FLUKA AV16 simulations, and in Section 5.2.2 show how the predictions have evolved since the TDR days. The FLUKA studies have investigated the radiation environment of the inner detector in more detail than the GCALOR simulations, and for some of the quantities such as energy deposition the FLUKA simulations are considered more reliable. In Section 5.2.3 the fluence predictions of GCALOR with the Jan03 layout are given. (A comparison of the FLUKA and GCALOR predictions for similar geometries is given in Section 7.2.3). In all simulations, PHOJET1.12 is used for generation of minimum bias events.

5.2.1 Fluences and doses

It is first interesting to inspect the charged hadron fluence map given in Figure 5.1. Charged hadrons are dominated by charged pions originating from the p-p interactions and constitute the most serious background for the innermost layers of the inner detector. It can also be seen from Figure 5.1 that the charged hadron fluence contours run parallel to the beamline, which is a consequence of the flatness of the charged particle rapidity plateau of minimum bias events.

Turning to the fluence map for all neutrons in Figure 5.2, we see that that these contours are quite different from those of the charged hadrons. Some neutrons are originating from the interaction point, as well as secondaries from the beampipe, but most neutrons come from albedo (backsplash from the surfaces of the calorimeters). The moderating material of the TRT and the JM moderator (on the face of the endcap calorimeter) ensure a copious production of thermal neutrons. A good fraction of the total neutron rates are thermal neutrons, as can be seen from inspection of Table 5.1 which shows neutron fluences for different energy ranges. Details of the different scoring regions are given in Figure 5.3.

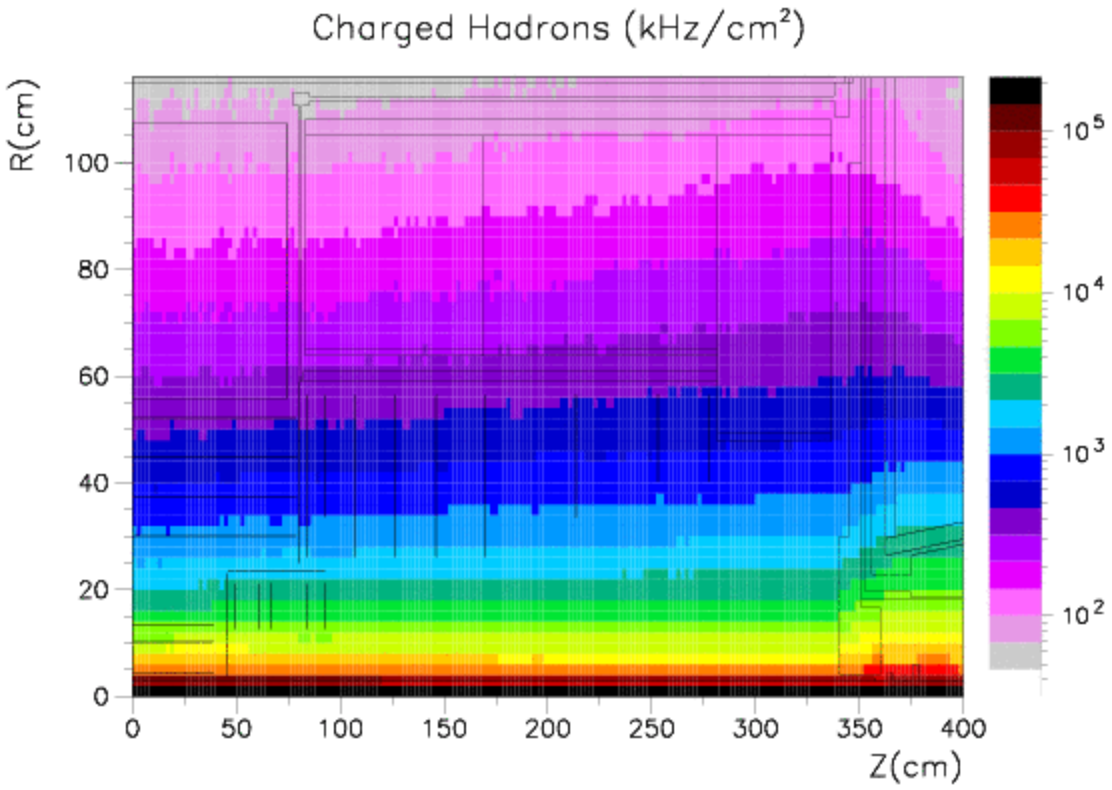

Figure 5.1 Charged hadron fluence rates in the inner detector.

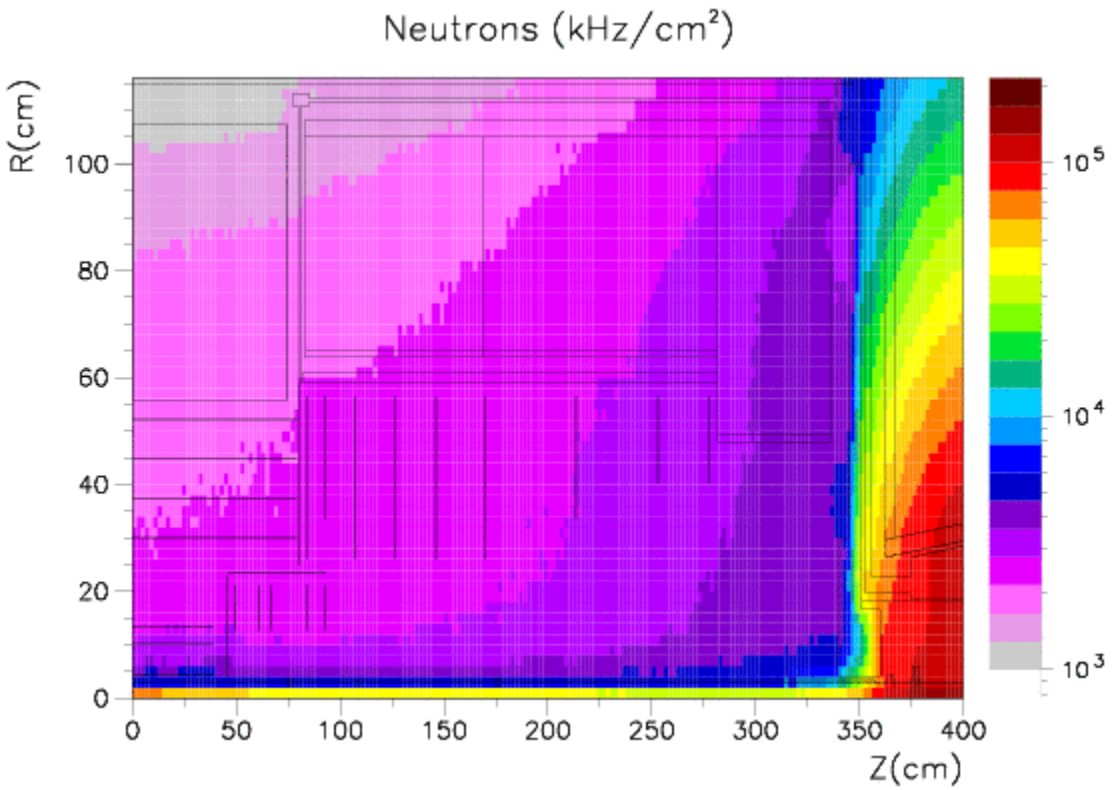

Figure 5.2 Total neutron fluence rates in the inner detector.

Region	Neutron fluence rates (kHz/cm^2)			
	n	>100keV	>10MeV	Thermal
PixB1	5741	4139	2839	1199
PixB3	2851	1242	589	1193
PixD5	2624	895	434	1224
SCTB1	2252	690	243	1160
SCTB4	2053	491	150	1173
SCTD9	3284	843	248	1541
TRTWI	4352	1312	438	1771
TRTWO	3843	994	181	1121
TRTBO	1201	383	82	384

Table 5.1 Neutron fluence rates in various inner detector regions.

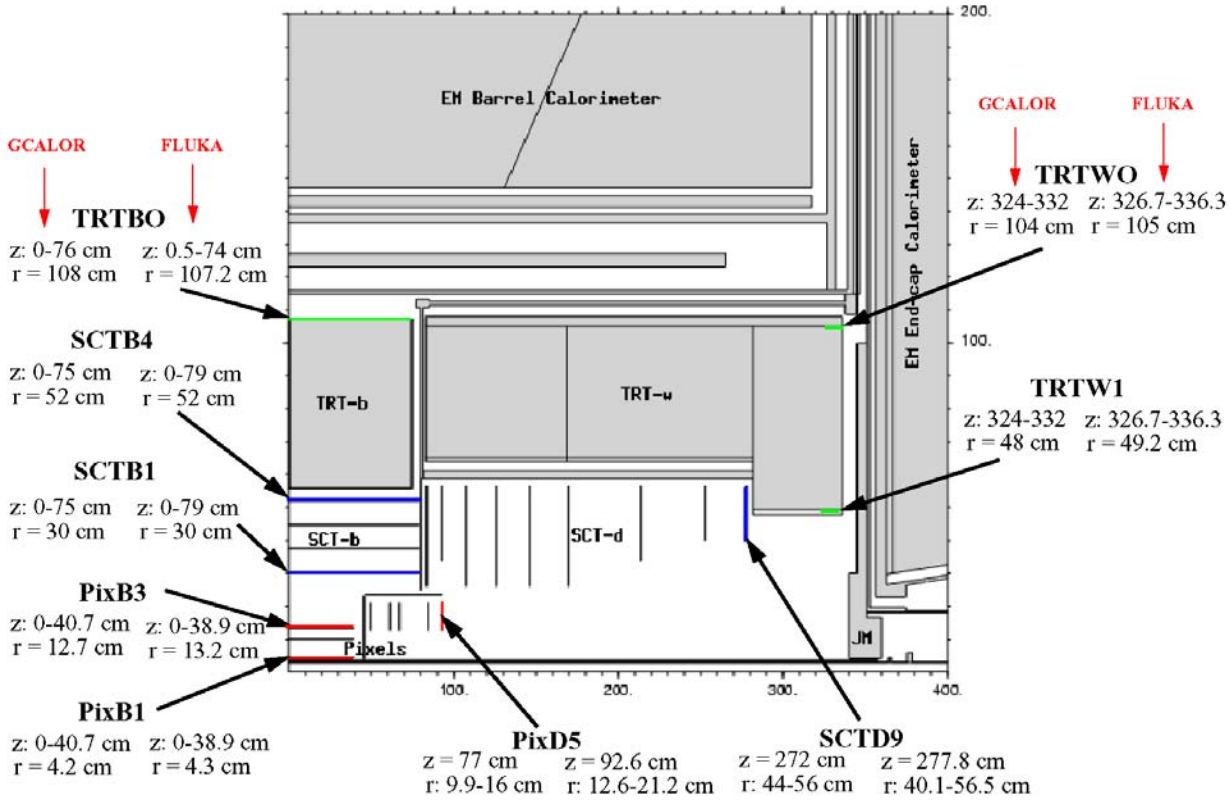

Figure 5.3 Slice in r-z of the AV16 geometry in and around the inner detector regions. Positions where fluences have been obtained are indicated, both for FLUKA and GCALOR.

It is clear that the inner detector contains an almost uniform "gas" of thermal neutrons, superimposed on a higher energy fluence leading to the fluence contours shown in Figure 5.2. The variation in fluence levels is much less for neutrons than for charged hadrons. The dominant source of neutrons is from the endcap calorimeters, especially the FCAL. The effect of the "polymoderator" on the face of the endcap calorimeters is to moderate the neutrons to lower energies where their contribution to the 1 MeV neutron equivalent fluence is smaller. The impact of the polymoderator is to reduce 1 MeV neutron equivalent fluences up to factors of two in the regions near the endcap calorimeters [52].

Combining neutrons and charged hadrons for energies greater than 20MeV, as shown in Figure 5.4, we obtain the Single Event Effect estimator (discussed in 6.1). The contours are similar to

those of the charged hadron plot, but differences appear in the calorimeter regions where the contribution from cascade neutrons starts to dominate.

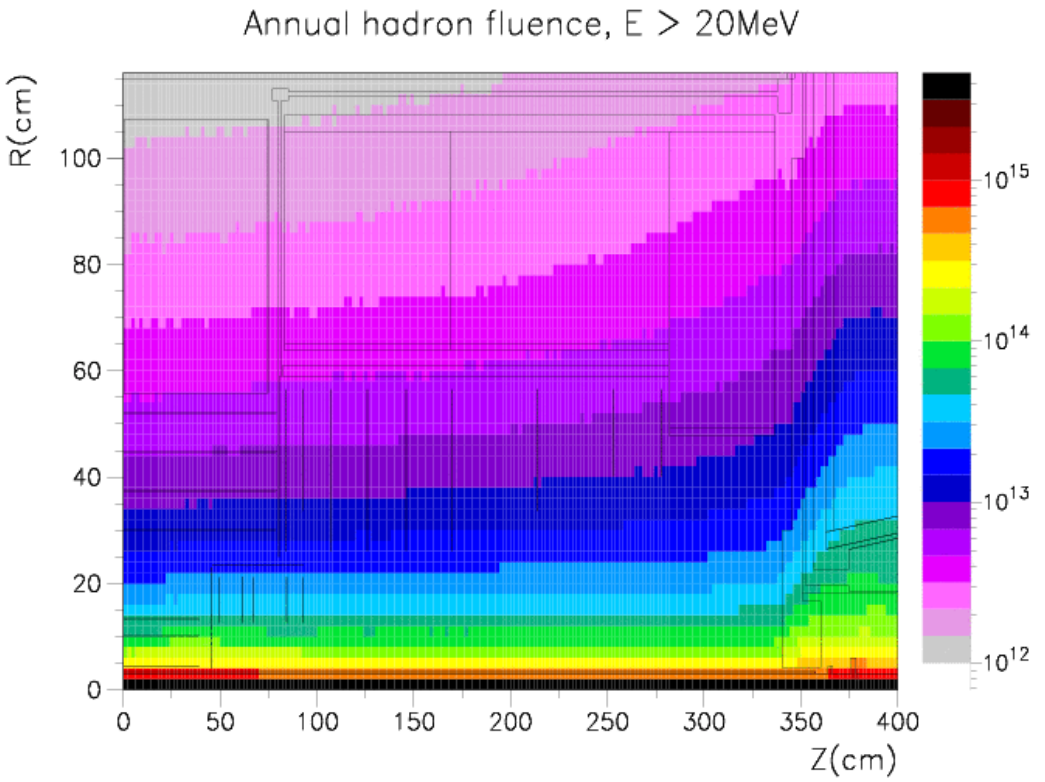

Figure 5.4 Hadron fluence rates E > 20 MeV.

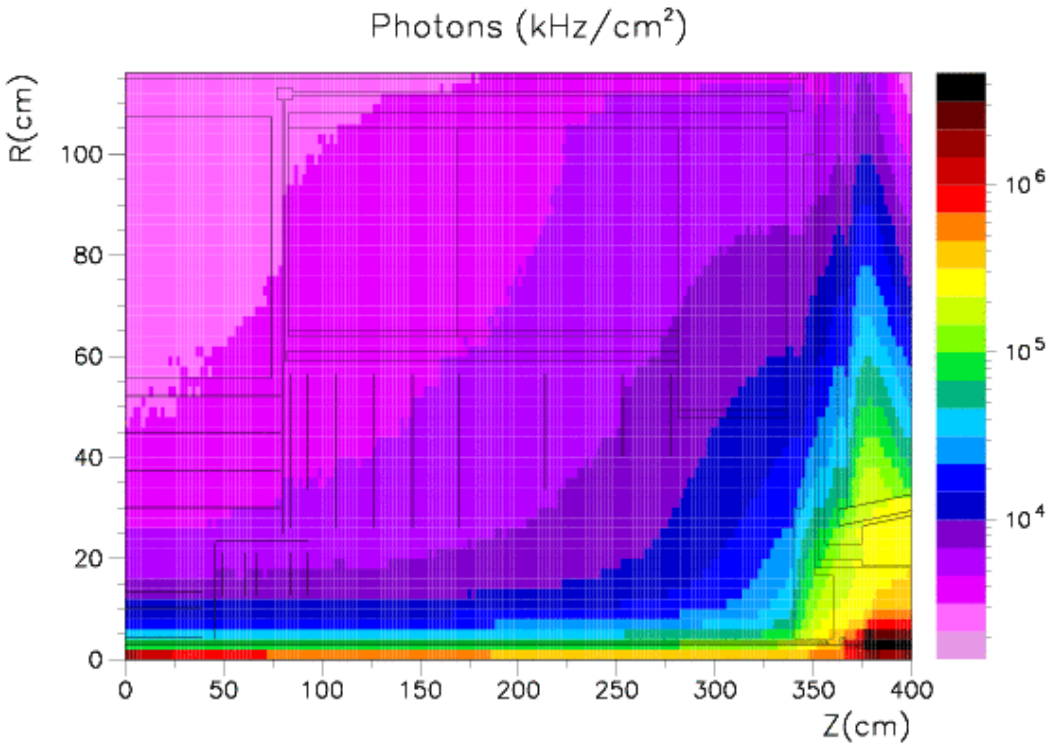

Figure 5.5 Photon fluence rates in the inner detector.

If we now look at photon fluences in the inner detector, Figure 5.5, we see that away from the beamline the fluence contours are similar to those of neutrons, indicating that most of the photons are being produced from neutron capture. Photons are also produced copiously from interactions in the beamline equipment (beampipe and flanges etc.) and it is important to minimise the material in this region. The latter also leads to the production of higher energy hadronic secondaries. Finally, another source of photons is from π^0 decay, which dominates the fluences at high energies.

Particle fluences and doses for each of the nine inner detector regions are given in Table 5.2. Fluences are obtained across the detector surfaces, whereas doses are obtained in the volumes associated with the detector regions. A colour map of dose is also given in Figure 5.6. Finally, given in Table 5.3 and Figure 5.7 are the 1 MeV neutron equivalent fluences, obtained by convolving particle spectra with the energy dependent Silicon damage functions. Close to the interaction point, for example in the pixel layers, charged pions dominate bulk damage in Silicon. However, further out in the SCT and TRT systems then it is the neutrons which are dominant.

Region	Particle fluence rates (kHz/cm^2)					Dose (Gy/Year)
	γ (>30keV)	p (>10MeV)	$\pi^{\pm}$ (>10MeV)	$\mu^{\pm}$ (>10MeV)	$e^{\pm}$ (>0.5MeV)	
PixB1	45764	2033	34071	303	8141	157882
PixB3	9147	284	4120	186	1731	25393
PixD5	8329	245	2884	211	1637	17382
SCTB1	4403	84	987	132	693	7586
SCTB4	3905	36	374	67	318	2959
SCTD9	7582	73	553	112	467	4505
TRTWI	12596	83	537	91	525	5625
TRTWO	5651	23	94	12	115	1249
TRTB0	2430	10	61	7	53	-

Table 5.2 Fluence rates and doses in the various inner detector regions, according to the FLUKA AV16 simulations. Statistical uncertainties are typically less than 10%.

Region	Annual 1 MeV neutron equivalent fluence ($\times 10^{12}$)			
	neutron	pion	proton	total
PixB1	47	198	21	267
PixB3	16	26	3.6	46
PixD5	10	16	2.8	29
SCTB1	8.4	6.4	1.1	16
SCTB4	5.8	2.6	0.52	8.9
SCTD9	9.3	3.5	0.91	14
TRTWI	15	3.3	1.0	20
TRTWO	9.6	0.58	0.28	10
TRTB0	4.1	0.45	0.16	4.7

Table 5.3 1-MeV neutron equivalent fluence rates.

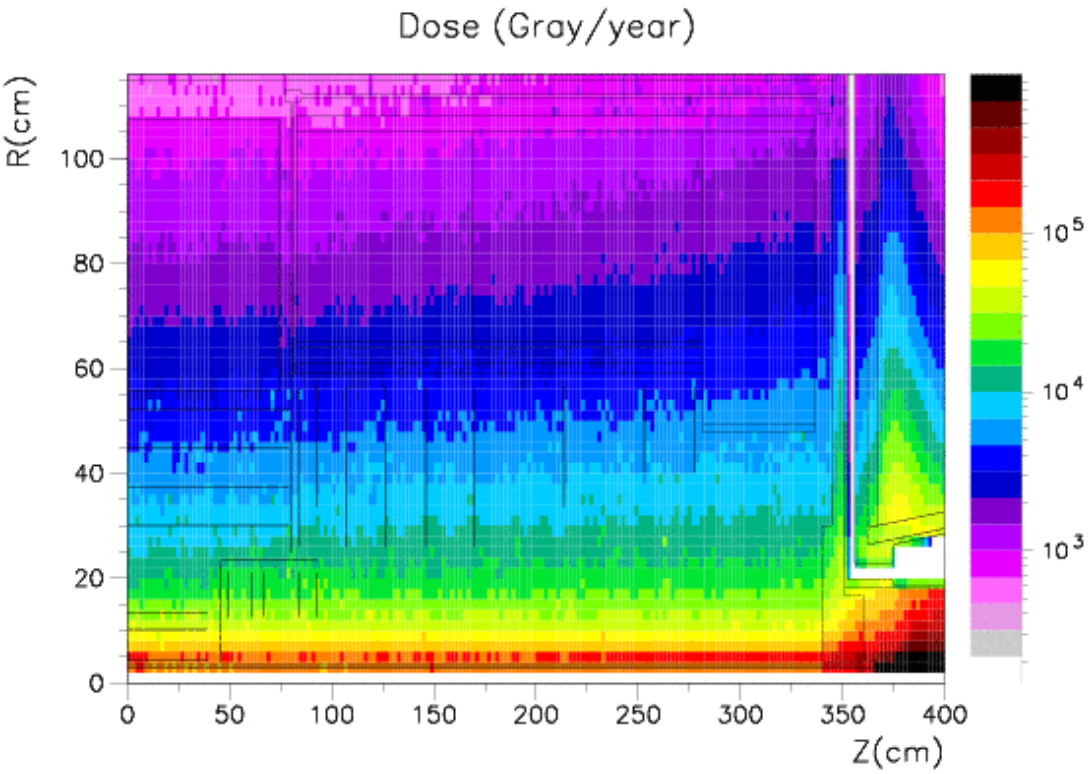

Figure 5.6 Annual doses (Gy/Year) assuming 10^7 s at high luminosity.

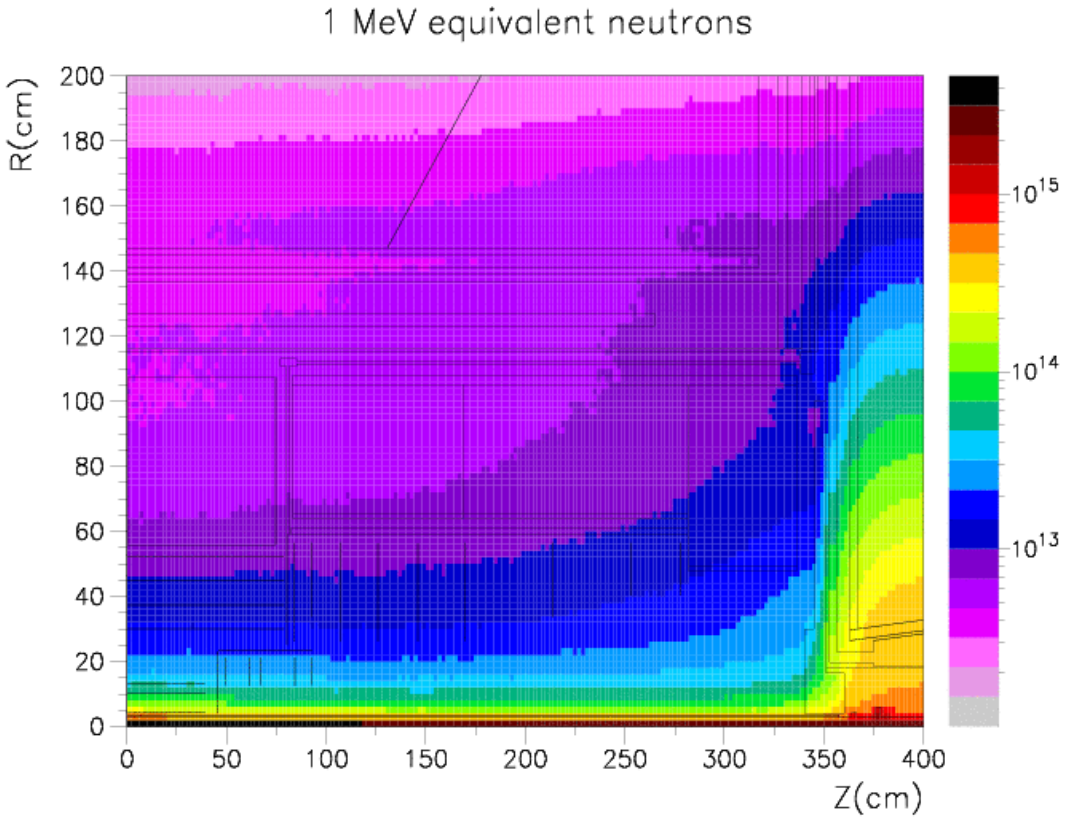

Figure 5.7 Annual 1 MeV neutron equivalent fluences assuming 10^7 s at high luminosity.

Finally, it should be noted that since the AV16 studies were performed, there have been several changes that might impact inner detector fluences and doses, giving justification for possible future studies. First, the design of the JM moderator has changed with respect to the AV16 version. However, the optimisation of the new design was done using GCALOR such that the situation is not worsened (see Section 8.2 for further details). Second, the beampipe design has been modified such that the "double-walled" design has been changed to a "single-wall with aerogel isolation", as described in Section 4.2.5. This is not expected to significantly impact backgrounds. And finally, it should be pointed out that in the simulations, not all the isotopes with high thermal neutron capture cross sections were included in the detector geometry and material description. This is usually because the details of the isotopic composition are not known, although in some cases it is because the relevant (n,γ) cross sections are not known. A good example of this is Xenon in the TRT, which contains several isotopes with large capture cross sections. We can assume that thermal neutron fluences will be reduced from capture, and that the photons will increase correspondingly. Unfortunately this important issue has not yet been studied.

5.2.2 Evolution of FLUKA predictions since the Inner Detector TDR

Table 5.4 shows the ratio of fluences obtained by comparing the FLUKA AV16 predictions with those obtained using the AV1 geometry (1999). These latter predictions correspond approximately to those obtained in the Inner Detector TDR (1997). Since then there have been changes in the modelling of the inner detector services, as well as an increase in the material associated with the beampipe and related equipment. Changes were also implemented in the calorimeters in accordance with the new "taskforce" description. A summary list of the main changes to the FLUKA Atlas geometry is given in Section 4.2.6. It is interesting to note that overall neutron and photon rates have gone down. The decrease is more significant close to the Endcap and is probably due to a reduction in the simulations of the density of the FCAL. Pion rates have not changed which are dominated by particles from the p-p interactions. The predictions of the PHOJET minimum bias generator are not very different from those of DTUJET jet used previously. Further discussion on the impact of the event generator is given in Section 7.3.

	Ratio AV16 / AV1			
	Total Neutrons	Thermal	Photons	Pions
Pixel B1	0.98	0.65	0.93	1.02
Pixel B3	0.76	-	0.87	1.03
Pixel D5	0.74	0.61	0.84	1.07
SCT B1	0.70	0.65	0.80	1.04
SCT B4	0.69	0.66	0.87	1.04
SCT D9	0.65	0.64	0.40	1.15
TRT-wi	0.66	0.63	0.41	1.19
TRT-wo	0.72	0.70	0.54	1.22
TRT-bo	0.70	0.75	0.72	1.01

Table 5.4 Ratio of fluences in the inner detector region as predicted by FLUKA for the AV16 and AV1 geometry layouts. The scoring regions are shown in Figure 5.3.

5.2.3 GCALOR predictions for the inner detector

Given in this section is a summary table of the fluence predictions of GCALOR using the Jan03 layout (additional results concerning electronics are given in Section 5.5). The full set of data is available from web pages referenced in Appendix V.

I.Det.	Particle fluence rates (kHz/cm^2)								TID (GY/Year)
	n	>100keV	>10MeV	γ	p	$\pi^{\pm}$	$\mu^{\pm}$	$e^{\pm}$	
PixB1	4250	2800	1740	30900	1350	19300	354	7190	113000
PixB3	2690	1260	578	9630	332	3910	265	1990	49800
PixD5	2730	1280	705	12900	535	5570	307	4450	28800
SCTB1	2100	680	216	4580	98	906	157	493	7830
SCTB4	2000	560	150	3750	47	376	72	334	3630
SCTD9	2510	894	242	7720	83	493	98	445	6440
TRTWI	2800	1222	-	10500	103	569	105	608	-
TRTWO	2200	817	-	4300	29	81	9	123	-
TRTBO	1550	466	-	2410	10	64	6	59	-

Table 5.5 Particle fluence rates and total ionization dose (TID) in the various inner detector regions, according to the GCALOR Jan03 simulations with PHOJET1.12.

Table 5.6 shows the ratios of fluences as obtained with FLUKA for the AV16 layout and GCALOR for the Jan03 layout. In general there is good agreement considering the differences between the two simulations.

I.Det.	Ratios of particle fluence rates FLUKA AV16 / GCALOR Jan03								Dose ratio
	n	>100keV	>10MeV	γ	p	$\pi^{\pm}$	$\mu^{\pm}$	$e^{\pm}$	
PixB1	1.35	1.45	2.21	1.48	1.51	1.76	0,86	1.13	1.40
PixB3	1.06	0.99	1.02	0.95	0.86	0.95	0.70	0.87	0.51
PixD5	0.96	1.39	0.62	0.65	0.46	0.52	0.69	0.37	0.60
SCTB1	1.07	1.01	1.13	0.96	0.86	1.09	0.84	1.41	0.97
SCTB4	1.03	0.88	1.00	1.04	0.77	0.99	0.93	0.95	0.82
SCTD9	1.31	0.94	1.02	0.98	0.88	1.12	1.14	1.05	0.70
TRTWI	1.55	1.07	-	1.20	0.81	0.92	0.87	1.16	-
TRTWO	1.75	1.22	-	1.31	0.79	1.16	1.33	1.07	-
TRTBO	0.77	0.82	-	1.01	1.00	0.95	1.17	0.90	-

Table 5.6 Ratios of particle fluence rates and dose, in the various inner detector regions, as predicted by FLUKA (AV16 layout) and GCALOR (Jan03 layout).

A coarser binning structure has been used in GCALOR for scoring fluences, which means "bin averaged" results are less reliable in regions where a strong “fluence-differential” exists, especially in the regions close to the beamline. In addition, the positions of the scoring regions are similar, but not identical as indicated in Figure 5.3. The consequences can be seen for example in the pion fluences dominated by pions originating from the p-p interactios: in the “PixD5” region, which covers the radial range 9.9-16cm in GCALOR and 12.6-21.1 cm in FLUKA, a ratio of 0.52 is observed while in “SCTB1”, where the radius is the same, a ratio of

1.09 is observed. Another difference between the two simulations is the more recent description of the JM polymoderator disk and plugs implemented in GCALOR Jan03, as described in Section 4.2.4. This influences for example the neutron rates in the most forward regions SCTD9, TRTWI and TRTWO. Finally, the ionising dose has been scored within the binning structure in GCALOR, unlike the FLUKA studies which investigated energy deposition inside the Silicon detector volumes. Differences that may originate from the transport codes themselves have been investigated with identical simplified geometry and scoring regions. They are reported in Section 7.2.2 and do not exceed 20%.

The evolution of the rates since TP43 as seen with GCALOR shows an increase of at most 10%. In FLUKA, the change has been more important having its origin in the FCAL density change (see Section 5.2.2).

5.3 Predictions for the Calorimeters, Service Gaps, and Channels

Both the neutron (Figure 5.8) and photon (Figure 5.9) maps show the hot spot in the first and second FCAL modules. The neutron map emphasizes the hadronic shower maximum at z = +- 5.1 m, almost between the modules and the photon map shows an electromagnetic shower development peaking earlier, around 4.9 m.

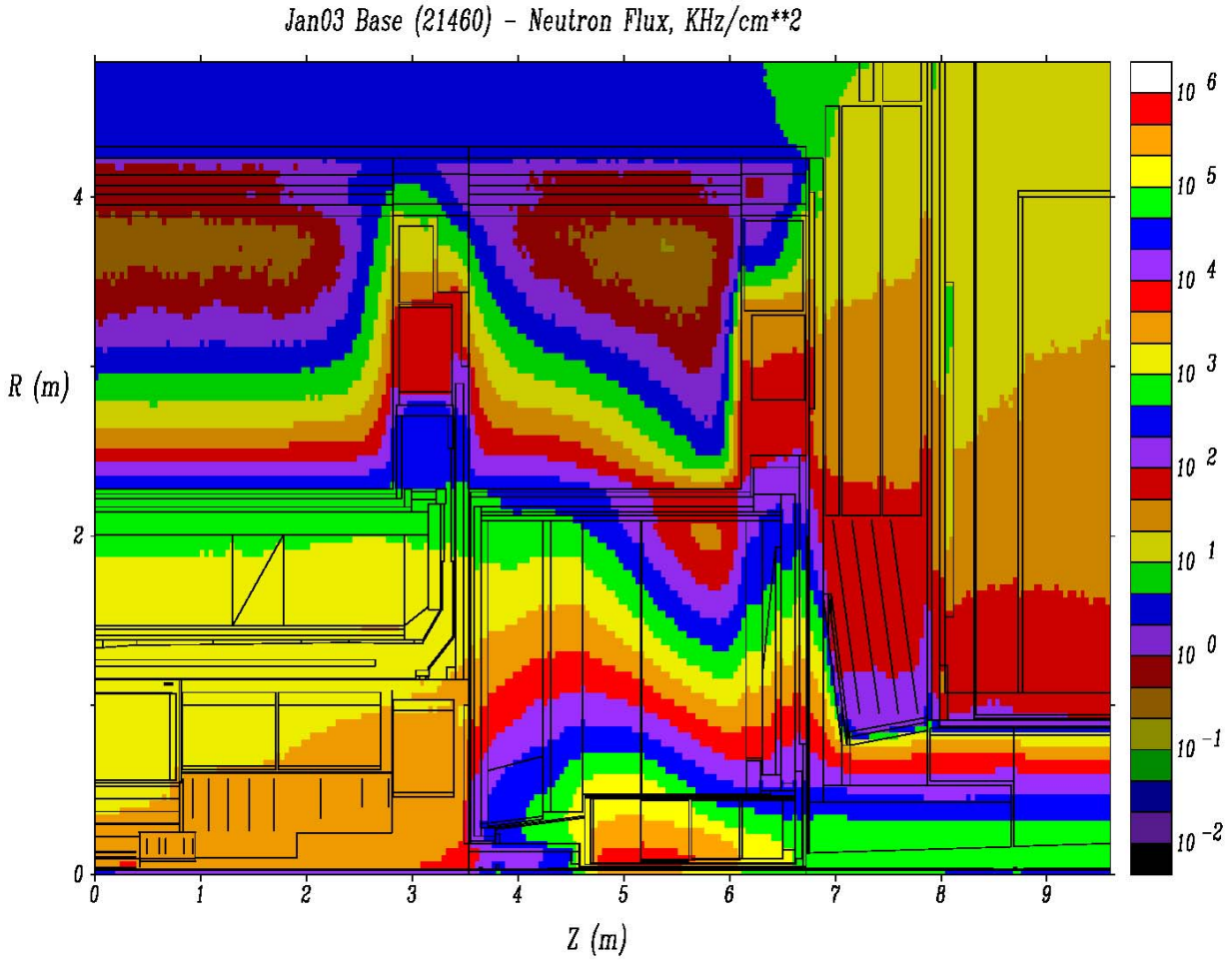

Figure 5.8 Total neutron flux in the calorimeter region (GCALOR – Jan03)

The photon map also shows photon production in the ion pump at z = +- 3.85 m, and in the beamline structures. In effect there is a "searchlight beam" of photons streaming from the rear bore of the FCAL but the shielding boundary inside the JN shows that it is relatively well contained.

The barrel/endcap services gap is nicely outlined by the photon map. One can see the "low density channel" between the cryostats in the region from z = 3.3 to 3.8 m, populated by aluminum cryostat walls, liquid argon, service and the beampipe. As one moves outward, beyond r = 2 m, where the EM barrel modules end, this channel widens into the gap between the TileCal modules, from z = 2.8 to 3.5 m, filled with cryostat feedthroughs, electronics crates and services. At larger r, the channel narrows again where the TileCal small modules are placed on the face of the extended TileCal. If we look at attenuation in the services gap, we see that the neutrons and photons are relatively well contained, with little "plume" into the inner muon system, while hadrons > 20 MeV are able to penetrate into the inner muon system (Figure 5.10). Note, however, that the hadron plume from this gap is still considerably smaller than the plume entering the barrel region behind the back of the forward calorimetry.

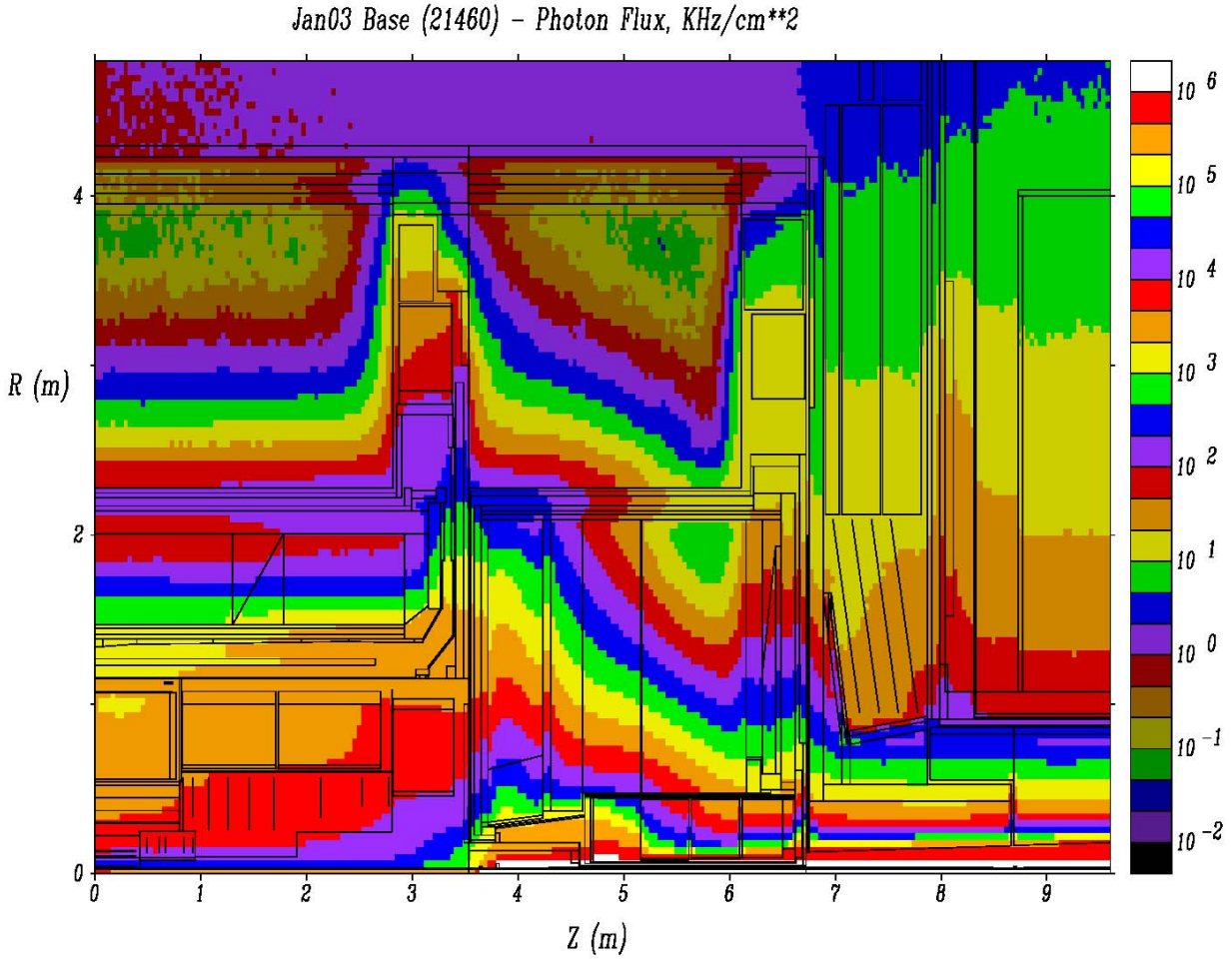

Figure 5.9 Photon flux in the calorimeter region (GCALOR- Jan03).

Another low density channel shows up most clearly in the total neutron plot (Figure 5.8). In the LArg endcap calorimeter, behind the HEC modules, the layers between z = 6.1 m and 6.8 m, where the JD flux return disk appears, are: liquid argon with cabling, copper plug 1, aluminum cold wall, vacuum, aluminum warm wall and air gap. There is also a smaller gap between the back of the FCAL plug (plug 3) and the JD copper core. As with the barrel/endcap gap region,

neutrons, photons and other fluxes can feed outward through this channel, again to encounter cryostat feedthroughs, crates and services, ultimately working their way to the muon system "in front" of the JD disk.

The behaviour of backgrounds at the JD thin corner where the CSC's are mounted is also evident from these plots. The neutron plots show that the 8 cm cladding zones on the faces of the JD cone and hub are doing their job. The neutron flux contours follow the cladding faces in a very reasonable fashion and this extends into the JTT region, where the 4 cm polyboron insert is also performing well. The photon fluxes are however more "interesting". Near the inner front of the CSC's they mirror the contours of the neutrons, showing that we are seeing mostly capture gammas at this point. But as one moves toward the forward toroid, additional photon flux is seen coming through the thin JTT, not associated with neutrons. These we interpret to be the products of hadronic shower development resulting mostly from beampipe secondaries hitting the inside of the JTT core: in simulation, this flux reduces sharply as beampipe material is removed. Finally, high energy hadron flux in the CSC region looks like punchthrough from paths through the dense shielding materials and could only be reduced by putting more dense material in this region. The global optimization points to the use of cladding on the JD because it gives large reductions in neutron and photon rates, whereas 8 cm of additional dense shield does little to reduce high energy hadron rates.

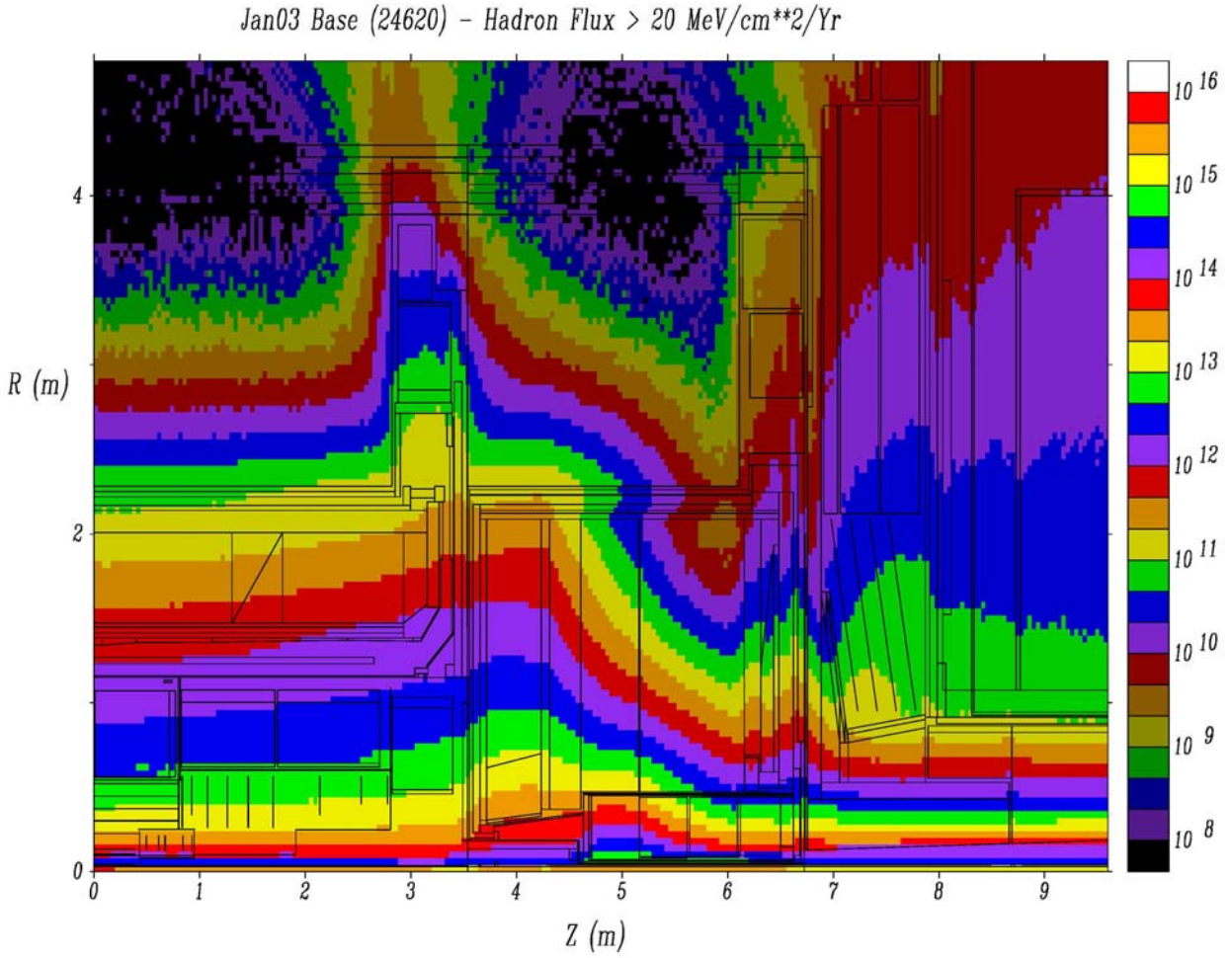

Figure 5.10 Hadron flux (>20 MeV) in the calorimeter region (GCALOR – Jan03).

5.3.1 Predicted fluences and doses at the location of calorimeter electronics

Table 5.7 shows Annual ionisation dose, 1 MeV equivalent and Single Event Effect fluences as predicted by GCALOR at the location of calorimeter electronics.

REGION	ZLO	ZHI	RLO	RHI	NIEL	TID	SEE
	cm	cm	cm	cm	1 MeV Neut Equiv /cm^2/yr	Gy/Yr	Fluence /cm^2/yr
LAR Barrel	300	350	290	340	0.185E+12	0.477E+01	0.378E+11
LAR Endcap	620	670	290	340	0.285E+11	0.639E+00	0.384E+10
TILE HV micro	210	210	400	400	0.475E+10	0.167E-01	0.139E+09
TILE HV opto	200	200	400	400	0.375E+10	0.987E-03	0.223E+09
TILE Mother	275	275	410	410	0.242E+11	0.216E+00	0.557E+10
TILE Integrator	210	210	410	410	0.433E+10	0.161E-01	0.244E+09
TILE Adder	260	260	410	410	0.175E+11	0.163E+00	0.295E+10
TILE Digitiser PC	275	275	410	410	0.242E+11	0.216E+00	0.557E+10
TILE Low Z Region	200	210	400	410	0.429E+10	0.551E-02	0.226E+09
TILE Med Z Region	270	280	400	410	0.254E+11	0.271E+00	0.615E+10
TILE S-link	150	150	410	410	0.213E+10	0.187E-01	0.605E+08
TILE LVPS	275	300	390	420	0.274E+11	0.378E+00	0.674E+10
TILE LVPS	610	635	390	420	0.370E+10	0.602E-01	0.779E+09
TILE Cal	300	300	410	410	0.205E+11	0.240E+00	0.545E+10
TILE Cal/Mezz	232	232	410	410	0.676E+10	0.298E-01	0.515E+09

Table 5.7 Annual ionisation dose, 1 MeV equivalent and Single Event Effect fluences at locations of electronics. The definition of the scoring regions is indicated in the table in terms of the R_{lo}, R_{hi}, Z_{lo}, Z_{hi}.

The readout electronics of the Liquid Argon calorimeters is located in the two service gaps, while Tilecal electronics is contained in "drawers" located inside the support girders of the modules.

5.4 Predictions in the the muon system

We now turn our attention to the muon system, and introduce maps zoomed out to show a full quadrant of ATLAS. In this region, we shall begin discussion with the map of hadron flux > 20 MeV, shown in Figure 5.11, to emphasise the properties of the dense "core" sections of the shield.

If we look at the prominent features in the map shown in Figure 5.11, we see the following.

(1) The JD corner and the JT core are the thinnest sections of dense shielding leading into the muon system. Although there is no sharp boundary between sources, we see that the JD corner is seeing punchthrough from the back of the endcap calorimeter, and radiation feeding outward from the region of the FCAL plug, up the low density channel at the back of the endcap. As we move further downstream into the JTT we see that the flux contours are becoming more parallel to the beamline. This signals the appearance of radiation coming from the beampipe "line source" of secondaries, hitting the inside of the JD and JTT, and

punching through the copper core of the JTT. In fact, this map at low statistics shows tracks pointing back to these sources, and there is a remnant of this pattern at the back outer edges. Note that the high energy hadron rate through much of the volume of the muon system is dominated by the large plume of radiation coming through the JT

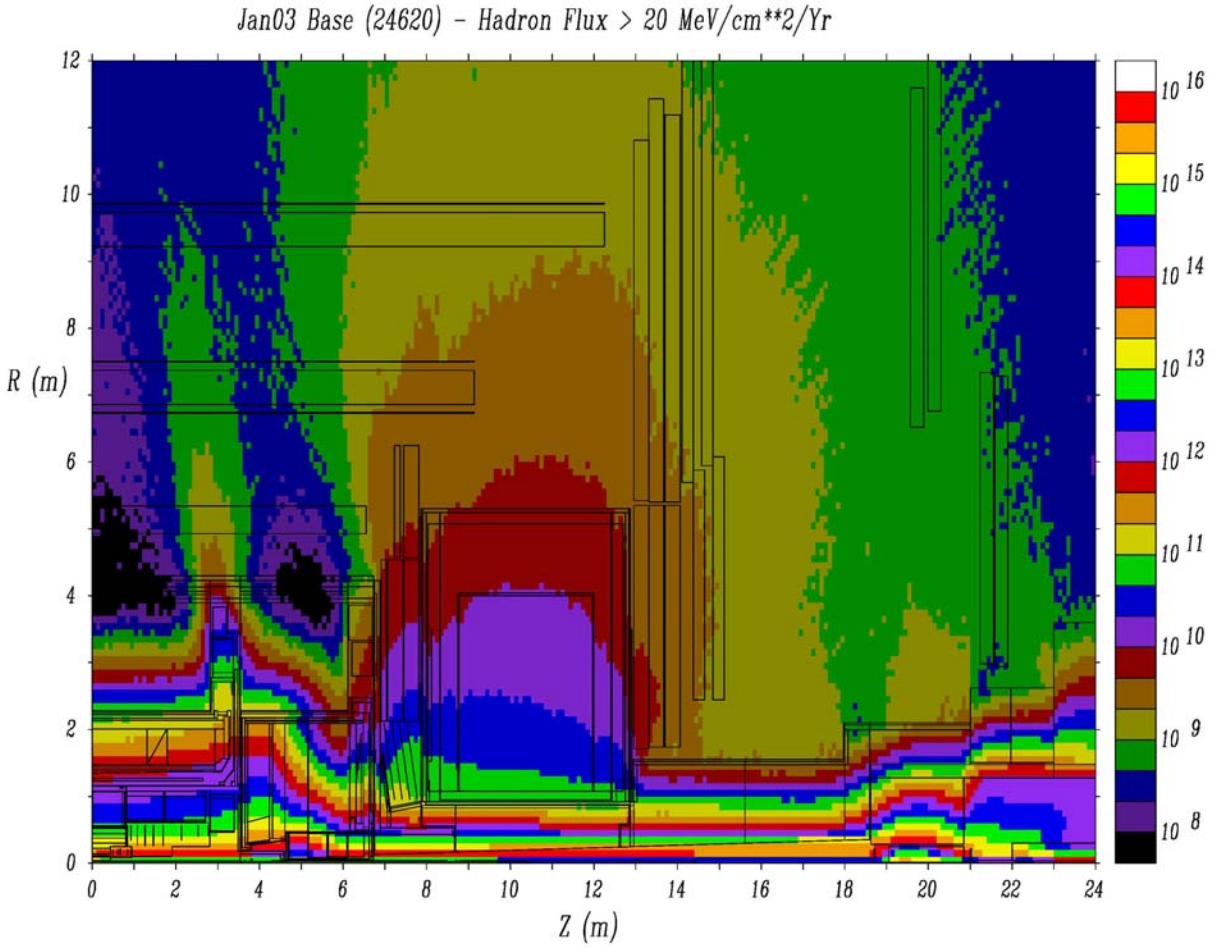

Figure 5.11 Hadron flux (>20 MeV) in the a full Atlas quadrant (GCALOR – Jan03).

(2) The JF massive shield is doing an excellent job shielding the TAS collimator hot spot. In the middle MDT region, the radiation coming through the JF shield is very low compared to that coming through the JT. (At the JF corner, one must be careful, because the contribution become comparable, and optimising the JF cladding inside the big wheel has helped lower the rates there.) In the zone immediately outside the TAS, at 20 m, there is a small plume punching through the shield. But this does not reach the outer MDT's because it is intercepted by the JN cast iron shielding disks. The conclusion is that the stepped design of the JF shield, while much reduced in tonnage, cost, and complexity compared to earlier conical designs, has enough dense shielding in the right places to make its high energy hadron background contributions negligible compared to other sources.

(3) It was noted earlier that hadrons > 20 MeV emerge from a plume outside the barrel/endcap services gap. This feature is seen more clearly in this map, but it is also even more apparent that its contribution to the hadron rates is small compared to that from the JT plume.

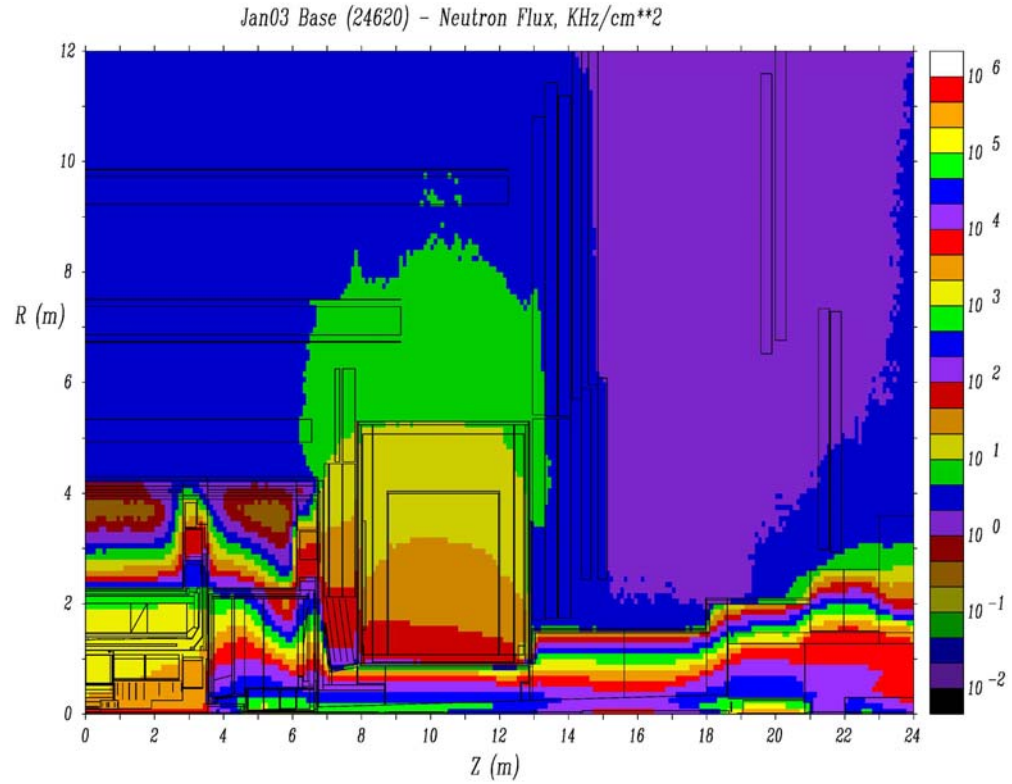

Figure 5.12 Total neutron flux in a full Atlas quadrant (GCALOR – Jan03).

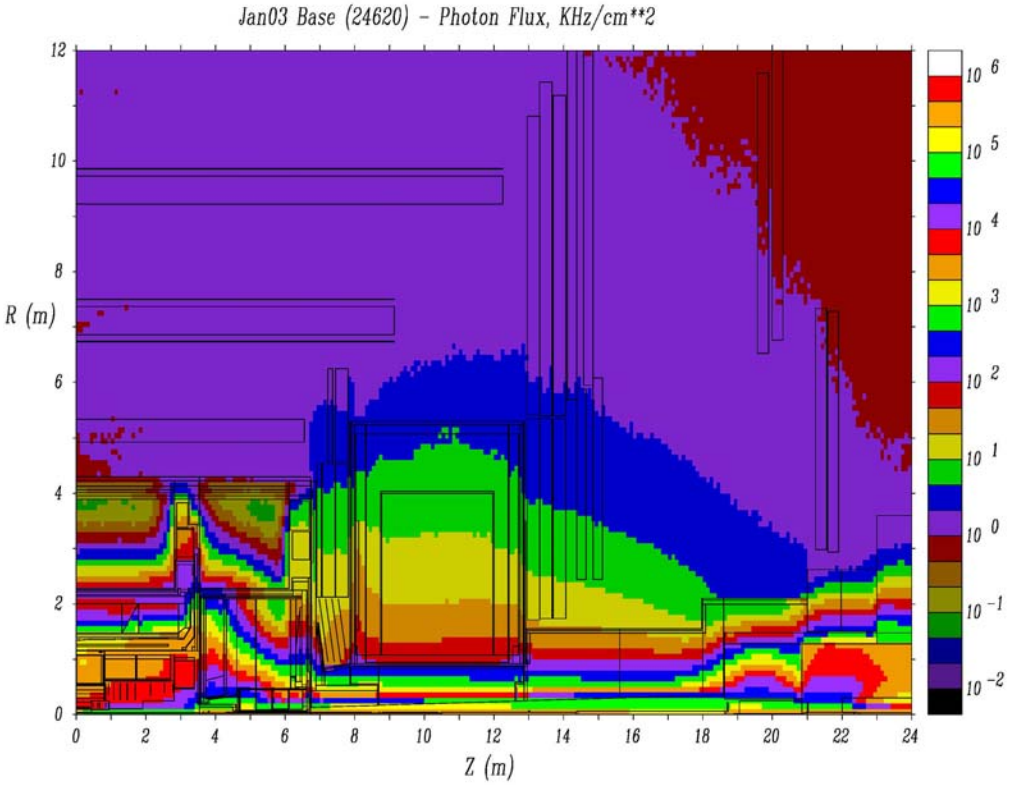

Figure 5.13 Photon flux in a full Atlas quadrant (GCALOR – Jan03).

We next look at the neutron (Figure 5.12) and photon (Figure 5.13) maps for the muon region. Since we have discussed these fluxes thoroughly up through the front of the JT, we focus here on the rest of the muon system. For neutrons, we notice that the cladding on the JF massive shield and the 8cm polyLiF JTV cladding on the back face of the JT toroid are doing an excellent job of protecting the middle MDT's in the big wheel.

In fact, the green plume emerging from the outside and outside-back of the toroid is coming through beyond where all cladding must stop due to expense, complexity, and mass. The outer forward MDT's are likewise protected, except at the innermost radius, where they experience the same green contour because the JN is not clad (it could be if necessary). These levels are really not a problem for the MDT's. For comparison, see the much higher rates in the inner forward MDT's, which are still considered acceptable as operating levels. Once again, the photon maps (Figure 5.13) are a bit more "interesting". Starting from the TAS region, we see the photon contours also following the shield, indicating that they are predominantly capture gammas associated with the above neutrons. But as one approaches the JT, the situation is analogous to that upstream of the JT: the photon contours "blow out" from the shielding and continue relatively parallel to the beamline, indicating that they are caused by shower punchthrough of secondary particles from the beampipe line source.

5.4.1 GCALOR Jan03 baseline background rates in the Muon System

The absolute background rates predictions obtained with GCALOR for the Jan03 baseline geometry averaged in scoring regions represented in Figure 5.14, are given in Table 5.8. The full set of GCALOR results can be found in the references listed in Appendix V.

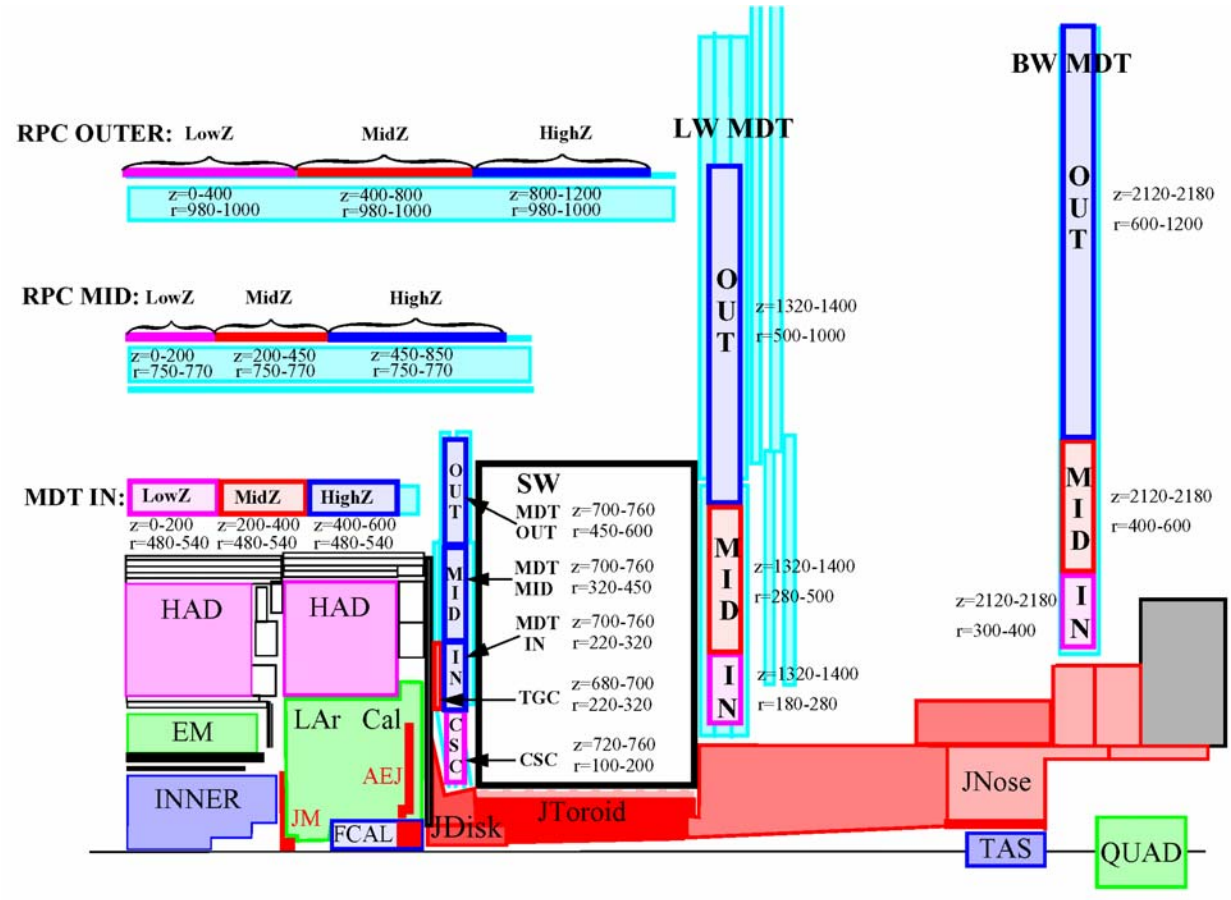

Figure 5.14 Scoring regions used by GCALOR to quote fluences in the Muon System in Table 5.8.

	Fluences (kHz/cm^2)				Fluences (Hz/cm^2)			
	Neutrons			Photons	Protons	$\pi^{\pm}$	$\mu^{\pm}$	$e^{\pm}$
	Total	>100keV	>10MeV		>10 MeV	>10 MeV	>10 MeV	>10 keV
Muon Barrel								
Inner Barrel:								
MDT IN low-z	2.70	0.38	0.018	0.98	1.10	0.36	1.51	10.5
MDT IN mid-z	3.06	0.57	0.106	1.14	2.34	0.41	2.44	12.6
MDT IN high-z	3.45	0.53	0.029	1.20	2.16	0.20	4.51	12.2
Middle Barrel:								
RPC MID low-z	2.59	0.33	0.032	1.03	0.90	-	0.37	8.4
RPC MID mid-z	2.83	0.39	0.053	1.10	1.57	0.03	0.47	10.5
RPC MID high-z	3.84	0.70	0.153	1.39	3.18	0.01	0.81	12.8
Outer Barrel:								
RPC OUTER low-z	2.71	0.33	0.041	1.05	0.37	0.01	0.25	7.7
RPC OUTER mid-z	3.36	0.51	0.101	1.28	1.03	0.01	0.40	9.9
RPC OUTER high-z	4.01	0.68	0.171	1.46	1.55	0.01	0.44	12.2
Muon Endcap								
Small Wheel Region:								
SW MDT OUT	7.7	1.91	0.43	2.4	8.3	0.37	3.4	25.
SW MDT MID	16.8	4.86	0.86	5.4	12.0	0.41	6.7	51.
SW MDT IN	34.1	10.3	1.85	11.2	23.1	2.01	20.0	95.8
SW TGC	36.6	8.73	1.06	9.9	18.0	0.82	20.7	93.
SW CSC	78.9	31.5	7.45	24.5	63.7	8.26	118.	200.
Large Wheel Region:								
LW MDT OUT	3.44	0.50	0.20	1.7	4.9	0.10	0.9	13.
LW MDT MID	4.04	0.81	0.35	4.4	10.0	0.03	3.0	18.
LW MDT IN	3.06	0.92	0.44	11.3	11.4	0.08	8.7	24.
Back Wheel Region:								
BW MDT OUT	1.73	0.40	0.049	0.84	0.92	-	0.48	5.0
BW MDT MID	2.01	0.46	0.060	1.15	1.41	0.03	1.23	7.8
BW MDT IN	2.67	0.64	0.067	1.46	0.93	-	2.98	8.9

Table 5.8 Fluences in the muon chambers locations at high luminosity (10^{34} cm^{-2}s^{-1}) as predicted by GCALOR for the Jan03 layout. Scoring regions are defined in Figure 5.14.

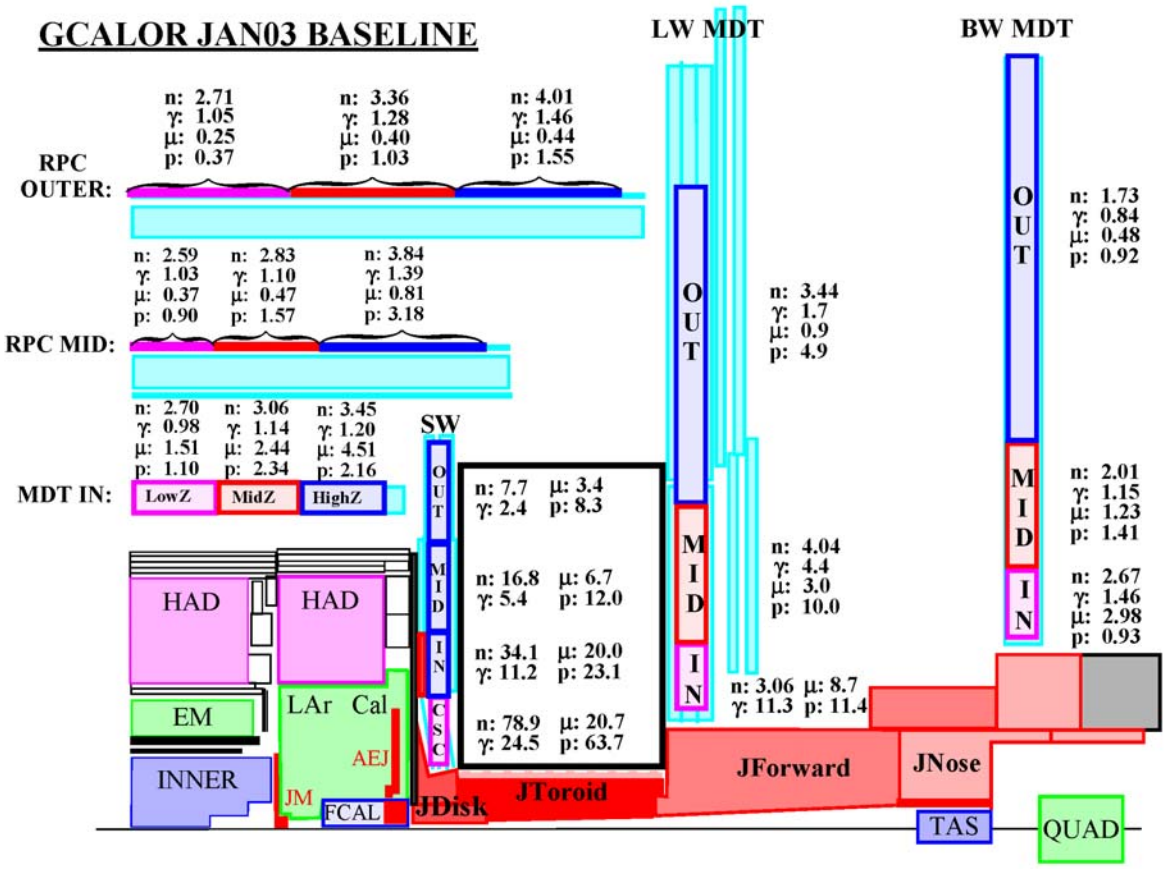

Figure 5.15 Fluences in the muon chambers locations at high luminosity (10^{34} cm^{-2}s^{-1}) as predicted by GCALOR for the Jan03 layout. Scoring regions are defined in Figure 5.14. The n and γ fluence is in units of KHz/cm^2 and the μ and proton fluence is in Hz/cm^2.

In the cavern, the electronics is located directly on the muon chambers or on the "footbridges" along the cavern walls. Ionisation dose, 1 MeV equivalent and Single Event Effect in the relevant regions are given in Table 5.9.

REGION	ZLO	ZHI	RLO	RHI	NIEL	TID	SEE
	cm	cm	cm	cm	1 MeV Neut Equiv /cm^2/yr	Gy/Yr	Fluence /cm^2/yr
MUON CSC Start 1	717.7	717.7	89.4	89.4	0.834E+12	0.173E+02	0.159E+12
MUON CSC End 1	694.1	694.1	204.7	204.7	0.147E+12	0.142E+01	0.169E+11
MUON CSC Start 2	735.3	735.3	89.4	89.4	0.642E+12	0.230E+02	0.127E+12
MUON CSC End 2	711.7	711.7	204.7	204.7	0.162E+12	0.229E+01	0.242E+11
MUON CSC Start 3	753.5	753.5	94.0	94.0	0.482E+12	0.183E+02	0.102E+12
MUON CSC End 3	730.8	730.8	204.7	204.7	0.169E+12	0.189E+01	0.293E+11
MUON CSC Start 4	771.1	771.1	94.0	94.0	0.448E+12	0.227E+02	0.870E+11
MUON CSC End 4	748.4	748.4	204.7	204.7	0.172E+12	0.238E+01	0.325E+11
MUON CSC Low R	712.0	756.0	90.0	94.0	0.623E+12	0.174E+02	0.127E+12
MUON CSC High R	694.0	748.0	200.0	204.0	0.167E+12	0.238E+01	0.264E+11
MUON TGC 1	1280.0	1290.0	715.0	1180.0	0.653E+10	0.165E+00	0.175E+10
MUON TGC 2	1470.0	1480.0	680.0	1180.0	0.344E+10	0.155E+00	0.117E+10
MUON RPC BMF	63.1	872.2	839.1	847.1	0.488E+10	0.814E-01	0.830E+09
MUON RPC BML	15.0	966.0	750.6	758.6	0.571E+10	0.115E+00	0.104E+10
MUON RPC BMS	13.5	945.5	839.1	847.1	0.501E+10	0.813E-01	0.875E+09
MUON RPC BOF	60.8	1267.9	1035.5	1043.5	0.469E+10	0.724E-01	0.907E+09
MUON RPC BOL	15.0	1225.2	985.3	993.3	0.483E+10	0.835E-01	0.929E+09
MUON RPC BOS	1.0	1383.2	1025.8	1033.8	0.463E+10	0.733E-01	0.922E+09

MDT Barrel 1	0.0	650.0	520.0	520.0	0.461E+10	0.949E-01	0.505E+09
MDT Barrel 2	0.0	900.0	720.0	720.0	0.580E+10	0.973E-01	0.957E+09
MDT Barrel 3	0.0	1250.0	950.0	950.0	0.529E+10	0.656E-01	0.996E+09
MDT Endcap 1	730.0	730.0	215.0	620.0	0.480E+11	0.611E+00	0.825E+10
MDT Endcap 2	1350.0	1350.0	190.0	1100.0	0.683E+10	0.741E+00	0.235E+10
MDT Endcap 3	2230.0	2230.0	260.0	1200.0	0.394E+10	0.994E-01	0.436E+09
FootBridge 1	0.0	500.0	1160.0	1200.0	0.292E+10	0.407E-01	0.360E+09
FootBridge 2	500.0	1000.0	1160.0	1200.0	0.491E+10	0.710E-01	0.910E+09
FootBridge 3	1000.0	1500.0	1160.0	1200.0	0.469E+10	0.955E-01	0.108E+10
FootBridge 4	1500.0	2000.0	1160.0	1200.0	0.280E+10	0.597E-01	0.674E+09

Table 5.9 Ionisation dose, 1 MeV equivalent and Single Event Effect at locations of electronics. The definition of the scoring regions is indicated in the table in terms of the R_{lo}, R_{hi}, Z_{lo}, Z_{hi}.

5.4.2 FLUKA AV16 background predictions in the Muon System.

The absolute background rates predictions obtained with FLUKA for the AV16 baseline geometry are given in Table 5.10 for the scoring regions represented in Figure 5.16. The full set of FLUKA results can be found in the references listed in Appendix VI. The AV16 geometry differs from the Jan03 baseline. Henceforth fluences cannot be directly compared. Systematic comparisons of the two transport programs are reported in Section 7.2.

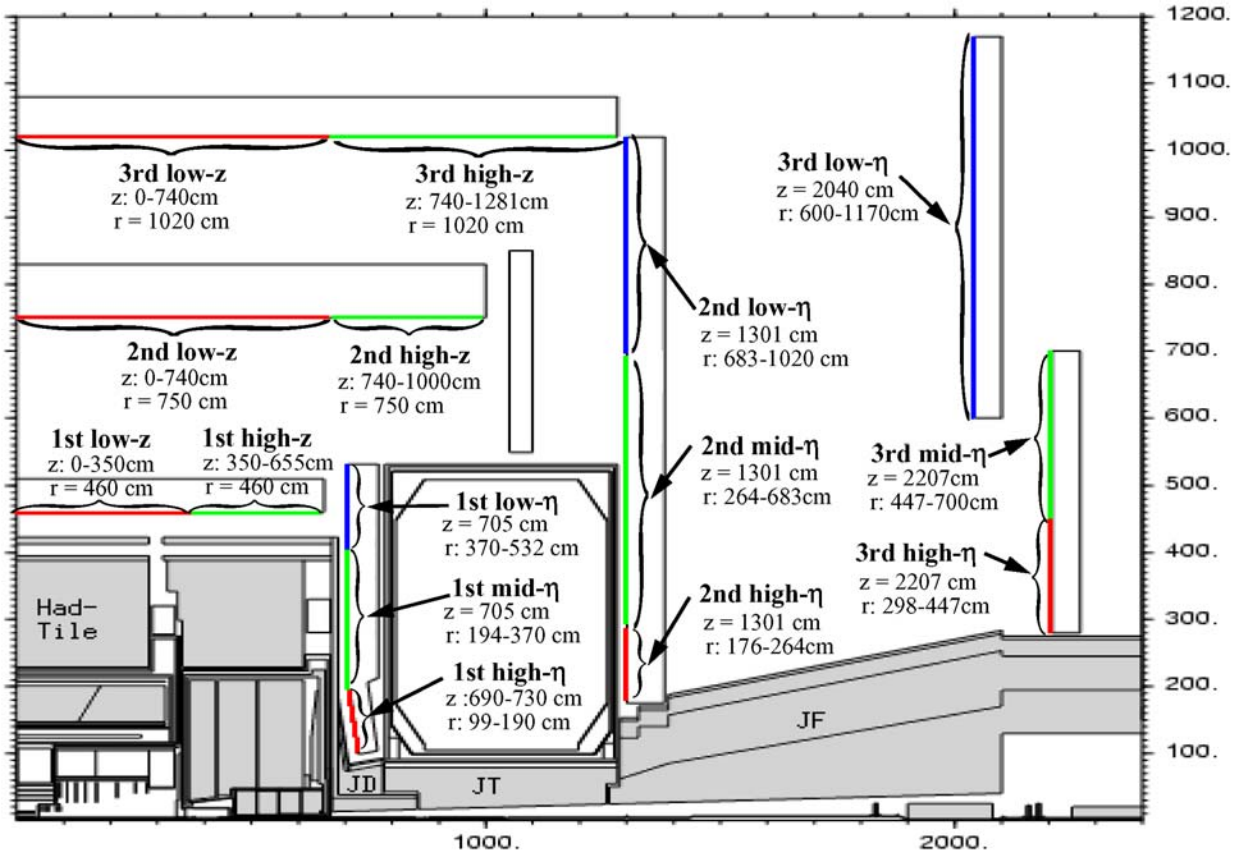

Figure 5.16 Scoring surfaces used by FLUKA to quote background rates in Table 5.10.

Position	Fluences (kHz/cm^2)				Currents (Hz/cm^2)			
	Neutrons			Photons	Ch.hads	Protons	μ^{+-}	e^{+-}
	Total	>100keV	>10MeV	>30keV	>10MeV	>10MeV	>10MeV	>0.5MeV
Barrel								
1st,low-z	5.08	1.47	0.10	1.81	2.79	1.89	1.89	9.30
1st,high-z	5.25	1.47	0.07	1.88	2.24	1.86	2.55	13.29
2nd,low-z	4.97	1.20	0.10	2.19	0.69	0.64	0.37	7.00
2nd,high-z	6.28	1.72	0.30	4.14	1.88	1.81	0.77	11.81
3rd,low-z	4.45	0.86	0.08	1.90	0.32	0.31	0.09	5.96
3rd,high-z	4.87	1.02	0.18	2.71	0.98	0.97	0.39	8.10
Forward								
1st,low-eta	14.23	4.80	0.66	4.93	4.89	4.38	3.60	33.57
1st,mid-eta	39.33	14.38	1.63	11.64	9.83	8.58	15.03	64.30
1st,high-eta	81.72	34.23	5.72	17.51	40.46	35.10	91.38	162.67
2nd,low-eta	5.55	1.51	0.25	3.18	1.98	1.93	0.25	11.91
2nd,mid-eta	8.36	2.61	0.49	4.43	6.45	6.20	1.20	23.58
2nd,high-eta	16.70	5.83	1.23	8.11	19.55	17.63	4.05	57.90
3rd,low-eta	3.16	0.48	0.06	1.40	1.53	1.47	0.27	7.41
3rd,mid-eta	3.09	0.47	0.05	1.31	1.25	1.21	0.32	6.41
3rd,high-eta	2.95	0.48	0.05	1.21	1.06	0.97	0.46	7.32

Table 5.10 Neutron and photon fluences and charged particles currents predicted by FLUKA for the AV16 geometry layout. Scoring surfaces used are shown in Figure 5.16.

The ratios of current to fluences as predicted by FLUKA for the AV16 layout are shown in Table 5.11. For isotropic fluences, the expected ratio is 0.5. Electron and positron fluences are isotropic while muons are not, as can be seen in Figure 5.17. Muons punching through the thin part of the JT shield are deviated by the endcap magnetic field.

	Current to fluence ratios		
position	**proton**	**$\mu^{\pm}$**	**$e^{\pm}$**
Barrel			
1st, low-z	0.79	0.82	0.54
1st, high-z	0.61	0.53	0.50
2nd, low-z	0.50	0.47	0.59
2nd, high-z	0.56	0.69	0.50
3rd, low-z	0.47	0.42	0.51
3rd, high-z	0.60	0.87	0.45
Forward			
1st, low-eta	0.41	0.72	0.52
1st, mid-eta	0.41	0.88	0.54
1st, high-eta	0.52	0.93	0.53
2nd, low-eta	0.51	0.34	0.52
2nd, mid-eta	0.54	0.51	0.41
2nd, high-eta	0.52	0.83	0.50
3rd, low-eta	0.79	0.71	0.60
3rd, mid-eta	0.86	0.98	0.63
3rd, high-eta	0.91	0.95	0.42

Table 5.11 Ratios of currents to fluences as predicted by FLUKA with AV16.

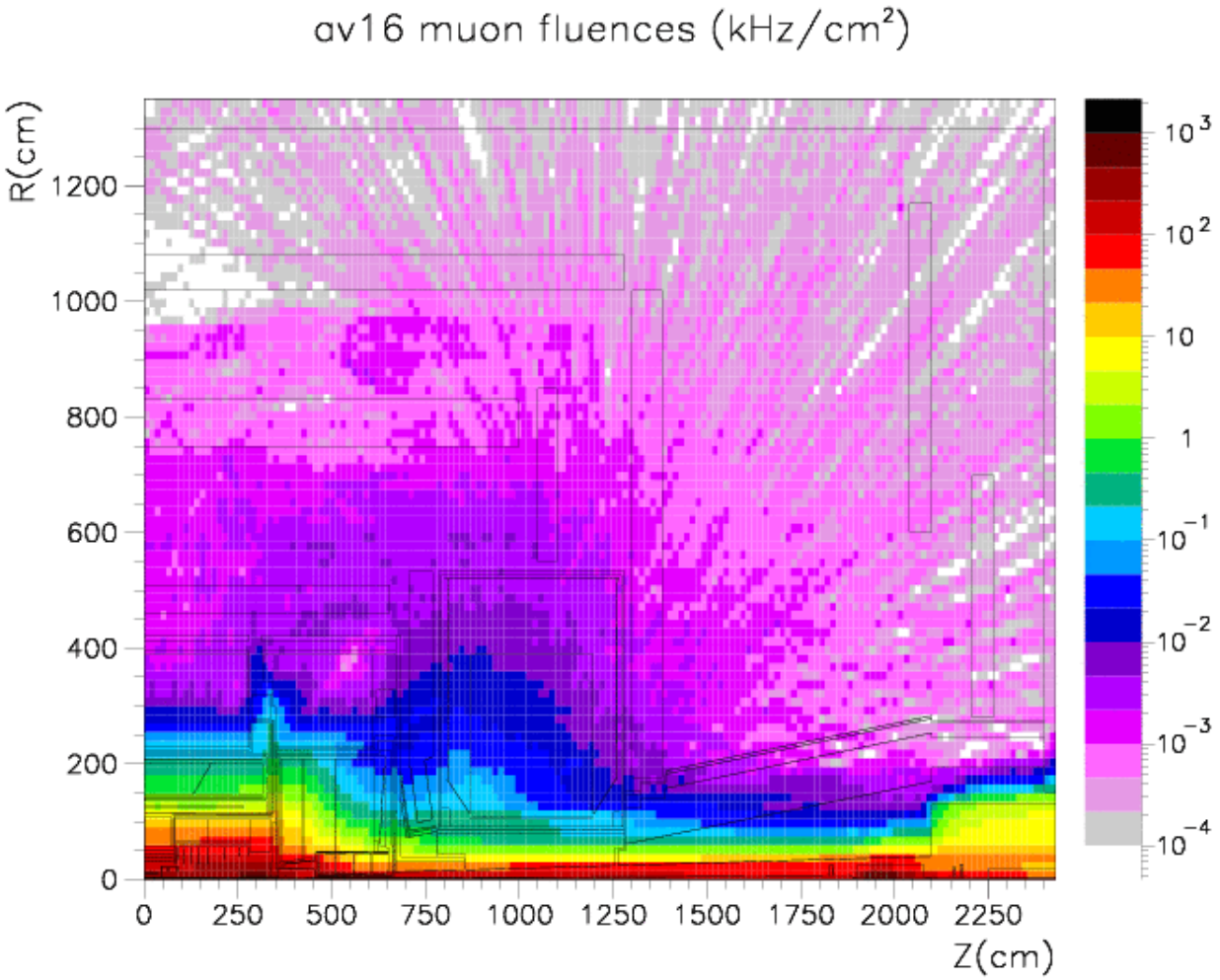

Figure 5.17 Muon fluences predicted by FLUKA for the AV16 geometry.

The main differences between the geometry of FLUKA AV16 and the Jan03 layout are the new forward shield design, the optimization of the JD/JTT regions and the inclusion of cladding on the back face of the JT toroid. The effect of these changes can be seen in
Table 5.12. The inclusion of cladding reduces neutron fluences in the large wheel. The change in the massive forward shield, although reducing substantially the mass, caused only 10 to 20 % increase in neutron and photon rates in the back wheel. There is a 10 to 20% improvement in the proton and muon rates in the forward region due to the optimization of the JD and JTT regions. This is also felt in the barrel region where a substantial fraction of the proton and muons fluences is coming from the JT region (see Figure 5.17 for muons and Figure 6.15 for protons).

	Ratio of Fluences Jan03/AV16				Ratio of Fluences Jan03/AV16		
	Neutrons			Photons	Protons	$\mu^{\pm}$	$e^{\pm}$
	Total	>100keV	>10MeV		>10 MeV	>10 MeV	>10 keV
Muon Barrel							
Inner Barrel:							
MDT IN low-z	0.99	0.95	1.00	0.98	0.66	0.90	0.83
MDT IN mid-z	0.99	0.92	0.93	0.98	0.69	0.90	0.72
MDT IN high-z	0.98	0.90	0.85	0.96	0.56	0.97	0.95
Middle Barrel:							
RPC MID low-z	0.98	0.92	0.94	1.02	1.45	0.61	0.95
RPC MID mid-z	0.99	0.93	0.95	0.98	1.17	0.57	1.17
RPC MID high-z	1.01	0.95	0.93	0.97	0.71	0.83	2.03
Outer Barrel:							
RPC OUTER low-z	0.98	0.89	0.91	0.99	0.59	0.37	1.07
RPC OUTER mid-z	1.00	0.93	0.94	0.98	0.93	1.60	1.02
RPC OUTER high-z	1.01	0.96	0.91	0.98	0.85	0.85	1.02
Muon Endcap							
Small Wheel Region:							
SW MDT OUT	0.98	0.93	0.41	0.96	0.91	0.75	1.28
SW MDT MID	0.94	0.90	0.95	1.00	0.78	0.71	1.07
SW MDT IN	0.94	0.90	0.94	1.05	0.74	0.93	1.00
SW TGC	0.91	0.89	0.99	1.00	1.19	1.02	0.95
SW CSC	1.14	1.01	0.90	1.05	0.77	0.89	0.93
Large Wheel Region:							
LW MDT OUT	0.93	0.89	0.87	0.99	0.82	0.60	1.00
LW MDT MID	0.65	0.70	0.81	0.97	0.82	1.05	1.00
LW MDT IN	0.39	0.53	0.96	1.00	0.97	1.13	0.87
Back Wheel Region:							
BW MDT OUT	1.04	1.05	1.23	1.15	0.96	1.12	1.00
BW MDT MID	1.06	1.18	2.00	1.17	1.74	1.48	1.56
BW MDT IN	1.08	1.14	2.23	1.16	0.89	1.59	1.00

Table 5.12 Ratio of fluences obtained with the Jan03 layout and a geometry similar to the FLUKA AV16. Fluences are given for the regions defined in Figure 5.14. Values for pions are not quoted due to lack of statistical precision.

5.4.3 Evolution of predicted rates since the Muon Technical Design Report

Both in GCALOR and in FLUKA, there have been relevant geometry updates with impact on the rates: introduction of the exact dimension and material of the calorimeters, update of the beam pipe and vacuum equipement, etc. However the most critical change has taken place in the JD/JT region.

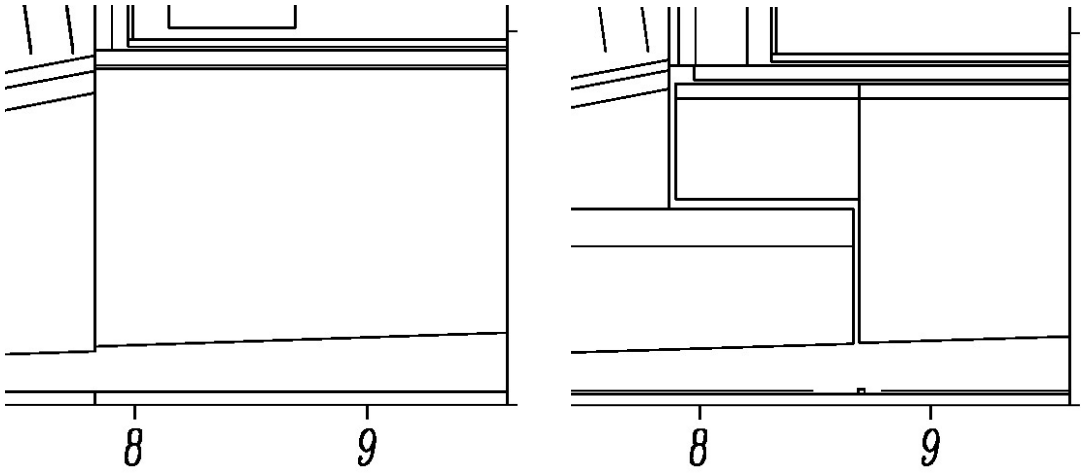

Figure 5.18 Zoomed view to the JT region, between 8 and 9 m along Z and 1 m radially, at the transition between JD and JT shielding elements: (left) TP43 layout and (right) Jan03 layout.

To illustrate this point, Figure 5.18 shows a zoomed view of the region between 8 and 9 m where the changes between the GCALOR TP43 layout and the Jan03 layout can be seen. The outer radius of the supporting tube was at 95 cm while in Jan03 is at 91.5 cm, a reduction of 3.5 cm. It used to be a single block and now there is a clearance of 3 cm. The copper part of the shield was 74 cm thick at 8.5 m and is now reduced to 67.5 cm. The Cu used to be "Pure Cu" with density 8.89 gr/cm^3 and an interaction length of 15.17 cm, while now it is brass with density 8.5 gr/cm3 and a corresponding interaction length of 16.25 cm. So, we passed from 4.9 λ_{int} to 4.15 λ_{int} which results in a factor 2.1 increase in rate. In addition, as can be seen in Figure 5.18, there is more material in the beam pipe, the second wall and a valve that has moved further away from the interaction point. This results in an increased source of radiation under this weak point of the shielding (see for example Figure 8.18). Finally, there used to be more "cladding" material inside the toroid, which had to be removed for engineering considerations. But, as studies detailed in Section 8.4 have shown, a cladding layer is indispensable, and it had to be accommodated inside the supporting tube, at the cost of removing more Cu. All these factors have contributed to the increase of the "plume" in the toroid region, especially for hard neutrons and protons as shown for example in Figure 5.12.

The ratios of fluences as obtained by GCALOR for the Jan03 layout and the TP43 layout are given in Table 5.13 for the regions described in Figure 5.14. Total neutron, photon and associated electron fluences have increased by a factor 2 to 3 in the forward region and in the high-z barrel region due to the development of the "plume" described before. The increase is relatively more important for high energy neutrons. It is also seen in the protons and to a lesser extend in the muons. The evolution shown here is due to the change in geometry. Rates have also changes due to the evolution of the transport programs, mainly the neutral kaon transport that resulted in a significant decrease in pion and muon fluences especially in the barrel region (see Section 3.2 for further discussion).

	Ratio of Fluences Jan03/TP43				Ratio of Fluences Jan03/TP43		
	Neutrons			Photons	Protons	$\mu^{\pm}$	$e^{\pm}$
	Total	>100keV	>10MeV		>10 MeV	>10 MeV	>10 keV
Muon Barrel							
Inner Barrel:							
MDT IN low-z	1.51	1.06	0.95	1.61	0.53	0.39	1.23
MDT IN mid-z	1.01	0.58	0.58	0.83	0.47	0.60	0.46
MDT IN high-z	1.70	1.36	1.32	1.74	2.01	1.04	2.17
Middle Barrel:							
RPC MID low-z	1.51	1.03	0.84	1.56	0.62	1.68	0.94
RPC MID mid-z	1.40	0.93	0.62	1.26	0.78	0.44	1.74
RPC MID high-z	1.96	2.12	2.64	2.01	2.03	0.79	2.30
Outer Barrel:							
RPC OUTER low-z	1.53	1.10	0.77	1.46	0.49	1.25	1.10
RPC OUTER mid-z	1.86	1.82	2.19	1.94	2.51	0.87	1.74
RPC OUTER high-z	2.10	2.72	3.14	2.35	2.54	1.33	2.30
Muon Endcap							
Small Wheel Region:							
SW MDT OUT	2.33	2.61	2.89	2.45	2.86	1.18	1.67
SW MDT MID	2.59	2.64	2.77	3.16	2.89	1.18	2.82
SW MDT IN	2.82	2.42	2.53	3.02	2.26	1.23	2.68
SW TGC	3.27	2.59	2.30	3.38	3.47	1.35	3.06
SW CSC	2.19	1.93	2.30	1.87	1.53	1.24	2.57
Large Wheel Region:							
LW MDT OUT	1.98	2.63	3.33	2.10	2.62	0.86	2.22
LW MDT MID	1.32	2.03	2.50	1.36	3.04	1.44	2.02
LW MDT IN	0.66	1.35	2.44	1.01	4.77	1.65	1.89
Back Wheel Region:							
BW MDT OUT	1.71	1.60	4.08	2.63	3.28	1.04	2.27
BW MDT MID	1.99	2.00	4.60	3.56	7.05	2.86	3.08
BW MDT IN	2.36	2.46	5.17	2.70	2.11	2.46	2.45

Table 5.13 Ratio of fluences obtained with the GCALOR Jan03 layout and the GCALOR TP43 geometry very similar to the FLUKA AV1 geometry and the one used at the time of the Muon Spectrometer TDR. Fluences are given for the regions defined in Figure 5.14. Values for pions are not quoted due to lack of statistical precision.

The ratios of fluences obtained with FLUKA for the AV16 and AV1 geometries are given in Table 5.14. They are similar to the ones obtained with GCALOR. Neutrons and photons have increased by a factor of the order of 1.5 in the central barrel and of the order of 3.0 in the region affected by the "plume" of the JT shield. A similar trend is seen in proton rates. While with GCALOR the ratios where shown only for the changes in geometry, with FLUKA the ratios reflect both the changes in geometry and the changes in the transport program. Muon rates are reduced by a factor 2 to 10, due to the improved neutral-kaon transport (see Section 3.2 for

further discussion). For the same reason, pion rates became negligible with respect to protons except for the inner barrel muon layer.

Position	FLUKA: ratios AV16 to AV1			
	Neutrons	**Photons**	**Protons**	**Muons**
Barrel				
1st, low-z	2.0	0.8	1.0	1.5
1st, high-z	2.5	1.4	2.1	1.0
2nd, low-z	1.8	1.5	1.6	0.4
2nd, high-z	1.8	3.5	1.9	0.5
3rd, low-z	1.4	1.5	1.6	0.9
3rd, high-z	1.8	2.9	2.4	0.8
Forward				
1st, low-eta	2.0	2.5	2.3	0.9
1st, mid-eta	2.5	2.5	1.9	0.9
1st, high-eta	1.6	1.9	1.7	1.0
2nd, low-eta	2.3	3.5	2.8	0.1
2nd, mid-eta	2.6	3.9	2.9	0.5
2nd, high-eta	2.4	4.8	3.6	1.0
3rd, low-eta	2.1	1.7	2.9	0.2
3rd, mid-eta	2.2	1.9	2.5	0.1
3rd, high-eta	2.1	1.9	1.8	0.1

Table 5.14 Ratios of FLUKA AV16 to AV1 fluences. The scoring regions are shown in Figure 5.16.

6 Impact of radiation on ATLAS

In this chapter we review the impact of radiation backgrounds on the ATLAS detector and its environment. We start in Section 6.1 with the inner detector regions, followed by the muon system in Section 6.2 and the calorimeter regions in Section 6.3. A brief general discussion on the impact on ATLAS electronics is given in Section 6.4. We finish with radiological issues, with radiation in USA15 being discussed in Sections 6.5.

The largest section of this chapter concerns the impact on the muon system in Section 6.2. The reason for this is that a complete new study was performed that investigated muon chamber efficiences and sensitivites, the results of which are reported here. This can be contrasted, for example, to the Si damage functions used in estimating the 1 MeV neutron equivalent fluences which were taken directly from the literature.

.

6.1 Impact of radiation on the inner detector

The results of the predicted radiation levels in the inner detector regions are given in Section 5.2. This section is dedicated to a discussion on the impact of such predictions. We start with the effect of radiation on silicon detectors and electronics, which concerns all the inner detector regions, then we look at how the predicted radiation levels have impacted the different subsystems, and the measures taken to understand the radiation tolerance of the designs.

6.1.1 Damage to Silicon detectors and electronics

There are two main mechanisms leading to the deterioration in the performance of silicon devices. First there is the effect of damage to silicon devices by ionising energy loss in the surface layers. In semiconductor oxide layers, such as SiO_2, electrons resulting from ionisation will quickly drift from the oxide layer, driven by the bias voltage. The holes left behind have low mobility, and will drift slowly to the Si-SiO_2 interface, where they will accumulate as a charged layer, modifying the operating characteristics of the device.

The second effect is bulk damage, or displacement damage, which dominates the damage to "minority carrier" devices (silicon detectors, bipolar electronics etc.). Experiments have shown that damage effects by energetic particles in the bulk of any material can be described as being proportional to the so called displacement damage cross section *D*. This quantity is equivalent to the Non Ionizing Energy Loss (*NIEL)* and hence the proportionality between the NIEL-value and the resulting damage effects is referred to as the *NIEL-scaling hypothesis*. The D or NIEL value is depending on the particle type and energy. According to an ASTM standard, the displacement damage cross section for 1 MeV neutrons is set as a normalizing value: *Dn(1MeV) = 95 MeVmb*. On the basis of the NIEL scaling the damage efficiency of any *particle* with a given kinetic energy *E* can then be described by the hardness factor *k*, defined as *kparticle (E)=Dparticle/Dn(1MeVn)*. Therefore, instead of *D(E)* the normalized values *D(E)/95MeVmb* are used, as illustrated in Figure 6.1. Further details of displacement damage to silicon can be found in [81].

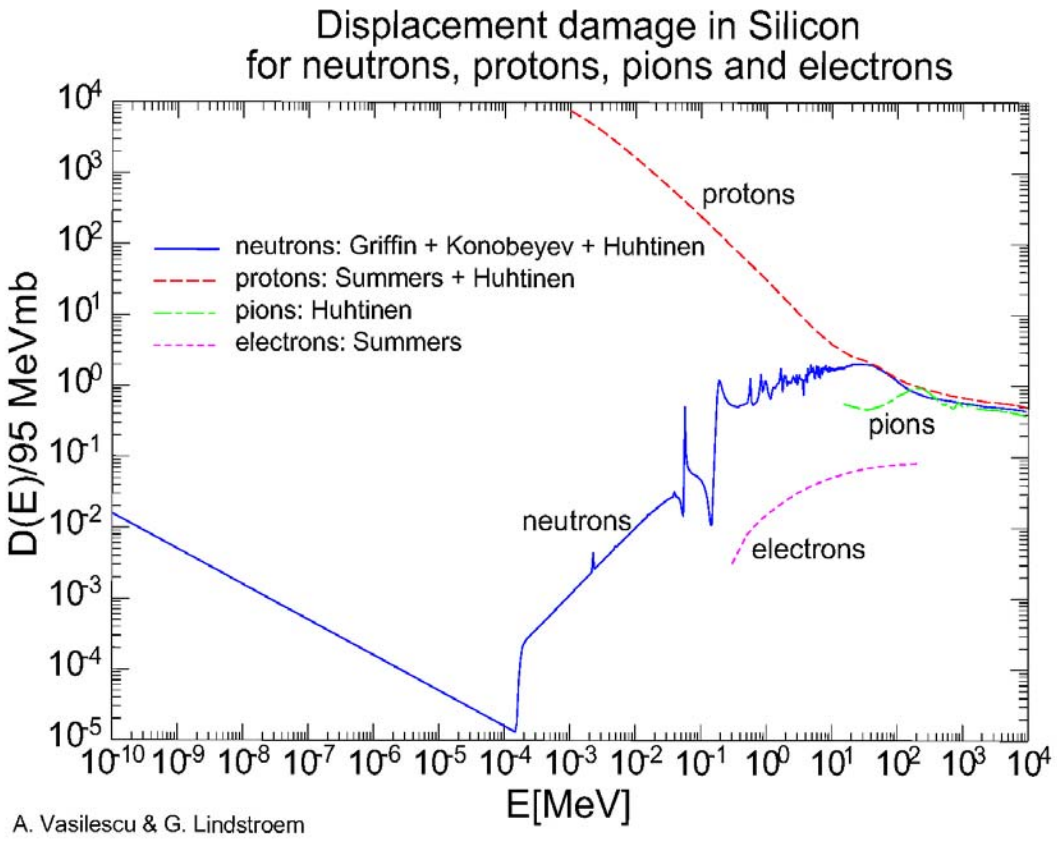

Figure 6.1 Displacement damage in Silicon for various particles and energy range (figure taken from ref. 81)

The understanding of radiation damage to LHC silicon detectors has been the focus of the CERN-RD48 (ROSE) collaboration [80]. In order to convert particle fluences to the required 1MeV-neutron-equivalent fluences, it is necessary to convolve the predicted particle spectra with the energy dependent "hardness factors" shown in Figure 6.1.

NIEL calculations have been made for protons and pions and have been calculated by several people as summarised in [81]. The proton curves have been benchmarked against a range of electronic device data, mainly minority carrier lifetime measurements [82], upto proton energy of 200MeV but above 200MeV data is sparse. NIEL curves have also been benchmarked against measurements of the current damage made with Si detectors for a few high energy points [81], but the NIEL does not appear to have been calculated for the CERN-PS energy of 24GeV. The limited data agree with the NIEL curve. For pions the NIEL curve has been benchmarked mainly in the 300MeV region [81] to test the hypothesis that the delta-resonance must be taken in account [84]. The agreement is reasonable; however the accepted NIEL is systematically low with respect to the data. Although, there is little data to benchmark the pion NIEL curve, the physics is similar to that involved in calculating the proton NIEL curve.

6.1.1.1 Uncertainty in NIEL

According to Huhtinen [84], the NIEL cross-sections are known at the level of 50%. This seems reasonable given that the data used to benchmark the NIEL curves has an error of ~30%, taking into account errors on fluence measurements and the spread of points.

For correcting back to 1-MeV-equivalent fluences, an uncertaintly of 50% should be taken for the relative damage factors. However, it should also be noted that using the 1-MeV-equivalent fluences to predict damage can be dangerous. It has been shown by RD48 that NIEL scaling does not work for calculating the effective doping concentration (Neff) in oxygenated Si, and for low proton energies for standard Si [85]. This applies both to the stable acceptor creation term and the reverse annealing term. Therefore care should be taken in predicting the depletion voltage based on 1-MeV-equivalent neutron fluences. Theoretical work by Huhtinen [86] appears to confirm this. The scaling of the current damage with NIEL, with the limited data available, appears to be valid. However, Huhtinen's theoretical work that correctly predicts the breakdown of NIEL scaling for Neff, also predicts a breakdown of the scaling of alpha particles.

6.1.2 Ionizating Dose Damage

Silicon detectors, and other detector components, are also subject to damage by ionising radiation, also referred to as "ionising dose". The dimensions are energy/unit-mass/unit-time, which we report in gray/year ("Gy/yr"). For conversion, 1 Gy = 1 joule/kg = 10^4 erg/g = 100 rad. The character of the damage due to this ionisation energy loss is quite different from displacement damage, in that it typically involves only the surface layers of detectors, since the low energy electrons and positrons responsible for the majority of the damage have little penetrating power in silicon. In simulation, this dose is calculated by accumulating the dE/dX losses reported in each tracking step. There are slight differences encountered in different transport programs, as will be discussed in more detail later.

Charged particles will induce ionization at an energy dependent rate, dE/dX, given by Bethe-Bloch formula, and photon backgrounds can be important since they interact readily to produce charged particles. In semiconductor oxide layers, such as SiO_2, electrons resulting from ionization will quickly drift from the oxide layer, driven by the bias voltage. The holes left behind have low mobility, and will drift slowly to the Si-SiO_2 interface, where they will accumulate as a charged layer, modifying the operating characteristics of the device. Normally, recombination would reduce this effect, but the removal of electrons from the ionization site by the bias voltage suppresses the recombination rate.

6.1.3 Impact on the TRT

There are three main effects on the TRT of the neutron and photon backgrounds: increased aging of the materials in the TRT and its electronics, increased counting rates, and induced radioactivity in the material of the TRT.

The charged tracks produced in the LHC beam interactions contribute considerably more than the neutron and photon backgrounds to all three of these effects in the TRT. The induced radioactivity in the material will not be discussed further and the reader is referred to the following references [65,68].

The maximum 1 MeV neutron equivalent fluence per high-luminosity year in the TRT system is predicted to be 2.7×10^{13} 1 MeV n/cm^2 at the inner part of the TRT type C wheels (the part of the TRT receiving the highest radiation). The TRT electrons are located in regions of lower exposure [52]. Samples of the most critical mechanical TRT components, including adhesives and plastic parts, were tested with up to 100 MRad of ionizing radiation and neutron fluences of up to 1×10^{15} 1 MeV n/cm^2. All samples survived without appreciable changes to their properties. Samples of the passive electronics components (capacitors, resistors, fuses and various printed

circuit boards) used in the TRT were exposed to 3 x 10^{14} 1 MeV n/cm^2 and 2 x 10^{14} p/cm^2. (Inner Detector TDR [69] section 12.2.)

The most critical test of the mechanical parts of the TRT has been the exposure of a complete TRT barrel module to the equivalent of 20 years of the expected neutron fluence at a reactor. During this exposure CO_2 was used as the active gas and the module was under reduced high voltage. The active detector elements (straws, wire, and glass wire-joints) survived the test, and the module was verified to be fully operational after the exposure. Of special importance was the fact that no gas leaks appeared in the straw volume. Also, the high-voltage behavior was found to be unchanged by the exposure [70].

The barrel electronics is estimated to receive 0.6x10^{13} 1 MeV n/cm^2 per high luminosity year and the end-cap electronics is predicted to receive 1.4x10^{13} 1 MeV n/cm^2 per high luminosity year. Including safety factors, the design goal for the TRT electronics is to survive 5 x 10^{14} 1 MeV n/cm^2 and 8 MRad of ionizing radiation. The inner part of barrel TRT electronics (closest to the beam) receives the largest doses [52].

Samples of the analog TRT front-end chips (the ASDBLR) were exposed to up to 5.3 x 10^{14} 1 MeV n/cm^2 and 7 MRad of photons. At an exposure of 1 x 10^{14} 1MeV n/cm^2 there was some increase in the current needed to set a discriminator threshold. The photon caused slight changes in the discriminator thresholds. Considerable concern remains about the effect of thermal neutrons on the Dmill process used to fabricate the ASDBLR since ASDBLRs irradiated at a reactor that contained a large thermal neutron component did suffer damage at high exposures [71].

Samples of the digital TRT front-end chip (the DTMROC) were exposed to up to 5.3 x 10^{14} 1 MeV n/cm^2 of neutrons and 8 MRad of photons. The main change was an increase in the output voltage of a DAC used to set the discriminator threshold in the ASDBLR. This change does not affect the drift time measurements made by the DTMROC, and can be removed by periodic recalibration of the DAC output over the lifetime of the ATLAS experiment. There were no other measurable changes to the DTMROC after irradiation [72].

Calculations of the increase in the TRT counting rate were made for the ATLAS Inner Detector TDR. In all cases, the counting rate caused by the radiation background was small compared to the rate induced directly from charged tracks. For example, for the inner full length TRT barrel, the counting rate from the LHC events is ~18 MHz, while the photons in radiation background cause a rate of about ~1 MHz. Averaging over the whole TRT, the rate of hits caused by the radiation background is ~10% of the rate associated with the LHC tracks [69 section 12.1,73].

6.1.4 Impact on the SCT

The maximum fluence per high-luminosity year in the ATLAS SCT system is predicted to be 1.8x10^{13} n-eq/cm^2 (1 MeV neutron equivalent) [52,69]. An estimate of the accumulated fluence over the lifetime of the experiment has also been obtained assuming: 1) the original LHC running scenario of three years of low-luminosity running followed by seven years of high-luminosity running; 2) a 50% safety factor to take into account uncertainties in the predictions. This has led to the value of 2x10^{14} n-eq/cm^2 being used by the SCT community in the design and qualification of their detectors. The design value for the maximum accumulated dose over the lifetime of the experiment is 100kGy. The main consequences of radiation damage to silicon detectors are an increase of detector leakage currents and the change of effective doping of the bulk silicon from n- to p-type (type inversion) followed by a steady increase of full depletion

voltage. These effects have been well studied by the SCT community [69] leading to a radiation tolerant design that will be operated at -7ºC. More recent reviews of the performance of detectors, readout-electronics and optical-links after irradiation can be found in [74], [75] and [76] respectively. Also of concern and studied has been single event effects in the readout electronics [75], and the radioactivation of SCT components [79].

6.1.5 Impact on the Pixels

The ATLAS pixel detector will be among a few first generation high rate pixel detectors at particle colliders. It has been designed to operate in the high track density and radiation environment near an LHC collision point with a nominal useful life of 10^{15}cm^{-1} 1 MeV neutron-equivalent particle fluence [77, 78]. The dominant contribution is from minimum ionizing charged pions. The ionizing damage is approximately 50 Mrad silicon equivalent. Even at low operating temperature such a dose will give rise to large leakage currents in silicon sensors which can only be managed by connecting a small volume of silicon to each readout channel. Thus píxel detectors have to be used and strip detectors would not be a viable option. The large particle density per event at LHC energies would also result in too high occupancy for pattern recognition with a strip detector.

Aside from increased leakage current, radiation damage will first type invert the sensor bulk and then gradually increase the depletion voltage. The pixel sensors have n bulk and n^+ implants on the readout side, with the p-n junction on the back side. This means that for unirradiated sensors the depletion begins from the back side and the pixels are not isolated from each other until full depletion. However, after type inversion the junction moves to the front side making the pixels isolated and operational even if the bulk cannot be fully depleted. Of course, maximum achievable depletion is still desirable to maximize the signal. Two key features make near-full depletion possible after the nominal full dose. A multiple guard ring structure on the back side of the sensors is capable of withstanding bias in excess of 600V (the design maximum operating voltage) without breakdown, and an oxygenation process is applied during fabrication which curbs the increase in depletion voltage due to charged particle bulk damage. On the sensor front side each pixel is DC coupled to the readout electronics. There is also a bias grid structure using a punch-through connection to each pixel that permits biasing the sensor without any electronics present.

The on-detector electronics are implemented in a suite of 4 IC's designed in a 0.25μm feature size bulk CMOS. These are the Front End chip (FE), the Module Control Chip (MCC), the DORIC and the VDC. The DORIC, connected to a PIN diode, performs optical to LVDS control data and clock decoding and conversion, while the VDC, connected to a laser diode, performs LVDS to optical output data conversion. All IC's have been designed in a commercial 0.25μm bulk CMOS process using a combination of full custom analog blocks and a range of design techniques (from auto-routed Very High Description Level, VHDL, to manually routed schematic level) starting from a custom digital library with enclosed geometry NMOS transistors for radiation tolerance. All chips have been tested to ionizing doses in excess of the 50 Mrad lifetime dose with little degradation. Another radiation effect that must be considered is the rate of Single Event Upsets (SEU), as there are of order 106 registers in every module. Studies indicate that some care must be taken in order to make circuits built in this technology robust to SEU at the level required for ATLAS operation, and there is ongoing work in this area.

6.2 Review impact on muon system

6.2.1 Muon Chamber Backgrounds

High particles fluxes in the muon system have a major impact on the spectrometer design. They influences parameters such as the rate capability of chambers, the ageing of the detector components, the granularity and redundancy of the trigger instrumentation, the pattern recognition efficiency, or the momentum resolution tails induced by incorrect hit association. They are two broad classes of background hits: primary collision products, such as prompt muons from heavy particle decays and hadronic debris of calorimeter showers; very low-energy secondaries from radiation background. The ATLAS muon instrumentation has been designed to offer the rate capability and robustness to the high occupancies required for running at nominal luminosity. In particular, the Level-1 trigger system is based on dedicated, fast and finely segmented detectors. The accidental trigger rate should remain below the rate expected from prompt muons (semileptonic decays of beauty and charm hadrons, plus light meson decays) including safety factors in predicted background rates. The adequacies of the muon system instrumentation and the Level-1 trigger system have been demonstrated at the time of the Technical Design Reports [55,40]. The shielding design should maintain the radiation background at these acceptable rates.

The radiation background affects the muon system in various ways: by generating uncorrelated noise hits, and by producing penetrating particles. The uncorrelated noise hits in the chambers may affect the pattern recognition, space-charge build-up and aging. The MDT chambers have been designed to handle up to 5 times the counting rates estimated at the time of the TDR [55]: 10 Hz/cm^2 in the middle of the barrel up to about 100 Hz/cm^2 at pseudo-rapidity ~2, while CSCs are specially designed for rates above 200 Hz/cm^2 and will be used in the most critical forward location. On the other hand penetrating particles are an important component of the background for the trigger. RPC and TGC chambers, organized in three stations of 2 (or 3) gas gaps each, provide transverse measurements used by the trigger to reject muons with p_T below a given threshold.

The sensitivity of the chambers to the neutron and photon background that have been used so far to estimate occupancy and trigger rates were based on measurement of earlier prototypes of chambers and Monte Carlo simulation. Table 6.1 summarizes the values were used until now in the estimates [55].

Chamber type	Neutron sensitivity	Photon sensitivity
MDT	$\sim 5\times10^{-4}$	$\sim 8 \times 10^{-3}$
CSC	$\sim 10^{-4}$	$\sim 5 \times 10^{-3}$
RPC/TGC	$\sim 10^{-4}$	$\sim 5 \times 10^{-3}$

Table 6.1 Average sensitivity of muon chambers to neutron and photon background used so far in trigger rate estimates.

The counting rates have been evaluated until now as follows:

(1) Single plane counting rate = $\mathbf{n}\times\varepsilon_n + \gamma\times\varepsilon_\gamma + (\boldsymbol{p} + \boldsymbol{\pi} + \boldsymbol{\mu} + 0.25\times\boldsymbol{e})$

(2) Penetrating particle rate = $0.1\times\gamma^*\varepsilon_\gamma + (\boldsymbol{p} + \boldsymbol{\pi} + \boldsymbol{\mu} + 0.25\times\boldsymbol{e})$

where penetrating particle stands for a particle giving a coincidence in a couple of adjacent RPC or TGC planes. "**n**" and "**γ**" stand for neutron and photon particle fluences respectively. "ε_n" and "ε_γ" are the corresponding average neutron and photon chamber sensitivities taken from Table 6.1. For charged particles, ***p***, ***π***, ***μ***, and ***e***, stand for currents that are instead of fluences (see discussion in the following paragraph). The efficiency for charged particles to produce a hit in a chamber is taken as 100%. Electron currents are multiplied by a factor 0.25 to avoid double counting of electrons produced in photon interactions in neighbouring material. The factor 0.1 multiplying the photon fluence in the penetrating particle rate is a rough estimate of the fraction of photon interactions that result in a coincidence of two adjacent planes.

Fluences and currents are two quantities that have the dimensions of number/unit-time/unit-area, but they do not have the same meaning. Fluence counts the rate of arrivals per unit area independent of particle direction, whereas current counts the rate crossing through a given plane, referred to area elements in the surface of the plane (more detail in Appendix II and in ref. [107]). The first quantity is proportional to the track length in a given volume and is appropriate for hits resulting from neutral particle interactions in the chamber. The second quantity gives a better estimate of the counting rate induced by charged particles crossing a chamber. FLUKA simulations provide directly charged particle currents while GCALOR simulations do not. In the latter case, charged particle currents were taken as 1/2 of the fluences, the expected ratio for isotropic fluences. Ratios of current to fluence have been evaluated more precisely for different particle species and chamber locations with FLUKA (see section 5.4.2 and Table 5.11). They have been used in the new chamber counting rate evaluation presented in Section 6.2.6.

Table 6.2 illustrates what are the relative contributions from the different terms in some of the regions. Single chamber counting rate is dominated by the photons, while neutrons contribute at the 10% level. Penetrating particle rates are shared between charged particles and photons in the forward region and dominated by photons and electrons in the barrel.

MDT Inner Forward	single	12% **n**	64% **γ**	8% **p**	7% **μ**	9% **e**
	penetrating		21% **γ**	27% **p**	24% **μ**	28% **e**
MDT Outer Barrel	single	12% **n**	74% **γ**	4% **p**	1% **μ**	7% **e**
	penetrating		35% **γ**	17% **p**	7% **μ**	41% **e**

Table 6.2 Relative contributions from different particle species to the single plane and penetrating particle counting rates, evaluated with formula (1) and (2) respectively. The most significant contributions have been underlined. The first set of data, labelled "MDT Inner Forward", corresponds to the Small Wheel MDT chamber closest to the beam. The second set of data, labelled MDT Outer Barrel, corresponds to MDT chambers of the outer barrel.

In the coming sections, we describe the detailed Monte Carlo simulations that have been carried out in order to reassess more precisely the average chamber efficiencies for the various particles species, chambers types and locations and the various trigger levels of coincidences. The detailed Geant3 set-up used in these simulations is shown in
Figure 6.2. The simulation was done using the detailed 3D magnetic field map. These efficiencies are then used in the new chamber counting rate evaluation presented in Section 6.2.6.

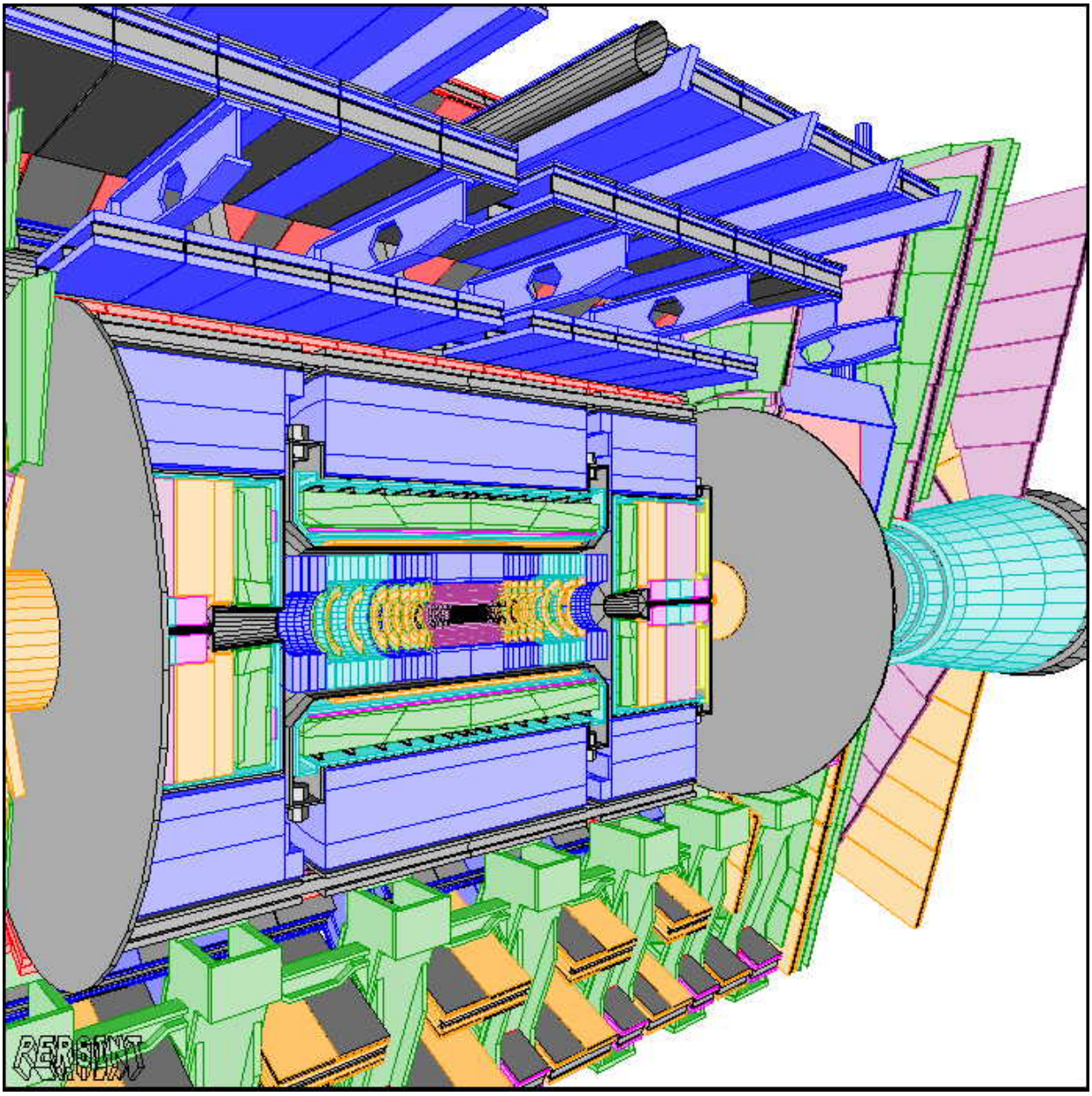

Figure 6.2 Atlas Geant3 layout used for chamber sensitivity calculations.

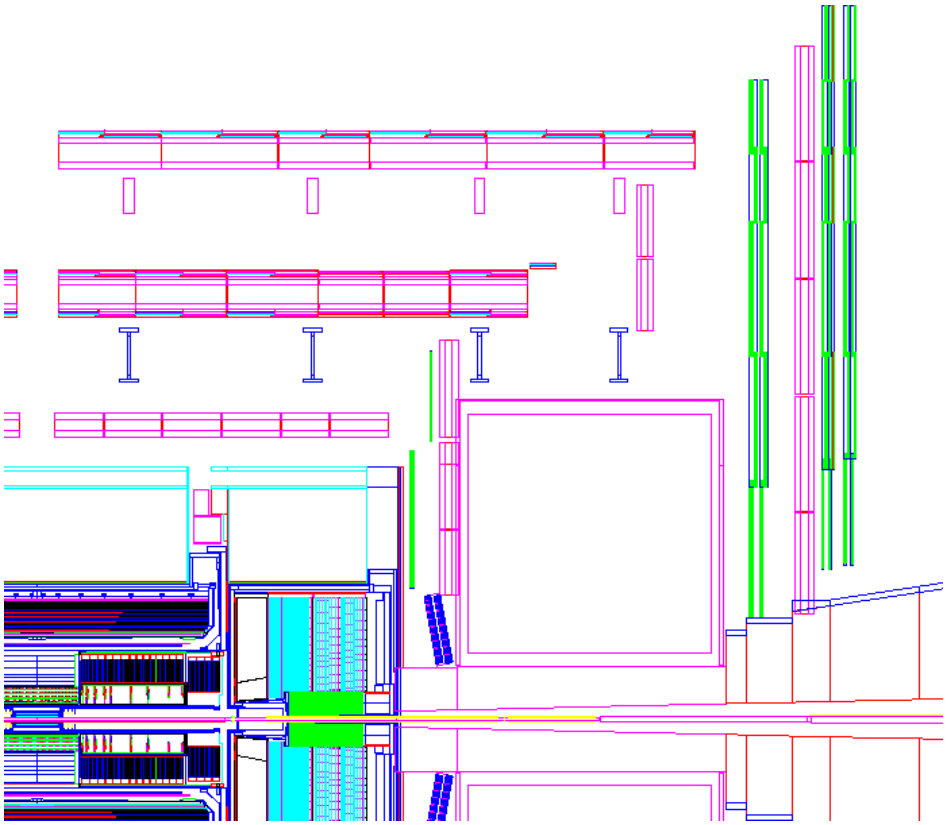

Figure 6.3 (R,Z) view of Atlas in the detailed GEANT3 simulation.

A (R,Z) projection of the various muon chambers is shown in Figure 6.3. A close-up view on a set of barrel MDT and RPC, together with their support, is shown in Figure 6.4 with a set of incident photons and the secondaries produced in their interactions.

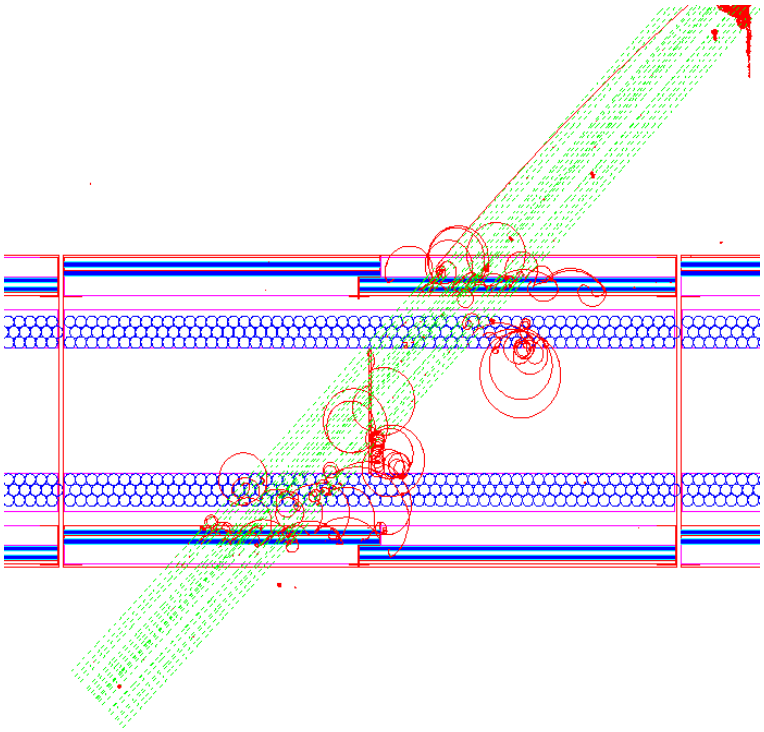

Figure 6.4 Details of the simulation of a BML chamber together with a set of incident photons (green) and the secondaries produced in their interactions (red): electrons and positrons.

The set-up simulated for the CSC is shown in Figure 6.5.

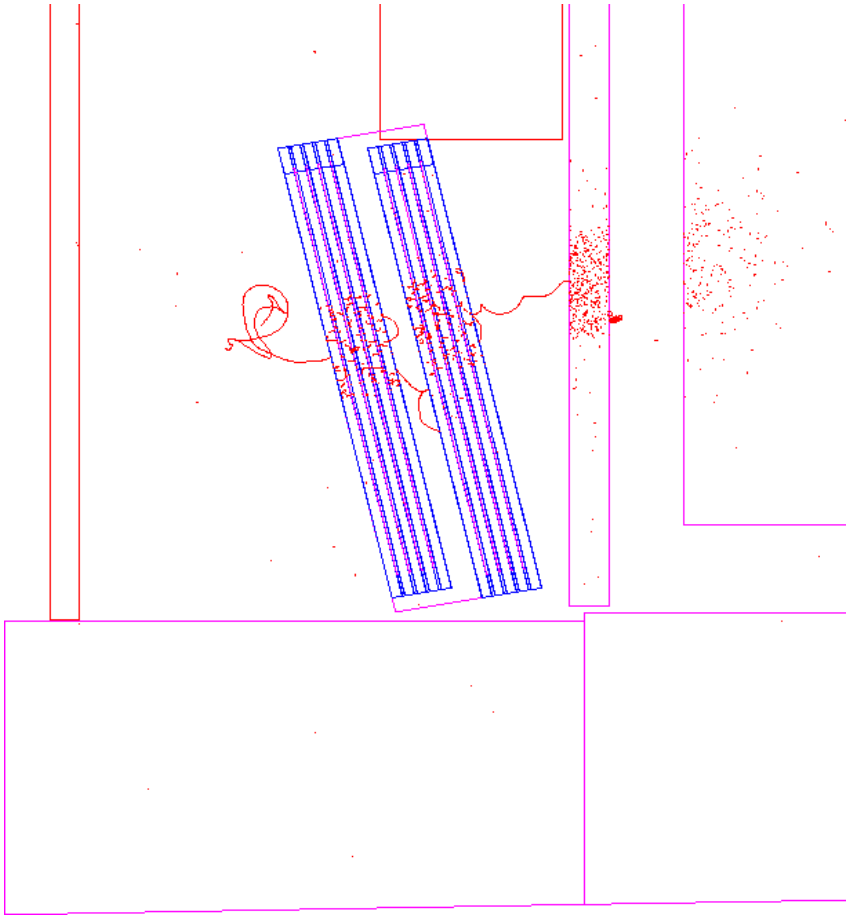

Figure 6.5 Layout of the CSC chambers

6.2.2 Efficiency for neutrons

In order to obtain a precise determination of the average efficiency per chamber, it is necessary to fold the energy dependent chamber efficiency with the incident neutron energy spectrum. These efficiencies have been calculated for the four types of chambers using the neutron average angular distribution for each chamber type. The gap or tube and gas characteristics used for the simulation are given in Table 6.3.

Chamber	Gas	Gap thickness or tube diameter
CSC	80%Ar+20%CO2	5 mm
RPC	Tetrafluoretane C2H2F4 94.7% + C4H10 5% + SF6 0.3%	2 mm
TGC	55%CO2+45%C5H12	2.8 mm
MDT	pressure 3 atm., 93%Ar+7%CO2	29.2 mm

Table 6.3 Gas composition and gap thickness or tube diameter for the various chamber types

The resulting efficiency for neutrons in the MDT is shown in Figure 6.6.

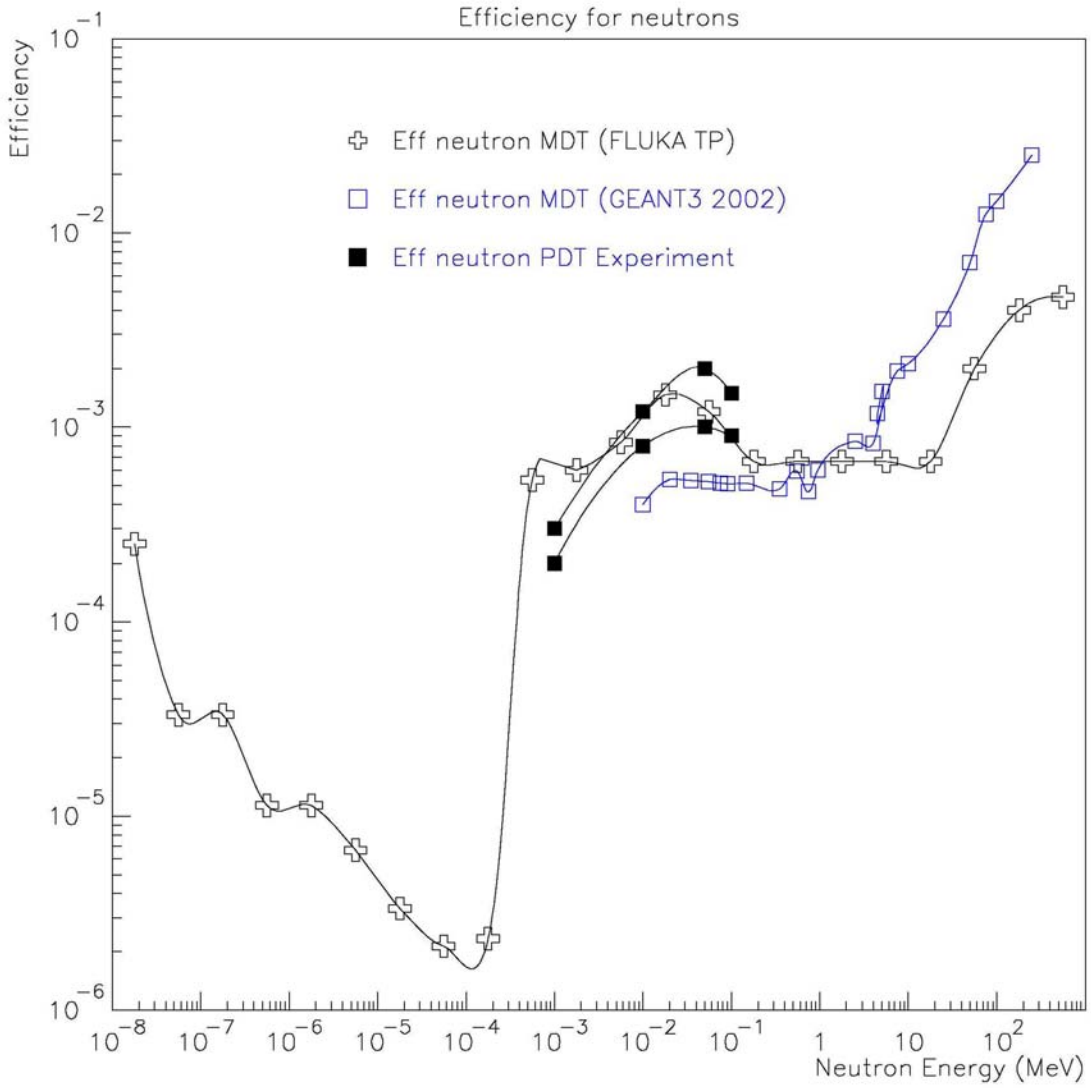

Figure 6.6 MDT Efficiency for neutrons: crosses show the old efficiency estimated with FLUKA for the MDT for the TP design with a gas composition of 90%Ar, 5%N_2,5%CH_4 at a pressure of 3 Atm; open squares show the new GEANT3 estimate for the final MDT design with 3 Atm of 93%Ar,7%CO_2; full squares are measurements made with Pressurized Drift Tubes at 3 Atm of 81.5%Ar, 15%CO_2,3.5%C_4H_{10} for different sensitive volumes [57]. See text a more detailed discussion.

There are three components that contribute to the efficiency. Neutron capture, most probable for thermal neutrons, with subsequent gamma emission and interaction are responsible for the efficiency up to approximately 0.1 keV. Then, from the chamber signal detection threshold (~ 1 keV) up to10 MeV, it is the recoil of gas nuclei with its associated ionization that produces the signal. At higher energies, charged secondaries, mainly protons from quasi-elastic neutron scattering in the chamber wall or surrounding material, are the source of the signal (see Figure 6.7).

At high energy, the steeply rising efficiency curve is very sensitive to the material surrounding the chamber, as illustrated in Figure 6.8.

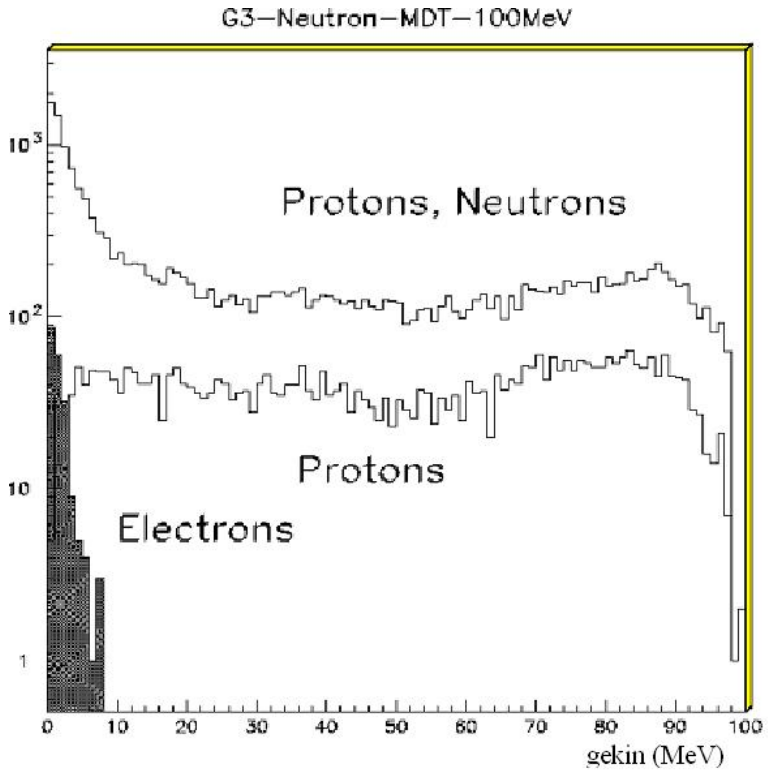

Figure 6.7 Kinetic energy distribution of the secondary particles produced in 100 MeV neutron interactions in MDT. The horizontal scale gives the kinetic energy in MeV. The vertical scale gives the number of secondary particles (a.u.)

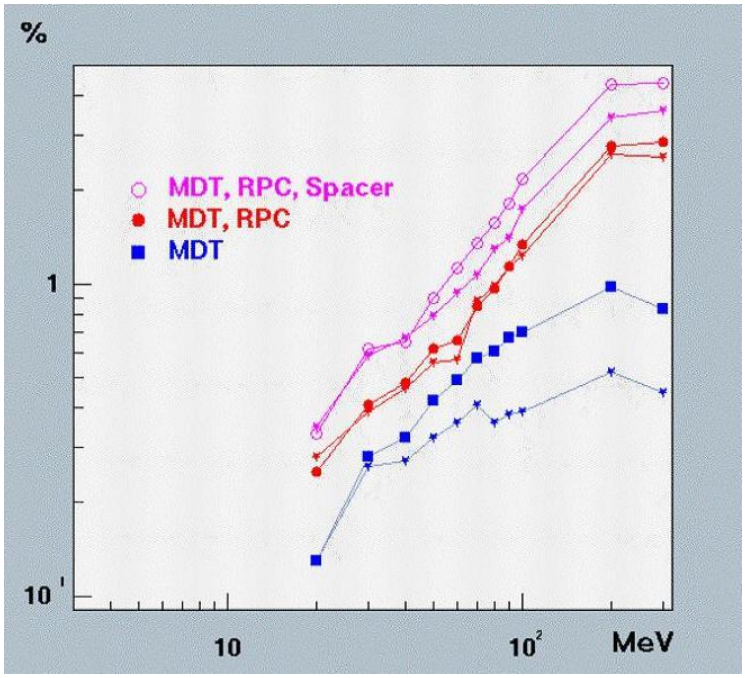

Figure 6.8 Dependence of the high energy neutron efficiency as a function of the kinetic energy of the neutron. The horizontal scale corresponds to the kinetic energy given in MeV. The vertical scale gives the average efficiency at each energy point in %. In this calculation, the neutrons cross the chambers at 45°. The chamber set-up is shown in Figure 6.4. The figure illustrates the sensitivity to the material distribution. Results are shown when elements are progressively included in the set-up. The lowest curve (small crosses) is for a single tube; the curve above (full square) is for one plane in a complete set of MDTs; full dots (or crosses, for the two directions of incidence) correspond to the case where the MDTs are surrounded by RPCs and the support material; open circles (and crosses) when there is a spacer along the trajectory.

In Figure 6.6, the new calculations (open squares) are shown. The effect of recoil nuclei, important in the neutron energy range 100 keV – 1 MeV, is not included by default in Geant3 and has been implemented according to the calculation described in [58]. The probability of interaction is proportional to the neutron path length that was obtained by summing the GEANT3 step length inside the tube. The new calculation is compared to the old estimate (open crosses) done with FLUKA for the MDT TP design [56]. The latter corresponds to the probability to fire one plane in a set of three layers of MDT tubes. The RPCs and the chamber supports were not included in the simulation. The 3cm diameter tubes had a 0.35 mm Al wall. The gas composition was 90% Ar, 5% N_2, 5% CH_4 and the pressure 3 Atm. The flux of neutrons was taken isotropic. Two sets of experimental points (full squares) are also shown [57]. They correspond to measurements with Pressurized Drift Tubes made at the JINR pulse neutron source. Measurements were done with Aluminium tubes of 50mm diameter and 1mm thick walls. Additional wires stretched in the tube at a radius of 13 mm served as shaping electrodes to reduce the sensitive volume when put under tension. The gas mixture was 81.5%Ar, 15%CO_2, 3.5%C_4H_{10} and the pressure 3 Atm. The data cover the energy range 1 KeV to 100 KeV where recoil from gas nuclei is the main mechanism for neutron detection. It is thus dependent on the volume and the gas composition and gas pressure. The lower data curve corresponds to data taken with an effective radius of the sensitivive region of 13 mm and the upper curve for 24 mm. The data are closer to the old TP efficiency estimate because of the importance of the contribution from recoil protons from the Hydrogen component of the gas. At higher energies, above a few MeV, differences between the new estimate and the TP estimate are expected because of the sensitivity to the material surrounding the chamber include in the new calculation but not in the old one.

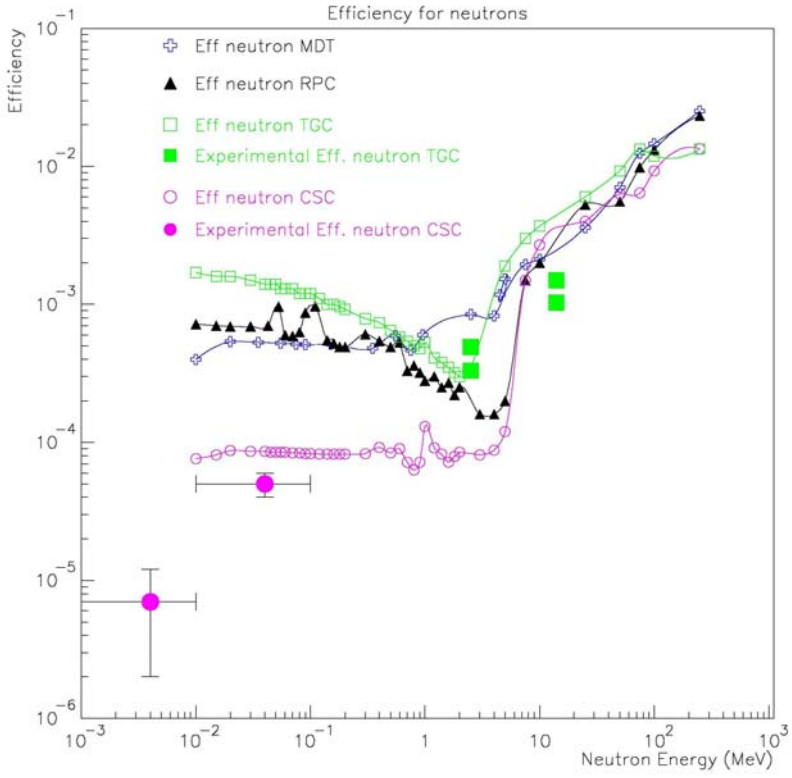

Figure 6.9 Efficiency for neutrons for the different chamber types as calculated with Geant3. Experimental measurements are shown for CSC [59,60] and TGC [61]. See text for more detailed comments.

The efficiencies have been calculated also for all other types of chambers. They are shown in Figure 6.9. The average neutron path lengths in the sensitive volumes used in the calculation are shown in Figure 6.10. They are about 80 % larger than the nominal tube diameter or gap width in the case of CSC, RPC and TGC, while for MDT it is similar. The figure also presents two experimental sets of measurements for CSC [59,60] and for TGC [61]. The CSC measurements were done with the GEM CSC prototype at low energy in the regime where nuclear recoil is important. The gas used in that experiment was 30%Ar, 50%CO_2, 20%CF_4. Measurements for TGC were done at 2.5 and 14 MeV. The lower set of data points are the efficiencies measured with a small size prototype chamber (10x15 cm^2) and the higher values are obtained with a standard size T8 type. At 2.5 MeV, the gas recoil and the interactions in the walls contribute about equally to the efficiency, while at 14 MeV interactions in the walls dominate. The experiment has been simulated with Geant4 and good agreement was found. We can conclude that experimental data are consistent with the Geant3 simulation considering expected differences due to gas composition, angular distribution and effect of material surrounding the chambers.

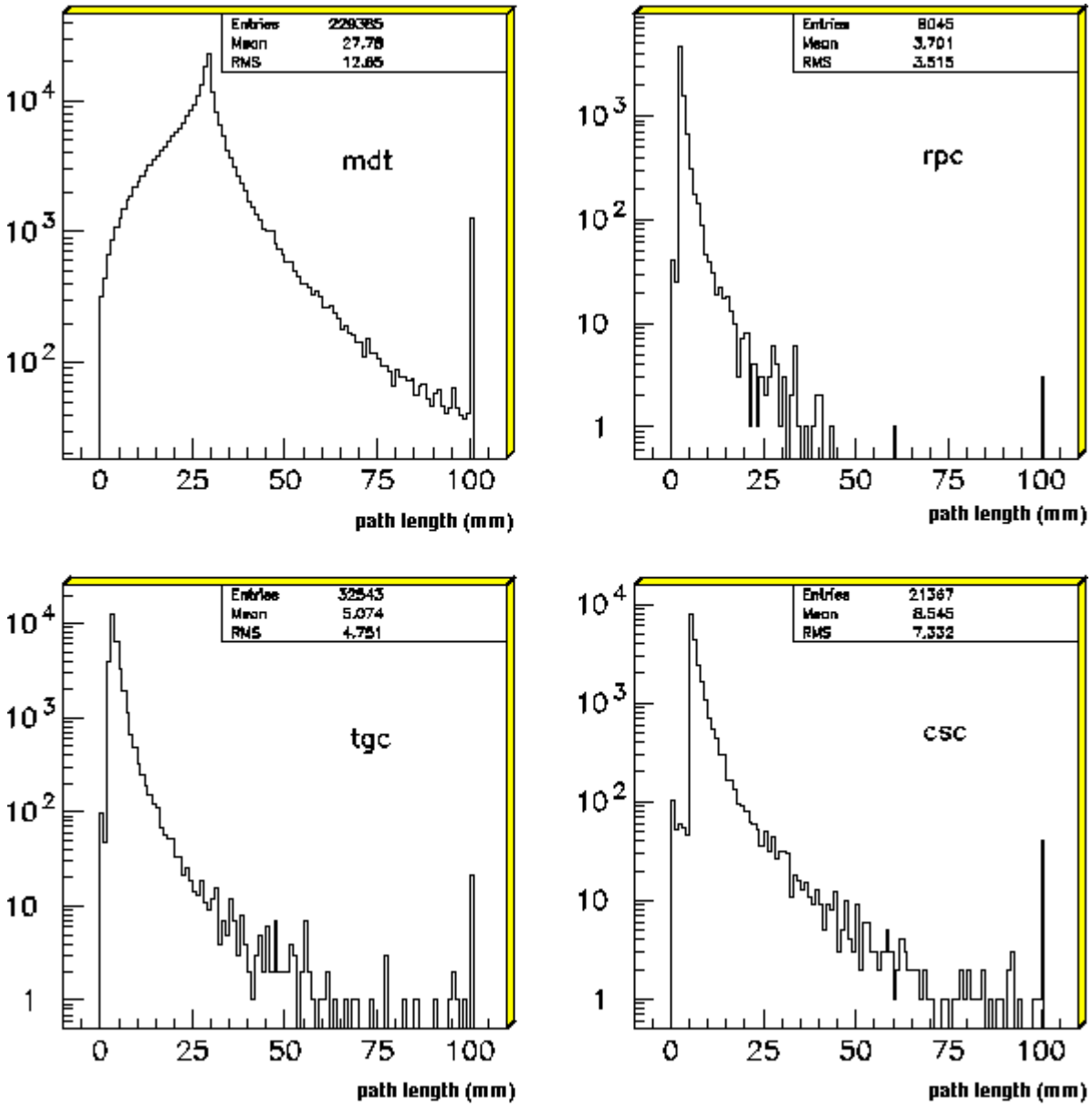

Figure 6.10 Neutron path length in the various chambers obtained from the G3 step length.

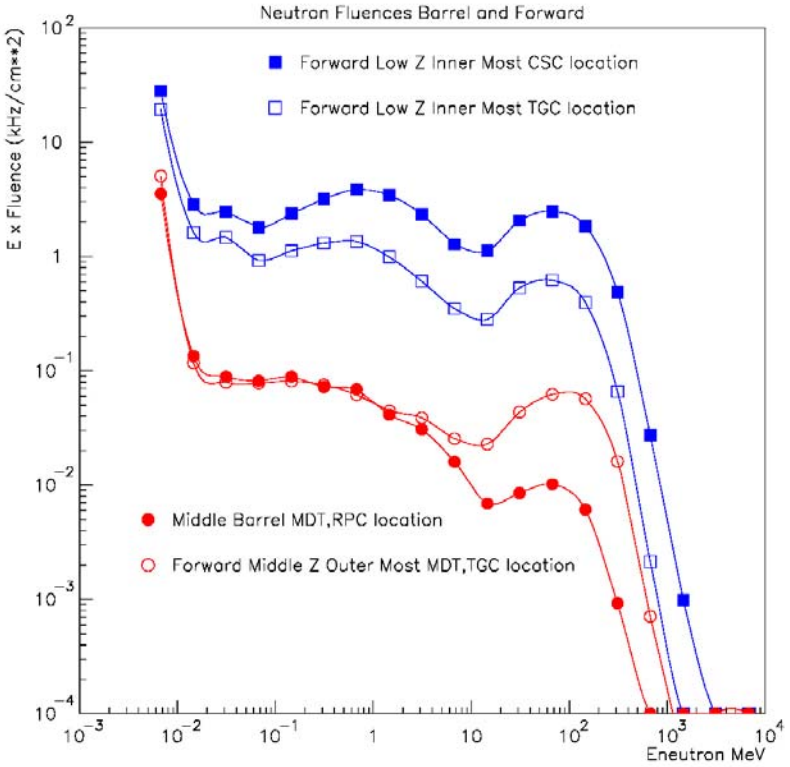

Figure 6.11 Neutron fluences in various regions of the muon spectrometer: all neutrons with energies below 10 keV are collapsed in a single bin. There are 6 orders of magnitudes (or 12 bins) down to the thermal neutron energy.

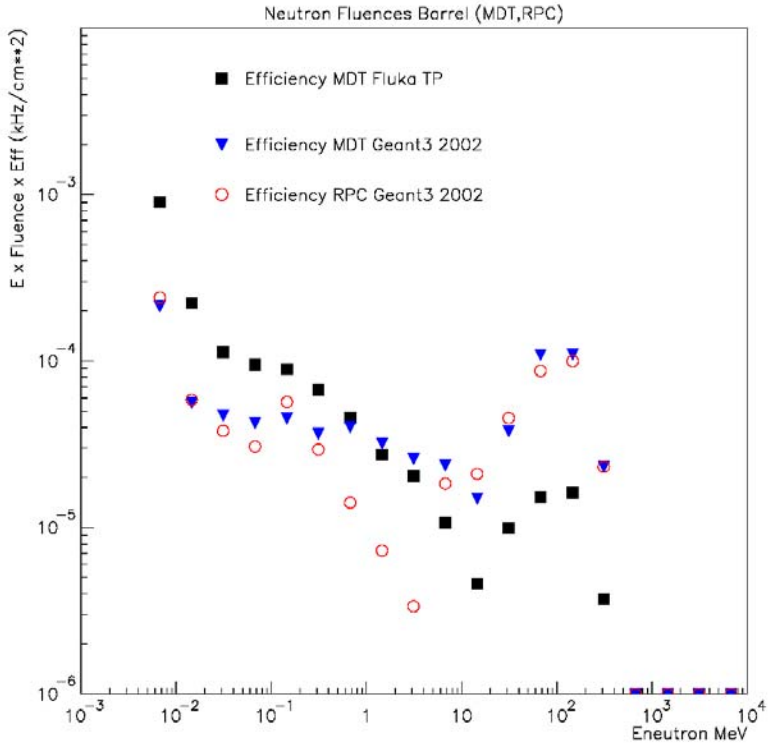

Figure 6.12 Neutron fluences in the middle barrel region folded with neutron efficiency curves for MDT and RPC. See text for details about treatment of the bin below 10 keV.

The neutron fluences, as predicted in various regions by GCALOR, are shown in Figure 6.11. The shape of the spectrum is flat from thermal energies up to about 100 keV characteristic of moderated neutrons [24]. All neutrons with energies below 10 keV are collapsed in a single bin: there are 6 orders of magnitude – or 12 bins – down to the thermal neutron energies. There is an evaporation peak around a few MeV and a quasi-elastic peak at about 100 MeV, more pronounced in the forward region. The neutron fluence spectra shown in Figure 6.11 have been folded with the corresponding neutron efficiency curves of Figure 6.9. The result is shown in Figure 6.12. The average efficiencies have been calculated for the different chambers and different locations. They are presented in Table 6.4.

Region	**Chamber Type**	**Efficiency** including energy range > 10 MeV	**Efficiency** excluding energy range > 10 MeV
Middle barrel	MDT (new Geant3)	2.0×10^{-4}	1.3×10^{-4}
	MDT (TP efficiency)	3.4×10^{-4}	3.3×10^{-4}
	MDT (TP efficiency) FLUKA spectrum	7.0×10^{-4}	
	RPC (new Geant3)	2.7×10^{-4}	2.0×10^{-4}
Forward, low Z Innermost radius	CSC (new Geant3)	10.7×10^{-4}	1.2×10^{-4}
	TGC (new Geant3)	12.1×10^{-4}	4.9×10^{-4}
	MDT (new Geant3)	10.0×10^{-4}	3.0×10^{-4}
	MDT (TP efficiency)	8.6×10^{-4}	2.6×10^{-4}
	MDT (TP efficiency) FLUKA spectrum	8.4×10^{-4}	
Forward, middle Z Outermost radius	TGC (new Geant3)	7.7×10^{-4}	3.6×10^{-4}
	MDT (new Geant3)	5.1×10^{-4}	1.1×10^{-4}
	MDT (TP efficiency)	3.9×10^{-4}	3.3×10^{-4}
	MDT (TP efficiency) FLUKA spectrum	7.2×10^{-4}	

Table 6.4 Average efficiency for neutrons for various regions and chamber types. See text for details about how the various values are obtained.

Let's first consider the case of the MDTs in the middle barrel region reported in the top section of Table 6.4. As discussed before, there are three components that contribute to the efficiency: gamma from neutron capture, recoiling nuclei and protons from quasi-elastic scattering. Gamma and protons are accounted for in the photon and proton fluences respectively and should in principle not be counted twice.

The contribution to the efficiency from the various components has been estimated. The first line of Table 6.4 gives the average efficiency folding the Geant3 neutron spectrum (assumed flat below 10 keV) with the Geant3 efficiency curve that takes into account the recoil of nuclei and the high energy interactions. An efficiency of 2.0×10^{-4} is obtained. Excluding the energy range above 10 MeV corresponding mainly to quasi-elastic proton production, the efficency drops to 1.3×10^{-4}. The second line shows the efficiency obtained when fitting with the Fluka TP efficiency curve excluding the neutron capture component. The higher value of 3.4×10^{-4} is due to the different gas composition and the higher efficiency due to nuclear recoil. The energy range

above 10 MeV contributes very little in that case because the chambers were simulated without the surrounding RPC's and the supports resulting in a lower efficiency in that energy range. If the thermal neutron capture would be included in the Geant3 estimate, the efficiency would increase by about 30%. In the third line, the average efficiency obtained by folding the TP efficiency curve (including capture) with the AV16 FLUKA neutron energy spectra is shown. The efficiency is about 50% higher than with the GCALOR spectra. Table 6.4 shows the average efficiencies obtained for the RPCs are similar to ones of the MDTs.

Let's now look at the end-cap region. Figure 6.13 shows the neutron spectra folded with efficiency in the CSC and the neighboring TGC chambers. Figure 6.14 shows, as another example, the neutron spectra folded with efficiency in the big wheel regions for the TGC and MDT situated at the largest radius. One can observe a very pronounced peak around 100 MeV due to the more intense high energy neutron component (see Figure 6.11) and the high sensitivity of the chambers to the fast recoil protons. In Figure 6.13 and in Figure 6.14 the proton fluences have also been drawn. Let us look first at the CSC case in Figure 6.13: the proton spectrum can be almost completely accounted for by the neutron interactions in the chambers, except for an excess of very energetic neutrons (a few GeV or more) presumably coming out of the shielding. The proton produced in the chamber only account for part of the protons, mainly the most energetic ones. The difference between the two cases can be understood by looking at the AV16 charged hadron fluences (dominated by protons) shown in Figure 6.15 . In the CSC, TGC, and inner forward regions, the rather intense hard neutron component coming out of the shielding interact in the chambers and produce a lot of protons, while in the outer regions the hard neutron component is less intense, and produce correspondingly less protons. However there is another source of protons that feed these regions: the protons produced in the interaction of hard neutrons in the toroid coils. In Figure 6.15 , one can see the coil structure acting as a source of protons that then propagate further in the hall and reach also the barrel region curved by the field.

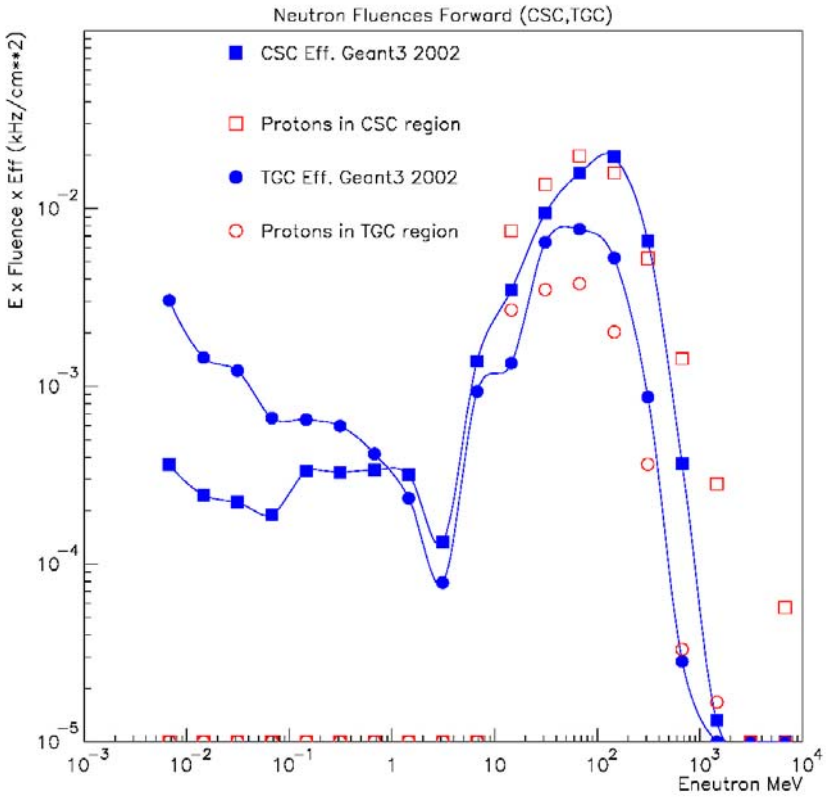

Figure 6.13 Neutron spectra folded with efficiency for CSC and neighbouring TGC chambers.

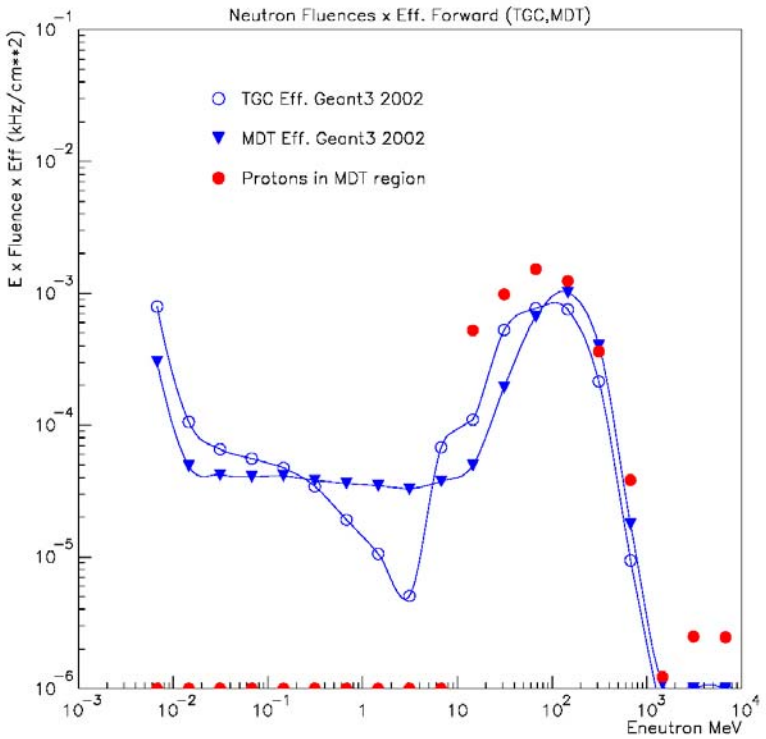

Figure 6.14 Neutron spectra folded with efficiency in the middle forward TGC and MDT chambers situated at the largest radius.

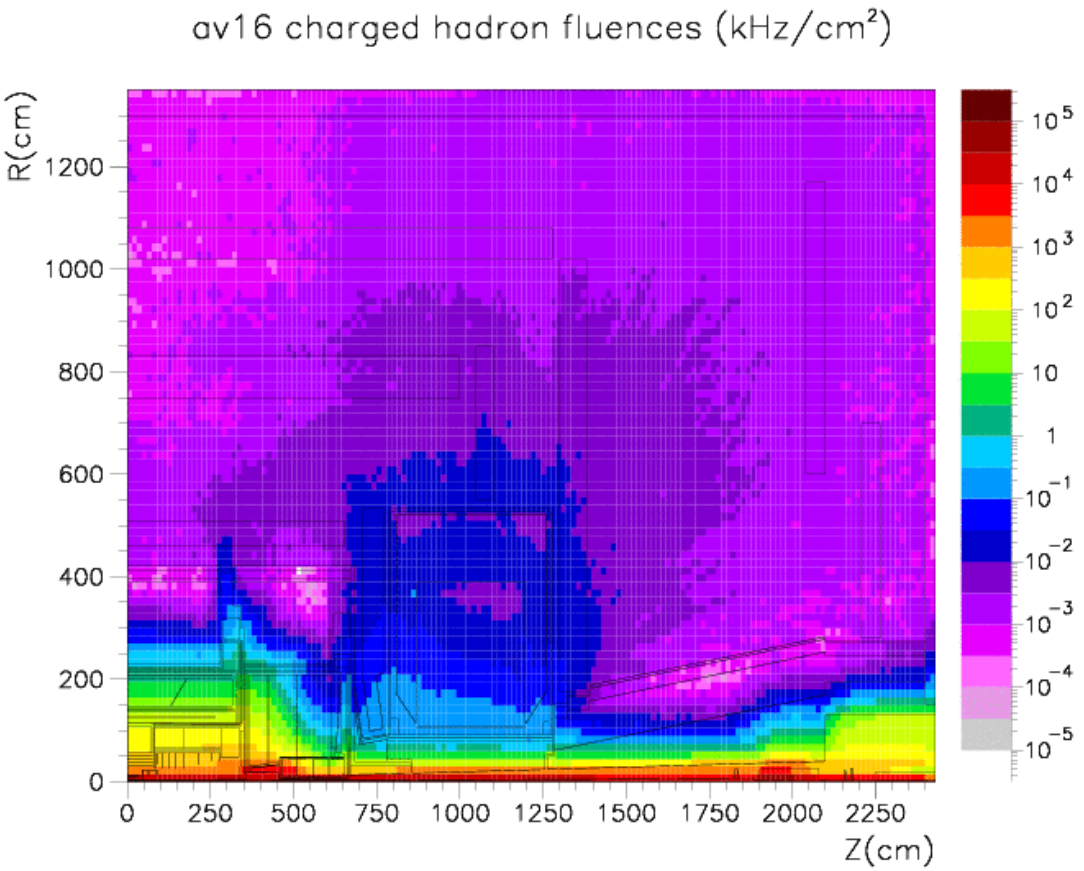

Figure 6.15 Charged hadrons (dominated by protons) as predicted by FLUKA

Turning again to the average neutron efficiencies for the various regions and chamber types given in Table 6.4, we see that the average efficiency changes from 2×10^{-4} in the barrel to 5×10^{-4} in the outer part of the big wheel and up to about 10×10^{-4} at the inner radius of the forward region. The higher values, as we have seen, are due to the more intense hard neutron component of the spectrum. However, to avoid double counting with protons fluences, it is better to exclude the contribution secondary protons. The rightmost column in Table 6.4 shows the average efficiencies excluding neutrons with energy above 10 MeV. The MDT values vary then from 1.1 to 3.0×10^{-4}.
In summary, for all the MDTs, we can use conservatively the value of 3.10^{-4}. In addition, the table shows that folding the same efficiency curve with the FLUKA spectrum instead of the GCALOR spectrum can give up to a factor 1.5 higher average efficiency. That factor can be taken as an estimate of the uncertainty on the average efficiency which is related the shape of the spectrum, in turn dependent on the transport program. The average efficiency used so far in calculation involving MDTs was 5×10^{-4}. The values we can quote for RPC, CSC, and TGC are 2.0×10^{-4}, 1.2×10^{-4}, and 5.0×10^{-4} respectively. They can be compared to the value of 1.0×10^{-4} used so far in calculation for all three types of chamber. Table 6.11, at the end of the section, summarizes all efficiencies.

6.2.3 Efficiency for photons

6.2.3.1 Single plane efficiency

The single plane efficiency for photons in the MDT chambers is shown in Figure 6.16.

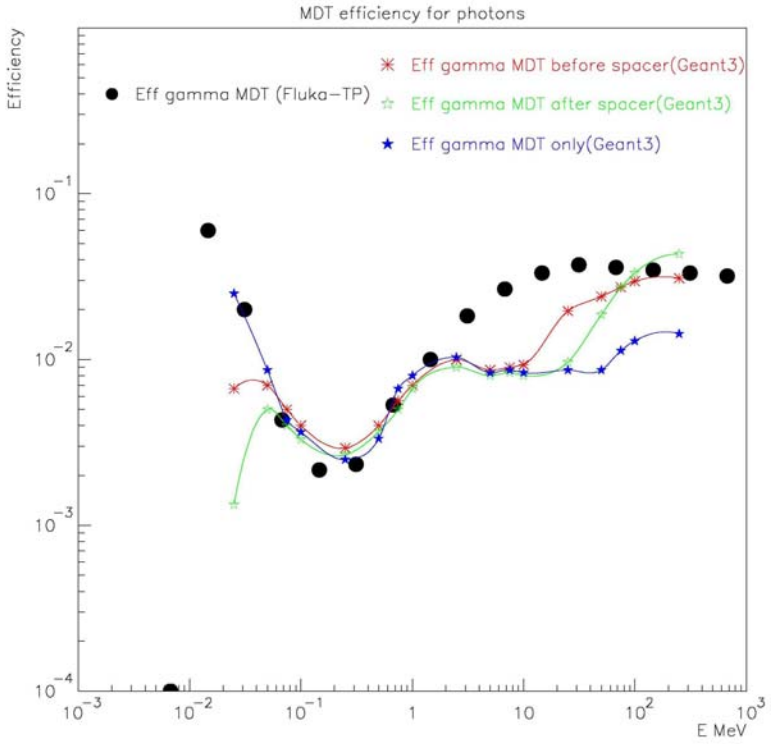

Figure 6.16 Efficiency for photons in MDT chambers as calculated with Geant3 (coloured stars) and as calculated with FLUKA for the MDT TP design (black circles).

It has been calculated with the setup presented in Figure 6.4 for photons incident at 45°. The efficiency below 100 keV is due to photo-electric effect in the gas, while the raising curve in the 1 MeV region is due to Compton scattering in the tube wall [62]. Around 10 MeV, pair production becomes important and interactions in the material surrounding the chamber do play a role. The efficiency curve calculated with FLUKA for the TP design is also shown. The calculation was done for an isotropic photon flux and for a set of three MDTs without the surrounding RPCs and chambers support. The curves are similar in the region where Compton scattering in the wall dominates. At low energy differences can be expected due to the different gas composition and sensitivity to surrounding material. At high energies, the latter has also an influence.

The single plane efficiency for RPC is shown in Figure 6.17. Photon absorption is relatively less important in this case.

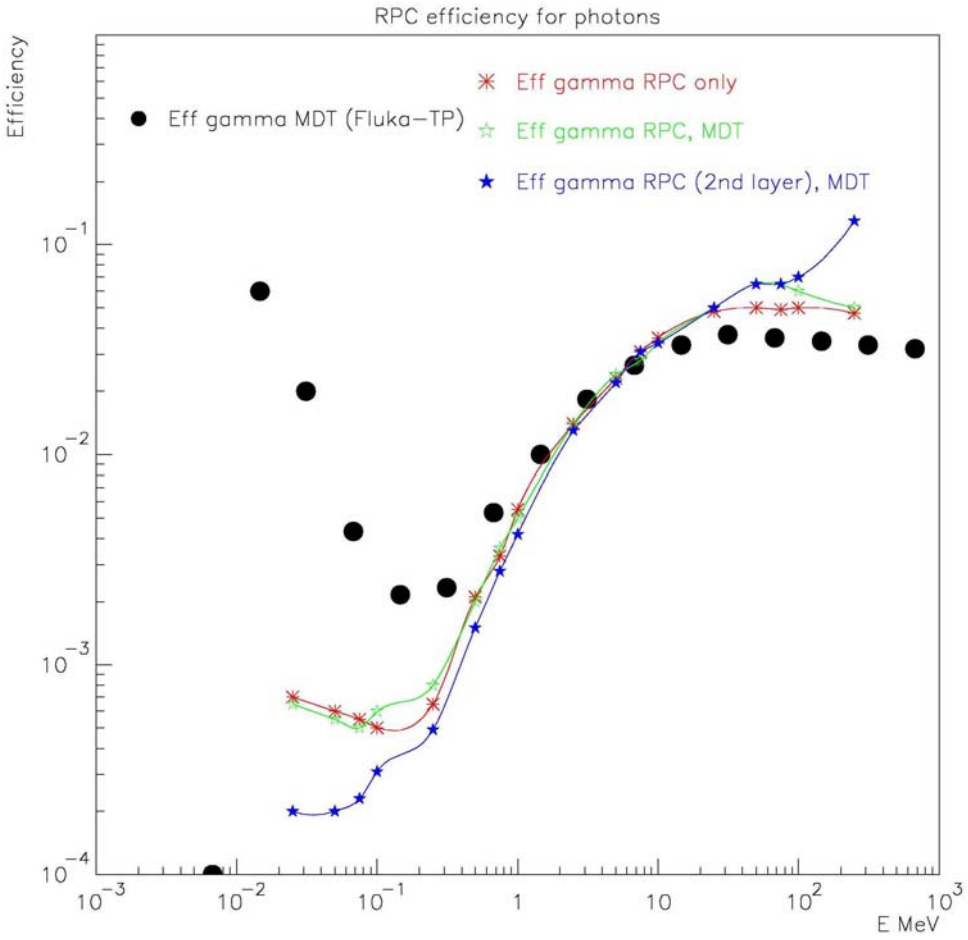

Figure 6.17 Single plane efficiency for photons in RPC chambers as calculated with Geant 3.

The efficiency for firing a single plane in a TGC triplet is shown in Figure 6.18. The efficiency has been measured experimentally with collimated sources of photons impinging perpendicularly to the chamber surface. The energy range covered was 20 keV to 1.8 MeV [63]. The Geant3 simulated efficiency is in quite good agreement with the experimental data. The experimental efficiencies have been simulated using EGS4. The data are well reproduced. The simulation shows that the G-10 plates are the dominant source of interaction.

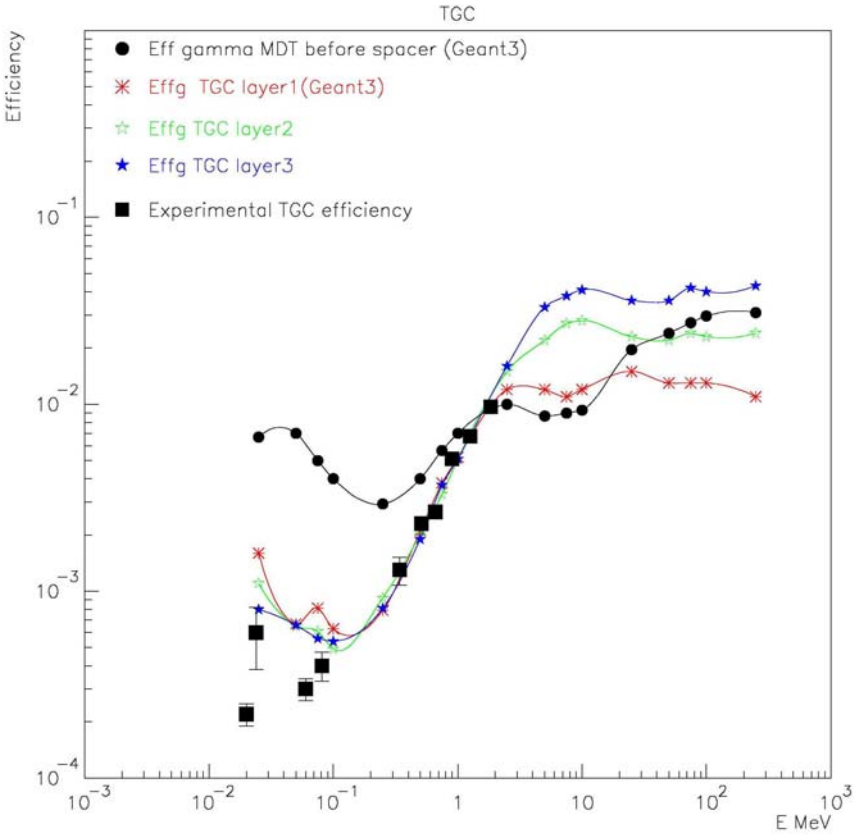

Figure 6.18 Efficiency for firing a single plane in a TGC triplet as simulated with Geant3. Experimental data are also represented [63].

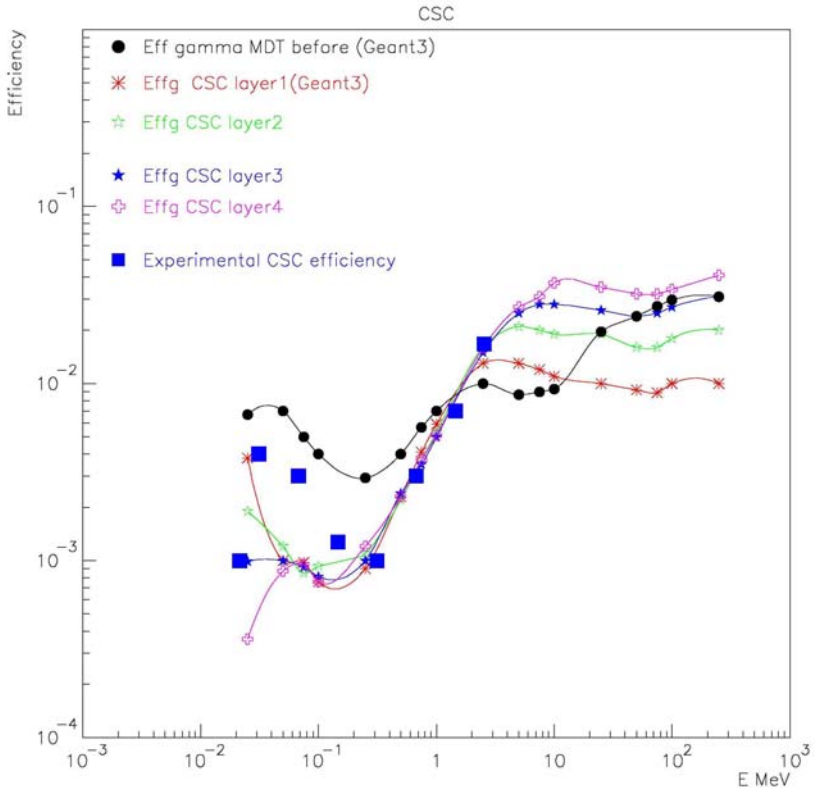

Figure 6.19 Efficiency for firing one the CSC plane. Experimental values are also available [60].

The efficiency for CSC is shown in Figure 6.19. Experimental data are available for the GEM CSC prototype filled with a gas mixture of 30%Ar, 50%CO_2, 20%CF_4 [60]. Good agreement is seen in the region dominated by Compton effect. Differences in the details of the chambers geometry and in the gas used in the simulation and in the experiment may explain the higher experimental efficiency below 100 keV.

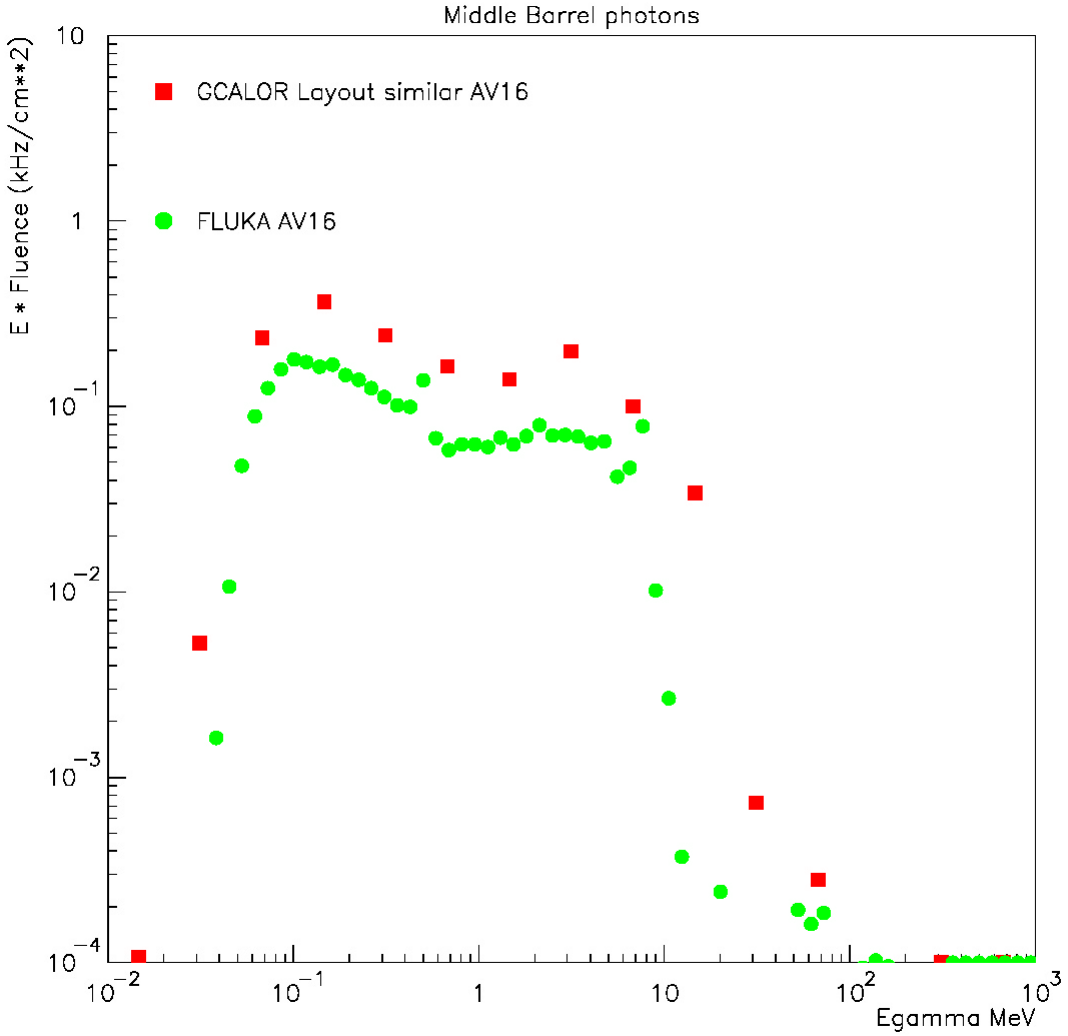

Figure 6.20 Photon energy spectrum in the middle barrel region as predicted by GCALOR (full squares) and FLUKA (full dots) for a similar geometry layout. The vertical scale provides absolute rates. The horizontal scales is logarithmic: 1 bin in Gcalor is equivalent to about 4 bins in Fluka.

The photon spectrum in the middle barrel region as predicted by GCALOR and FLUKA are shown in Figure 6.20. Apart from the difference in normalization, some difference in the shapes is observed in the region above 10 MeV.

The average MDT and RPC photon efficiency have been calculated with the GCalor energy spectrum and the AV16 FLUKA spectrum by folding the spectra with the efficiency. The RPC single plane efficiency folded spectra are shown in Figure 6.21.

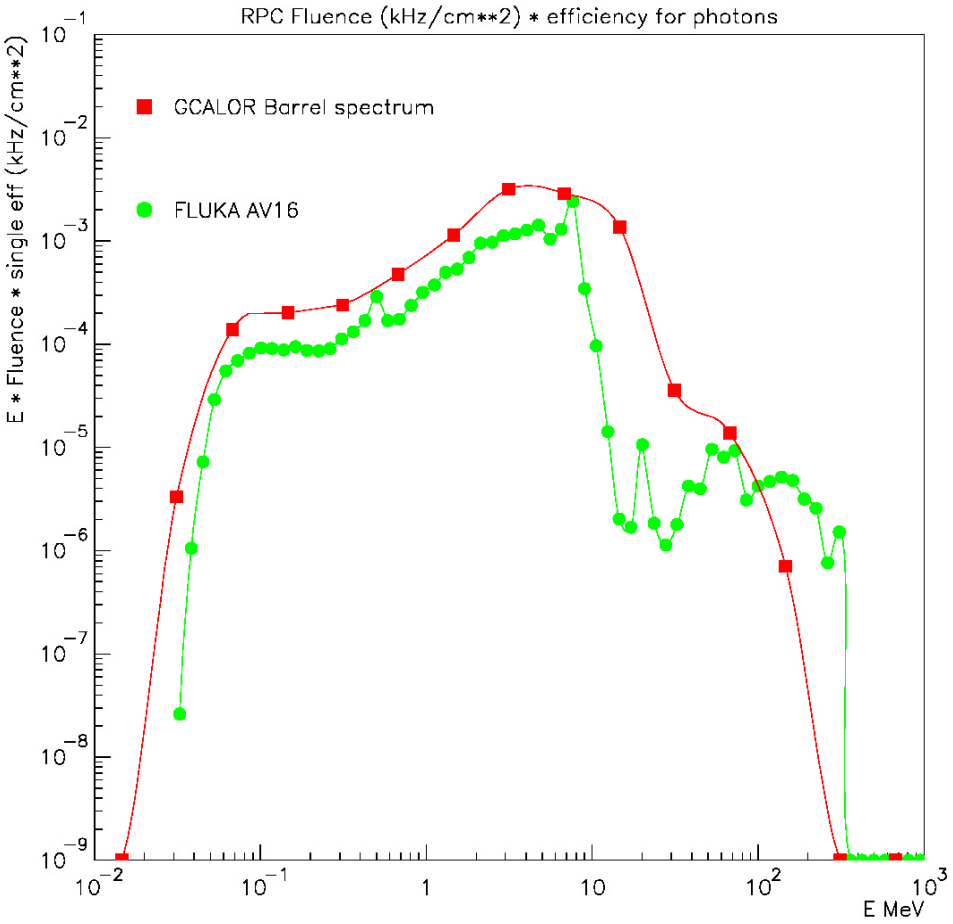

Figure 6.21 Photon energy spectra folded with the efficiency for firing a single RPC plane

The results are given in Table 6.5 for RPC and MDT.

	Average MDT single plane efficiency	Average RPC single plane efficiency
Middle Barrel Gcalor spectrum ⊗ G3 sensitivity	0.0050	0.0054
Middle Barrel Gcalor spectrum ⊗ old FLUKA sensitivity	0.0081	
Middle Barrel AV16 FLUKA spectr. ⊗ G3 sensitivity	0.0055	0.0065
Middle Barrel AV16 FLUKA spectr. ⊗old FLUKA sensitivity	0.0068	
Endcap Middle Station Gcalor spect. ⊗ G3 sensitivity : high η – low η	0.0047 – 0.0052	
Endcap Middle Station FLUKA sp. ⊗ G3 sensitivity : high η – low η	0.0057 – 0.0056	

Table 6.5 Average single plane MDT and RPC efficiencies folding the photon energy spectra with the Geant3 efficiency calculation and the old FLUKA calculation done at the time of the TP.

The average efficiency obtained when fitting the Geant3 photon spectrum with the new Geant3 efficiency function is 40% lower than when fitting with the Fluka TP efficiency function. The difference arises from the energy range above a few MeV. In order to obtain a more precise estimate of the efficiency in that energy range, a simulation with the fully detailed geometry and performed with the correct angular and spatial distribution of photons for each set of chambers would be required. On the other hand, the sensitivity to the shape of the spectrum is only about 20%. All the values given in Table 6.5 indicate values consistent with or somewhat lower than the ones used so far by the Muon System for their rate estimates (see Table 6.1). The uncertainty in the new estimates of chamber efficiency is also within the factor 1.5 used until now. Integrated fluences in the barrel are typically 1 kHz/cm^2 at high luminosity, hence counting rates of the order of 5 Hz/cm^2 are expected.

6.2.3.2 Efficiency for firing a doublet and satisfying the low p_T trigger criteria

An important characteristic of the RPCs is the probability for a photon to fire a couple of planes inside a station. So far it was assumed that 10% of the photons would be able to satisfy the coincidence. The efficiency for satisfying the coincidence has been calculated: the coincidence window is 3 strips, (-1,0,+1) in strip number. An isotropic angular photon distribution has been assumed which is, in good approximation, the case for the barrel region (see Figure 6.24). An example of a photon that produces an electron by Compton scattering that in turn produces a signal in a couple of plane is shown on the left of Figure 6.23. Figure 6.22 shows the probability that a photon fires two planes as a function of the energy of the photon. It is a sharply raising curve around a few MeV.

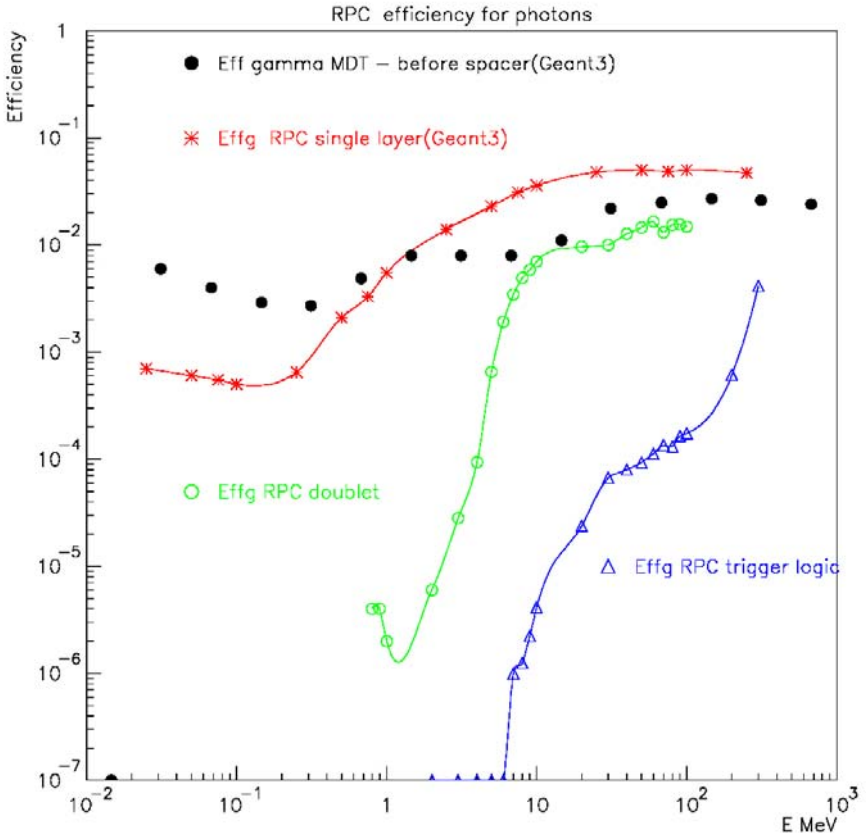

Figure 6.22 Gamma efficiency for RPC: stars for a single layer, open circles for firing a doublet, open triangles for fulfilling the trigger logic. The single plane efficiency of TP MDT is given for comparison (full dots).

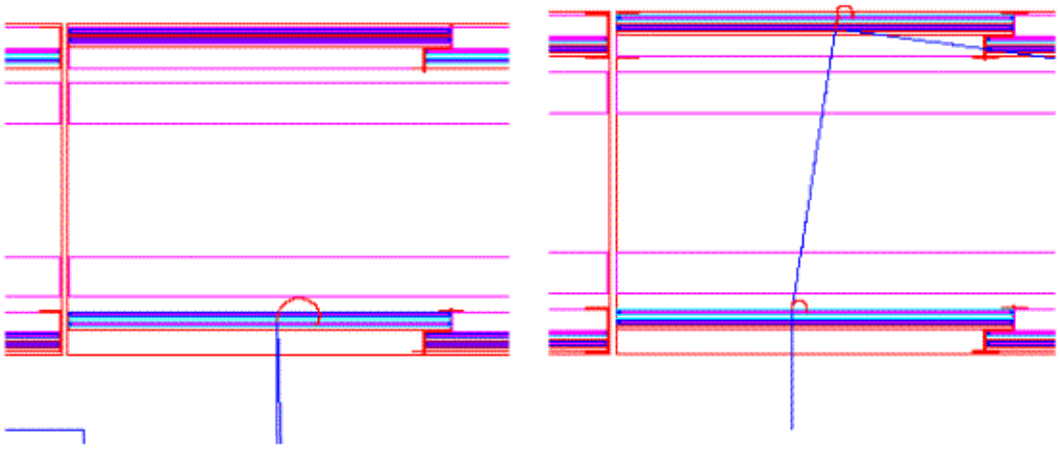

Figure 6.23 Example of 10 MeV photon that triggers two planes (left) and 3 planes (right).

The probability that the photon interaction fulfils the muon trigger logic in the eta projection is also shown in the figure. At these energies, the photons mainly undergo Compton scattering, producing sometime energetic electrons able to cross two planes. But, in addition, the scattered photon may continue, unhampered by the magnetic field, reach the next station and produce a second electron. An example of such an event is given in the right handside of Figure 6.23. That effect (called hereafter "Double-Compton") has not been so far considered in the trigger rate estimates. A critical element is the angular distribution of the photons that has to be taken into account.

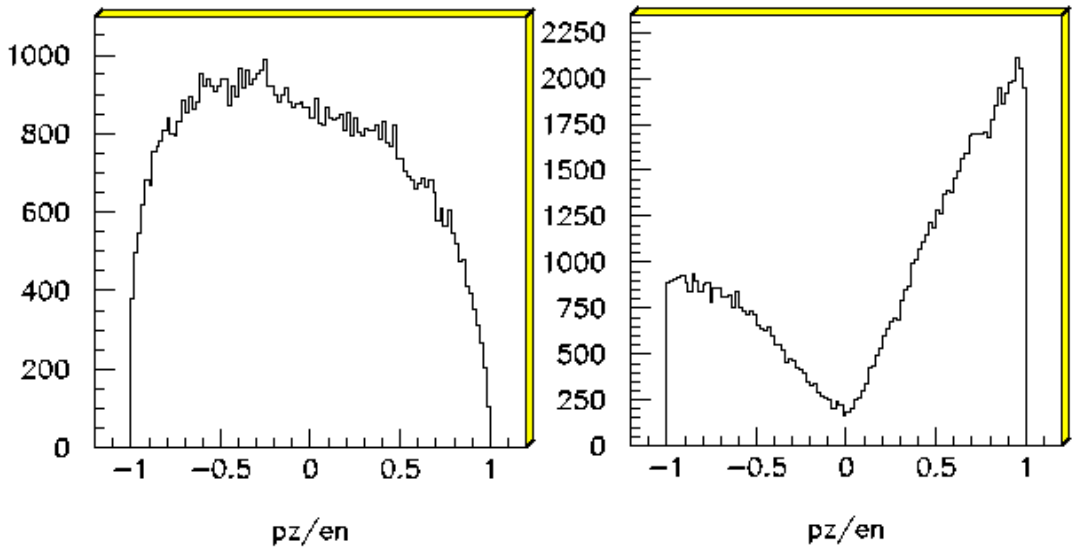

Figure 6.24 Component of the photon momentum along the Z axis in the barrel region (left) and in the endcap region (right).

The photons are very isotropic in the barrel but less so in the forward TGC region, as shown in Figure 6.24. About ¾ of the photons enter the TGC from the side on the interaction point. The detailed simulation of the full trigger logic has been included in the Geant3 simulation. The criteria that have to be fulfilled are: at least 3 out of 4 RPC hits; for a RPC station with both RPC fired require that the difference in the strip number is -1, 0 or +1; impose that abs(z_1-$z_4 \times y_1/y_4$)<15cm for the eta-view and abs(x_1-$x_4 \times y_1/y_4$)<7cm for the phi view where the index 1 refers to the inner most RPC and 4 to the outermost RPC surrounding the middle MDT chambers. The efficiency curves are shown in Figure 6.22. A relevant feature of the doublet and trigger efficiency curve is the very fast raising edge that overlaps with the end-point of the photon energy spectrum. Let's first consider the case of RPC in the barrel. The energy spectra of

Figure 6.20 have been folded with the efficiency for firing a doublet of RPC. The result is shown in Figure 6.25.

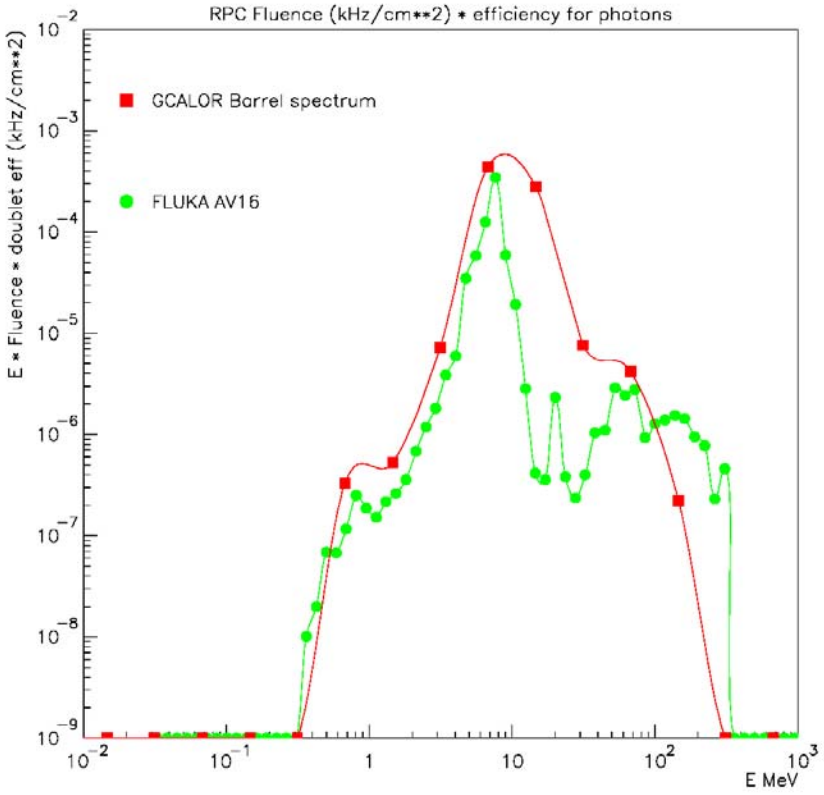

Figure 6.25 Folded photon energy spectra with the efficiency for firing a doublet.

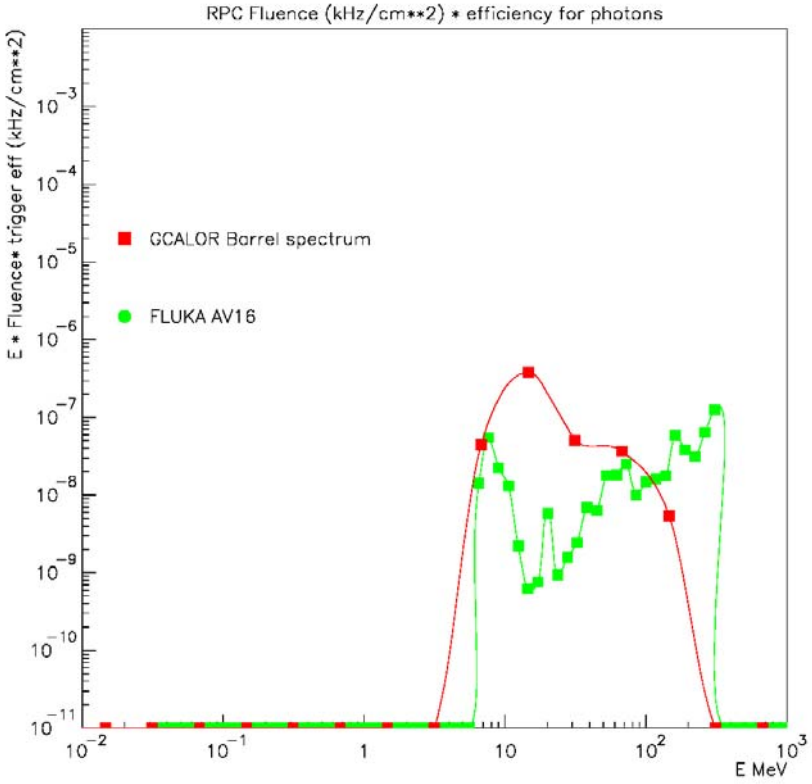

Figure 6.26 Folded energy spectra with RPC trigger efficiency.

The result of folding with the trigger efficiency curve is shown in Figure 6.26. Table 6.6 summarizes the efficiencies and expected counting rates.

		Average efficiency	Counting rate at low luminosity
Single plane	GCalor	$6.5\ 10^{-3}$	0.7 - 1 Hz/cm^2
	FLUKA	$5.4\ 10^{-3}$	1.2 - 2.2 Hz/cm^2
Doublet	GCalor	$5.0\ 10^{-4}$	5 - 7 10^{-2} Hz/cm^2
	FLUKA	2.210^{-4}	5 – 9 10^{-2} Hz/cm^2
Low p_T Trigger	GCalor	$3.5\ 10^{-7}$	340-490 Hz (barrel)
	FLUKA	$1.9\ 10^{-7}$	420-790 Hz (barrel)

Table 6.6 Averaged efficiency for firing a single RPC plane, a doublet of RPC and fulfilling the low p_T trigger logic in the barrel. Counting rate are given for low luminosity for GCALOR Jan03 baseline and FLUKA AV16. The range in rates corresponds to low and high Z, respectively. The counting rates for the barrel are calculated for a surface of 10^7 cm^2.

While the single plane efficiency obtained by folding with the GCalor and FLUKA energy spectra agree at the level of 20%, the doublet and trigger efficiency differ by a factor 2. This is a consequence of the difference in the shape of the high energy photon spectra between GCalor and FLUKA. Comparisons between transport programs (see section 7.2) have shown larger differences in the flux above 20 MeV, typically a factor 5, reflecting the fact that experimental data for benchmarking of the transport programs are scarcer at high energy. Table 6.8 summarizes the efficiencies and expected counting rates.

We turn now to the case of the TGC. Examples of photons firing 3 out 4 planes in a TGC doublet and fulfilling the full endcap trigger logic are shown in Figure 6.27.

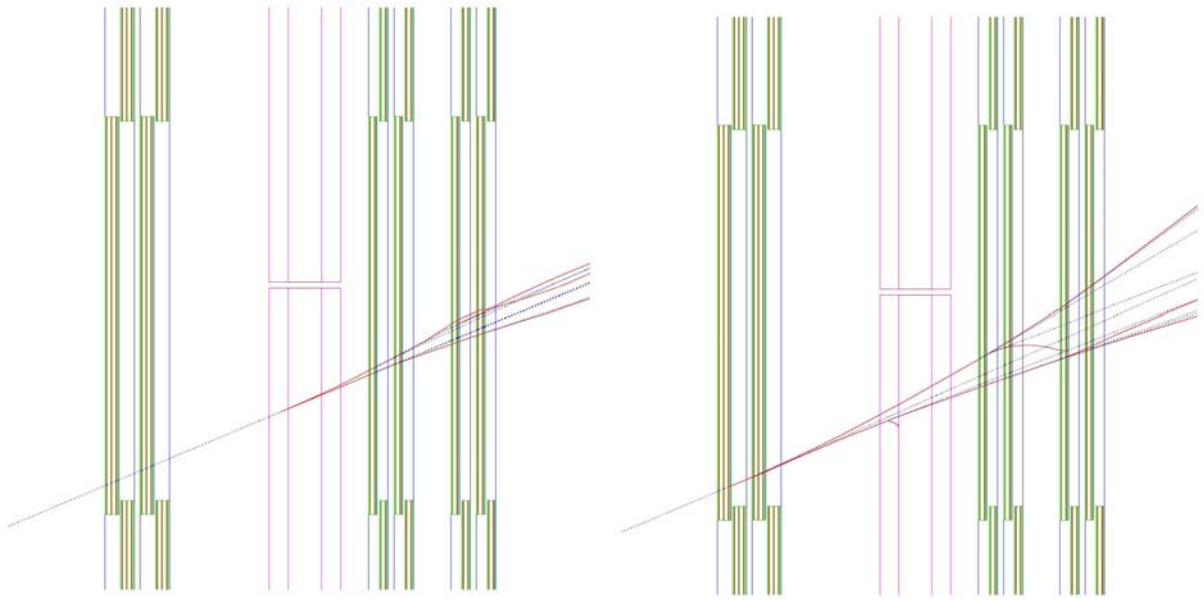

Figure 6.27 Example of 200 MeV photon that triggers 3 out of 4 planes (left) and the full trigger logic 3-out-4 and 2-out-3 (right).

The various efficiency curves for the TGC triplet and the two TGC doublets, estimated with the correct angular distribution, are shown in Figure 6.28 . The probability of firing 3 out of 4 planes in a TGC doublet is about an order of magnitude higher than in a RPC doublet, due to the different angular distribution of the photons and the lower magnetic field. It should be noted that

the size of the coincidence windows that was used in the simulation is wider than the nominal trigger window sizes. Table 6.7 summarizes the window definitions foreseen for the trigger and the values used in the simulation.

	Window Size	Low Luminosity	High Luminosity	Simulation
3-out-4 coincidence	abs(r4-r1*z4/z1) radial-view abs(r4-r1*z4/z1) phi-view	< 5 cm < 3 cm	< 1.7 cm < 2.0 cm	< 10 cm < 6 cm
2-out-3	abs(r3-r1*z3/z1) radial-view abs(r3-r1*z3/z1) phi-view		< 4 cm < 2.0 cm	< 10 cm < 6 cm

Table 6.7 Window size in the endcap for low and high luminosity. The column labelled simulation gives the window size that was used for the efficiency calculation reported here.

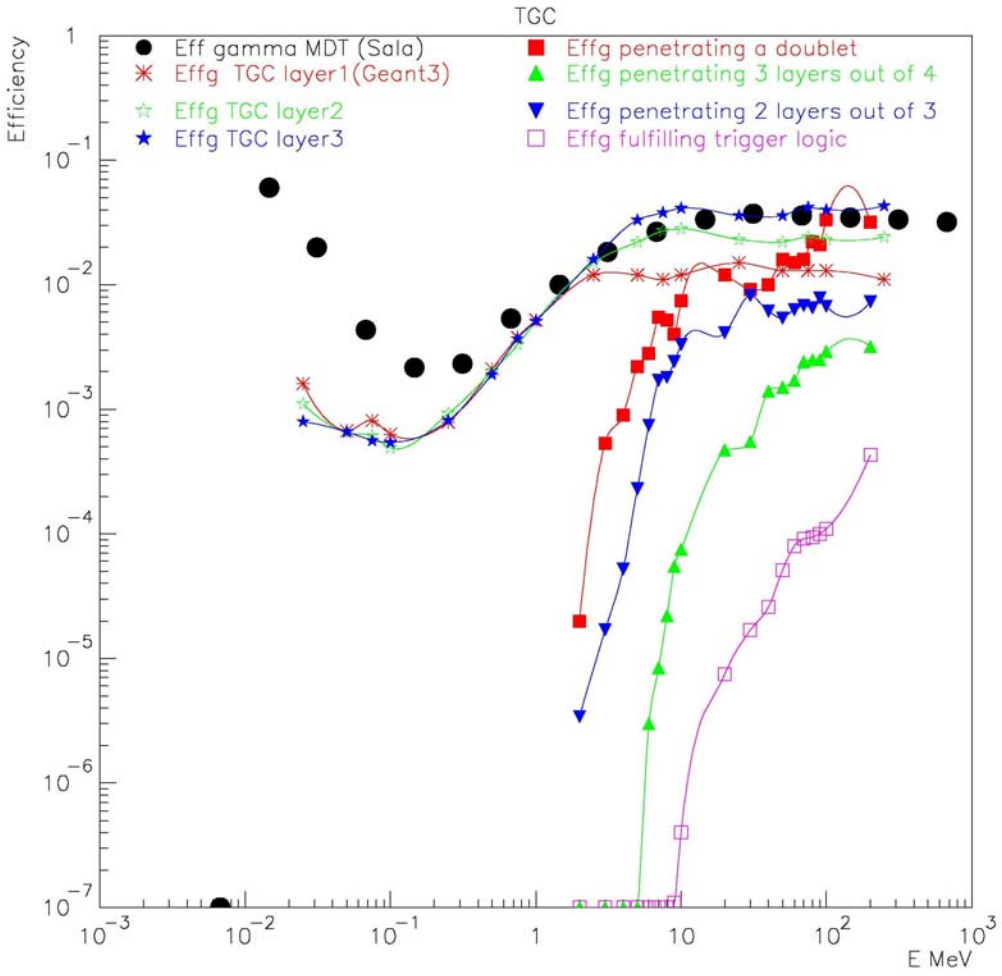

Figure 6.28 Efficiency for firing various combinations of planes in the TGC triplet and the two doublets.

When the full endcap trigger logic is applied (a coincidence of 3 out of 4 in a doublet with 2 out of 3 in a triplet with window size definition as given in Table 6.7), the efficiency is considerably reduced. Only very energetic photons, with energy larger than 10 MeV, can trigger.

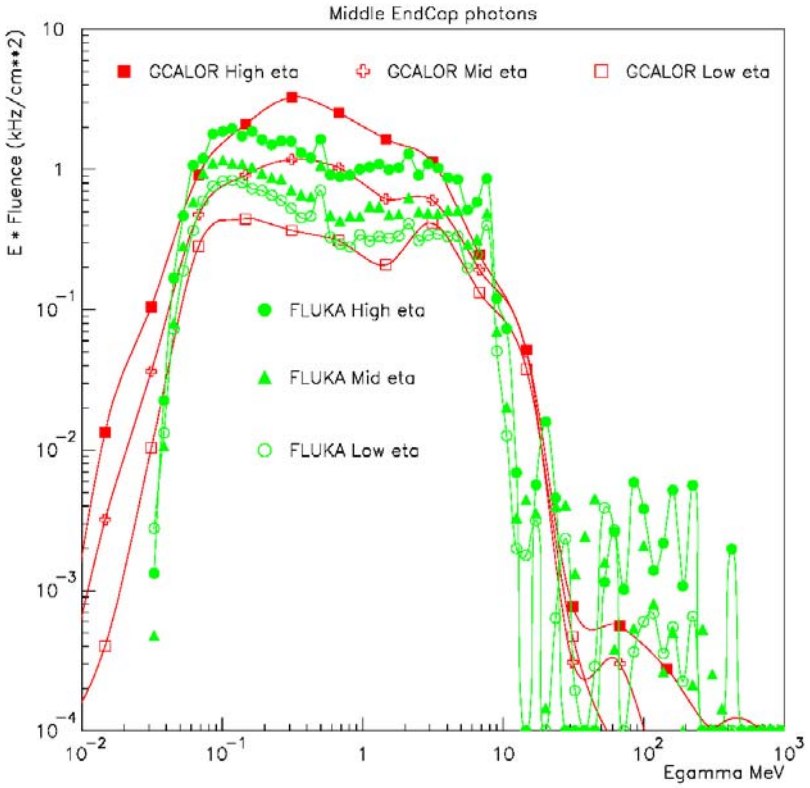

Figure 6.29 The photon energy spectra in the big wheel as predicted by GCalor and FLUKA.

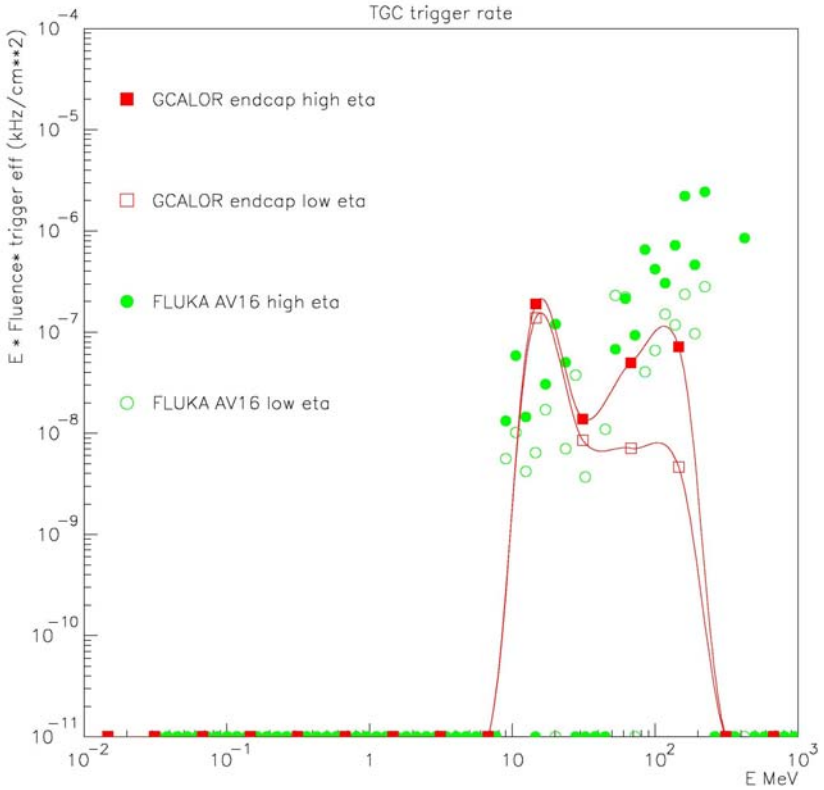

Figure 6.30 GCalor and FLUKA energy spectra folded with the TGC low pT trigger efficiency.

The shape of the energy spectra in the big wheel is shown in Figure 6.29 for GCalor and FLUKA for three regions of pseudorapidity, delimited by radii of 180, 280, 500 (700) and 1000 (1200) cm respectively. The shapes of the distributions are globally similar, however they are relevant differences. FLUKA predicts a sharper edge at 10 MeV, but also predicts a tail of very energetic photons (~100 MeV). This will induce differences in the trigger efficiencies.

	Surface	**Fluences at low luminosity ($10^{33}cm^{-2}s^{-1}$)**	**Fluences at nominal luminosity ($10^{34}cm^{-2}s^{-1}$)**
GCalor	0.13 / 0.54 / 3.66 10^6 cm^2	1.13 / .45 / .17 kHz/cm^2	11.3 / 4.5 / 1.7 kHz/cm^2
FLUKA		.81 / .44 / .32 kHz/cm^2	8.1 / 4.4 / 3.2 kHz/cm^2
	Average efficiency	**Counting rate at low luminosity**	**Counting rate at nominal luminosity**
Single plane GCalor	4.4 / 5.1 / 6.7 10^{-3}	5.0 / 2.3 / 1.1 Hz/cm^2	50 / 23 / 11 Hz/cm^2
FLUKA	5.7 / 5.5 / 5.5 10^{-3}	4.6 / 2.4 / 1.8 Hz/cm^2	46 / 24 / 18 Hz/cm^2
Doublet GCalor	2.0 / 3.5 / 5.7 10^{-4}		
FLUKA	3.7 / 3.6 / 3.8 10^{-4}		
3-out-4 GCalor **Low p_T Trigger**	1.2 / 2.4 / 4.0 10^{-6}	0.35/1.17/4.98 kHz total 6.5 kHz summing the 2 endcaps	
FLUKA	3.5 / 2.6 / 2.6 10^{-6}	0.74/1.24/6.09 kHz total 8.1 kHz summing the 2 endcaps	
2-out-3 Gcalor	4.9 / 9.5 / 16.0 10^{-5}		
FLUKA	9.6 / 9.5 / 10.0 10^{-5}		
High p_T Trigger GCalor	2.7 / 4.4 / 7.2 10^{-8}		80 / 214 / 896 Hz total 1190 Hz summing the 2 endcaps
FLUKA	2.2 / 0.9 / 1.0 10^{-7}		466/ 428 / 2342 Hz total 3236 Hz summing the 2 endcaps

Table 6.8 Efficiencies for firing TGCs in the big wheel: values are given for high/mid/low η regions. Low and High p_T trigger rates are quoted. The window size used in the simulation (see Table 6.7) is larger than the size foreseen at the experiment. Hence rates quoted here are overestimated.

Folding the photon spectra with the low pT endcap trigger efficiency, results in the distributions shown in Figure 6.30. The contribution comes mainly from the very energetic photons. The statistics available in the simulation for these energetic photons is not large. GCalor for example has an associated statistical error per bin of the order of 30%. In addition, as already pointed out, the two programs differ more in their prediction in that region. FLUKA predicts about a factor 10 more 100 MeV photons than GCalor. The resulting average efficiencies for the various coincidences and the corresponding counting rates are given in Table 6.8.

6.2.4 Efficiency for charged hadrons

Protons (and pions) are rather energetic, having energies above 20 MeV. They fire a plane or a couple of RPC planes with 100% probability. As we have seen in section 6.2.2 on neutron efficiency, the protons are produced mainly by interaction of energetic neutrons in the material and hence their rate may vary locally (see Figure 6.8). We have seen also that one of the important sources of protons are the endcap toroid coils that are exposed to a flux of hard neutrons. It is not the case for the barrel coils where the neutron energy spectrum is softer. This was verified by some GCalor dedicated simulation [64]. In the new calculations presented in this report, with the improved neutral kaon transport, protons are the most relevant hadron flux while pions are negligible (see Table 5.8).
The efficiency for protons to fullfil the low pT trigger has been studied in the past by S.Robins [65]. The efficiency was calculated with Geant3 and the trigger simulation program ATRIG and with a standalone trigger simulation program. The results are shown in Table 6.9. As will be seen in section 6.2.6, the contribution of the protons will turn out to be one of the dominant factors and deserves to be thoroughly revisited.

	ATRIG	Standalone
Barrel low pT trigger	$1.2\ 10^{-2}$	$1.2\ 10^{-2}$
Endcap low pT trigger	$1.7\ 10^{-2}$	$3.4\ 10^{-2}$

Table 6.9 Probability for protons to fulfil the low PT trigger.

6.2.5 Efficiency for electrons and the effect of the muon chambers material

A study of the effect of the Muon Chambers material was carried out with FLUKA. In the case of electrons, most of the $e^{\pm}$ background is produced locally in the muon chamber material, and is therefore accounted for in the photon sensitivity functions. This point was studied in detail with FLUKA comparing simulations with and without the inclusion of the muon chamber material in the setup. A simplified muon chamber description is used in the simulation, as shown in Figure 4.18. The chamber material is approximated by low density aluminum (0.09 gr/cm^2) uniformely distributes in the chamber volume and adjusted such that the approximate radiation and interaction lengths are reproduced.

Inspection of Figure 6.31 shows that the toroid field is clearly acting as a shield to the electrons generated outside the magnetic field regions while the low energy electrons (~MeV) produced inside the toroid field are presumably trapped loopers. The effect of introducing chamber material in the inner and middle barrel regions is very clear, with many more interactions being generated. This suggests that the $e^{\pm}$ are predominantly produced locally in these regions. However, in the forward regions there is less difference between $e^{\pm}$ fluences with and without the chamber material.

Table 6.10 shows the ratios of fluences and currents across the scoring surfaces given in Figure 4.18. Ratios for $e^{\pm}$ are only given for the outer barrel and forward positions where significant $e^{\pm}$ statistics exist in the no material case. One observes that:

- The chamber material dominates the production in the first and second barrel chambers but not in the third

- Significant changes are seen in "2nd-forward" region where the chamber material clearly contributes to photons and $e^{\pm}$ production, but does not dominate.

- Ratios obtained for 1st-forward indicate photons and $e^{\pm}$ production decreases with introduction of chamber material which suggests some shielding effects.

- 10-15% increase in neutron fluences due to interactions in chamber material in most regions (but no change in outer barrel and outer forward).

What is relevant for the trigger is the fraction of electrons that is able to fire a RPC or a TGC doublet. Figure 6.32 shows that probability as a function of the electron energy as simulated with Geant3. One sees that the onset of the curve is at about 5 MeV reaching a maximum around 10 MeV. The column on the right in Table 6.10 gives the fraction of $e^{\pm}$ with energies greater than 5 MeV. This was used in the past as an approximate method to estimate which fraction of the electron flux should be consired as capable of firing a doublet and this is presumably where the 0.25 factor has been obtained. From the new calculation it can be seen that in the barrel region typically only 10% of electrons have energies > 5 MeV, and in the forward region some 10% to 20%.

	av16-no-material/av16-default			av16-default
Position	Neutrons	γ	e^{+-}	$e^{+-} > 5$ MeV
Barrel				
1st,low-z	0.91	1.03	–	0.16
1st,high-z	0.86	1.02	–	0.10
2nd,low-z	0.91	0.92	–	0.09
2nd,high-z	0.89	0.82	–	0.10
3rd,low-z	1.00	1.07	0.91	0.06
3rd,high-z	0.98	0.97	0.83	0.06
Forward				
1st,low-eta	0.95	1.12	1.55	0.12
1st,mid-eta	0.90	1.02	1.20	0.09
1st,high-eta	0.88	0.96	1.10	0.09
2nd,low-eta	0.94	0.82	0.44	0.12
2nd,mid-eta	0.85	0.80	0.67	0.17
2nd,high-eta	0.85	0.82	0.75	0.21
3rd,low-eta	1.00	1.00	0.86	0.10
3rd,mid-eta	0.99	1.02	1.07	0.15
3rd,high-eta	1.00	0.97	0.91	0.13

Table 6.10 Neutron, photon and $e^{\pm}$ ratios obtained by removing muon chamber material and comparing to default av16 FLUKA geometry. Also given in final column is fraction of electrons with energy >5MeV, obtained from AV16 geometry.

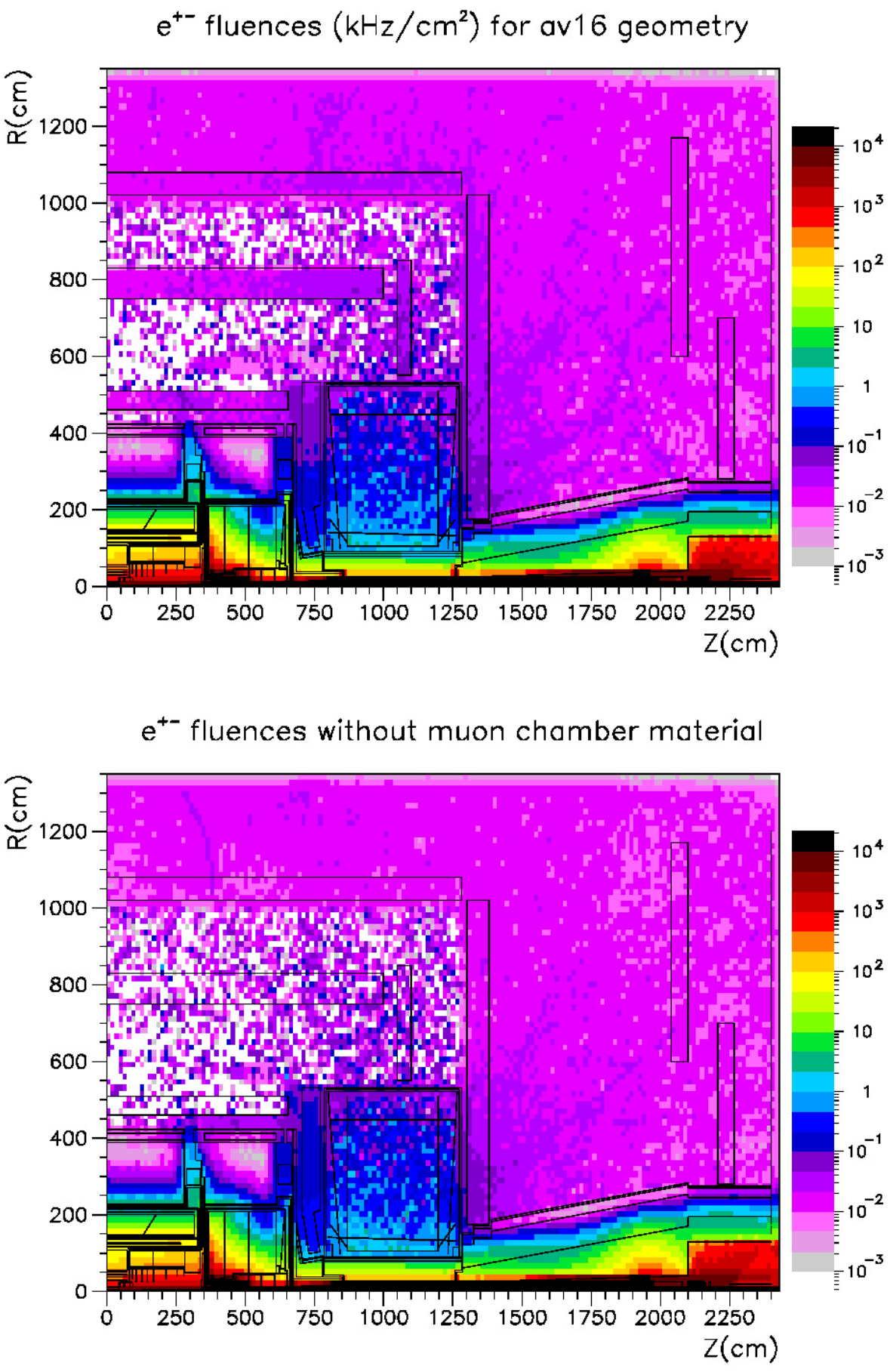

Figure 6.31 Electron fluences with and without muon chamber material

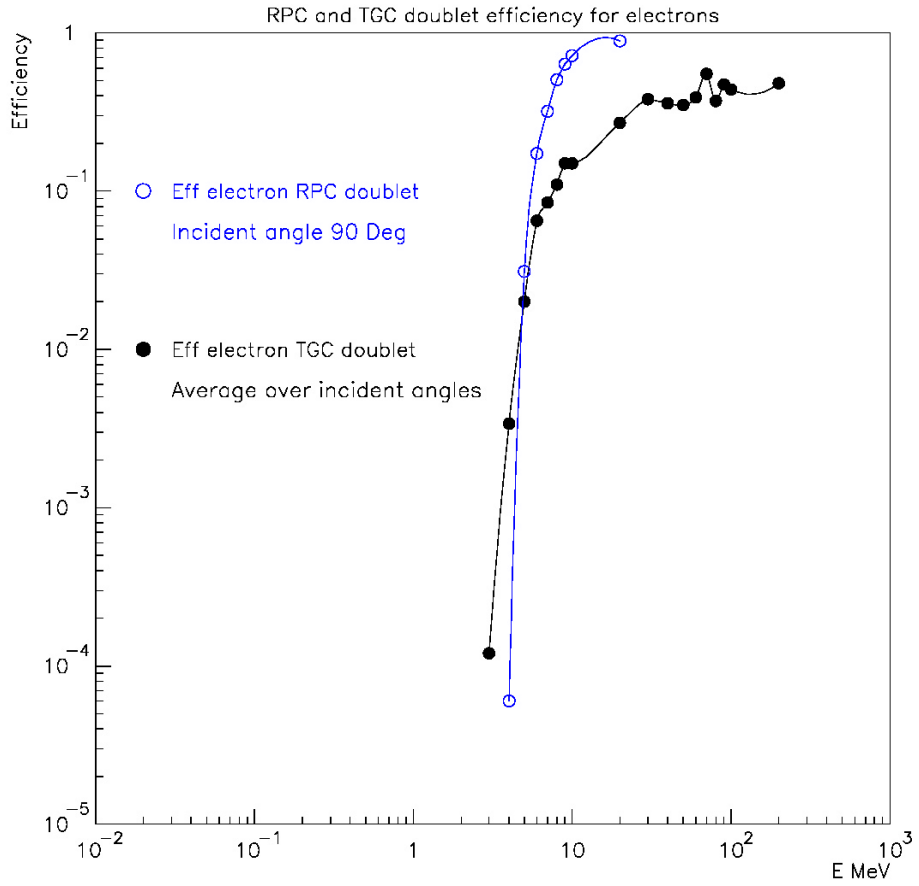

Figure 6.32 Probability for an electron to fire a RPC doublet and to fire a TGC doublet.

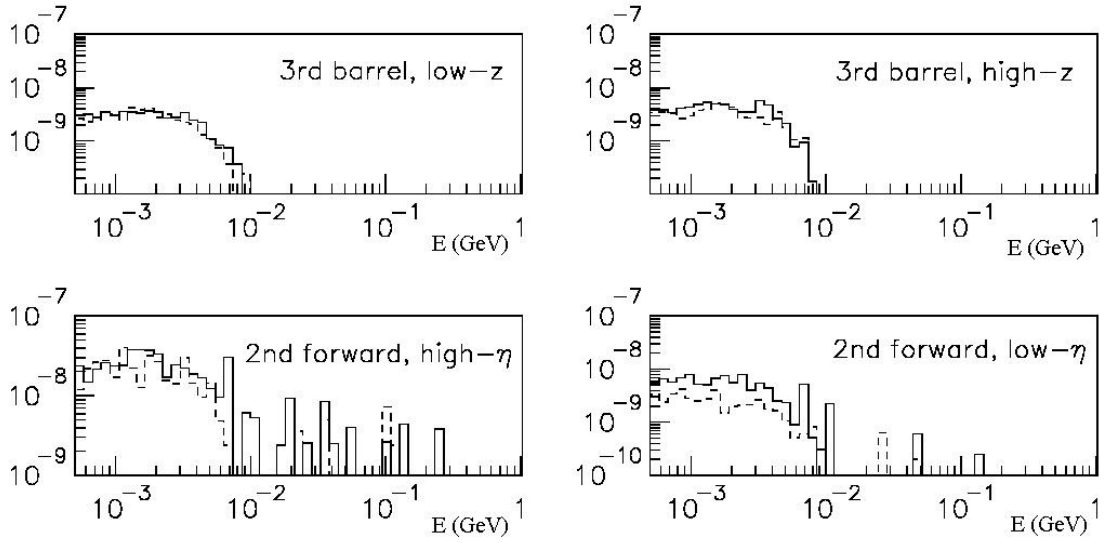

Figure 6.33 Electron spectra with chamber material (full line) and without (dashed line) in the barrel (top) and the big wheel (bottom).

From the new simulation, we see that we can use 5% of the electron flux in the barrel and 10 % in the endcap instead of 25% as done in the past. This is very conservative because of double counting. In the case of the middle barrel chambers, most of the electrons are produced in the chamber material and hence are accounted for already in the efficiency for photons to fire a doublet. In the endcap, only about half of the electrons are produced locally. However, the

inspection of the high energy component of the electron spectrum in Figure 6.33 shows that it is predominantly produced in the chamber.

6.2.6 Summary of studies of effect of radiation and uncertainties

The impact of radiation background on the muon system has been systematically reviewed. The chamber efficiencies for neutrons, photons and electrons have been calculated for each type of chamber with the detailed Geant3 geometry taking into account the angular distribution of the particles. In general, fluxes are isotropic in the barrel, while in the endcap a substantial fraction of the particles comes from the interaction region or from the main sources of radiations. The average chamber efficiencies have then been obtained by folding the relevant energy dependent efficiency curve with the energy spectra at the various chamber locations. Table 6.11 summarizes all the results.

GCALOR							
	neutron	single-plane photons	double-plane photons	double-compton			fraction of electron rate
				3/4	2/3	3/4*2/3	
MDT (BA)	$3.0\ 10^{-4}$	$5.0\ 10^{-3}$					5%
MDT (EC)	$3.0\ 10^{-4}$	$4.7/5.2\ 10^{-3}$					10%
CSC	$1.2\ 10^{-4}$	$7.4\ 10^{-3}$					10%
RPC	$2.0\ 10^{-4}$	$6.5\ 10^{-3}$	$5.0\ 10^{-4}$	$3.5\ 10^{-7}$			5%
TGC	$5.0\ 10^{-4}$	$4.4/5.1/6.7\ 10^{-3}$	$2.0/3.5/5.7\ 10^{-4}$	$1.2/2.4/4.0\ 10^{-6}$ (**)	$4.9/9.5/16.\ 10^{-5}$	$2.7/4.4/7.2\ 10^{-8}$ (**)	10%
FLUKA							
	Neutron (*)	single-plane photons	double-plane photons	double-compton			fraction of electron rate
				3/4	2/3	3/4*2/3	
MDT (BA)		$5.5\ 10^{-3}$					5%
MDT (EC)		$5.7/5.6\ 10^{-3}$					10%
CSC		$6.0\ 10^{-3}$					10%
RPC		$5.4\ 10^{-3}$	$2.2\ 10^{-4}$	$1.9\ 10^{-7}$			5%
TGC		$5.7/5.5/5.5\ 10^{-3}$	$3.8/3.6/3.7\ 10^{-4}$	$3.5/2.6/2.6\ 10^{-6}$ (**)	$9.6/9.5/10.\ 10^{-5}$	$22./8.9/10.4\ 10^{-8}$ (**)	10%

(*) Average neutron efficiencies obtained by folding the old TP efficiency with FLUKA spectrum is 50% higher than with GCALOR spectrum

(**) The window size used in the simulation is larger than the size foreseen in the trigger. The efficiency quoted is an upper limit

Table 6.11 Summary of average efficiencies obtained by folding efficiency curves with the GCALOR spectra (top) and the FLUKA spectra (bottom). In the endcap, the values are given for high/mid/low η values, respectively.

Single plane efficiencies, as well as the probability to fulfil the various Level-1 trigger coincidences, have been calculated. The new values for single plane efficiency are in general similar or somewhat lower than previous assumptions. The new estimate of single plane counting rates are given in Table 6.12 and shown in Figure 6.34. They are calculated according to the formula:

$$\text{Single plane global counting rate} = \mathbf{n}\times\varepsilon_n + \gamma\times\varepsilon_\gamma + \boldsymbol{p} + \boldsymbol{\pi} + \boldsymbol{\mu} + \mathbf{f_e}\times\boldsymbol{e}$$

where "**n**" and "**γ**" stand for neutron and photon particle fluences, and "***p***", "***π***", "***μ***" and "***e***" stand for proton, charged pion, muon and electron currents. Fluences are taken from GCALOR Jan03 predictions of Table 5.8 given for the regions shown in Figure 5.14. For charged particle currents are used instead. They are obtained from the GCALOR fluences corrected by the ratio current to fluence calculated by FLUKA (see Table 5.11). ε_n and ε_γ are the efficiencies for firing a single plane for neutron and photon respectively. $\mathbf{f_e}$ represents the fraction of the electron fluence which is not already accounted for in the photon interactions producing a hit in the chamber. The values of these efficiencies are taken from Table 6.11.

	counting rate (Hz/cm^2)		
Muon Barrel	**LowZ**	**MidZ**	**HighZ**
Inner Barrel:			
MDT	8.4	10.4	11.4
Middle Barrel:			
MDT	6.8	7.9	10.8
RPC	8.1 (1.4)	9.3 (2.1)	12.5 (3.4)
Outer Barrel:			
MDT	6.5	8.6	10.1
RPC	7.8 (1.0)	10.2 (1.9)	11.9 (2.3)
Muon Endcap	**OUT**	**MID**	**IN**
Small Wheel Region:			
MDT	23	40	103
TGC			100 (35)
CSC			347
Large Wheel Region:			
MDT	13	32	68
TGC	17 (5)	32 (9)	66 (17)
Back Wheel Region:			
MDT	6	9.	12

Table 6.12 Single plane counting rates at nominal luminosity. Penetrating particle rates are given in parenthesis.

The counting rates in the barrel are of the order of 10-12 Hz/cm^2 both for MDT and RPC. They are dominated by the photon contribution at the level of 75-85% followed by neutron and proton contributions of about 5-10% each. Muons and electrons contribute only a few percents. Pions are negligible except in the inner barrel where, as a result of punchthrough, they account for a few percents of the rate and the muon contribution increases to about 15%. In the CSC, photons only account for about half of the rate while muons account for 30 % and protons for 10%.

If we compare the predicted MDT counting rates with the values quoted in the section on rate environment in the Muon Spectrometer TDR [55], we see that they are similar in all regions except for the Large Wheel "Inner" and "Middle" regions where they have doubled. The region with highest counting rate is still the "Inner" Small Wheel with 100 Hz/cm^2, as it was at the time of the TDR. An overall factor of 5 uncertainty on these rates was estimated, the result of a conservative linear superposition of a factor 1.3 on the p-p cross-section, a factor 2.5 on fluences and 1.5 on single plane efficiencies. All our studies and comparisons with available experimental data have confirmed that these estimates are still valid.

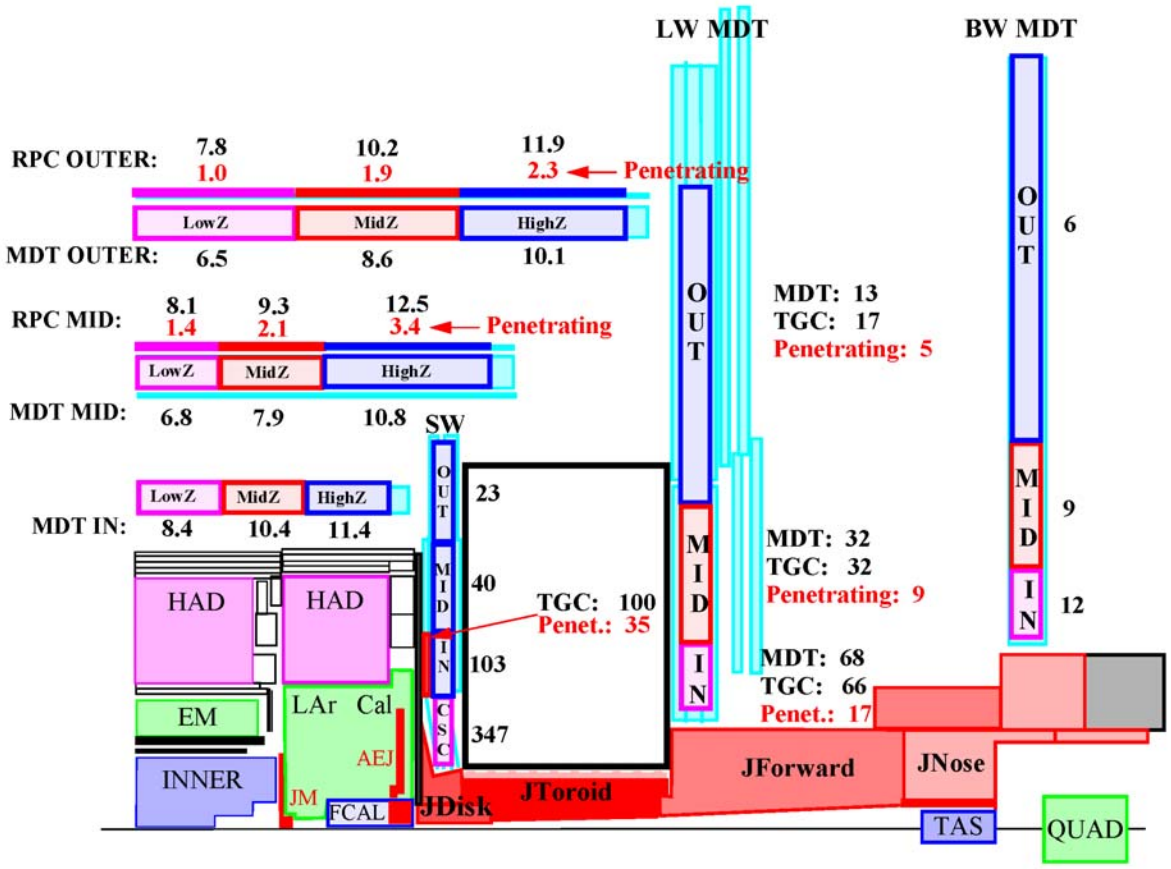

Figure 6.34 Average single plane and penetrating counting rates (Hz/cm^2) at high luminosity in the various scoring regions.

The penetrating particle rate is evaluated as follows:

$$\text{Penetrating counting rate} = f_p\,\gamma^*\varepsilon_\gamma + p + \pi + \mu + f_e\,^*e$$

where "γ" stands for photon fluence, ε_γ is the efficiencies for photons to fire a single plane while f_p gives the fraction of these interactions that result in a coincidence in two adjacent planes. "p", "π", "μ" and "e" stand for proton, charged pion, muon and electron currents and f_e represents the fraction of the electron fluence which is not already accounted for in the photon interactions producing signals in the chambers. So far, in the trigger rate estimates f_p was assigned a value of 10%. Inspection of Table 6.11 shows that the new estimates of this fraction for RPC and TGC range between 4 and 8%. New estimates of penetrating particle rates are given in Table 6.12 and shown in Figure 6.34. Photons and protons account for about 70% of that rate, muons and electrons for the remaining 30%, pions are negligible. We have seen that the uncertainty on f_p is

of the order of a factor 2, due to the sensitivity of the high energy part of the spectrum. However it applies to only 30% of the rate.

"Double-Compton photon scattering", an effect not considered so far, is able to fulfill the 3-out-4 logic in a pair of RPC or TGC doublets and gives a new contribution to the low-p_T trigger rate. In case of the RPC, the trigger logic window sizes in the simulation were adjusted to the real size while for the TGC, they were wider. Hence, the predictions in the endcap should be considered as an upper limit. The uncertainty on these rates is of the order of a factor 3.

Figure 6.35 shows the trigger rate estimates for the low-p_T trigger. Both in the barrel and in the endcap, rates of accidentals are low and applying the factor 5 overall uncertainty still lead to rates well below prompt muon rates. In the barrel, Double-Compton is of the same order as the accidentals. But again, after applying uncertainty factors, the rates are still below prompt muons. In the endcap, Double-Compton dominates over accidentals. As discussed in detail in Section 6.2.3.2, this is an upper limit. Applying the uncertainty factor to that rate brings it close to the prompt muons. It is thus recommended to make a more precise estimate of that effect, although it will likely be acceptable. The contribution of protons to the trigger, based on old efficiency estimates, is of the order of the prompt muons in the barrel and higher in the endcap. It is thus important to try to have a much more precise simulation of that effect. In the case that it would be confirmed that protons may be responsible of high trigger rates, more robust trigger schemes can be implemented as described in detail in [66]. It has been shown that, with the described schemes, the trigger rate induced by the background can be reduced below the physics rate, although at the price of somewhat lower muon trigger efficiency.

Figure 6.36 shows the trigger rate estimates for the high-p_T trigger. Rates of accidentals are low and acceptable, even when applying very conservative uncertainties. In the endcap, an upper limit on the probabibility for photons to fulfill high p_T trigger logic has been evaluated (see Table 6.8). This lead to an upper limit on trigger rates of the order of 1-3 kHz. Since uncertainties on these probabilities are higher (a factor 5-10), it is recommended to make a more precise evaluation.

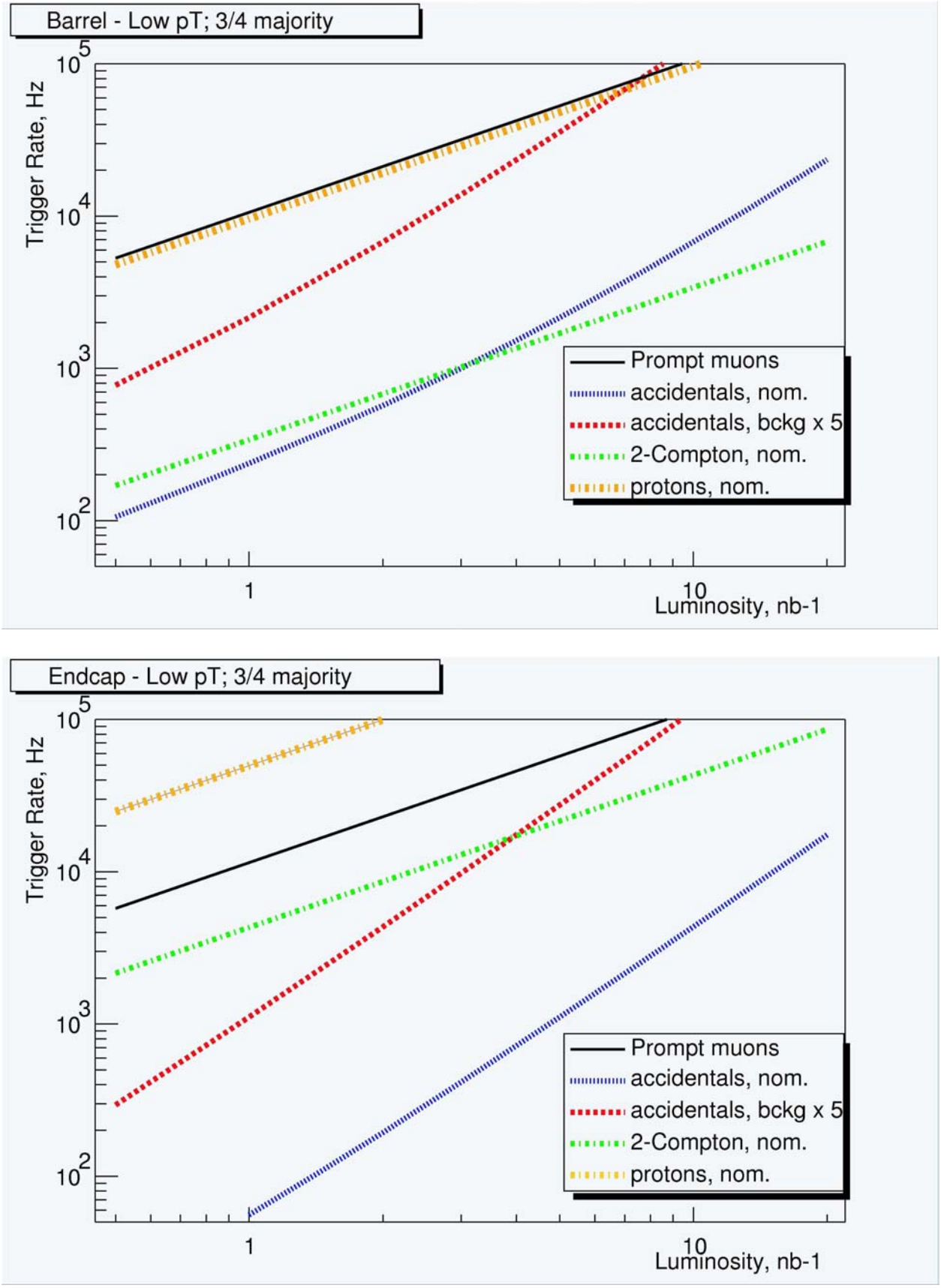

Figure 6.35 Low pT Trigger rates estimates done with the fluxes predicted by Gcalor and with the efficiencies obtained for the Gcalor energy spectra. In the case of charged particles, currents are used instead of fluxes using the flux-to-current conversion factor from Table 5.11.

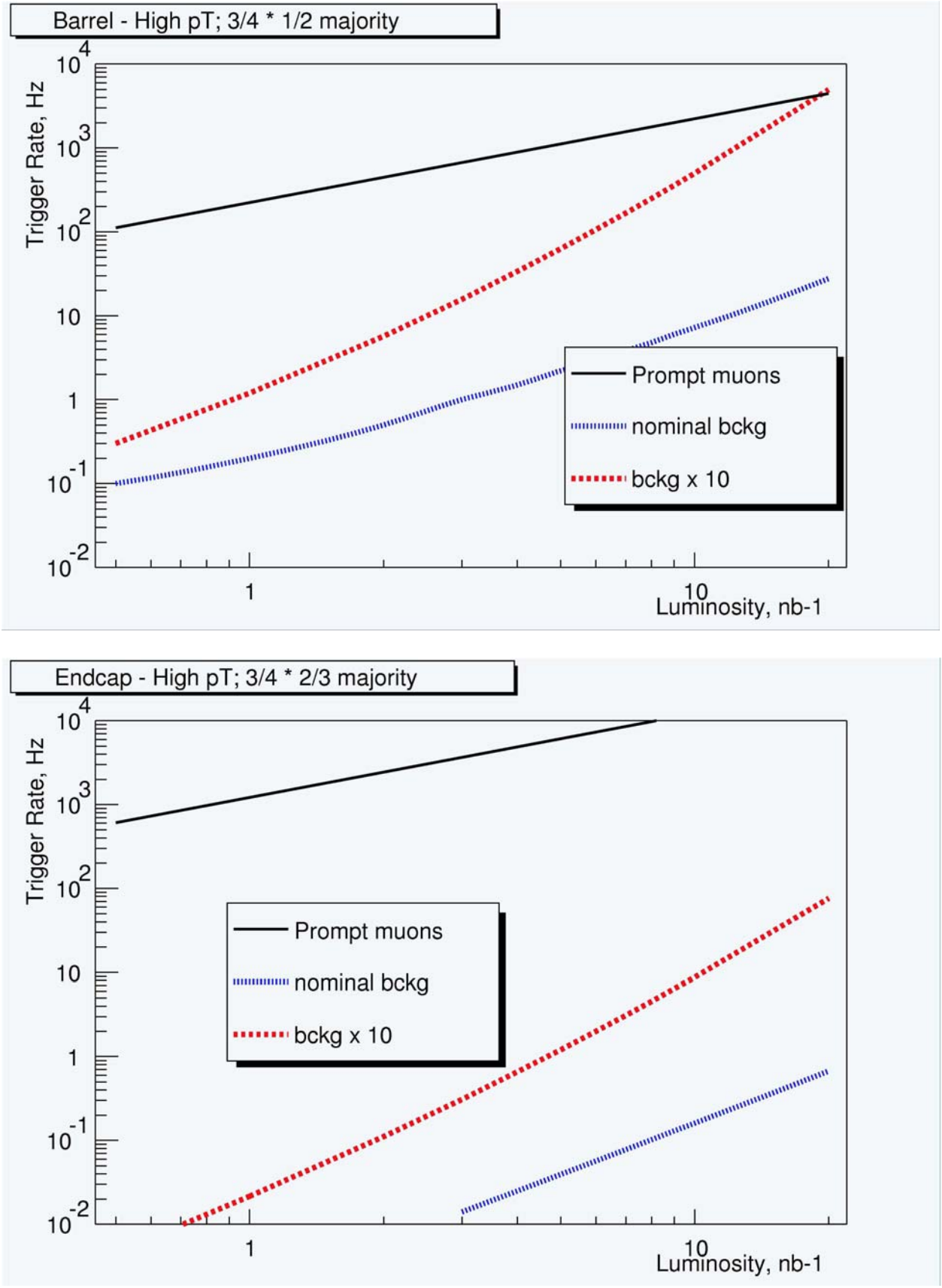

Figure 6.36 High pT Trigger rates estimates done with the fluxes predicted by Gcalor and with the efficiencies obtained for the Gcalor energy spectra. In the case of charged particles, currents are used instead of fluxes using the flux-to-current conversion factor from Table 5.11.

6.3 Review impact on calorimeter

In ATLAS, all calorimeter segments that face the inner detector are Liquid Argon (LArg) technologies. Up to a pseudorapidity of approximately $\eta = \pm 1.7$, these are followed by scintillating tile calorimeters (TileCal), both barrel and endcap. In the remainder of the coverage, up to $\eta = \pm 5.0$, the calorimeter is Liquid Argon only (see Figure 2.1). In all regions of the calorimeter one must consider the possibility that radiation could degrade the calorimeter's sensitive elements (electrode structures or scintillating tiles) or signal readout systems (signal cabling, passive electronics, active electronics, power supplies, regulators, etc.). The TileCal and LArg technologies are sufficiently different that we shall discuss the radiation issues for them separately.

TileCal System: The TileCal is a sampling calorimeter consisting of steel absorber material and scintillating plates read out by wavelength shifting (WLS) fibers. The steel is impervious to radiation damage, and at the background rates seen in the TileCal, activation is not a problem. TileCal module irradiation tests have therefore concentrated on possible damage to the scintillator and WLS fibers. These elements can have their light yields reduced by ionizing radiation—including the ionization induced by interacting background neutrons. The work in this area consisted of radiation damage tests on scintillating tiles and WLS fibers using Cs^{137} and Co^{60} gamma sources, along with simulation studies of the effects of this damage (and the damage caused by neutrons) on jet energy response. The worst light losses after 10 years of LHC operation with an integrated luminosity of 10^6 pb^{-1} are expected to be 5% in the first longitudinal sampling section, and less for others. Taken together, these studies [87] conclude that the uncalibrated jet response is degraded by about 1-2% and that, after calibration, the effects from radiation damage are negligible.

The TileCal photomultiplier tubes (PMT's) and front end electronics are in 'drawers' positioned between structural steel support girders at the back of the TileCal modules. In both the barrel and endcap, this region is well shielded by the total depth of the ATLAS calorimeters. The most exposed regions are at the ends of the drawers, where there are gaps for inner detector services and electronics. Careful modeling of these gaps has been done in GCALOR simulation, and the background rates expected in the drawer regions will not cause operating problems for the PMTs or their local signal electronics. But the high voltage distributor system for the TileCal is complex, and has been tested for all foreseeable background effects to assure that it will operate reliably in the ATLAS radiation environment [88].

LArg Calorimeters: Long experience with Liquid Argon calorimeters has shown that the argon itself is not susceptible to radiation damage, either short term or long term. However, the radiation rates in the ATLAS forward calorimeter (FCAL) region are exceptionally high, and there was concern that activation of the argon through production of Ar^{41}, with a half-life of 1.82 hours, might lead to signal or safety problems. A simulation performed at Los Alamos in 1994 showed that the equilibrium value of the activity will be .90 curies for the three FCAL modules at full luminosity of $10^{34}/cm^2/s$ [21]. This poses no problem for the operation of the calorimeter, and the short half-life of Ar^{41} makes this a negligible dose source during accesses.

The absorber and structural materials used in the ATLAS LArg calorimeters are primarily metals known to be radiation resistant and 'stable', meaning that they do not release potential poisons into the argon: steel, copper and brass alloys, and aluminum alloys. But to achieve short

interaction lengths, the absorbers of the second and third FCAL modules at each end are made of small sintered tungsten pellets, called 'slugs'. Since there had been no experience with this material immersed in liquid argon at high radiation rates, it was decided to test it. The irradiation tests [89] were performed as part of an ongoing program at Dubna, and the result is that the *upper limit* for outgassing from the slugs is 0.1 ppm with a fast neutron dose of 1.5 x 10^{16}/cm^2. (No outgassing was observed.)

Of greater concern was the possibility that electrode materials, primarily polymers, might be damaged, or poison the argon, in the presence of background radiation. Again, the region with the highest radiation rates *by far* is the forward calorimeters. From the beginning, electrode and readout materials were chosen to have the highest possible radiation resistance for the design. The spiral support fibers, that electrically insulate the electrode rods from their surrounding tubes, are made of poly-ether-ether-ketone (PEEK), a strong and flexible fiber with the same (or better) radiation resistance to mechanical damage as the polyimide kapton. The small interconnect boards at the readout ends of the modules are made of kapton with electrodeposited copper traces. [The first module is read out from the upstream end, and the second, from the downstream. There are no readout boards in the gap between them, which is also the position of the hadronic shower maximum. EM shower maximum is in the middle of the first module. This keeps the interconnect boards in the lower radiation areas of the FCAL.] Finally, the signal cables are miniature coaxial cables with kapton as the dielectric and cladding material (made by AXON France). This completes the list of electrode and readout elements in the hottest region of the calorimeter. The only other pieces of the chain inside the cryostat are the summing boards (polyimide circuit board, copper, transformers, HV protection resistors and HV blocking capacitors), placed behind the HEC modules in a region with much lower backgrounds.

All of these materials are safe with respect to mechanical damage for the doses in their particular regions over the lifetime of the ATLAS operation at a luminosity of 10^{34}/cm^2/s. But they were also tested for outgassing, and for electrical and mechanical tests of components [90]. At the IBR-2 reactor at JINR, Dubna, these parts were exposed to high neutron and γ doses inside a test cryostat. In addition to outgassing tests, capacitance and impedance measurements were made on the coaxial cables, and peeling tests (kapton and copper strips), were made on the PC boards. More recently, the FCAL electronics components (resistors, capacitors, transformers, summing board and connectors) have been tested at the same facility. No poisoning of the argon was observed from any components, and electrical measurements of resistors, capacitors, and transformers after irradiation showed no significant deviation from nominal values.

An extensive series of liquid argon pollution tests was also performed at the SARA fast neutron radiation facility in Grenoble [91]. In these tests the argon purity was monitored by an alpha cell immersed in the test cryostat, allowing a direct measurement of the purity parameter most directly related to calorimeter performance. The EM barrel and endcap accordion calorimeters contain a larger variety of electrode materials and electronic components than do the FCAL, and these were tested extensively in a series of runs. The list includes FR4 and G10 board, Prepreg epoxy, Hexcel-Honeycomb (electrode gap spacers), MicroD connectors, signal cable harnesses, EM accordion electrodes, HEC (EST) electrodes, and presampler assemblies. The overall conclusion of these studies was that after 10 years of LHC full luminosity operation, the accumulated pollutants would create one percent or less attenuation of the signal, a very acceptable limit. As noted in the references, the SARA facility was closed in 1998, and work was resumed at the CERI facility in Orleans.

For liquid argon calorimeters, there is another effect of fundamental importance when operating in a high radiation environment: positive ion buildup due to low positive ion mobility [92]. The

rate of ionization created by electromagnetic and hadronic showers can be large enough to cause the accumulation of positive ions in the liquid argon gap, which then distorts the electric field. This in turn degrades the signals from the drifting electrons, and can shut down operation altogether. This effect is a complex function of many variables (as described in [92]), but fortunately diminishes as the square of the electrode gap, as the gap is reduced. For this reason the ATLAS FCAL is a new design scheme employing thin-gap rod-and-tube electrodes, with gap thicknesses of order 250 μm. This feature, along with the other design parameters, gives the FCAL a safety factor of about 50 relative to the worst case experimental value for the positive ion mobility in liquid argon, for the hottest part of the calorimeter at $10^{34}/cm^2/s$ luminosity. (As noted elsewhere in this report, the highest ionizing radiation rate in the ATLAS detector is at EM shower maximum in the FCAL.)

Finally, we note that a number of additional electronic tests have been done in the course of LArg calorimeter development and engineering [93].

6.4 Review of impact on electronics

It is difficult in a short description to characterize regions of ATLAS electronics that are "most critically affected" by radiation backgrounds. It is anticipated, of course, that the Pixel layers nearest the interaction point will need to be replaced at some time due to ionization and displacement damage from hadrons coming from the I.P. But other electronics is expected to last for the lifetime of the experiment or, nominally, for 10 years of operation at a luminosity of $10^{34}/cm^2/s$. In the inner detector volume, where radiation rates are very high, radiation resistant electronics have been used. But in the muon system, where rates are much lower, the electronics is primarily consumer-off-the-shelf (COTS), to reduce cost. (And there are similar issues with LArg and TileCal electronics, where radiation resistance is coupled to the rates.) This implies that all electronic packages in ATLAS must be studied for their resistance to the backgrounds in the particular regions where they are placed. The responsibility of the ATLAS Radiation Backgrounds Working Group and the Radiation Taskforce has been to provide and update the backgrounds information - both in the tabular form above, and occasionally in the form of spectra- for use by ATLAS collaborators. In parallel with this, ATLAS subsystems collaborators have for years been performing radiation tests and simulation analysis on electronics they have developed for detectors, front-ends, trigger and data acquisition electronics, data links, power supplies, and power distribution components [24]. This effort is ongoing, and will probably continue at some level up through the beginning of ATLAS data taking.

The high radiation levels in ATLAS can affect electronic components by one or both of the following routes: (1) the slow accumulation of radiation damage over long periods of time as the experiment runs, leading to signal degradation or destruction of components, or (2) individual interactions of background particles (mostly high energy hadrons) with electronic components, causing large local ionization deposits that corrupt data ("single event upsets") or destroy components ("single event damage"). In principle, these effects extend to all components in the trigger and data acquisition system, both analog and digital: preamps and front-ends, pipelines and processors, optical and wire data links, monitoring electronics, voltage regulators and power supplies, etc. And because the inner detector silicon microstrip and pixel detectors are essentially electronic devices, these are vulnerable to the same classes of damage as the data acquisition system. More information can be found in the Atlas Radiation Hard Electronics web page [54].

6.5 Review impact on USA15 and US15

The hall USA15 will host electronic at the side of the experimental cavern. It is a 20m diameter cylindrical structure which axis is perpendicular to the axis of the beam at the height of the beam line and is separated from the experimental cavern by a flat 2 m thick concrete wall. On the other side of the experimental cavern, there is another hall US15 that may eventually host electronic racks in case of overflow of USA15.

Controlled access will be granted while the accelerator is running; hence it is important to estimate the dose levels that will be reached in that room. The rules documented in the Radiation Safety manual [23] indicate that the average dose rate should be lower than 25 μSv/h, while the maximum transient rate allowed is 100 μSv/h. The stay in the room for an individual is limited only by the total annual dose allowed of 15 mSv per year. 1. However France and other European countries are expected to change the legal limit from 20 mSv to 6 mSv per year. CERN will have to follow and lower its limit from 15 mSv to 6 mSv and this means that all limits at CERN will have to go down with a factor 6/15=0.4. The limit for a simple controlled area will for example go down from 25 microSv/h to 10 microSv/h.

The hall USA15 will host electronic at the side of the experimental cavern. It is a 20m diameter cylindrical structure which axis is perpendicular to the axis of the beam at the height of the beam line. The room is separated from the experimental cavern by a flat 2 m thick concrete wall which inner face is situated at 16.7m from the interaction point. The electronics will be distributed in two floors: level 1 has the floor at 1.8 m below the beam axis, while level 2 is situated at approximately 3.6m above the axis. Figure 6.37 shows the experimental cavern UX15 and the electronics hall USA15, as well as another hall US15 that may eventually host electronic racks in case of overflow of USA15.

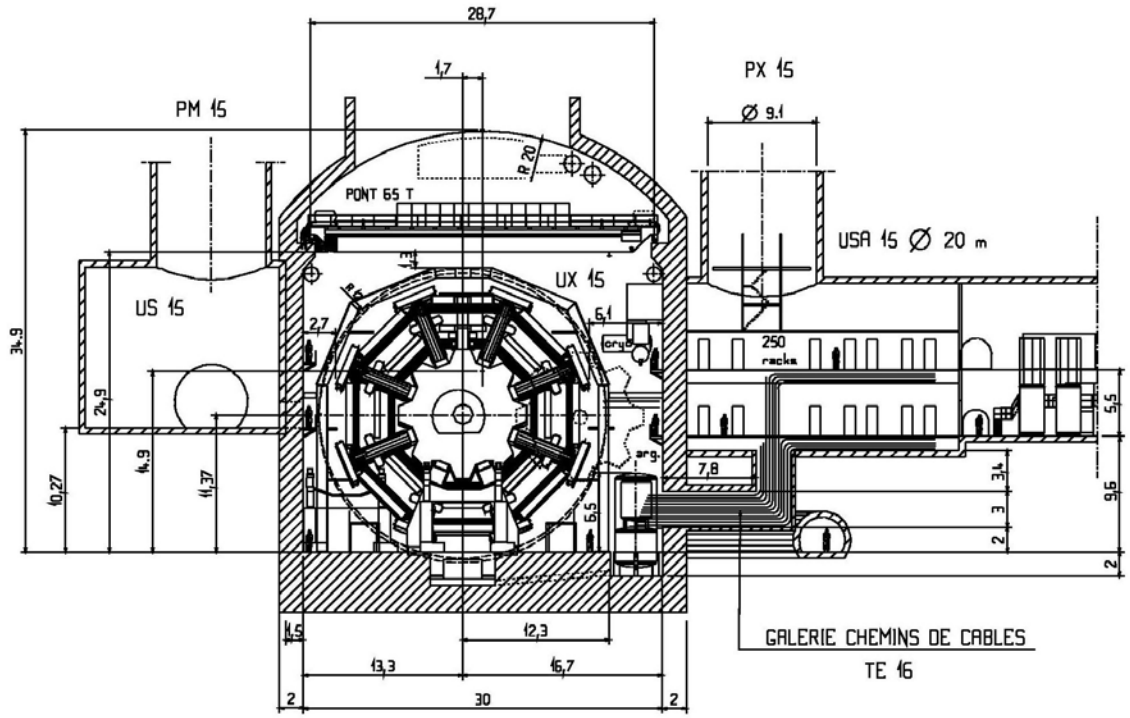

Figure 6.37: View of the experimental hall UX15 (center), the electronic hall USA15 (to the right) and the hall US15 (to the left).

Controlled access will be granted while the accelerator is running; hence it is important to estimate the dose levels that will be reached in that room. The rules documented in the Radiation Safety manual [23] indicate that the average dose rate should be lower than 25 μSv/h, while the maximum transient rate allowed is 100 μSv/h. The stay in the room for an individual is limited only by the total annual dose allowed of 15 mSv per year.

A study of the level of radiation in USA15 has been performed with FLUKA at the time of the ATLAS Technical Proposal [24]. In these calculations, the dose was given in 3 zones: a central one, at the height of the beam line where the 2 floors with electronic racks are situated (the one of interest), a lower one extending to the bottom of ATLAS hall, and a top one to the ceiling of the hall. At that time, some variations of the dose were also observed along z corresponding to the weaker point of the shielding but they were less pronounced than today and less important than the vertical ones, hence the choice made then of vertical subdivision only. The vertical subdivision is still valid today however the concrete 2 m wall is now situated at 16.7 m instead of 13m from the beam line. In the current standard simulation geometry, the hall is cylindrical with a radius of 13m in FLUKA and 12m in GCALOR.

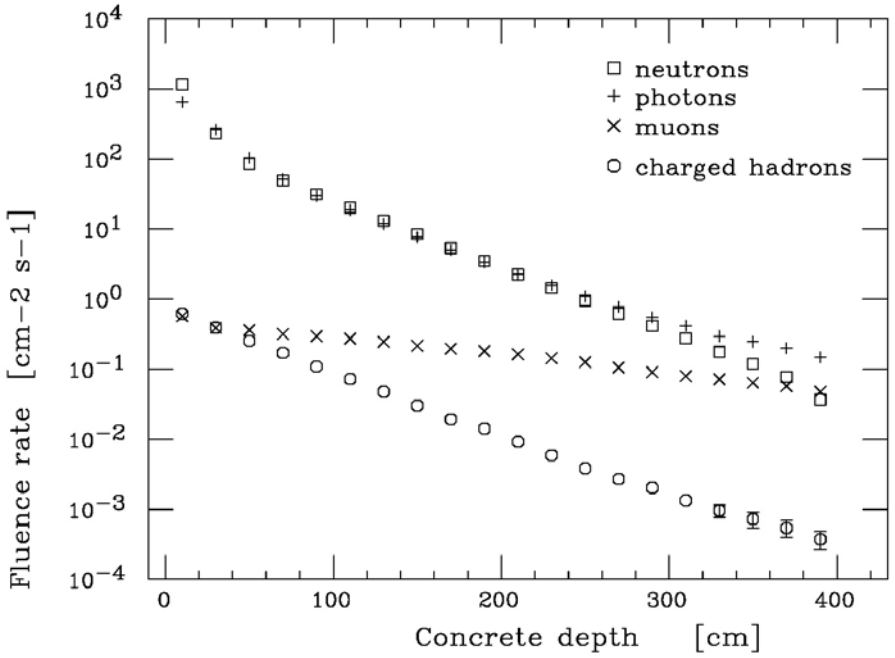

Figure 6.38 The fluence rate of different particles, averaged over the whole wall length, versus depth inside the concrete wall. The error bars (due to statistical error only) are smaller than the symbols almost everywhere (Fig taken from ref.24).

Figure 6.38 shows the absorption inside the concrete wall for different particle types. As discussed in reference [24], there is an initial higher slope due to the rapid absorption of low energy neutrons and photons. Then equilibrium between neutron and photon is reached with an attenuation length (~ 40 cm) typical of the lateral shape of hadronic cascade governed by the neutrons of few hundred MeV. It can be seen in Figure 6.39 that the shape of the neutron spectrum does not change with depth after the initial soft component absorption. The higher energy neutrons are the ones that drive the propagation trough the material, but most of the dose is coming from lower energy neutrons that are in equilibrium with the fast component. The muons are only important after 3-4 meters of concrete. They generate a slower decreasing tail (~ 125 cm), as seen in Figure 6.38.

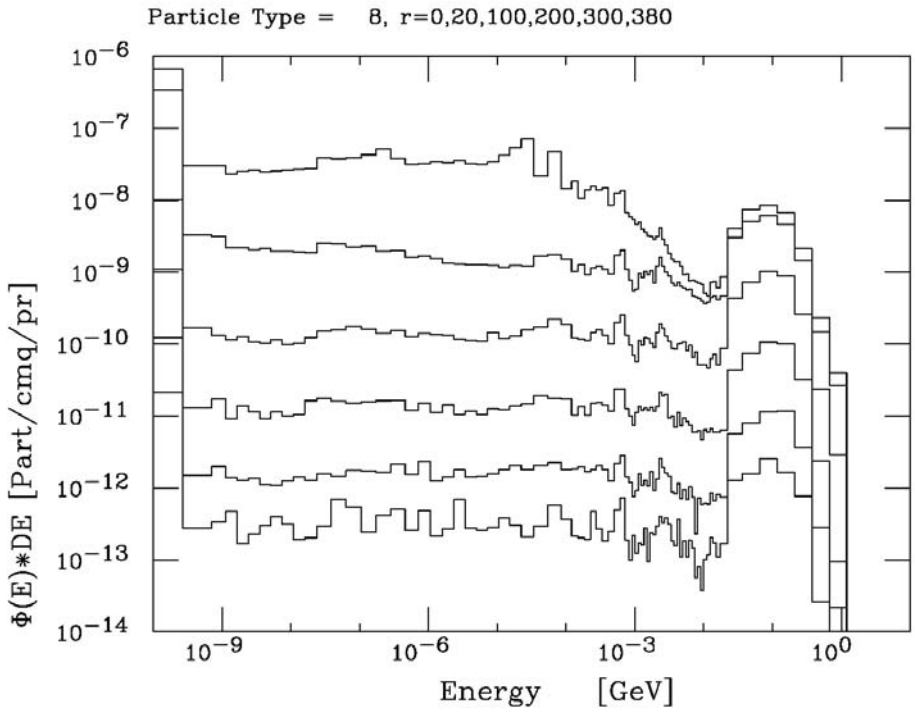

Figure 6.39 The neutron spectra at different depths (0, 20,100, 200, 300, 380 cm) inside the concrete wall (Fig taken from ref.24).

In reference [24], the total dose equivalent was obtained summing the contributions of the different particles types folded with the corresponding conversion factors [30]. The result is shown as crosses in Figure 6.40

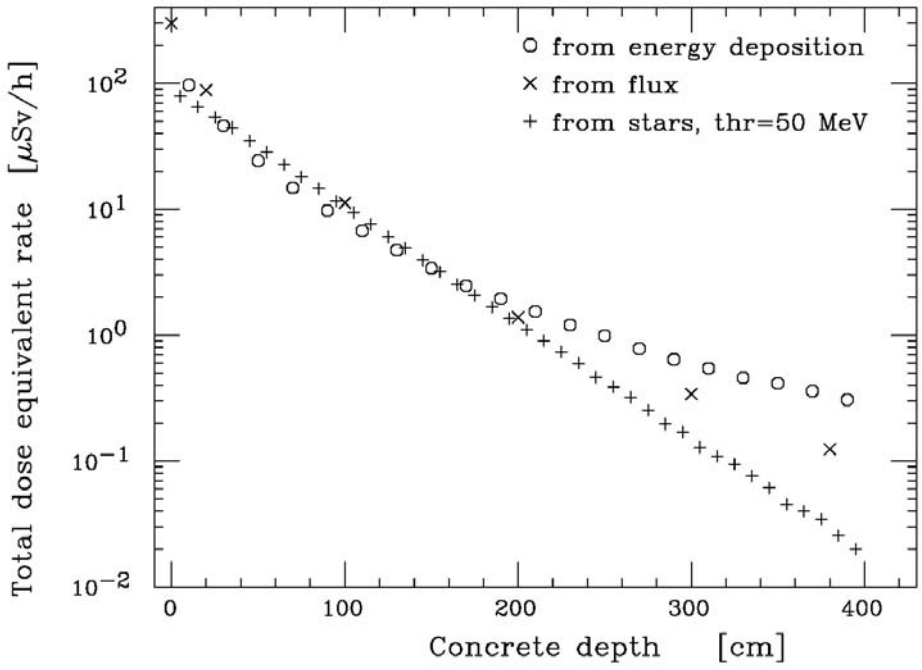

Figure 6.40Total dose equivalent rate, averaged over the whole hall length, versus the concrete depth for different kind of dose estimators.

Also shown in the figure is the dose estimated from the energy deposition applying an average quality factor Q = 5 (open circles). A third method consisted in obtaining the dose from star

densities (>50 MeV) multipliying by a conversion factor of 4.5 10^{-8} Sv cm^3/star [31]. In the first 2 m of concrete, the three methods agree well. Beyond that the differences are due to the increasing importance of the muon contribution.
In order to scale these results to the current estimate of fluences in the hall, the best normalization is given by the high energy "neutron" peak that is responsible for the penetrating component. From earlier simulation, the data that are available are the total neutron fluences (E >0) of the TP13 shielding configuration used for the ATLAS TP and for the calculation of the dose in USA15 (see Figure 6.41), as well as the data from TP43h (=AV1) the configuration at the time of the muon spectrometer TDR.

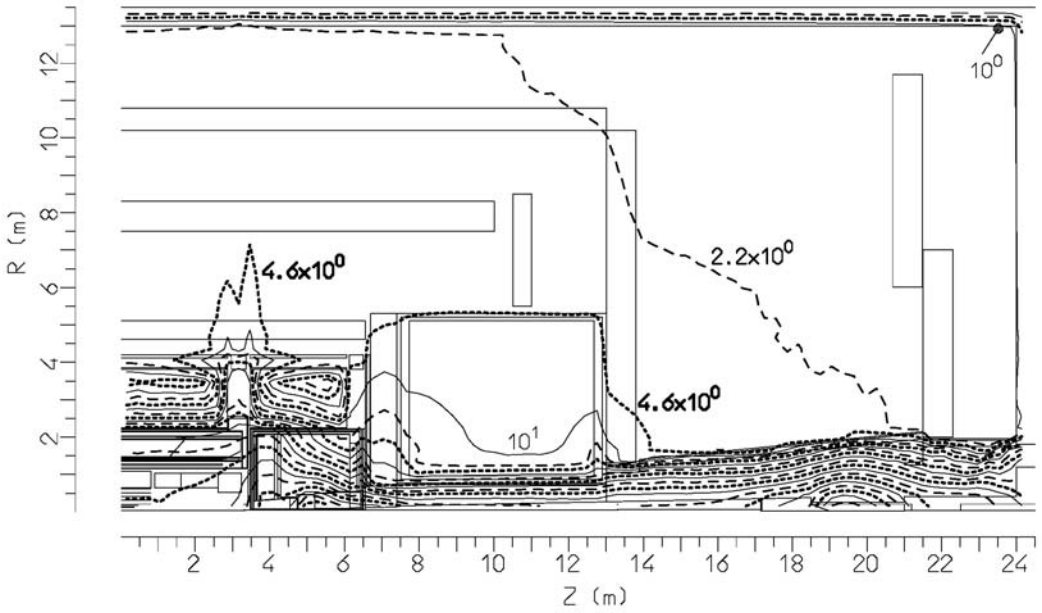

Figure 6.41 Neutron (thermal ones included) background fluence rate (kHz/cm^2) in the TP shielding configuration. Figure taken from ref. [24]

They are compared to the fluences obtained with AV16 (see Figure 6.42 and Table 6.13).

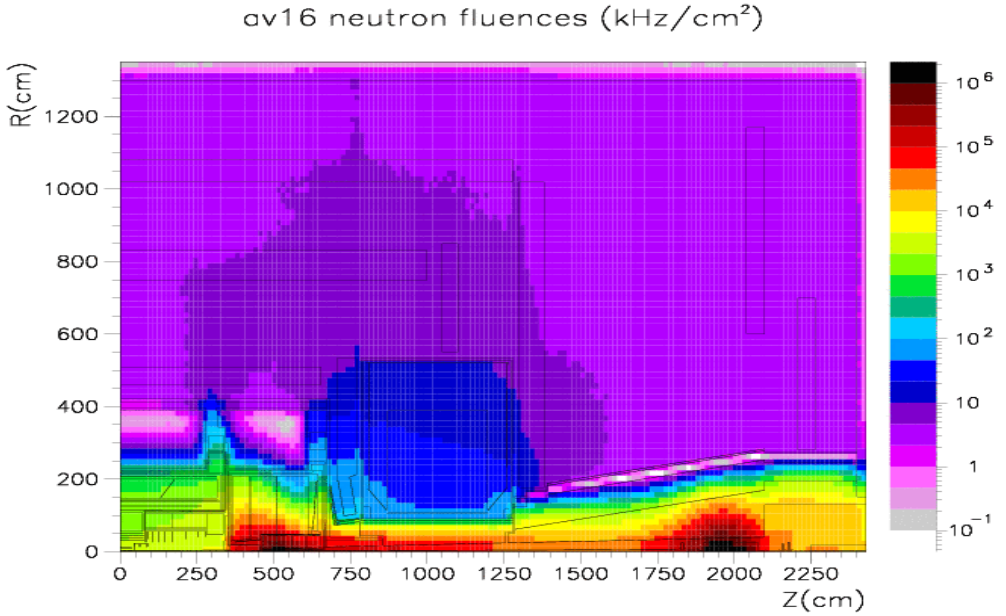

Figure 6.42 Neutron (thermal ones included) background fluence rate (kHz/cm^2) in the AV16 configuration.

There is an increase in the fluence rate in AV16 due to the stronger "leakage" through the JT region.

	Neutrons All kHz/cm^2				Neutrons >10 MeV kHz/cm^2		Photons >30keV kHz/cm^2		
	TP13	**TP43h**	**AV16**	**GCalor**	**TP43h**	**AV16**	**TP13**	**TP43h**	**AV16**
Barrel									
1rst low z	4.8	6.5	5.1		-	0.10	1.7	1.7	1.81
high z	4.0	3.4	5.2		-	0.07	1.5	0.9	1.88
2nd low z	3.3	3.2	5.0		-	0.10	1.3	1.1	2.19
high z	3.0	2.5	6.3	~4.9± 0.5	-	0.30	1.4	0.9	4.14
3rd low z	2.8	2.3	4.5		0.05	0.08	1.2	1.0	1.90
high z	2.4	1.8	4.9	~5.1± 0.6	0.07	0.18	1.1	0.8	2.71
Forward									
2nd low z	2.4	1.6	5.5		-	0.25	1.2	0.7	3.18
3rd low z	1.7	0.8	3.2		-	0.06	0.9	0.5	1.40

Table 6.13 Ratio of neutron and photon fluences between the TP geometry layout and the current layout as predicted by FLUKA The definition of the scoring region can be found in 0. The central values quoted for GCALOR correspond to the June02 baseline and the "error" to range of variations observed in the shielding optimization process (see sect. 8.4).

The fluence rate for neutrons > 10 MeV is not available for TP13 but they are for the configuration TP43h. This shielding configuration yielded lower neutron and photon fluences in all indicators of the region with radius larger than 6 m. The ratio AV16 to TP43h are 1.9 (2.7) for neutron (E>0) fluences in the 3rd low z (3rd high z); the ratio is 1.6 (2.7) for neutrons with E>10 MeV. We can conservatively the factor 2.7 as being the increase of the energetic neutrons at Z= 10 m. On the other hand, the wall of USA15 is now located at 16.7m instead of 13m at the time of the TP. To estimate the corresponding decrease of fluences at the wall, the radial dependence of the flow has been studied.

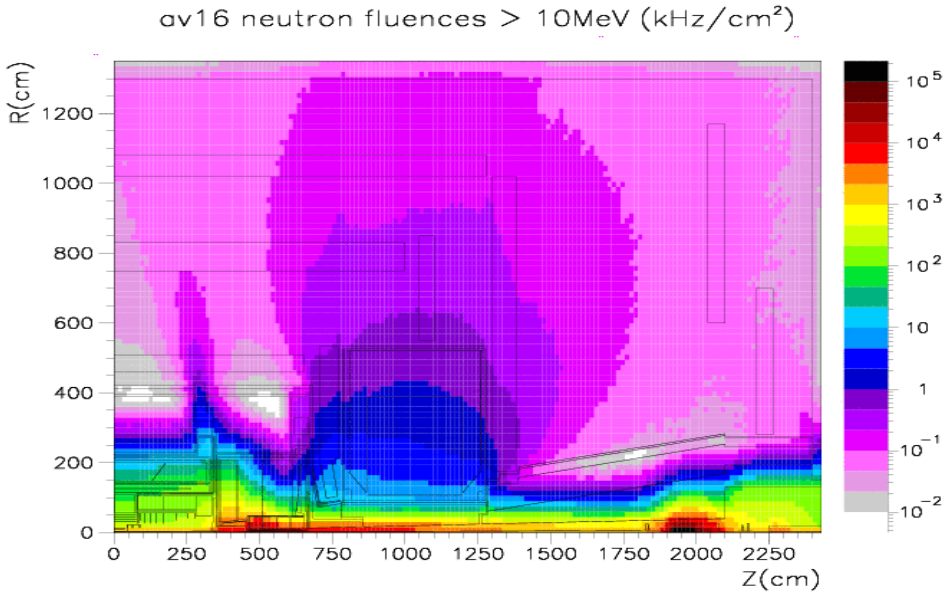

Figure 6.43 Background fluence rate (kHz/cm^2) from neutrons >10 MeV in the AV16 configuration.

Figure 6.43 shows the colour fluence map of AV16 for high energy neutrons where the "leak" in the JT region can be oberved. The radial dependence of the high energy neutron fluence was fitted at Z = 7.5m and Z = 10 m. The result of the fits are shown in Figure 6.44: the radial dependence is close

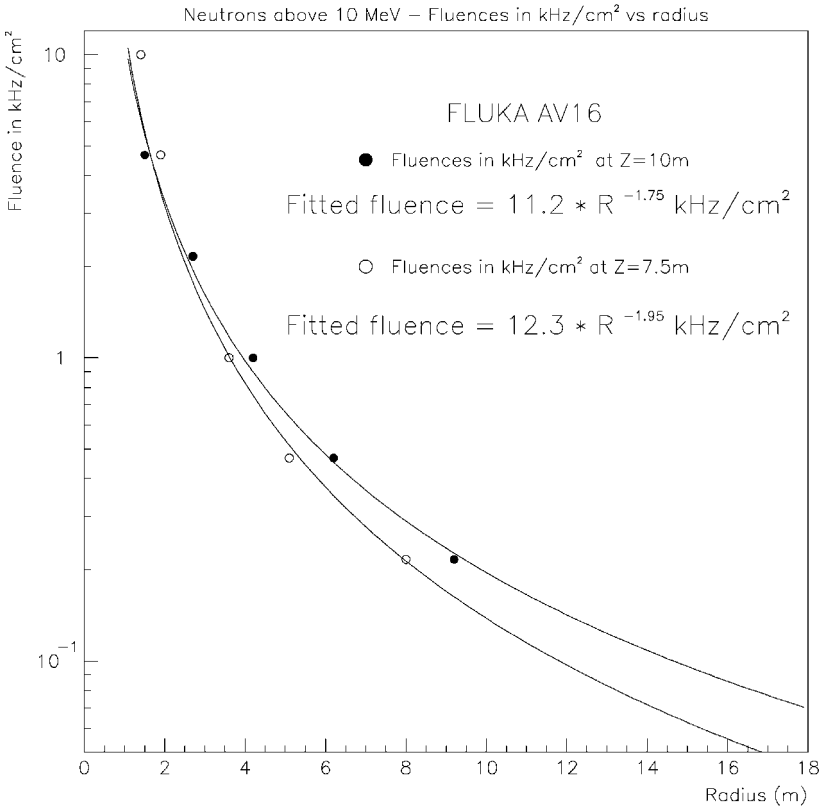

Figure 6.44 Radial dependence of the high energy neutron fluence at two positions in Z.

to $1/R^2$. Using the result of the fit at Z = 10m, the less favorable case, one can deduce a reduction of a factor 0.64 due to the increased distance of the wall from the "source". Combining the increase in fluence rate and the decrease due to the distance leads to a factor **1.7** increase in the energetic neutrons at the entrance of the wall.

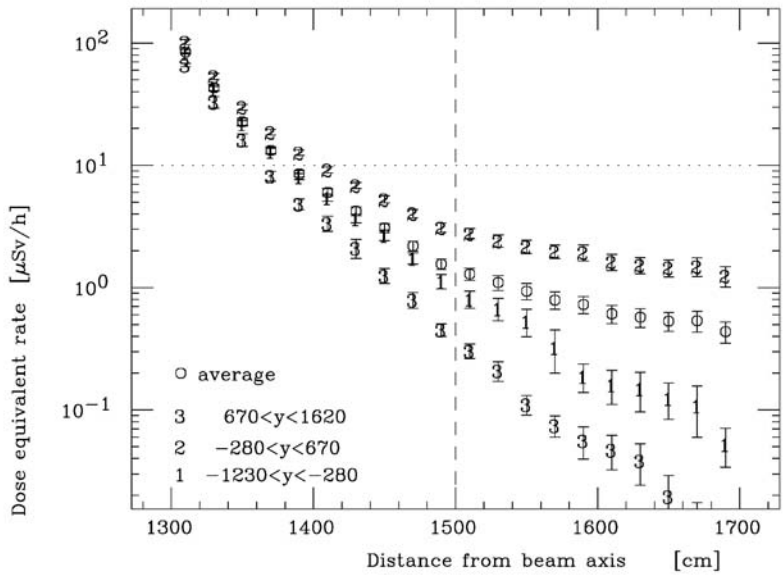

Figure 6.45 Dose equivalent rate, averaged over the whole wall length, versus the distance from the beam line. Together with the average over the wall height the different contributions coming from the three different vertical regions are plotted. The first surface of the concrete wall is at 1300 cm, the dashed line is at 200 cm depth. Figure taken from reference [24].

In the TP calculation, as shown in Figure 6.45, a 2m thick concrete wall reduced the dose rate to 3 μSv/h in the vertical region 2, the one corresponding to the USA15 tunnel. The value is quoted for the nominal luminosity of 10^{34} $cm^{-2}s^{-1}$. The current estimate with AV16 is then **5 μSv/h**, still below the original design goal for a calculated dose rate of 10 μSv/h which leaves a security margin (factor 2.5 uncertainty in the prediction) compared to the allowed level for controlled area of 25 μSv/h.

As discussed in Section 7.2, the agreement between the transport programs for neutrons is quite good: FLUKA and GCALOR agree within 30% for high energy neutrons on identical geometries, while MARS predicts levels 30-55% lower. Table 5.11 shows also the predicted values with GCALOR for the June02 baseline configuration together with the variation observed for different configurations studied during JT optimization (see sect. 8.4). The agreement with FLUKA is good and the variations due to the exact configuration of JT are not so large. Another element to consider is the density of Concrete: the one used in TP13 was 2.42 gr/cm^3, while the standard density of concrete is 2.35 gr/cm^3. This only gives a 15% lower absorption in a 2m wall. In the case that the US15 cavern, the distance to the wall is 13.3 m, so in this the factor 0.64 reduction does not apply and the estimate dose with AV16 is **8 μSv/h**.

7 Uncertainties: comparison of Monte Carlo programs and benchmarking data

7.1 Introduction

Radiation background predictions at high-luminosity hadron collider experiments rely heavily on general-purpose Monte Carlo particle transport programs such as FLUKA, GEANT3-CALOR and MARS. It is therefore reasonable to question the reliability of such predictions. Typically, any reputable particle transport program will have been benchmarked against appropriate experimental data. However, the radiation environments at such benchmarking-experiments are usually complicated and obtaining data for all the components of the radiation field is difficult, so ambiguities remain. Furthermore, in making predictions for LHC experiments, the transport codes are being extended into a regime never encountered before. Therefore, the simulations really are predictive and will include corresponding (large?) uncertainties. For example, ATLAS currently assumes a safety-factor of 2.5 from the showering processes in its FLUKA predictions of particle rates in and around the muon system. This value was based on past experience (previous benchmarked data etc.) and the confidence of the FLUKA authors in the quality and coverage of the physics models implemented in FLUKA. Section 7.2 describes the comparison that has been carried out between different transport programs for LHC-like environment while Section 7.3 gives a comparison of minimum-bias event generators. Section 7.4 summarizes recent experimental shielding benchmarking data of direct relevance to ATLAS.

7.2 Particle transport studies: comparison and systematics

The aim of the studies [97] described in this section is to compare the predictions of different Monte Carlo shower codes for LHC-like radiation environments. In the first study, the most recent versions of FLUKA(2001) [98] and MARS14(2002) [99] are compared for a simple well defined geometry. Both programs have been extensively used for many years in the high-energy physics, accelerator and radiation shielding communities (in particular, FLUKA at CERN and MARS at FERMILAB). Both programs have also been extensively benchmarked. For the low-energy neutron transport MARS uses MCNP4 which is regarded as the most reliable of all neutron transport codes. (Standalone-FLUKA should not to be confused with GEANT3-FLUKA, which uses the hadronic routines of the 1992 version of FLUKA.) The advantages of such comparisons, as compared to benchmarking-experiments, are (1) comparisons can be made in LHC-like environments and (2) the systematic uncertainties associated with experiments are eliminated. The obvious disadvantage is that both codes could be wrong in the same way. However, the FLUKA and MARS codes have been developed completely independently and are based on different physical models, tracking algorithms and geometry description, and such a comparison should give confidence where the codes agree, and possible cause for concern when they disagree.

The second and third studies involve comparisons between FLUKA and G3-CALOR [8]. The bulk of the ATLAS radiation background effort has been done with these two codes and it is important to check their consistency. Unlike the case of FLUKA and MARS, FLUKA and G3-CALOR share some common ancestry via G3-FLUKA. G3-CALOR activates the same routines as G3-FLUKA for pions and nucleons with energies greater than 10GeV (and all other particles anyway). Below this energy and down to thresholds of 2.5GeV for pions and 3.5GeV for nucleons, a hybrid treatment is implemented in which a fraction of the interactions is performed

as in G3-FLUKA and the remainder of the fraction is simulated by the so called scaling model. The value of the fraction varies linearly going from 0 at threshold to 1 at 10GeV. It should be noted that in the current ATLAS simulations using G3-CALOR, neutral-kaon transport is performed with the GHEISHA routines.

The range of physics coverage of one code may be more extensive than another. For example, the FLUKA code has evolved and improved continually since the 1992 version used in G3-FLUKA. A comparison with data [101] of standalone-FLUKA and the three different hadronic event generators (G-FLUKA, G-CALOR and G-GHEISHA) at the single interaction level was performed in 1996. Deficiencies in all the GEANT packages were highlighted and discussed. In particular, G3-CALOR was shown to significantly underestimate particle multiplicities in the "scaling energy range", especially where pion-interactions are concerned. However, the impact of such deficiencies on predicting "macroscopic" radiation backgrounds will be problem dependent. For example, the ATLAS muon-system radiation environment is dominated by neutrons and capture-photons, and the predicted pion rates are much smaller.

7.2.1 FLUKA versus MARS comparison in a cylinder

Both FLUKA and MARS have been used for many years in the high-energy physics, accelerator and radiation-shielding communities, and are reputed as being two of the most reliable codes for simulations where high-energy hadron interactions and their cascades down to low-energies are important. Both programs have been extensively benchmarked against experimental data over a wide energy range for both hadronic and electromagnetic showers. Comparisons of FLUKA with MARS should give a good measure of any uncertainties associated with radiation background predictions. The danger of course with such comparisons is that the predictions of both codes could be wrong the same way. However, FLUKA and MARS have been developed completely independently and are based on different physical models, tracking algorithms and geometry descriptions, and such comparisons should give confidence where the codes agree, and possible cause for concern (or further investigation) when they disagree.

FLUKA2001 is compared to MARS14(2002) for a simple cylindrical beam-stop geometry, as illustrated in Figure 7.1, in which the lateral development of particle fluxes and energy-deposition was investigated. Based on an original study by Huhtinen and Mokhov [100] using FLUKA and MARS14(2000), the current study has been extended to include copper, an important shielding material in the ATLAS shielding design. The length of the target geometry is 200cm and consists of a central core of radius 40cm, surrounded by a 60cm shielding-layer. In the simulations, both steel (Fe) and copper (Cu) are used for the core. For the shielding-layer; steel, concrete (Conc) and magnetite-concrete (Bmcn) are all used. Surrounding the shielding-layer are 10cm layers of borated-polyethylene (BPE) and air respectively. All these materials are typical of shielding materials used in hadron-collider experiments such as ATLAS and CMS; their details are given in Table 7.1 Elemental composition of materials used in FLUKA vs MARS study.

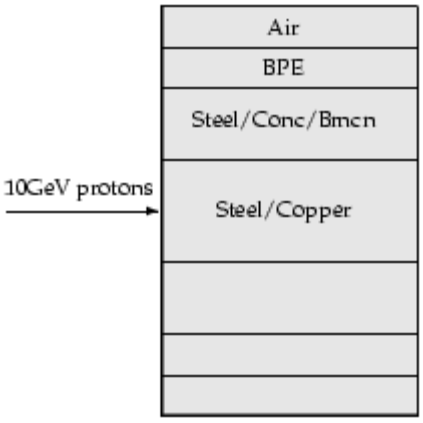

Figure 7.1 Target geometry used in FLUKA vs MARS comparisons. The induced lateral cascades are representative of the situation in the ATLAS and CMS forward-shieldings.

Material	density	H	B	C	N	O	Na	Al	Si	K	Ca	Fe	Ni	Cu
steel	7.87	-	-	0.1	-	-	-	-	0.1	-	-	98.6	1.0	0.2
concrete	2.35	0.6	-	3.0	-	50.0	1.0	3.0	20.0	1.0	20.0	1.4	-	-
mag-conc	3.67	0.7	1.3	-	-	35.0	1.3	2.0	2.0	-	2.7	55.0	-	-
BPE	0.93	11.6	5.0	61.2	-	22.2	-	-	-	-	-	-	-	-
copper	8.96	-	-	-	-	-	-	-	-	-	-	-	-	100
air	0.0012	-	-	-	80	20	-	-	-	-	-	-	-	-

Table 7.1 Elemental composition of materials used in FLUKA vs MARS study.

The particle cascades in the target-geometry are initiated by a 10GeV proton beam along the central-axis of the cylinders. This is a good choice of energy for two reasons: (1) It is just above the few-GeV range, which is the hardest and most complex regime for all Monte Carlos to model due to the transition from particle to nuclear physics; therefore the codes are being compared where the uncertainties are likely to be the largest. (2) The secondaries from the proton-proton inelastic interactions have much lower energies than the ~TeV collision energies and the resulting cascades are dominated by particles in the energy range below 10GeV. In addition, a higher primary energy would mainly increase the longitudinal extent of the cascade, and not change much the lateral cascade. Particles are transported down to energies of 200keV, except neutrons which are transported down to thermal energies. Below the 200keV energy cut-off, the particle energy is ranged out to rest in an approximate way. If applicable, particles eventually decay or are captured. Energy-integrated fluences and energy-deposition are obtained in the z-range 50cm $\rightarrow$100cm (corresponding approximately to maximum of shower development) and in radial steps of 2cm. In addition, energy-spectra have been obtained within the same z-boundaries, inside the BPE layer surrounding the cylinder (radial range 100cm$\rightarrow$110cm).

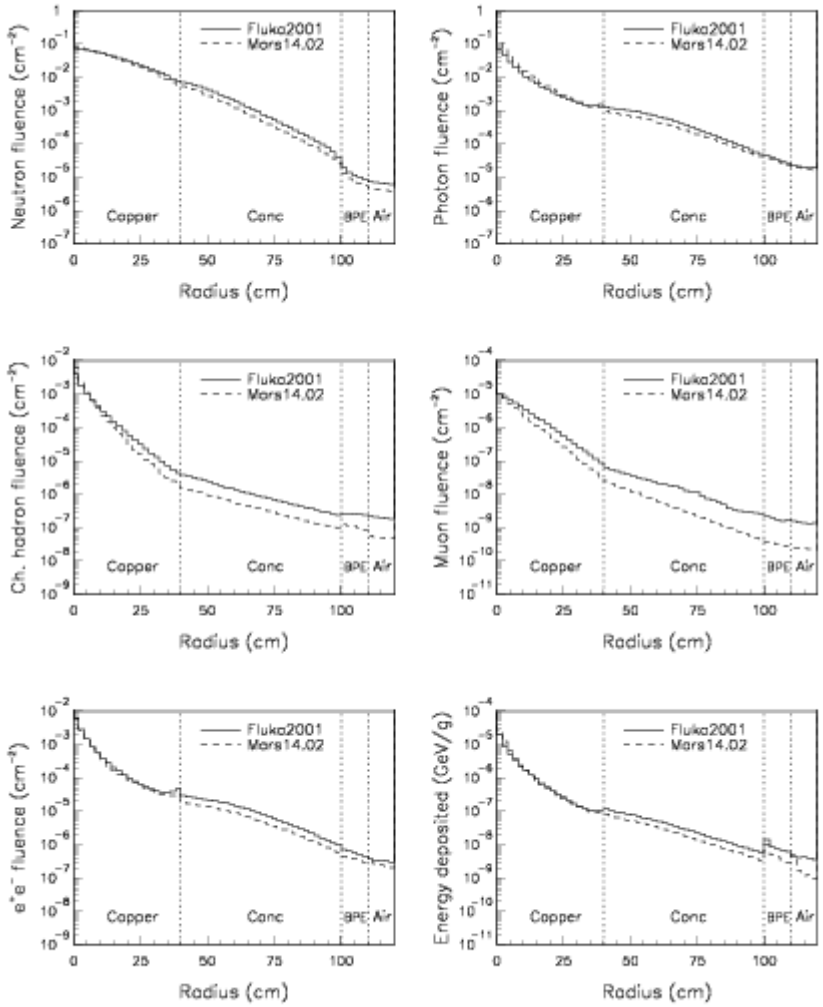

Figure 7.2 Radial dependence of total-fluences and energy-deposition for the "Cu+Conc" case. Good agreement is observed for neutrons, photons, e+e- and energy-deposition for all radii (for the iron dominated simulations the corresponding agreements are excellent). In all the simulations, the biggest differences are seen for muons, especially at large radii.

Shown in Figure 7.2 is the radial dependence of total-fluences and energy-deposition for the "Cu+Conc" case. Good agreement is observed for neutrons, photons, e+e- and energy-deposition for all radii. The corresponding comparisons for the "Fe+Conc", "Fe+Bmcn" and "Fe+Fe" simulations give even better agreement, while the "Cu+Fe" results are similar to "Cu+Conc". Larger differences are observed, but still reasonable, in the charged-hadron comparisons at large radii. It should be noted that protons dominate the charged-hadron fluxes for radii greater than ~40cm. In all the simulations, the biggest differences are seen for muons, up to a factor of 6 at large radii.

Given in Table 7.2 are ratios of total-fluence and energy-deposition obtained in the "BPE-layer" for all the different material configurations, showing that agreement at large radii is always within a factor of 2 for neutrons, photons, e+e- and energy-deposition, and always within a factor 2.5 for charged-hadrons. Typically the FLUKA predictions are greater than MARS for all components of the radiation field. A notable exception is for photons in the "Fe+Bmcn" case, in which the MARS photon predictions are ~1.5 times greater than FLUKA. The "magnetite-

concrete" is essentially a mixture of steel and concrete and it is surprising to find a significant difference in the mixture while there is good agreement in the individual components.

Material environment	neutrons			photons	e+e-	protons	muons	Energy-deposition
	total	>100keV	>10MeV	>200keV	>200keV	>200keV	>200keV	
Fe+Conc	1.3	1.3	1.4	1.0	1.2	2.1	5.2	1.4
Fe+Bmcn	1.2	1.3	1.4	0.6	1.1	2.0	low-stats	1.4
Cu+Conc	1.5	1.6	1.6	1.1	1.5	2.3	5.7	1.7
Fe+Fe	1.3	1.5	1.6	1.1	0.9	2.1	low-stats	1.3
Cu+Fe	1.5	1.8	1.8	1.4	1.1	2.3	low-stats	1.6

Table 7.2 FLUKA over MARS total-fluence and energy-deposition ratios obtained in the "BPE-layer" for the different material configurations. Statistical uncertainties on fluxes used in the given ratios are typically: less than one percent for neutrons, photons, e+e- and energy-deposition; a few percent for protons and 10→15% for muons.

Given in Figure 7.3 are particle spectra in the BPE layer for the "Cu+Conc" case. Good agreement is observed for neutrons of all energies and for photons and e+e- with energies less than ~10MeV. Comparisons for the other material configurations are typically better, although this is not the case for photons in the "Fe+Bmcn" case (see comment above). Discrepancies are observed in all the comparisons for photons and e+e- for E > 10MeV, typically factors ~5 and ~4 respectively, although the E > 10MeV part of the spectra gives only a small contribution to the total fluence, especially for photons.

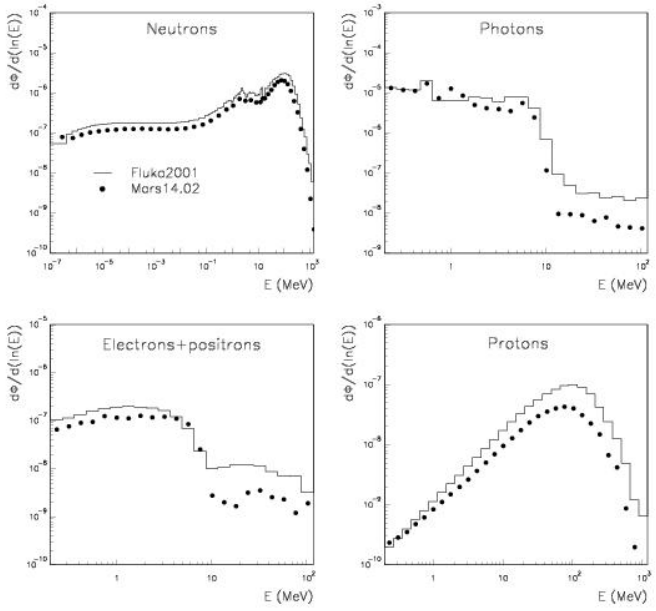

Figure 7.3 Particle spectra in the BPE layer for the "Cu+Conc" case. Good agreement is observed for: neutrons of all energies; photons and e+e- for E < 10MeV. Differences are observed in all the comparisons for photons and e+e- for E > 10MeV; typically factors ~5 and ~4 respectively.

7.2.2 Comparison with simple geometry

The bulk of the ATLAS radiation background studies, optimisations etc., has been performed using standalone-FLUKA and G3-CALOR, where expertise has been available. However, the simulations have evolved independently, resulting in non-identical geometries, material definitions, magnetic-fields and scoring regions; making comparisons of the two programs at the cascade level difficult. This was the motivation for a study in which the predictions of FLUKA and G3-CALOR could be compared for a simplified, but identical, "ATLAS-like" geometry (see Figure 7.4). Table 7.3 shows the scoring surfaces used in FLUKA/GCALOR comparison studies.

In the simulations, the same p-p event source was used (PHOJET version 1.12) and particle cascades were transported down to the following limits: neutrons → thermal-energies; photons → 30keV; charged hadrons and muons → 10MeV; e+e- → 0.5MeV. Below these limits the particle energy is ranged-out to rest in an approximate way, whereas in GCALOR the energy is dumped at that step.

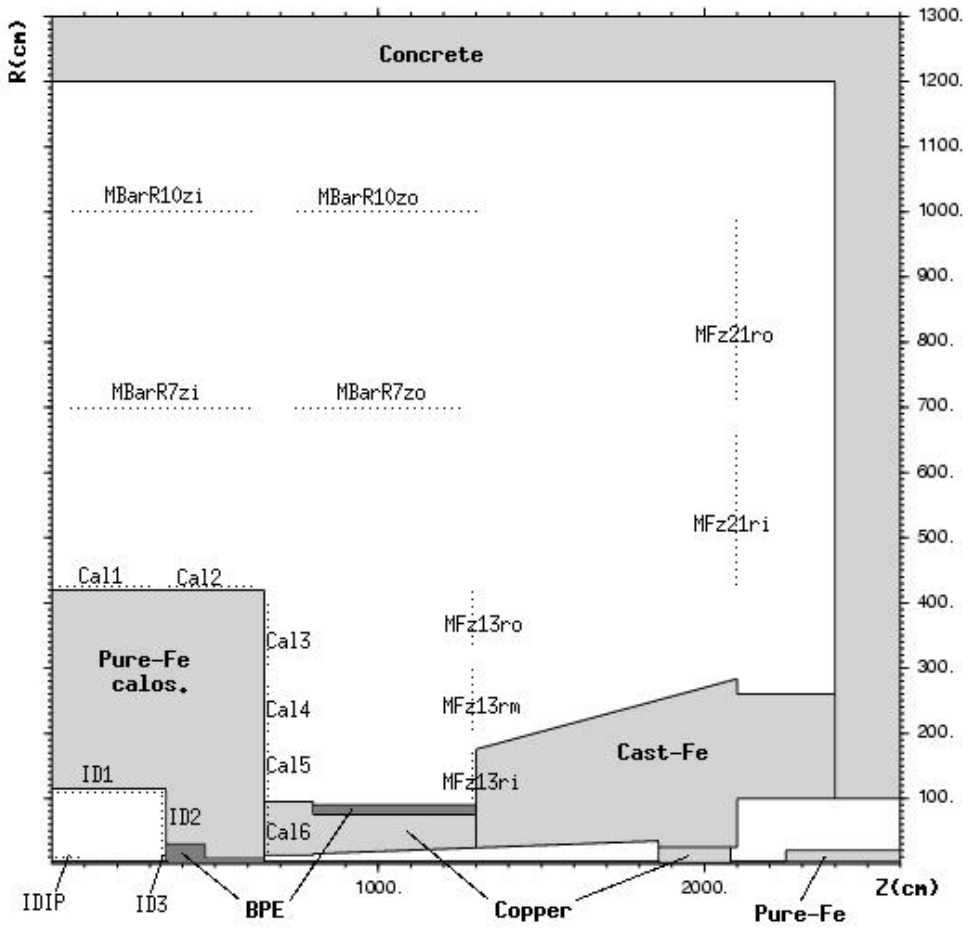

Figure 7.4 Cross-section view of one quadrant of the "hybrid" geometry used in the FLUKA vs GCALOR comparisons. Also shown are the names of the scoring-surfaces where fluences are obtained; "MB" and "MF" refers to "muon-barrel" and "muon-forward" respectively.

Region Label		Zmin	Zmax	Rmin	Rmax
Calo Barrel	Cal1	-350.	350.	420.	420.
Calo Tile	Cal2	350.	650.	420.	420.
Calo EC Otr	Cal3	650.	650.	275.	420.
Calo EC MdO	Cal4	650.	650.	175.	275.
Calo EC Mid	Cal5	650.	650.	95.	175.
Calo EC Inr	Cal6	650.	650.	30.	95.
MBar MidBar	MBarR7zi	-650.	650.	700.	700.
MBar MidEnd	MBarR7zo	650.	1300.	700.	700.
MBar OtrBar	MBarR10zi	-650.	650.	1000.	1000.
MBar OtrEnd	MBarR10zo	650.	1300.	1000.	1000.
MFwd MidOtr	MFz13ro	1300.	1300.	275.	420.
MFwd MidMid	MFz13rm	1300.	1300.	175.	275.
MFwd MidInr	MFz13ri	1300.	1300.	90.	175.
MFwd OtrOtr	MFz21ro	2100.	2100.	700.	1000.
MFwd OtrMid	MFz13rm	2100.	2100.	420.	700.
MFwd OtrInr	MFz13ri	2100.	2100.	290.	420.
ID Barrel	ID1	-350.	350.	115.	115.
ID Endcap	ID2	350.	350.	30.	115.
ID FCAL	ID3	350.	350.	3.	30.
ID I.P.	IDIP	-100.	100.	3.	3.

Table 7.3 Scoring surfaces used by FLUKA and GCALOR to report fluences.

The dominant materials defining the ATLAS radiation environment are iron and copper (calorimeters, shieldings, collimators and beampipe). The effect of the hydrogenous materials such as borated-polyethylene (BPE) and concrete is important for low-energy (<10MeV) neutrons, and gammas from neutron-capture.

Comparisons are presented for three different cases:
(1) all materials are pure-Fe of density 6g/cm^3, except concrete cavern-walls
(2) all materials are pure-Cu of density 6g/cm^3, except concrete cavern-walls
(3) an "hybrid" material description using: pure-Fe (6g/cm^3), cast-Fe (7.2g/cm^3), pure-Cu (8.96g/cm^3), BPE (0.93g/cm^3) and concrete (2.35g/cm^3) to "approximate" the ATLAS situation as illustrated in Figure 7.4. The BPE and concrete mixtures are very similar to those used in the FLUKA vs MARS study described in Section 7.2.1. The cast-Fe mixture is 96.5% Fe and 3.5% carbon.

An example of neutron fluences, for cast-Fe, is shown in Figure 7.5. The main features of the background are visible: containment in the calorimeters and the JF region, leakage in the JT region.

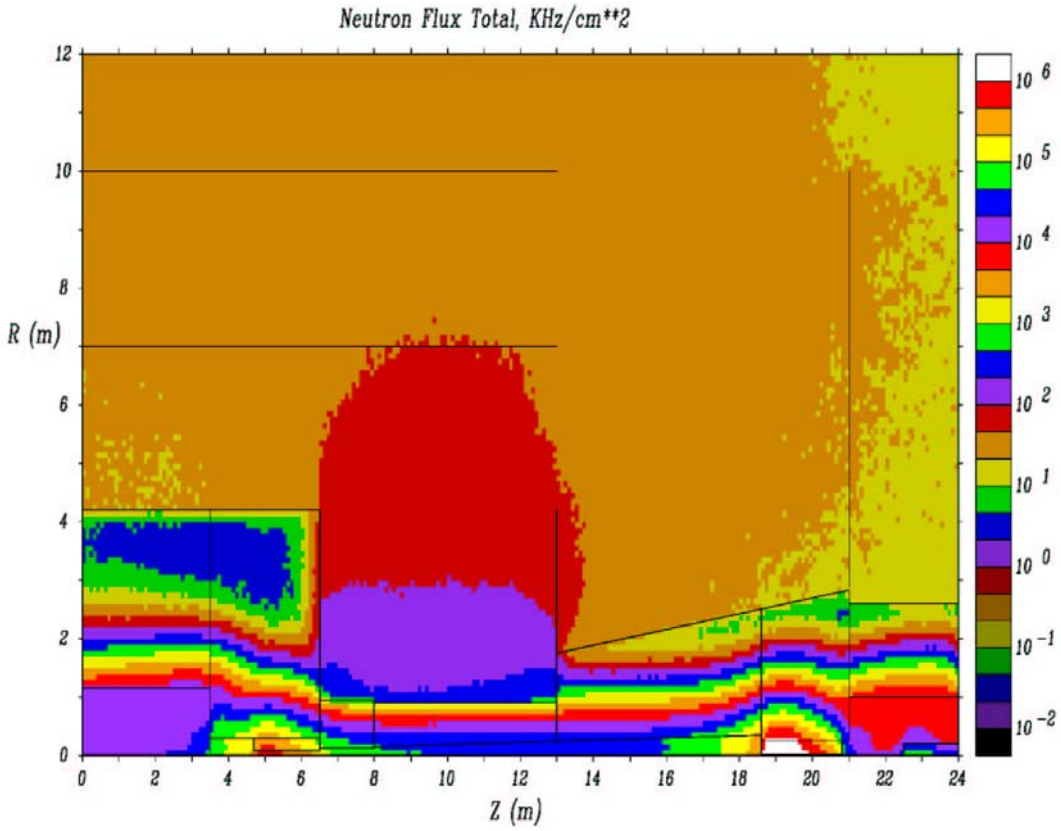

Figure 7.5 G3-CALOR Neutron Fluences with the simplified Atlas geometry with cast-Fe.

In general there is good agreement between FLUKA and G3-CALOR, as can be seen from inspection of Table 7.4. The "inner-detector" comparisons are typically within ~20%; although this is to be expected for all particles except neutrons as they are dominated by secondaries from the proton-proton collisions. Neutron fluences in the inner-detector, however, are dominated by cascade-neutrons "back-splashing" from the calorimeters.

FLUKA/GCALOR	Material environment	Neutrons		photons	e+e-	protons	muons
		total	>10MeV	>30keV	>0.5MeV	>10MeV	>10MeV
Outer-detector regions	Fe+conc	1.0->1.2	0.9->1.3*	1.2->1.3	1.1->1.4	1.3->1.6	1.0->2.2
	Cu+conc	1.5->1.7	0.9->1.3*	1.3->1.9	1.3->2.4	1.2->1.8	1.1->2.1
	Fe+Cu+conc+BPE	1.0->1.2	0.9->1.3*	1.2->1.4	1.2->1.5	1.1->1.6	1.0->2.8
Inner-detector regions	Fe	1.0->1.1	0.8->1.0	0.8->1.1	1.0->1.3	0.8->0.9	0.9->1.0
	Cu	1.0->1.2	0.8->1.0	0.8->1.1	1.0->1.2	0.8->0.9	0.9->1.0
	Fe+BPE	0.9->1.1	0.7->0.9	0.8->0.9	0.9->1.2	0.8->0.9	0.9->1.0

Table 7.4 FLUKA/GCALOR ratios for particle predictions in the three different material scenarios. For the "hybrid" case, particle rates in the inner-detector regions are mostly influenced by cast-Fe + BPE, whereas all materials are relevant for the outer-detector case. The >10MeV neutron ranges marked with an asterix do not include the "Cal1" ratios, which are signifantly higher (factors 3.4, 3.1 and 3.4 for "Fe+Conc", "Cu+Conc" and "Fe+Cu+conc+BPE" respectively).

More important are the comparisons in the “outer-detector” regions, in which hadronic and electromagnetic cascades are transported through many interaction lengths and many scatterings are involved. As for the real ATLAS geometry, the energy-flow of particles into the “outer-detector” regions is up through the shielding material at 650cm < Z < 1300cm, where there is much less material to contain the hadronic cascades.

In the “pure-Fe” and “hybrid” simulations, there is excellent agreement for the neutrons and photons when energy-integrated particle rates are compared. Larger differences are seen in the corresponding "all-copper" simulations, although still typically within a factor of 2. Comparison of neutron spectra and photon spectra for E<10MeV also show good agreement. Large discrepancies appear, however, for photons having energies > 10MeV in all the material environments, as can be seen in "copper" photon spectra of Figure 7.6. The source of these discrepancies is presumably due to different cross section data sets for (n,gamma) interactions. Concerning neutrons for E>10MeV, there is good agreement in all cases except for the “Cal1” region, where the FLUKA predictions are ~3 higher than GCALOR. Studies have shown that neutron rates >10MeV in this region, which are much smaller than elsewhere, are dominated by particles originating from interactions in the cavern ceilings, and not directly from the shielding region at 650cm < Z < 1300cm as in the other cases.

Charged particles are dominated by protons, muons and e^+e^-, and the corresponding comparisons are reasonable; typically within a factor 2 for protons and 2.5 for the e^+e^- and muons. For charged pions and kaons, larger differences are sometimes seen (factor ~3.5) in the outer-detector regions. Fortunately rates are typically much smaller than the other radiation components and do not contribute significantly to the total rates. However, in regions where hadron-cascades are still being developed, for example “Cal6”, the pion component is important. For the case of “Cal6”, the charged-pion fluence predictions agree to within a factor of 2 for both the "pure-Fe" and “Copper” simulations.

No data is presented for neutral-kaon comparisons. Again, the absolute rates are typically much smaller than the other components of hadron-collider radiation fields. However, on a cautionary note, it is possible for their significance to increase when investigating particle fluences inside magnetic fields. This is because low-momenta charged particles are unable to penetrate the magnetic-field regions and the dominant charged-particle component may originate from KLong decay inside the magnetic fields.

It should be noted that, unlike MARS, GCALOR shares some common ancestry with FLUKA in that GCALOR activates the same high-energy hadron interaction routines as the 1992 version of FLUKA. Therefore some of the “agreement” in the predictions may be inherent, and some of the “disagreement” may be due to the many improvements made to the FLUKA code over the past 10 years. However, the transport of low-energy neutrons (<20MeV) and corresponding gamma production, which dominate the "outer-detector" radiation environments, is handled differently (MICAP point-wise cross-sections versus FLUKA multi-group treatment).

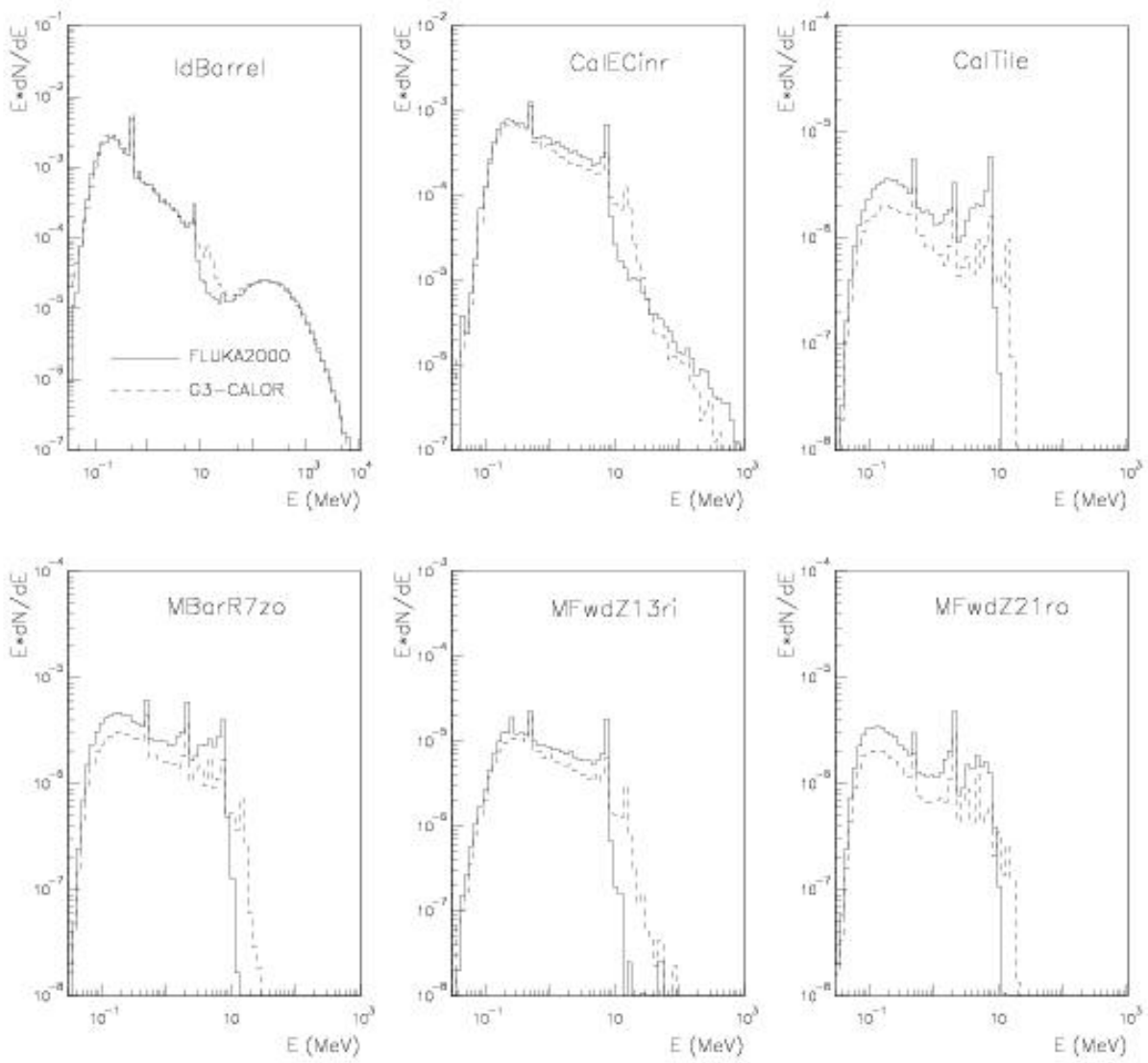

Figure 7.6 Photon spectra obtained in the "copper simulations" (worse case). The photons are dominated by those with energies less than ~10MeV, where agreement is typically less than a factor 2. The peak at 0.51MeV corresponds to positron annihilation, and the peaks at 2.2MeV and 7 MeV correspond to neutron-capture on hydrogen and copper respectively. Clear disagreement can be seen for photons E>10MeV.

7.2.3 FLUKA and GCALOR comparison with full ATLAS geometry

The FLUKA2001 AV16 radiation background predictions for the full ATLAS geometry are compared to GCALOR for a very similar, but not completely identical, geometry and material descriptions. Both programs use PHOJET for generation of minimum-bias events and assume a p-p interaction rate of 8.10^8 $cm^{-2}s^{-1}$ at high luminosity. For the >10MeV fluences, 77000 (100000) p-p events were transported in FLUKA (G3-CALOR). Neutron, photon and e^{+-} fluences were obtained using ~10000 p-p events in both programs. The FLUKA scoring surfaces (see Figure 5.16) have been used in the comparisons. GCALOR scoring regions have been made as similar to FLUKA scoring surfaces as allowed by the 10x10cm granularity of GCALOR maps. The ratios of fluences are provided in Table 7.5.

Concerning neutrons and photons, the agreement is typically within a factor of two. The exception to this is seen for the >100keV neutron fluences in the inner-barrel regions, where FLUKA predicts a factor 2 to 3 more than G3-CALOR.
Proton fluence comparisons are quite good and well within a factor of 2. Muon comparisons are reasonable everywhere (typically within a factor of 2) except 3rd-forward region where a factor of 3 difference is observed. It is interesting to note that muon fluence predictions are consistently higher in G3-CALOR than in FLUKA while it is usually the other way around. Good agreement is seen for e^{+-} fluences in the barrel system; less so in the forward region but always within factor 3. Uncertainties on charged pion ratios are large due to statistics, but FLUKA is typically predicting much higher rates than G3-CALOR. The same effect has been observed in the simple geometry comparison (see 7.2.2). However, as seen in Table 5.10 for FLUKA and Table 5.8 for GCALOR, charged particle rates in and around ATLAS muon system are dominated by protons, muons and electrons.

	Fluences Ratios (Fluka2000/G3-Calor)							
	Neutrons			Photons	Protons	π^{+-}	μ^{+-}	e^{+-}
Position	Total	>100keV	>10MeV	>30keV	>10MeV	>10MeV	>10MeV	>0.5MeV
Barrel								
1st,low-z	1.73	2.72	–	1.57	1.20	5.25	0.74	1.42
1st,high-z	1.46	2.35	–	1.43	1.05	2.89	0.99	1.24
2nd,low-z	1.53	2.26	–	1.75	0.64	1.17	0.93	1.21
2nd,high-z	1.28	1.59	–	2.39	0.82	9.29	0.93	1.65
3rd,low-z	1.47	1.95	–	1.58	0.68	0.91	0.79	1.26
3rd,high-z	1.24	1.48	–	1.81	0.86	1.30	0.96	1.30
Forward								
1st,low-eta	1.16	1.37	–	1.29	1.22	3.43	0.93	1.79
1st,mid-eta	1.00	1.23	–	0.99	1.12	1.67	0.89	1.25
1st,high-eta	0.95	0.87	–	0.72	0.98	0.83	0.63	1.22
2nd,low-eta	1.26	2.29	–	1.94	0.73	5.48	0.93	2.53
2nd,mid-eta	1.07	1.84	–	1.08	0.91	2.93	0.69	2.70
2nd,high-eta	1.00	1.45	–	0.55	1.32	5.07	0.41	2.67
3rd,low-eta	1.88	1.30	–	1.64	1.45	3.50	0.59	2.50
3rd,mid-eta	1.56	1.02	–	1.44	1.63	12.50	0.32	1.68
3rd,high-eta	1.01	0.71	–	1.00	1.44	5.26	0.34	2.76

Table 7.5 Ratio of fluences obtained with FLUKA and GCALOR

7.3 Comparison of minimum-bias event generators

In order to investigate uncertainties associated with minimum-bias event generators on radiation backgrounds, the ATLAS radiation environment was simulated using both PHOJET1.12 and PYTHIA6.2 (setting MSTP(82)=4 in PYTHIA to use the multiple interaction model with the complex scenario option); FLUKA(2001) was used in both cases to cascade the particles through the detector material. Figure 4.18 gives an identication of where fluences are scored. A proton beam luminosity of 10^{34} $cm^{-2}s^{-1}$ is assumed in deriving particle rates. All inelastic processes were included (diffractive + non-diffractive), giving a total inelastic cross sections of 84.5mb and 79.3mb for PHOJET1.12 and PYTHIA6.2 respectively. Elastic interactions were not included since in this process, the protons scatter at very small angles and interact much further downstream.

PHOJET/PYTHIA	neutrons		photons	e+e-	protons	muons	pions
	total	>10MeV	>30keV	>0.5MeV	>10MeV	>10MeV	>10MeV
Inner-detector regions	1.08->1.11	1.06->1.11	0.99->1.15	1.0->1.1	1.1	1.1	1.1
Muon-barrel regions	1.09->1.12	1.09->1.21	1.09->1.18	0.9->1.2	1.0->1.2	1.0->1.2	low-stats
Muon-forward regions	1.09->1.15	1.05->1.14	1.06->1.13	0.9->1.4	1.0->1.2	1.1->1.6	low-stats

Table 7.6 PHOJET/PYTHIA fluence ratios in and around ATLAS. Differences are typically less than 20%. The only notable exception is for muons in parts of the forward-muon system where ~50% differences are observed.

Given in Table 7.6 are the ratios of the PHOJET predictions compared to PYTHIA for radiation backgrounds in and around the ATLAS detector. Differences in predicted fluences are typically less than 20%. The only notable exception is for muons in parts of the forward-muon system where ~50% differences are observed. This was found to be due to differences in charged-pion and kaon production for energies greater than ~5GeV and their subsequent decay into muons before interacting in the calorimeters. (Note that low-energy muons do not transverse the ATLAS magnetic-fields.) This demonstrates that the <20% agreements are only valid for energy-integrated fluences.

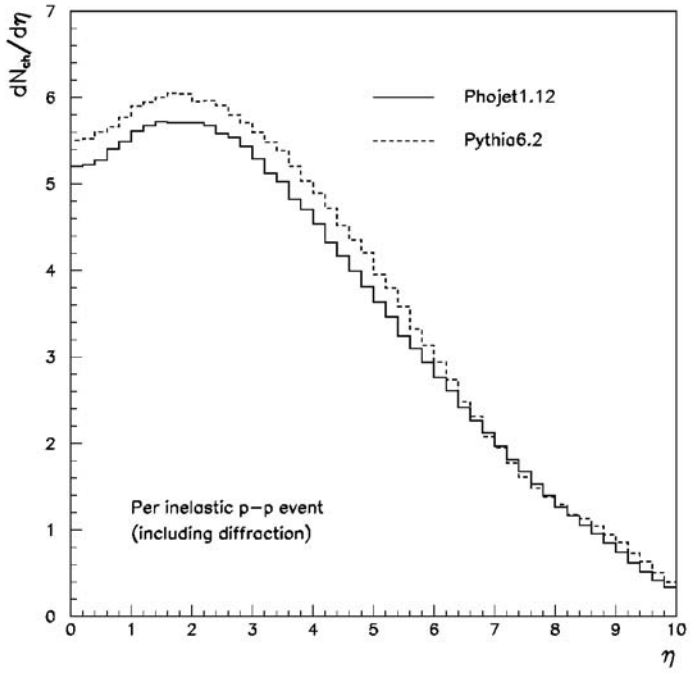

Figure 7.7 Charged particle multiplicity vs pseudorapidity for PHOJET1.12 and PYTHIA6.2.

The charged particle multiplicity pseudorapidity distribution predicted by PHOJET1.12 and PYTHIA6.2 are shown in Figure 7.7. The energy dependence of pion production from PHOJET1.12 and PYTHIA6.2 in the rapidity range $1< \eta< 2$, corresponding to the forward-regions, is seen clearly in Figure 7.8.

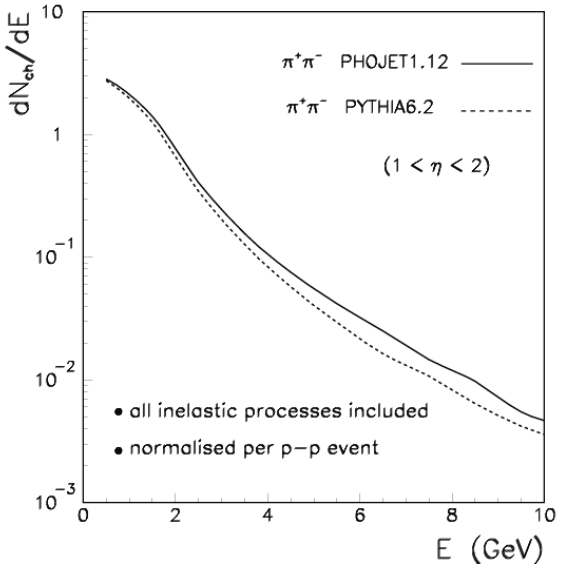

Figure 7.8 Pion energy-spectra predicted by Phojet1.12 and Pythia6.2: agreement is observed at low-energies which dominate the pion fluxes; larger differences appear at higher energies

7.4 Experimental data on shielding of direct relevance to ATLAS

7.4.1 Neutron and photon background benchmarking in LHC-experimental environment

E.Gschwendtner, H.Vincke et al. [96] have set up an experimental arrangement approaching rather closely the situation of the ATLAS end-cap region. A mixed pion, proton and kaon beam hit an iron absorber with a thickness of 11-14 absorption lengths. Behind the absorber, the absolute yield and energy of the particles, mainly photons and neutrons, emanating from the final stages of the shower processes in the absorber was measured with a BGO detector. Measurements were taken close to the shower axis (6-10cm) and off the axis (56-60cm). While close to the beam axis, events are dominated by multi-particle late shower processes; off the beam axis events consisted mainly of single photons from (n,γ) and (n,n'γ) interactions.

The data were compared to simulation with FLUKA. The simulation reproduced the BGO calibration source spectra with ~ 2% accuracy. The normalized total signal rates agreed at a 20% level. Good agreement is also seen for the energy spectra. Average energy depositions agreed to better than 10%.

An attempt was also made to extrapolate these data to the ATLAS conditions although several important differences have to be taken into account. The End-Cap muon chambers see about 3-6 times more flux coming from beam line than from the IP trough calorimeter. An additional 25% comes from reflection on the cavern wall. Using the TP36 FLUKA ATLAS simulation, and taking into account the above factors, the predicted photon fluence rate emerging from the calorimeter is 4-8 kHz/cm^2 to be compared to the rate of 7.3 kHz/cm^2 estimated by interpolating test beam data to the same number of absorption lengths.

7.4.2 Experimental test of neutron shielding for the Atlas forward region

Experimental tests devoted to the optimization of the neutron shielding for the ATLAS forward region were performed at the CERN PS by the Prag groups [26,27]. A 4 GeV proton beam was directed onto an iron block of 40x40x80 cm^3 shielded on one side. The beam hit the block at 25 cm from the shielding layer., Various types of polyethylene were tested: pure polyethylene PE, borated polyethylene BPE with 3% of weight of B, lithium filled polyethylene LiPE with 10% of weight of Li, all with 8 and 16cm thickness. A 5cm thick iron/lead shield was optionally added. The effectiveness of the various types of shields was measured with precise gamma-ray spectroscopy performed with a HPGe detector. The following gamma-rays were measured: 478 keV from the $^{10}B(n,\alpha)$ reaction, 847 keV from the $^{56}Fe(n,n'\gamma)$ reaction as a measure of the number of inelastic reactions in the iron block itself, 2223 keV from the $^{1}H(n,\gamma)$ reaction as a measure of the number of thermal neutrons captured by hydrogen in any type of polyethylene and the 7631+7645 keV doublet from the $^{56}Fe(n,\gamma)$ as a measure of the thermal neutrons captured in the iron block itself. Other detectors measured the neutron fluences.

A Monte Carlo simulation of the setup was done with GEANT-FLUKA [45,102] using MICAP [103] for the neutron transport. The GAMLIB library [104] was added to MICAP to describe radiative capture (n,γ) and inelastic scattering (n,n'γ) of some of the relevant elements such as Fe, Cu, Pb and Ge. The simulations did not take into account the experimental zone environment such as the various experimental equipment, the wall and the floor that produces background radiation that affects the measurement, especially in case of an effective shielding.

	B peak 478keV		Fe peak 847keV		H peak 2223keV		Fe peak 7631& 7645keV	
	Exp.	M-C	Exp.	M-C	Exp.	M-C	Exp.	M-C
8cm BPE	1	1	1	1	1	1	1	1
16cm BPE	0.629	0.363	0.615	0.390	0.875	0.500	0.812	0.623
16cm PE	-	-	0.839	0.863	1	1	1	1
16cm LiPE	-	-	0.940	0.981	0.051	0.023	0.357	0.205
16cm BPE	1	1	1	1	0.035	0.014	0.260	0.184
16cm BPE + 5cm Fe	0.026	0.017	0.657	0.766	0.007	0.002	0.093	0.056
16cm BPE + 5cm Pb	0.005	-	0.187	-	0.004	0.0006	0.031	0.007

Table 7.7 Comparison between Monte-Carlo simulations and experimental results for areas of selected spectral gamma peaks. Peak area values in the table are normalized to the maximal values for every energy separately; - means that data are not available or at background level.

Table 7.7 shows the experimental data and the results of the Monte Carlo simulation. When PE is replaced by LiPE, a significant suppression of the H peak as well as a suppression of high energy γ-rays from neutron capture on Fe are observed, as expected. There is no additional γ-ray production that accompanies neutron absorption. The 847 keV peak originating from inelastic scattering on Fe remains approximately the same. If BPE is used, both the H peak and the high energy γ-line from neutron capture on Fe are suppressed, as for LiPE. As the cross-section of thermal neutron capture on B is higher than Li, the suppression is improved significantly. The intense generation of 478 keV capture gammas is a disadvantage of BPE with respect to Lithium. However, 5 cm of Fe are enough to suppress them by a factor 50. The suppression in 5cm of Pb is substantially larger. Monte Carlo results agree with the data within a factor 2 or better. In case of high absorption, the simulated rates tend to be lower than the data, but these are more affected by the neutron induced background in the experimental zone that is not included in the simulation.

8 Shielding optimization

8.1 Introduction

In an ideal world, for every detector subsystem subjected to background radiation, there would be adequate space for shielding to make the effects of these background sources negligible. In real detector design, however, such as the process that created ATLAS, the first priority is to position detector subsystems to optimize performance determined by physics criteria such as acceptance, resolution, and hermiticity. There is awareness, of course, during the earliest design phases that the detector must be buildable and accessible; that electronic and cryogenic services must be provided; and that shielding is needed to protect components from harmful radiation backgrounds.

Realistic engineering of some components begins years after the initial design phases, when subsystem envelopes are largely fixed. At this stage, even if major pieces of shielding have been "sketched in" from the earliest design phases, the engineered shield must stay inside a fixed set of boundaries. Inevitably, realistic engineering design reduces the space available for shielding as it evolves a more realistic description of supports, services, dimensional tolerances, and alignment tolerances. In addition, the shielding must accommodate the movements associated with detector accesses and the tolerances associated with these motions. These tolerances are often detector-specific. For cryostats, one must also account for shrinkage during cool-down. For large magnets, the motions created as the coils are energized must also be allowed for.

For engineering safety, clearance gaps are defined in a systematic way. "Envelopes" are the boundaries (surfaces) between subsystems or detector components that divide the detector space into contiguous (touching) regions. To allow for the treatment of dimensional and alignment tolerances, after envelope shapes and dimensions are determined, clearance margins are specified for each surface, somewhat inside the envelopes, varying from one subsystem to another; to account for differences in materials, fabrication methods, and the motions described above. Detector or shielding components are designed to "nominal dimensions", which in many cases are accounting for the mechanical and alignment tolerances among their own parts. If the outer surfaces of these components are facing another component at an envelope boundary, the nominal dimensions must be "smaller than" the envelope dimensions by at least the amount of the clearance margin. As one can see, this procedure by definition introduces a gap (usually an air gap), at each boundary between components. If all is designed properly, nothing touches except at designated suspension points.

If we put together all the effects discussed above, we see that the space available for shielding, and the engineering of the shield, are affected by geometry and by the design and development sequence as follows:

- The "physics envelopes" are determined in the conceptual design phase of the experiment, with some regard to radiation backgrounds, but at a time when the design is not specified in enough detail to study them realistically. These envelopes become the primary geometrical constraints on the placement of radiation shielding.

- The "engineering phase" of the detector and its shielding clarifies the subsystem shapes, support structures, and services. Inevitably the space for the shielding is reduced, penetrations are introduced for supports and services, and gaps appear to allow for mechanical and alignment tolerances. Sometimes this space reduction can have dramatic effects if it occurs in regions where the shield is already "thin", such as in the core of the ATLAS forward toroid.

- Some of the losses in shielding power can be regained through more clever choices of materials and the optimization of cladding layers on the surface of the shield. But this process is not simple since, in the thin-shielding regime, further thinning of the shield can 'promote' a background that was not previously a problem to being the most serious threat to detector operation. In this case, the nature of the optimization must adapt to include the new background without forgetting the previous sources.

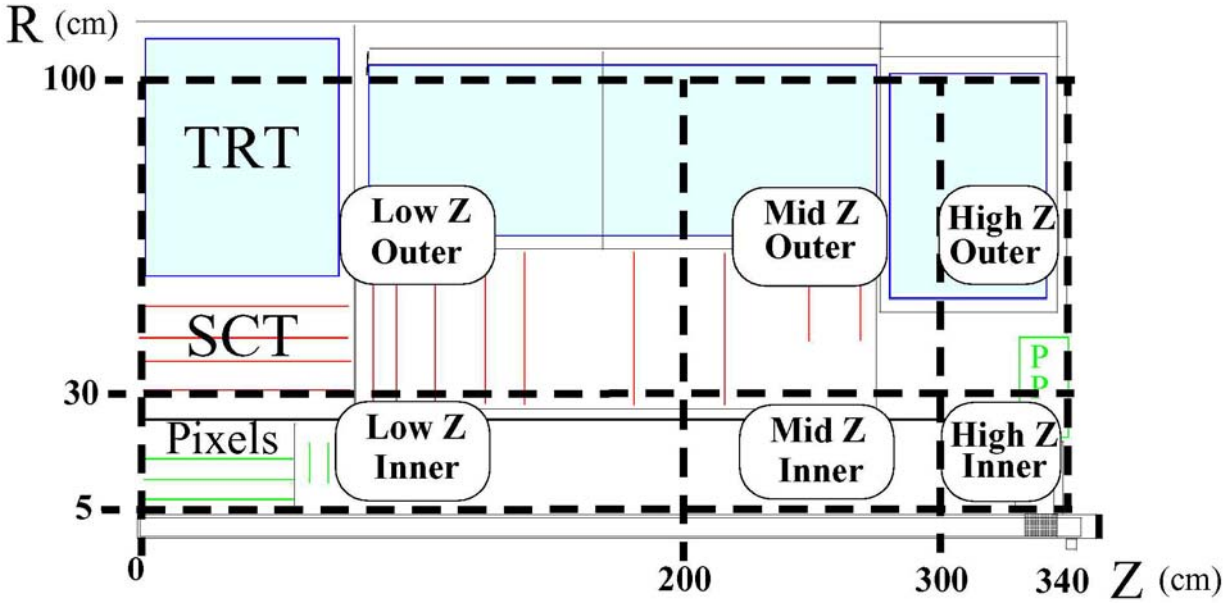

Figure 8.1 The scoring regions in the inner detector used in the GCALOR optimization studies of the JM moderator shield.

The shielding optimization that is discussed in this chapter took place in the end of the engineering phase. It was an iterative procedure which was carried out during year 2001 and 2002. This optimization resulted in a new shielding and beampipe design which is now frozen to permit the tendering process of the various shielding elements to take place. The iterative optimization procedure consisted of varying the design of a given component in simulation and calculating the background rates for this "option" geometry relative to rates in the baseline geometry of the time the simulation was carried out. To first approximation, if change in the geometry improved the backgrounds, it was adopted (along with others in the same simulation cycle) as part of the new baseline geometry. But there are other criteria involved in adopting a change, such as cost, ease of fabrication, and any impact the change might have on the detector response. If any of these are adversely affected to an unacceptable level, the change was not adopted.

Specifically, in any given cycle of shielding optimization, the baseline geometry was simulated, along with a series of option geometries where design parameters, or perhaps entire shielding components, were changed "one at a time". These option geometries were then compared pair-wise to the baseline geometry to study the differential changes in background rates or spectra

relative to the baseline. In some cases, design changes in one region of the detector did not affect the rates in some distant region of the detector in any measurable way. When this occurred, two or more such changes may have be made at once in a given option geometry, as long as they were all in mutually-decoupled regions. Since the optimization study has taken years to complete, several different baseline rates have been used in the comparisons in addition to the latest Jan03 baseline described in chapter 5.

In making the comparisons among geometry options, there are three ways to organize the information that we have found to be convenient and efficient: (1) tables by region, listing the rates of critical fluxes for each option, and the ratios relative to the option listed first in the table; (2) histograms of rates as a function of r in a given band zmin-zmax, or as a function of z in a given band rmin-rmax, with options overlaid in different colours; or (3) ratios of critical rates for any given pair of options, displayed on top of a graphic of one quadrant of ATLAS. The third method was invented by Vincent Hedberg, and has proved to be quite useful for making optimization choices. Throughout this section we will occasionally show tables, histograms, or quadrant graphics to assist in the explanation of optimization choices. There is a web page with a collection of the results [59]. In the next sections, the various shielding elements are reviewed one by one.

The scoring regions in which the background rates were studied in the optimization were in some case different from what was used in the studies presented previously. Figure 8.1 show the scoring regions in the inner detector used in the optimization studies of the JM moderator shield while Figure 8.2 show the scoring regions in the muon detector used in the design of the other parts of the shielding and the beampipe.

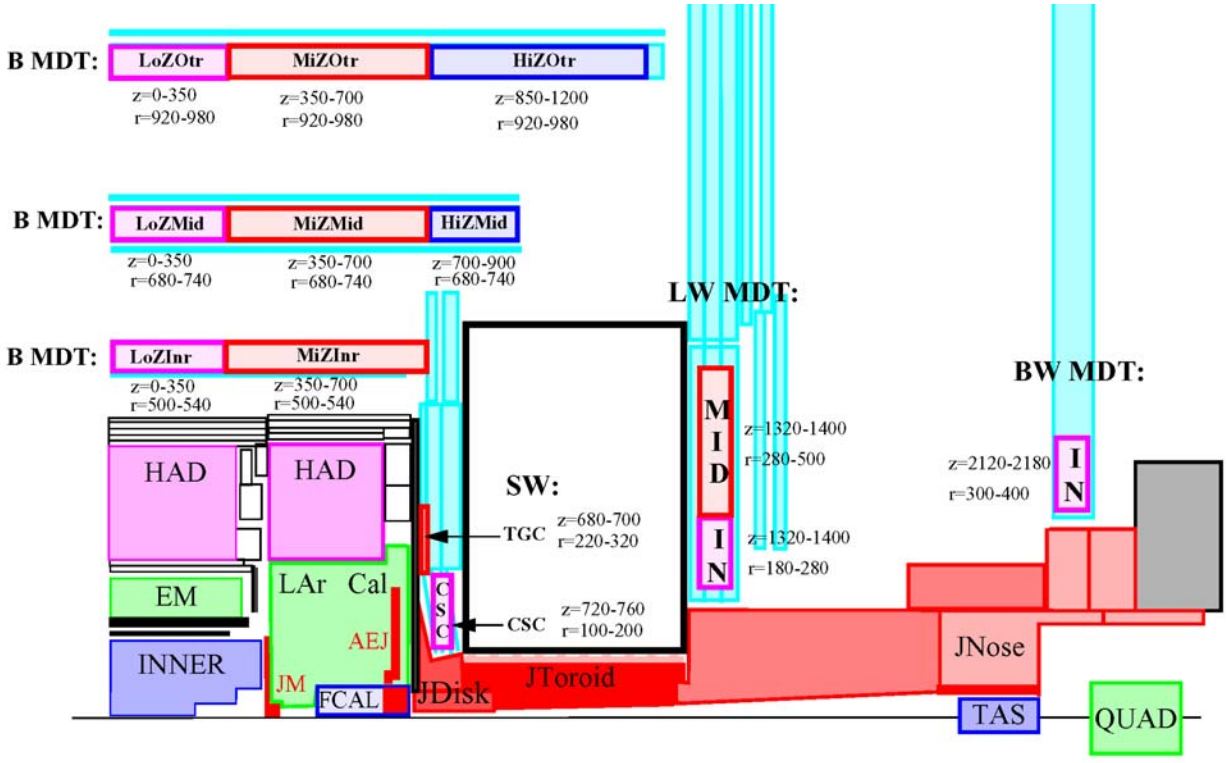

Figure 8.2 The scoring regions in the muon spectrometer used in the optimization studies.

8.2 Optimisation of JM

In most sections of this chapter, we will discuss the rates in design options normalised to the current baseline (JAN03). But since most of the JM optimisation was performed in November and December, 2001, we will refer changes to these earlier baselines, and work chronologically through the optimisation steps.

As described in detail in the baseline geometry section, JM now includes a doped polyethylene moderator disk on the face of the endcap calorimeter, and doped polyethylene in the FCAL alcove. The old design that existed through November, 2001, is shown Figure 8.3. The disk is bolted to the face of the endcap calorimeter, and the inner JM ("the plug") is supported by the beampipe support, filling as much of the region in front of the ion pump as possible (Figure 8.3).

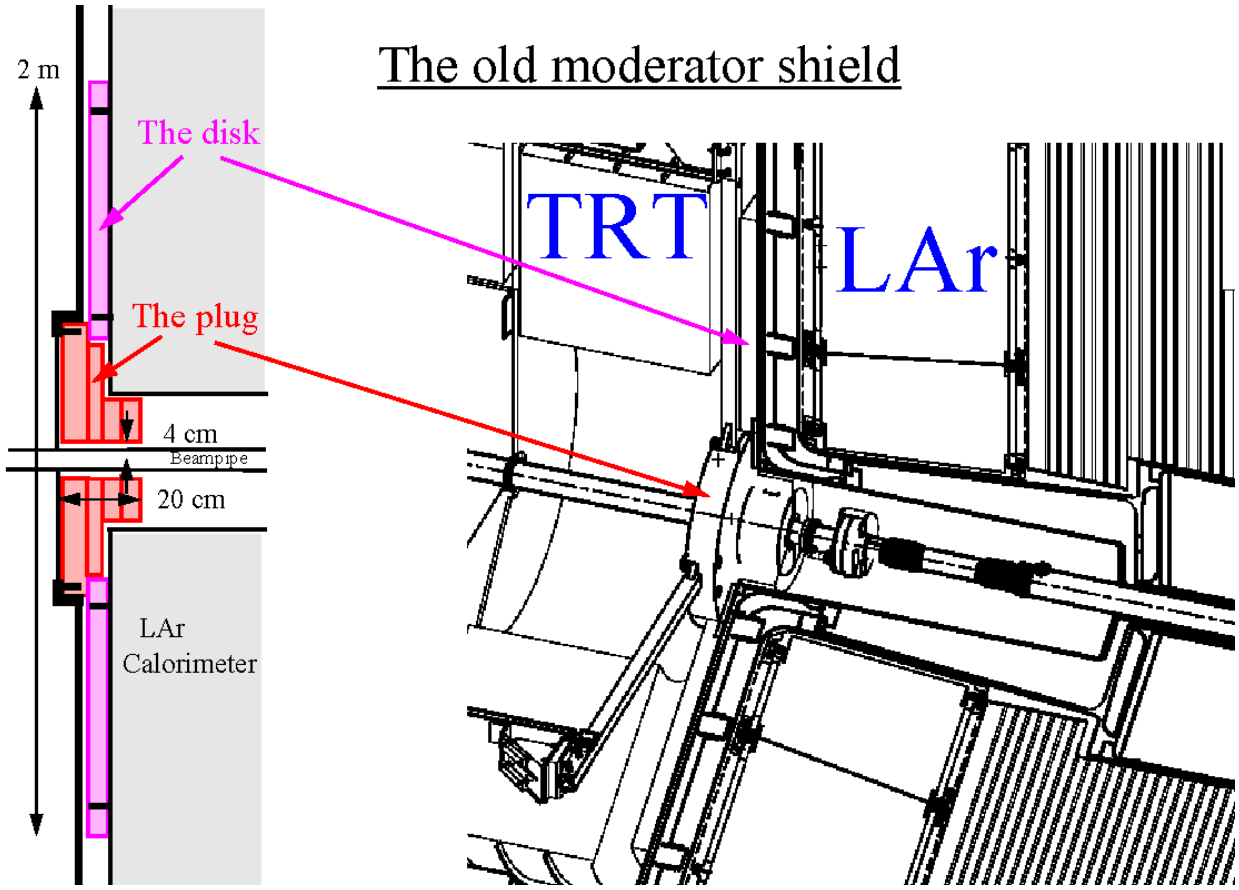

Figure 8.3 The old moderator shield layout

This design requires thickening the beampipe structures to support the weight of the plug, and makes access to the pixel detector services difficult since the inner JM surrounds flanges and supports. In November, 2001, a new design concept emerged, shown in Figure 8.4.

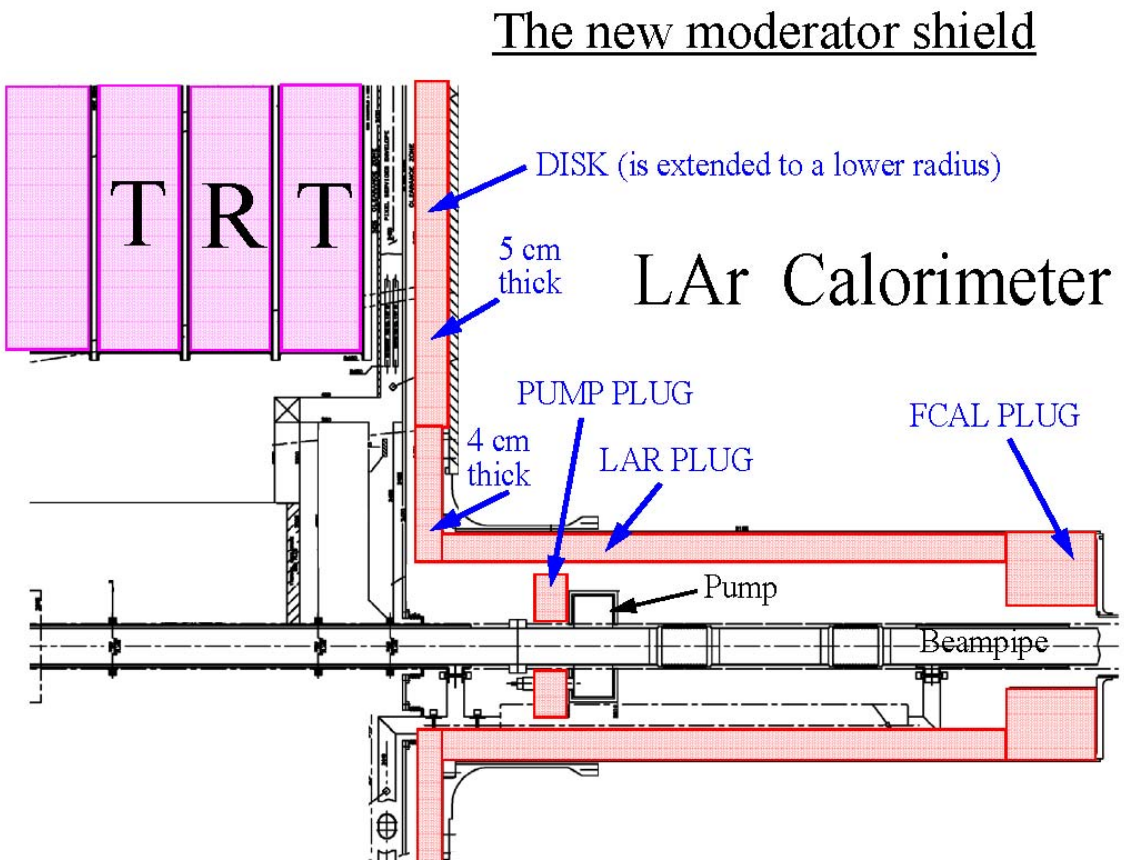

Figure 8.4 The new moderator shield layout.

Here, most of the JM is mounted on the endcap cryostat, lining the alcove and the cryostat wall into the FCAL. There is also a small block in front of the ion pump—which studies below will show is not needed. The naming convention we have adopted is to call the long poly cylinder lining the cryostat wall the "LAR PLUG", the shorter cylinder in front of the FCAL the "FCAL PLUG", and the small piece in front of the ion pump, the "PUMP PLUG".

As for the moderator materials, in November through December design options, all JM pieces are made of polyethylene doped with LiF (2.7% lithium by weight). Following a December option study (see below), the JM pieces have been turned into borated polyethylene (5% boron by weight), as is the case in the current, JAN03, baseline.

Performance of the new FCAL alcove liner, compared to the old large beampipe plug

The new design first appeared as an option in November, 2001, and became the baseline in December, 2001. In each design, the LAR PLUG extends from the front of the endcap calorimeter to the front of the FCAL PLUG, and both of these plugs have an outer radius that matches the inner radius of the alcove, within tolerances. The PUMP PLUG inner radius fits close to the beampipe.

Scoring regions were introduced which divided the inner detector into six zones, three in z and two in r, working outward from the interaction point (Figure 8.1). Below, Table 8.1 compares the

new design to the old. To relate this first design to other options that will be considered below, we give in the table the dz x dr thicknesses of the three plugs in the new design.

PERCENT CHANGE FOR: Nov New JM / Nov Baseline

Plug dimns: LAR dz X 5 cm, FCAL 30 cm X 13.5 cm, PUMP 5 cm X 6.7 cm

	N<100keV	N>100keV	Photons	Pions	Had>20MeV	NEq/cm^2/Yr
Low Z Inner	-3%	-1%	0%	0%	0%	0%
Mid Z Inner	-4%	-2%	2%	0%	0%	0%
High Z Inner	0%	0%	8%	0%	0%	0%
Low Z Outer	-3%	-3%	3%	-2%	0%	-2%
Mid Z Outer	-3%	-2%	6%	-1%	-1%	-2%
High Z Outer	-4%	-3%	1%	-2%	-1%	-2%

Table 8.1 Comparison of the new and old moderator design.

As we see, neutron rates in the new design are slightly better than in the old, and photon rates are slightly worse, but none of the changes are significant. The new overall design concept was therefore adopted as the December, 2001, baseline.

8.2.1 Optimisation of Inner JM Components and Dimensions

The next studies focussed on understanding the importance of each plug, and on optimising the dimensions:

Option: Omit the LAR PLUG

We can see from Table 8.2 that the LAR PLUG, lining the alcove with 5 cm of poly, is essential for reducing neutron backgrounds.

PERCENT CHANGE FOR: Dec JM1 / Dec01 Baseline

Plug dimns: LAR **Omitted**, FCAL 30 cm X 13.5 cm, PUMP 5 cm X 6.7 cm

	N<100keV	N>100keV	Photons	Pions	Had>20MeV	NEq/cm^2/Yr
Low Z Inner	11%	3%	1%	0%	0%	0%
Mid Z Inner	24%	10%	1%	0%	0%	1%
High Z Inner	59%	26%	2%	0%	0%	4%
Low Z Outer	8%	5%	3%	0%	0%	3%
Mid Z Outer	14%	8%	3%	0%	0%	4%
High Z Outer	17%	7%	4%	0%	0%	4%

Table 8.2 Effect of the 5 cm poly LAR PLUG.

After studying the flux maps, we have concluded that the primary source for these neutrons is the inner face of the EMEC. Hadronic showers developing early are spraying neutrons transversely in the direction of the FCAL and beamline. As these cross through the cryostat warm wall toward the beamline, they may be effectively intercepted, moderated, and captured in the doped polyethylene of the LAR PLUG.

Option: Omit the PUMP PLUG

In contrast to the LAR PLUG, the PUMP PLUG has very little effect on the backgrounds. The only effect, as shown in Table 8.3, is seen as a small (2%) increase in neutron flux at High Z Inner, where expected. We interpret this as showing that the pump presents so little material by comparison with other structures that its albedo is negligible. Also this plug does not extend all the way to the inner bore of the LAR PLUG, and is therefore not hermetic. Finally, the LAR PLUG has many times more mass, and is doing the bulk of the moderation in this alcove.

PERCENT CHANGE FOR: Dec JM2 / Dec01 Baseline

Plug dimns: LAR dz X 5 cm, FCAL 30 cm X 13.5 cm, PUMP **Omitted**

	N<100keV	N>100keV	Photons	Pions	Had>20MeV	NEq/cm^2/Yr
Low Z Inner	0%	0%	0%	0%	0%	0%
Mid Z Inner	0%	0%	0%	0%	0%	0%
High Z Inner	2%	0%	0%	0%	0%	0%
Low Z Outer	0%	0%	1%	0%	0%	0%
Mid Z Outer	0%	0%	0%	0%	0%	0%
High Z Outer	0%	0%	0%	0%	0%	0%

Table 8.3 Effect of the pump plug.

Option: Thin the FCAL PLUG from dz = 30 cm to dz = 20 cm

Table 8.4 shows that the FCAL PLUG may be reduced to dz = 20 cm without decreasing its effectiveness.

PERCENT CHANGE FOR: Dec JM3 / Dec01 Baseline

Plug dimns: LAR dz X 5 cm, FCAL 20 cm X 13.5 cm, PUMP 5 cm X 6.7 cm

	N<100keV	N>100keV	Photons	Pions	Had>20MeV	NEq/cm^2/Yr
Low Z Inner	0%	0%	0%	0%	0%	0%
Mid Z Inner	0%	-1%	0%	0%	0%	0%
High Z Inner	1%	0%	0%	0%	0%	0%
Low Z Outer	0%	0%	0%	0%	0%	0%
Mid Z Outer	0%	0%	0%	0%	0%	0%
High Z Outer	0%	0%	0%	0%	0%	0%

Table 8.4 Effect of reducing the length the FCAL plug.

Option: Thin the FCAL PLUG to dz = 10 cm, increase its inner r, and omit PUMP PLUG

Table 8.5 shows that the FCAL PLUG may be reduced further to dz = 10 cm, with increased inner radius, and the PUMP PLUG omitted, with negligible effect on the rates.

PERCENT CHANGE FOR: Dec JM8 / Dec01 Baseline

Plug dimns: LAR dz X 5 cm, FCAL 10 cm X 12.0 cm, PUMP 5 cm X 6.7 cm

	N<100keV	N>100keV	Photons	Pions	Had>20MeV	NEq/cm^2/Yr
Low Z Inner	1%	1%	0%	0%	0%	0%
Mid Z Inner	1%	1%	1%	0%	0%	0%
High Z Inner	3%	2%	1%	0%	0%	0%
Low Z Outer	0%	1%	1%	0%	0%	0%
Mid Z Outer	0%	0%	0%	0%	0%	0%
High Z Outer	0%	0%	0%	0%	0%	0%

Table 8.5 Effect of reducing the radial thickness of the FCAL plug.

8.2.2 Optimisation of the Dopant in the JM Polyethylene

In addition to optimising the shapes and dimensions of the inner JM plugs, we looked into the effect of available dopants on the performance of the JM moderator.

Option: Change to undoped polyethylene in JM disk and plugs

In the extreme, we investigated what would happen if the dopant (in this case LiF) was omitted:

PERCENT CHANGE FOR: Dec 0% Dopant / Dec01 Baseline

	N<100keV	N>100keV	Photons	Pions	Had>20MeV	NEq/cm^2/Yr
Low Z Inner	11%	0%	0%	0%	0%	0%
Mid Z Inner	36%	-1%	1%	0%	0%	0%
High Z Inner	72%	-2%	2%	0%	0%	-1%
Low Z Outer	7%	-1%	3%	-1%	0%	-1%
Mid Z Outer	24%	-2%	6%	-1%	0%	-1%
High Z Outer	60%	-2%	8%	0%	0%	-2%

Table 8.6 Effect of removing the dopant in the JM disks and plug.

It is clear from Table 8.6 that the increase in low energy neutrons and photons in the inner detector would make this option unacceptable.

Option: Increase dopant (LiF) to 10% by weight in JM disk and plugs

In this option, the LiF concentration was increased from 2.7% to 10% by weight. Table 8.7 shows that there is no advantage in doing this, and there are indications that reducing the hydrogen content of the moderator is making the N>100keV flux worse.

PERCENT CHANGE FOR: Dec 10% Dopant / Dec01 Baseline

	N<100keV	N>100keV	Photons	Pions	Had>20MeV	NEq/cm^2/Yr
Low Z Inner	1%	0%	0%	0%	0%	0%
Mid Z Inner	1%	3%	0%	0%	0%	0%
High Z Inner	-1%	7%	0%	0%	0%	1%
Low Z Outer	2%	2%	0%	0%	0%	1%
Mid Z Outer	2%	7%	0%	0%	0%	4%
High Z Outer	-1%	11%	-1%	-1%	1%	6%

Table 8.7 Effect of increasing the dopant concentration in the JM disks and plug.

Option: Change JM plugs dopant from LiF to Boron

As in other regions of the detector, it was not clear whether the best dopant to increase the neutron capture efficiency would be LiF, or boron (with large cross section but at the expense of additional capture gammas).

Table 8.8 shows that polyboron seems to be slightly better in this application than polylithium. We assume that the additional capture gammas are being absorbed effectively in the aluminum cryostat walls of the FCAL alcove. Note that the dopant of the disk was not changed in this study.

PERCENT CHANGE FOR:	Dec JM7 / Dec01 Baseline					
	N<100keV	N>100keV	Photons	Pions	Had>20MeV	NEq/cm^2/Yr
Low Z Inner	-1%	0%	0%	0%	0%	0%
Mid Z Inner	-2%	-1%	0%	0%	0%	0%
High Z Inner	-6%	-1%	1%	0%	0%	0%
Low Z Outer	-1%	0%	0%	0%	0%	0%
Mid Z Outer	-2%	0%	0%	-1%	0%	0%
High Z Outer	-2%	-1%	0%	-1%	0%	-1%

Table 8.8 Effect of changing the JM plug dopant from LiF to Boron.

Option: Change JM disk dopant from LiF to Boron

It was also studied what effect a change of the dopant in the JM disk would have. Figure 8.5 show how the particle flux change when the lithium in the polyethylene is changed to boron. The high-energy (>100 keV) neutron rate that is important for detector damage is unchanged. The photon rate goes up with as much as 10% while the low-energy neutron rate goes down with up to 25%. This trend is what one would expect since boron has a larger neutron capture cross section but produces more photons than lithium. In the JAN03 baseline the dopant of the disk was kept as lithium but during the final engineering phase of the moderator shield it was changed to boron (5% B_4C by weight).

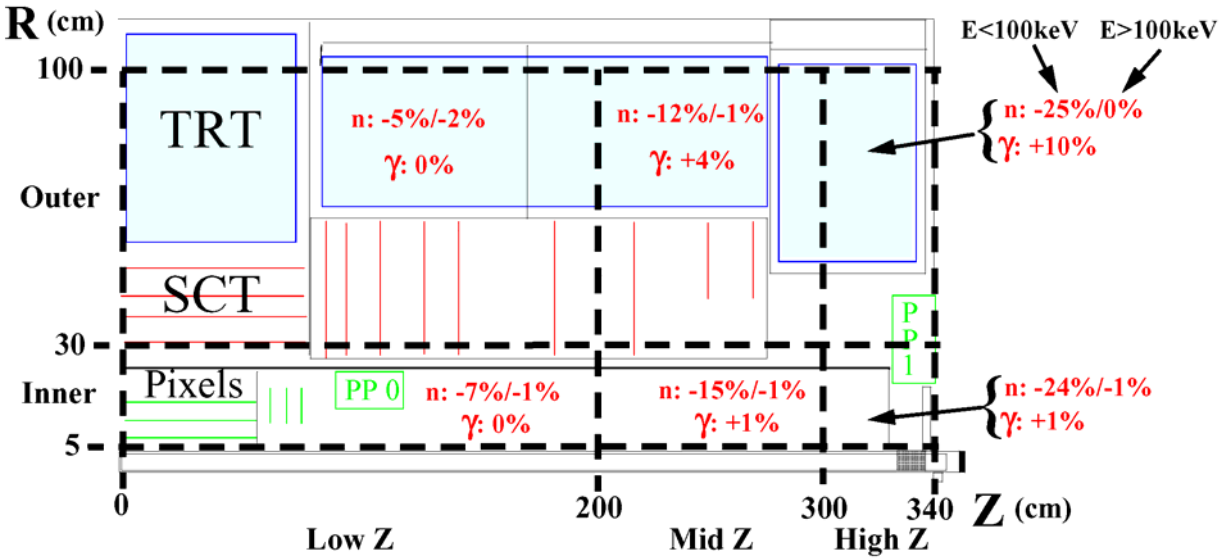

Figure 8.5 The change of neutron and photon rates in the inner detector when the dopant in the JM disk is changed from lithium to boron.

Rates in the JAN03 Baseline Geometry compared to the DEC01 Baseline

Following the JM optimisation studies listed above, it was decided for the new baseline to (1) use boron as the dopant in the JM plugs, leaving the JM disk polylithium, (2) omit the PUMP PLUG, and (3) thin the FCAL PLUG further to dz = 10.0 cm and dr = 12.0 cm, giving a final set of dimensions as follows: Plug dimns: LAR dz X 5 cm, FCAL 10 cm X 12 cm, PUMP omitted. The comparison of the DEC01 with the JAN03 baseline is made in Table 8.9. The rates have crept up just slightly in the current baseline compared to December 2001. Less than half of this increase was caused by the reduction of the FCAL PLUG and the omission of the PUMP PLUG. The rest is due to small changes in the description of the beampipe flanges and ion pump in this region between the December baseline and the present.

PERCENT CHANGE FOR: Jan03 Baseline / Dec01 Baseline

	N<100keV	N>100keV	Photons	Pions	Had>20MeV	NEq/cm^2/Yr
Low Z Inner	2%	1%	0%	0%	0%	0%
Mid Z Inner	4%	3%	2%	0%	1%	0%
High Z Inner	1%	3%	3%	0%	0%	0%
Low Z Outer	1%	1%	2%	0%	0%	0%
Mid Z Outer	3%	2%	1%	0%	0%	1%
High Z Outer	5%	3%	0%	0%	0%	1%

Table 8.9 Relative rate changes between the Dec01 baseline and the Jan03 baseline.

8.3 Optimisation of the JD shielding

Much of the JD region consists of functional and/or structural components (see section 4.1.7). The large disk must be iron (steel) in order to return magnetic flux effectively and provide a 'backbone' for the support of TGC chambers in the small muon wheel. The tube attached to the centre of the disk is made of stainless steel, acting (1) as a support for the sliding hub on its outer surface, (2) as a holder for copper alloy shielding inside its bore, and (3) as the chicane interface to the JTT. (The sliding hub, in turn, supports the "small wheel" detectors.) Geometrical constraints determine most of its major dimensions, and the design goal for this "thin" shielding region is to fill as much of the available JD volume as possible with dense shielding or cladding.

Optimisation of the JD shielding properties has involved simulation of a large number of design variants, where materials (and some dimensions) of the core, cone, hub and cladding have been changed. In many cases, especially if the fractional changes are small, the effects are noticable only in the CSC's, inner TGC's, and inner-forward MDT's, i.e., the detectors nearest to the beamline at the back of the endcap calorimeter. Here we list the changes made, one at a time, relative to the baseline geometry, and report their effects. In each case, only the most important changes to the background rates will be noted. The scoring regions used in these studies are given in Figure 8.2.

Option: The JD copper alloy core is changed to tungsten

In general, increasing the density of material in the innermost shielding for any region is expected to reduce the rates outside the shielding. In this spirit, it has been suggested by a

number of people to try tungsten in place of copper in the core of the JD. Table 8.10 shows that the backgrounds reductions in many regions are in the 15% to 30% range, and that this critical corner affects a large fraction of the muon system volume. However, these gains are not large compared to gains using other tactics, and the cost of tungsten is very large: approximately 1.5 MCHF to change Cu to W in the core of the JD. For this reason, this option is seen as appropriate for a possible future upgrade (in the event that it is needed) rather than something to be incorporated in the baseline.

PERCENT CHANGE FOR: JD Cu to W / Jul01 Baseline

	N<100keV	N>100keV	Photons	Had>20MeV	Counts	Triggers
SW CSC	-14%	-29%	-21%	-30%	-18%	-11%
SW TGC	-10%	-26%	-19%	-33%	-18%	-17%
LW MDT In	-4%	-9%	-2%	-2%	-3%	-5%
LW MDT Mid	-8%	-5%	-4%	-6%	-4%	-4%
BW MDT In	-7%	-7%	-5%	-9%	-1%	19%
B MDT HiZMid	-10%	-22%	-17%	-25%	-15%	-10%
B MDT HiZOut	-11%	-13%	-12%	-14%	-14%	-23%

Table 8.10 Effect of changing the JD core from Cu to W. The trigger statistics is marginal in this comparison.

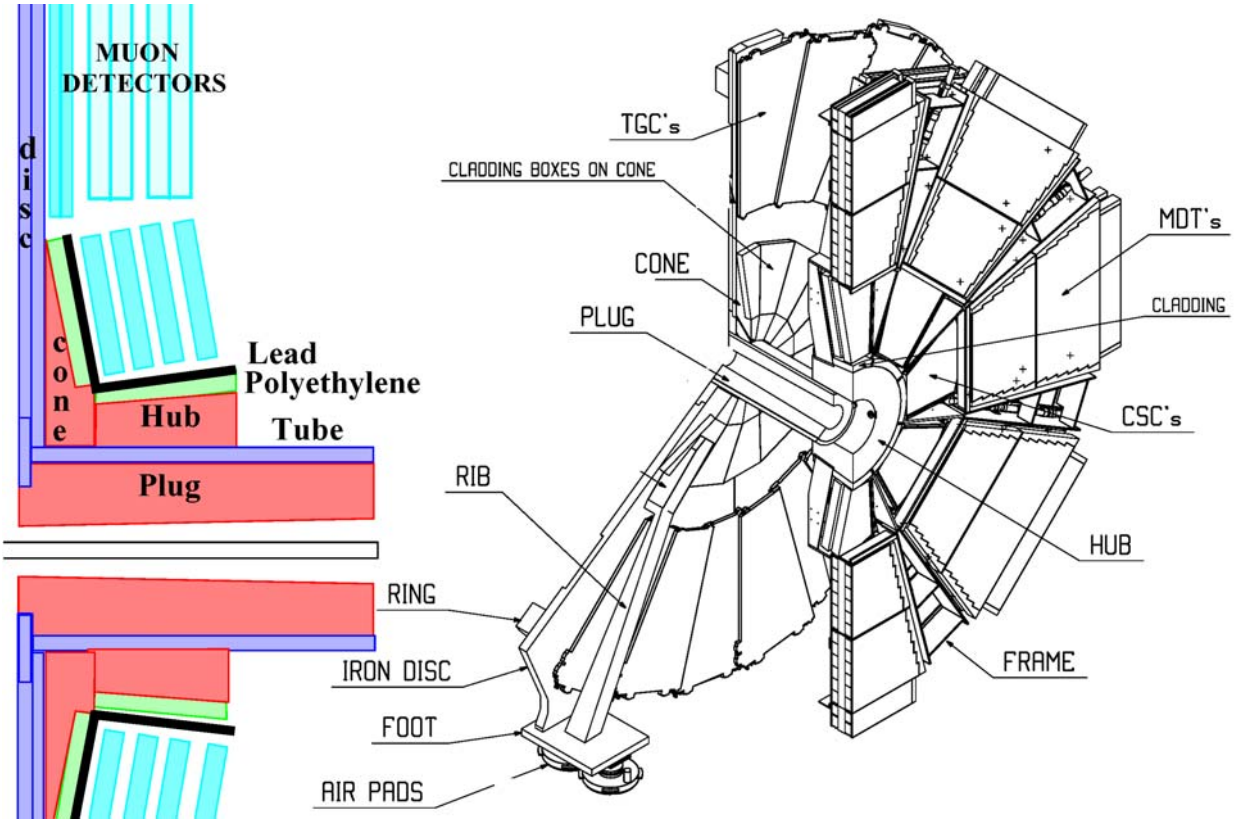

Figure 8.6 The JD region and the muon detectors surrounding it. The drawing on the right shows the Small Muon Wheel in its retracted position which is used when the muon detector is serviced.

Option: The first 1/7th of the JD copper alloy, in z, is changed to tungsten

A compromise solution related to the previous option was also investigated. Only the first 7th, in z, of the JD core Cu was changed to W, to reduce the cost by about a factor of seven. Table 8.11 shows that typical reductions would be in the 5% to 10% range and, as with the option above, this is seen only as a possible future upgrade because of the added cost and complexity.

PERCENT CHANGE FOR: Dec JM1 JD7thW / Dec01 Baseline

	N<100keV	N>100keV	Photons	Had>20MeV	Counts	Triggers
SW CSC	-3%	-9%	-3%	-10%	-3%	-3%
SW TGC	-1%	-7%	-4%	-7%	-7%	-16%
LW MDT In	-2%	3%	0%	2%	1%	3%
LW MDT Mid	-2%	1%	1%	0%	0%	-2%
BW MDT In	1%	8%	2%	0%	1%	-4%
B MDT HiZMid	-2%	-5%	-2%	-5%	-1%	1%
B MDT HiZOut	-2%	-5%	0%	-2%	-1%	-1%

Table 8.11 Effect of a partial change of the JD core from Cu to W. The trigger statistics is marginal in this comparison.

Option: The JD inner bore radius is changed

The hole for the beampipe has a constant radius of 47 mm in the FCAL region. All the shielding elements surrounding the beampipe after the FCAL (the JD-plug , the JT-plug and the JF-core) has a conical hole for the beampipe with a 2.2^0 opening angle. This means that the front part of the JD plug has a radius of 129 mm and that the hole in the JD plug is much larger than the hole in the FCAL.

A study has been made in which the hole in the JD plug was reduced to see if this would improve the background situation. In this simulation the JD-plug had the same hole as the FCAL, i.e, a hole with a fix radius of 47 mm. The results are given in Table 8.12. Instead of protecting the small wheel against background radiation, the additional material at low radius acts as a source of more background. For the large wheel the added material do, however, lower the rates. The overall conclusion is that this is not an improvement.

PERCENT CHANGE FOR: Dec Pb JDBore / Dec01 Baseline

	N<100keV	N>100keV	Photons	Had>20MeV	Counts	Triggers
SW CSC	73%	84%	32%	94%	39%	40%
SW TGC	55%	67%	54%	91%	47%	27%
LW MDT In	8%	-10%	-38%	-17%	-35%	-27%
LW MDT Mid	10%	-6%	-30%	-14%	-26%	-20%
BW MDT In	4%	4%	-12%	-10%	-11%	-15%
B MDT HiZMid	25%	36%	25%	51%	26%	26%
B MDT HiZOut	18%	8%	11%	8%	14%	22%

Table 8.12 Effect of changing the JD inner bore radius.

Option: The JD cone is omitted and cladding placed on the face of the JD disk

The JD cone consists of 16 pieces of copper alloy with cladding. Studies have been made to see if this cone can be simplified. The most drastic change would be to remove the copper cone entirely and only keep the cladding, see Table 8.13. This has not been done in the present baseline geometry because of the roughly 20% increase in rates of N>100keV and Had>20MeV in the CSC region.

PERCENT CHANGE FOR: Dec JM2 JDNoCone / Dec01 Baseline

	N<100keV	N>100keV	Photons	Had>20MeV	Counts	Triggers
SW CSC	10%	17%	8%	23%	17%	32%
SW TGC	1%	13%	6%	20%	5%	2%
LW MDT In	0%	2%	0%	3%	0%	0%
LW MDT Mid	1%	4%	1%	3%	1%	2%
BW MDT In	1%	8%	10%	1%	7%	-2%
B MDT HiZMid	4%	8%	5%	9%	2%	-7%
B MDT HiZOut	3%	5%	3%	6%	4%	4%

Table 8.13 Effect of removing the JD cone and placing cladding on the JD disk.

Option: The JD cone is changed from copper to iron

In the present design the JD cone is made out of a copper alloy. A cheaper alternative would be to make the cone out of cast iron. Table 8.14 shows that such a change would increase the background rate in the sensitive CSC region and the cone has therefore been kept as copper alloy in the present baseline.

PERCENT CHANGE FOR: Dec JM3 JDConeFe / Dec01 Baseline

	N<100keV	N>100keV	Photons	Had>20MeV	Counts	Triggers
SW CSC	27%	10%	7%	3%	8%	5%
SW TGC	12%	5%	6%	1%	5%	1%
LW MDT In	3%	3%	0%	3%	0%	-2%
LW MDT Mid	5%	7%	0%	2%	0%	-8%
BW MDT In	5%	1%	9%	3%	2%	-20%
B MDT HiZMid	8%	4%	7%	1%	3%	-6%
B MDT HiZOut	6%	1%	3%	0%	3%	2%

Table 8.14 Effect of changing the JD cone from a Cu alloy to Cast Iron.

Option: The JD cladding on the cone and hub is replaced by copper alloy

Early studies by Alfredo Ferrari using standalone FLUKA showed that backgrounds of total neutron and photon fluxes in the CSC/TGC region could be greatly reduced by replacing the outer few cm of the JD hub and cone with cladding material. Studies at that time used a cladding layer of polyethylene doped with LiF to moderate and then capture neutrons, followed by a layer of lead to absorb photons resulting from neutron capture or from the tails of electromagnetic showers. The present design uses borated polyethylene instead of poly-LiF, since boron has a

larger captured cross section, and in this location the lead removes the more-energetic photons resulting from neutron capture in boron.

At first, it may seem foolish to remove dense material (Cu) in one of the thinnest shielding regions of ATLAS. But Table 8.15 shows that the bad effects of the neutron and photon backgrounds in this region greatly overshadow a small increase that occurs in the hadrons above 20 MeV.

PERCENT CHANGE FOR: Jan03 JD Clad Cu / Jan03 Baseline

	N<100keV	N>100keV	Photons	Had>20MeV	Counts	Triggers
SW CSC	223%	164%	64%	-17%	61%	19%
SW TGC	139%	98%	37%	-15%	39%	9%
LW MDT In	18%	2%	2%	0%	1%	0%
LW MDT Mid	20%	-2%	5%	-2%	2%	-8%
BW MDT In	5%	0%	8%	-1%	4%	-8%
B MDT HiZMid	56%	22%	23%	-8%	22%	9%
B MDT HiZOut	40%	1%	19%	-3%	20%	18%

Table 8.15 Effect of changing the JD hub cladding to Cu

In the JAN03 baseline, the thickness of the doped poly layer is 5.0 cm, and the lead is 3.0 cm. These numbers have been found by methodically varying the thicknesses of these two layers in simulation, optimizing the reduction of neutron and photon fluxes while keeping the increase in high energy hadron rates within acceptable limits. All layers must be present in sufficient thickness to be effective in their given roles: copper (with a shorter radiation length than iron), to attenuate EM shower tails and hadronic punchthrough; polyethylene, to moderate neutrons; dopant, to capture neutrons that have been moderated; and lead, to absorb the final photons. And given the spatial constraints in this corner of the experiment, this is an optimisation in many dimensions.

A Series of Options: The JD cladding materials are varied

The cladding situated on the surfaces of the hub and the cone has been studied in many simulations. The cladding consists of a layer of polyethylene which moderates the energies of neutrons so that they can be captured by dopant in the same layer. This capture process creates new photons which are stopped by a photon filter made of steel or lead.

In the first study, the photon filter material was changed from lead to steel. The result was a small decrease of the neutron rate in the small wheel while the photon rate increased sharply. The large photon rate change in the small wheel was not seen in the barrel, and the choice of photon filter in the small wheel has apparently not much influence on the background rate in the barrel.

Table 8.16 gives the result of the simulation[7]. From this study it was obvious that, even if more neutrons are produced in the heavier lead layer, the photon filter in the JD had to be made of lead since it stops photon more effectively than steel.

[7] *In this simulation the cladding on the JF was also changed and the rate changes in the LW and BW regions were not due to the change of the JD cladding. These values are therefore not given in this table nor in the following tables in this section.*

PERCENT CHANGE FOR: Nov Clad Pb>Fe / Nov Baseline

	N<100keV	N>100keV	Photons	Had>20MeV	Counts	Triggers
SW CSC	-12%	-17%	111%	-1%	78%	45%
SW TGC	-5%	-11%	39%	-1%	30%	19%
B MDT HiZMid	-4%	-7%	5%	1%	2%	-6%
B MDT HiZOut	-3%	-2%	2%	-1%	2%	3%

Table 8.16 Comparison of a lead with a steel photon filter.

In another study, the boron dopant in the baseline configuration was removed. The result given in Table 8.17 shows a very high increase of thermal neutron and photon rates in the small wheel and the barrel. The conclusion was that the dopant is clearly needed.

PERCENT CHANGE FOR: Dec 0% Dopant / Dec01 Baseline

	N<100keV	N>100keV	Photons	Had>20MeV	Counts	Triggers
SW CSC	120%	-5%	86%	0%	68%	37%
SW TGC	36%	-4%	74%	0%	57%	36%
B MDT HiZMid	15%	-2%	45%	0%	36%	21%
B MDT HiZOut	9%	-1%	36%	0%	32%	30%

Table 8.17 Effect of removing the dopant of the cladding.

One can then try the opposite by increasing the dopant from 5% to 10% (by weight) but this will also increase the background rate as seen in Table 8.18. The reason is that too much polyethylene has now been turned into boron and this lowers the moderating capabilities of the cladding.

PERCENT CHANGE FOR: Dec 10% Dopant / Dec01 Baseline

	N<100keV	N>100keV	Photons	Had>20MeV	Counts	Triggers
SW CSC	7%	4%	-1%	0%	-4%	-12%
SW TGC	4%	2%	0%	0%	-2%	-10%
B MDT HiZMid	9%	0%	5%	0%	2%	-5%
B MDT HiZOut	10%	1%	5%	1%	8%	18%

Table 8.18 Effect of increasing the concentration of dopant.

A simulation was also made in which the polyethylene was loaded with lead and doped with boron and the photon filter on the outside was removed (Table 8.19). With 62% lead (by weight) the neutron rates went down but the photon and counting rate went up:

PERCENT CHANGE FOR: JMPP JDBPPb O2Fe / Feb Baseline

	N<100keV	N>100keV	Photons	Had>20MeV	Counts	Triggers
SW CSC	-23%	-26%	41%	1%	32%	34%
SW TGC	-10%	-18%	9%	0%	8%	16%
B MDT HiZMid	-7%	-3%	0%	0%	-1%	-3%
B MDT HiZOut	-7%	-2%	-3%	0%	-4%	-5%

Table 8.19 Study of a single cladding layer made of Lead and Boron loaded polyethylene.

If the lead part was increased to 87% then both the neutron and the photon rates went up and the proposal to load the polyethylene with lead was therefore rejected. See Table 8.20.

PERCENT CHANGE FOR: JMPP Dens JDBPPb / Feb Baseline

	N<100keV	N>100keV	Photons	Had>20MeV	Counts	Triggers
SW CSC	44%	10%	18%	1%	19%	17%
SW TGC	22%	3%	5%	1%	8%	10%
B MDT HiZMid	12%	1%	5%	0%	4%	-2%
B MDT HiZOut	7%	-2%	2%	0%	2%	4%

Table 8.20 Effect of increasing the Lead part to 87% in the polytethylene.

In another study the boron dopant was changed to cadmium which has a larger capture cross section. The neutron rate then went down as expected but capture photons were created which increased the photon rate significantly, as seen in Table 8.21:

PERCENT CHANGE FOR: noJMFCPl CadClad5 / Feb Baseline

	N<100keV	N>100keV	Photons	Had>20MeV	Counts	Triggers
SW CSC	-54%	-59%	39%	-21%	35%	55%
SW TGC	-30%	-41%	-1%	-18%	-2%	9%
B MDT HiZMid	-20%	-19%	-8%	-10%	-8%	-1%
B MDT HiZOut	-18%	-9%	-11%	-4%	-12%	-14%

Table 8.21 Effect of changing the Boron dopant to Cadmium.

If only the last 5mm of the polyethylene was doped with cadmium there was no increase in the photon rate but the decrease of the neutron rate was on the other hand modest (see Table 8.22).

PERCENT CHANGE FOR: Feb Cad Mid 5mm / Feb Baseline

	N<100keV	N>100keV	Photons	Had>20MeV	Counts	Triggers
SW CSC	-16%	-9%	0%	-2%	0%	1%
SW TGC	-7%	-6%	-2%	-2%	0%	6%
B MDT HiZMid	-4%	0%	-1%	-1%	0%	5%
B MDT HiZOut	-4%	0%	-2%	0%	-1%	3%

Table 8.22 Effect of a partial replacement of Boron by Cadmium.

The overall conclusion from the simulations with cadmium as a dopant was that the gain in reduced particle rate was not worth the additional problem of dealing with this toxic substance.

A Series of Options: The JD cladding thickness is varied

The original cladding on the JD cone and hub consisted of 7 cm of polyethylene and 3 cm of lead. Since the standard thickness of the polyethylene that we want to purchase is 8 cm, a simulation was made with this thickness, i.e., 1 cm of copper was changed to polyethylene. The effect of going from 7 cm to 8 cm was insignificant, as seen in Table 8.23.

PERCENT CHANGE FOR: Nov Clad 8cm / Nov Baseline

	N<100keV	N>100keV	Photons	Had>20MeV	Counts	Triggers
SW CSC	-7%	-1%	1%	3%	1%	2%
SW TGC	-3%	0%	0%	1%	0%	1%
B MDT HiZMid	-3%	0%	-1%	3%	-1%	-1%
B MDT HiZOut	-2%	-2%	-3%	1%	-2%	0%

Table 8.23 Effect of changing the thickness of the polyethylene.

A study was also made in which the polyethylene thickness was decreased instead of increased. The 7 cm polyethylene layer was reduced to 5 cm and the copper parts were increased by 2 cm. The results are given in Table 8.24. The rates changed very little and the final manufactured design has 7 cm of polyboron on the hub and 5 cm on the cone. Both with a 3 cm thick photon filter made of lead.

PERCENT CHANGE FOR: Nov R=155 P5cm / Nov Baseline

	N<100keV	N>100keV	Photons	Had>20MeV	Counts	Triggers
SW CSC	4%	-5%	1%	-1%	0%	-3%
SW TGC	2%	-6%	1%	-1%	0%	-1%
B MDT HiZMid	-1%	-3%	-1%	1%	-2%	-4%
B MDT HiZOut	-1%	-2%	-1%	0%	-1%	0%

Table 8.24 Effect of decreasing the polyethylene thickness.

8.4 Optimisation of End-cap Toroid Shield, JT

As described in section 4.1.8 above, the forward toroid coil cryostats intrude into the muon acceptance along the line $|\eta| = \pm 2.7$, unlike other objects in the forward muon system. They in turn require a cylindrical support tube at inner radius, which constrains the shielding to stay within its own inner radius. Near the beamline, the shield must stay outside the $|\eta| = \pm 4.65$ line to allow for mechanical clearance during access. These two requirements lead to an exceptionally thin region for the placement of radiation shielding inside the JT.

This very constrained space does not permit "optimal" shielding design, and, as in the JD region, tradeoffs must be made among the rates of various background particle species. Under these circumstances, copper, though more expensive than iron or steel, is the preferred dense shielding material because of its shorter radiation length (for comparable interaction length), and because its neutron resonance windows are not as transparent as those of iron or steel.

The most major design change in the JT region since 1998 was the removal of epoxy-LiF "blocks" inside the body of the JT toroid structure approximately 1.5 m from the beamline, in favor of a 4.0 cm doped polyethylene layer just inside the outer radius of the support tube (replacing of copper shield). One problem with the blocks was that they introduced appreciable mass to be supported along with the cryostat. They would also have been costly and difficult to install (manually) in the confined spaces. And finally, they did not offer full containment of backgrounds from the beamline, in either phi or z. The phi coverage was slightly more than 50%, and the blocks ended well before the front and back outer walls of the toroid, leaving large gaps at each end. Like water in a leaky barrel, neutrons were having no difficulty finding paths through these gaps, and this "lumped" approach to the shielding was inefficient.

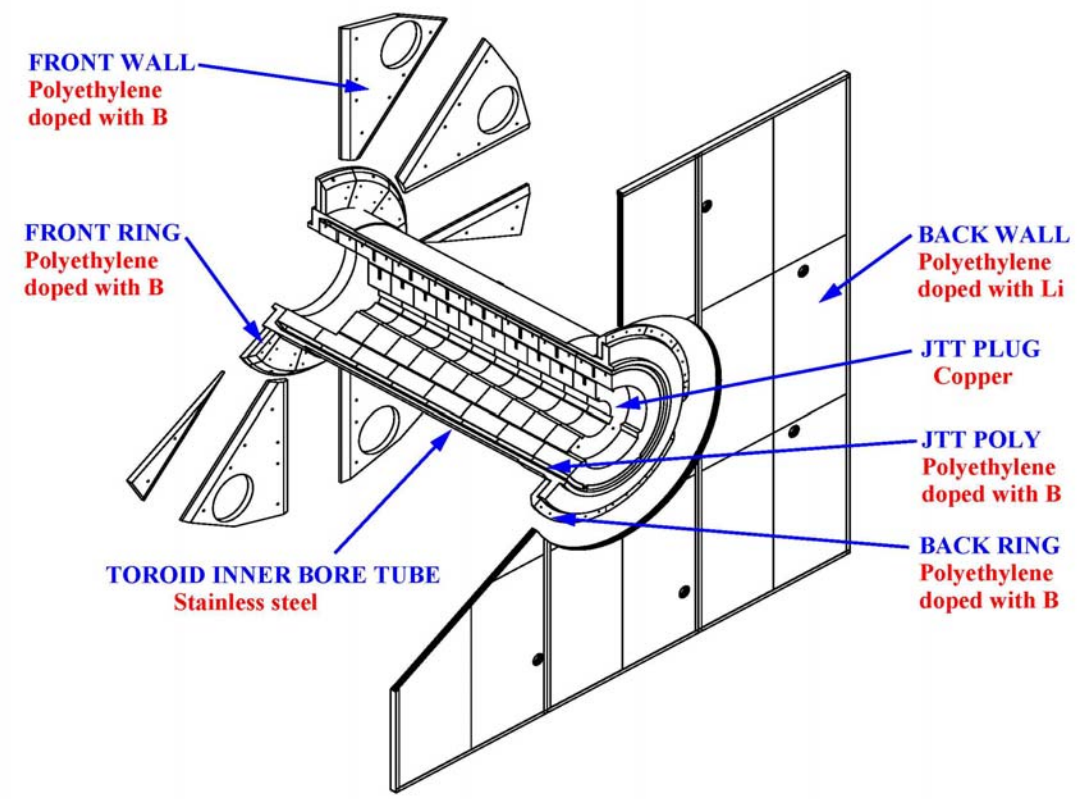

Figure 8.7 The various JT shielding elements in the endcap toroid region.

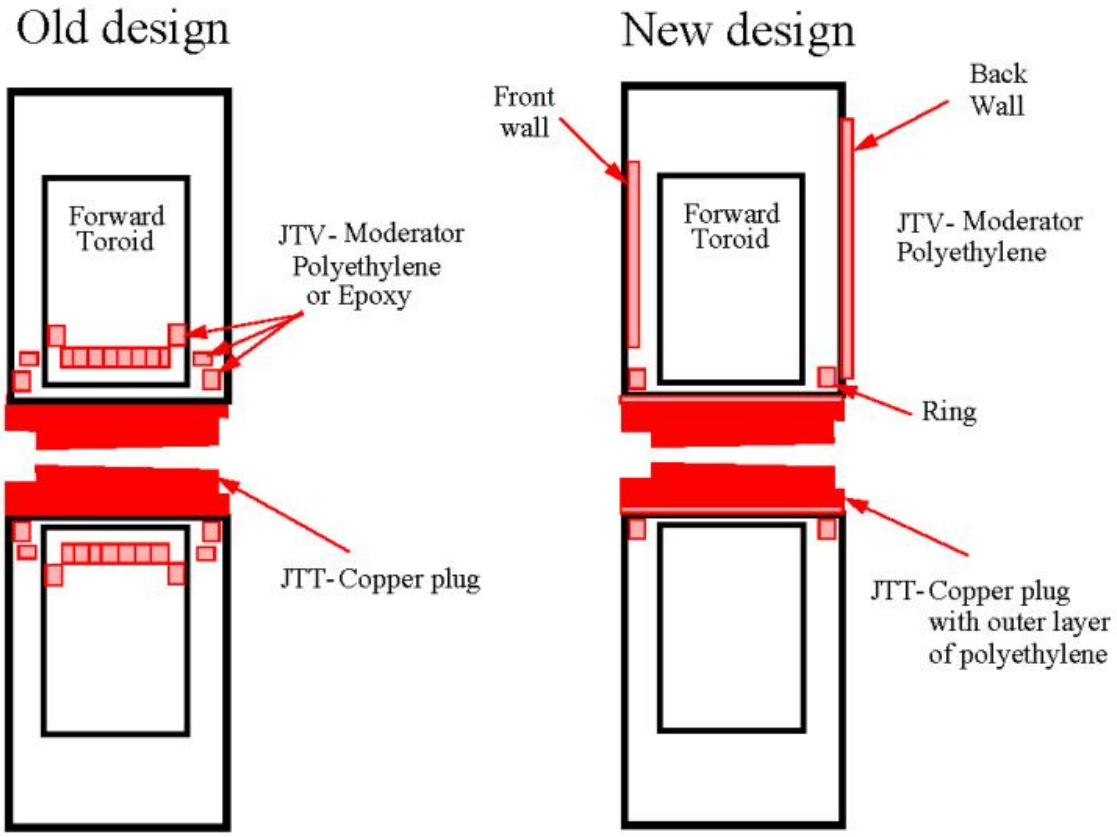

Figure 8.8 Change in the cladding design

As in studies of the JD region, it was somewhat surprising to see that replacing dense copper by doped polyethylene in this "thin" shield gave greatly improved results—for essentially the same reasons. In the JTT, polyboron may be used without a lead layer because it is surrounded by the stainless steel of the toroid inner bore tube. In addition, photons must pass through centimeters of aluminum in the JT walls and thermal shields before reaching muon detector elements.

Figure 8.7 shows the design of the JT shielding in the JAN03 baseline. The JT shielding is divided into two parts. The JTT part is the plug surrounding the beampipe. On the outside of this plug is the layer of polyethylene which works as a neutron moderator and which is also part of the JTT. The second part of the JT shielding is called the JTV and consist of the various polyethylene layers situated inside and outside the endcap toroid cryostat. These parts are called the front and back wall and the front and back ring. In the original design of the JT there was no cladding around the plug or on the walls of the toroid cryostat. Instead there was cladding between the coils of the toroid as indicated in Figure 8.8.

The evolution of the cladding design into the present one has been a step by step procedure which included very many simulations. It is impossible to present all of them in this document and therefore a selection of simulations showing the influence of different shielding parameters will be given.

The effect on the rates of high energy neutron (>100 keV), high energy hadrons (>20 MeV) and photons in the inner region of the Large wheel (LW MDT In) is summarized in Table 8.25 and Figure 8.9.

Simulation option	R(JF)	Polyethylene JTT	JTV	JF	JF shape	Flange	Rate n	Rate Had	Rate Pho
1. TP43	170	0/0	0	30+Pb	cone	no	730	226	11.6
2. July baseline	165	7-4	0	10+Pb	cone	no	1870	420	11.9
3. Aug baseline	165	7/0	4	10+Pb	cone	no	1010	340	12.2
4. Aug JDJD conical	165	7/0	4	10+Pb	cone	no	1030	324	12.7
5. Aug smaller JF	165	7/0	4	10+Pb	cyl	no	1060	367	12.3
6. Sep JDJF con R1575	158	7/0	4	10+Pb	cone	no	1100	389	12.7
7. Sep JDJF conical	150	7/0	4	10+Pb	cone	no	1280	455	13.0
8. Sep smaller JF	150	7/0	4	10+Pb	cyl	no	1330	417	12.5
9. Sep JTBack SmallJF	150	7/2	4	10+Pb	cyl	no	1360	499	12.0
10. Oct JT 2cm	150	2/2	4	10+Pb	cyl	no	1320	491	12.1
11. Sep JT 4cm SmallJF	150	4/4	4	10+Pb	cyl	no	1400	526	11.5
12. Oct baseline	150	4/4	4	10+Pb	cyl	no	1290	523	11.7
13. Nov baseline	150	4/4	4	10+Pb	cyl	yes	1400	537	11.6
14. Nov Clad Pb>Fe	150	4/4	4	10+Fe	cyl	yes	1250	534	12.3
15. Nov clad 8cm	150	4/4	8	10+Pb	cyl	yes	1190	493	11.2
16. Nov JF r=155	155	4/4	4	10+Pb	cyl	yes	1290	488	11.4
17. Nov R=155 P5cm	155	4/4	4	5+Pb	cyl	yes	1320	456	11.4
18. Dec baseline	155	4/4	8	5+Fe	cyl	yes	951	411	11.7

where
R(JF) = The radius in cm at the front part of the JF
Poly JTT = Thickness in cm of polyethylene at the front/back part of the JTT
Poly JTV = The thickness of polyethylene on the back wall of the toroid
Poly JF = The thickness of polyethylene at the front part of the JF
JF shape = Cone means conical shape, Cyl means cylindrical shape
Flange = Beampipe flange added at z=13m
Rate n = Rate of neutrons > 100 keV in Hz/cm^2
Rate Had = Rate of hadrons > 20 MeV in Hz/cm^2
Rate Pho = Rate of photons in kHz/cm^2

Table 8.25 Effect of the various cladding options on neutron (>100 keV), hadron (>20 MeV) and photon rates.

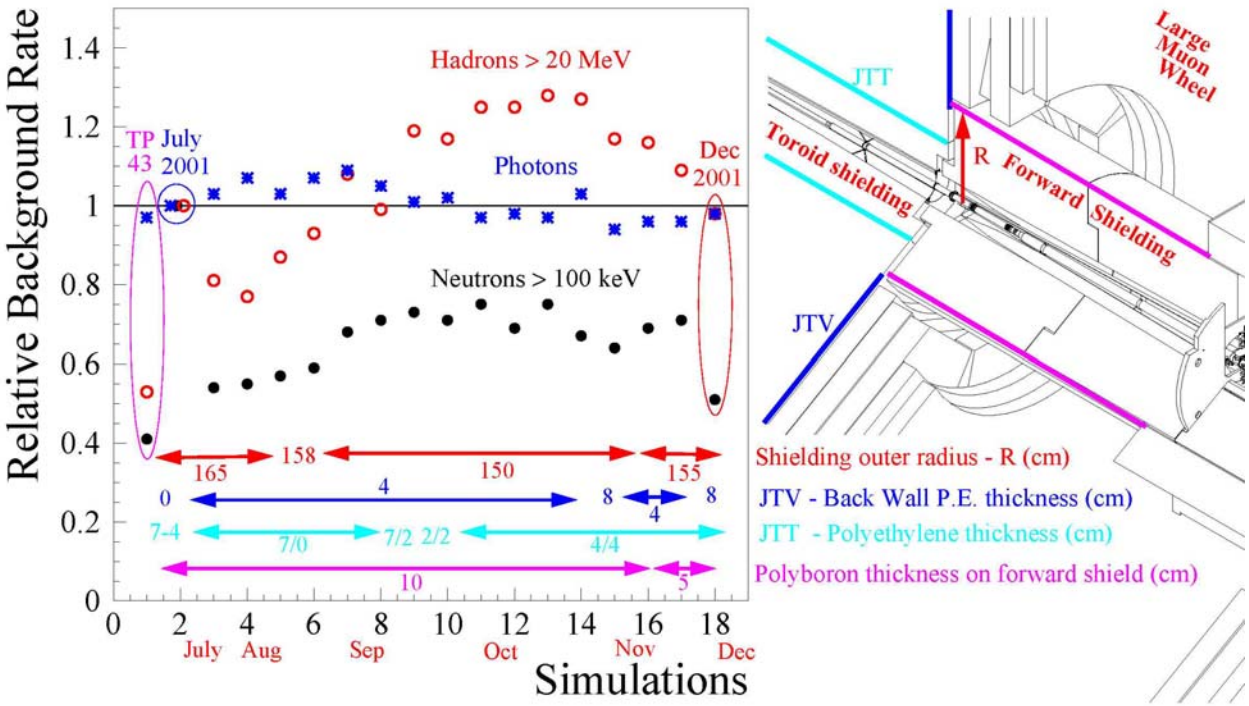

Figure 8.9 Relative neutron, hadron and photon background rate as a function of the cladding options described in Table 8.25.

8.4.1 Optimisation of shielding inside the toroid bore tube, JTT

Having given an overview of the optimization process, we now give more detail on a few of the crucial JTT simulations.

The beampipe hole is enlarged

The hole for the beampipe in the JD, JT and JF is conical with a 2.2 degree opening angle. Simulations have been made in which the hole has been increased to see if this would lower the background rates. Below is the results from a simulation in which the bore in the JTT was changed in such away that the radius was increased by 3 cm in the front and nothing in the back. The result was not encouraging, as shown in Table 8.26.

PERCENT CHANGE FOR: Aug SmallJF LargeB / Aug Smaller JF

	N<100keV	N>100keV	Photons	Had>20MeV	Counts	Triggers
SW CSC	7%	6%	9%	8%	9%	8%
SW TGC	5%	7%	7%	9%	7%	6%
LW MDT In	18%	22%	8%	21%	9%	13%
LW MDT Mid	14%	17%	9%	16%	11%	15%
BW MDT In	5%	1%	9%	2%	7%	-1%
B MDT HiZMid	12%	7%	10%	10%	7%	-3%
B MDT HiZOut	12%	12%	12%	11%	10%	1%

Table 8.26 Effect of enlarging the beam pipe hole.

Change copper alloy in the JTT to pure copper

Practicality and economy determine that most shielding components made of copper must be made of cast copper alloys including a few percent each of metals such as zinc, tin, and lead. However, the TAS collimator is being fabricated from C11000 copper, which is more than 99.9% pure, and of higher density than the alloys. For this reason, we simulated an option with the JTT copper replaced by C11000. As Table 8.27 illustrates, rates improve in the 5-10% range for all tabulated backgrounds, but the present judgement is that the cost of C11000 copper is too high, relative to advantages, to accept this option.

PERCENT CHANGE FOR: Jan03 JTTPureCu / Jan03 Baseline

	N<100keV	N>100keV	Photons	Had>20MeV	Counts	Triggers
SW CSC	-2%	-3%	-1%	0%	0%	5%
SW TGC	-3%	-4%	-4%	-2%	-3%	-2%
LW MDT In	-12%	-4%	-3%	-7%	-2%	2%
LW MDT Mid	-12%	-9%	-5%	-8%	-5%	-6%
BW MDT In	-2%	0%	-1%	-3%	-3%	-9%
B MDT HiZMid	-13%	-6%	-9%	-5%	-8%	-3%
B MDT HiZOut	-12%	-10%	-9%	-7%	-7%	1%

Table 8.27 Effect of changing Brass to Pure Copper.

Change the JTT polyboron layer to copper

In this option, the 4.0 cm doped polyethylene was omitted and replaced with copper, as in the old concept for shielding in this region. The effects of this replacement are very similar to the effects in the JD: large increases in the neutrons and photon backgrounds, with small reductions in the hadrons above 20 MeV. The effects extend all the way to the outside of the cavern and the barrel region and such a change would be completely unacceptable, as shown in Table 8.28.

PERCENT CHANGE FOR: Jun02 No JTT 4cmPly / Jun02 Baseline

	N<100keV	N>100keV	Photons	Had>20MeV	Counts	Triggers
SW CSC	72%	16%	5%	0%	12%	12%
SW TGC	103%	24%	17%	-2%	25%	18%
LW MDT In	149%	2%	20%	-13%	23%	29%
LW MDT Mid	203%	3%	43%	-14%	48%	43%
BW MDT In	66%	0%	61%	-3%	56%	43%
B MDT HiZMid	192%	35%	85%	-7%	86%	53%
B MDT HiZOut	208%	48%	96%	-10%	98%	57%

Table 8.28 Effect of changing the boron cladding to copper.

Vary the thickness of the polyethylene layer

Several studies have been made to determine an optimal thickness of the polyethylene layer in the JTT. The thickness has to be chosen as a trade-off between higher hadron rates if the layer is made thicker and higher neutron and photon rates if the layer is made thinner. In the table below is given, as an example, a comparison between a layer which is 4 cm thick (the baseline scenario) and a layer which is 7 cm thick in the first half and 4 cm thick in the second half of the JTT. The differences, as shown in Table 8.29, are small and go in different directions in different scoring regions and for different particle background.

PERCENT CHANGE FOR: Sep JTBack SmallJF / Sep JT 4cm SmallJF

	N<100keV	N>100keV	Photons	Had>20MeV	Counts	Triggers
SW CSC	-6%	-1%	6%	-1%	3%	-1%
SW TGC	-2%	0%	2%	-5%	3%	-1%
LW MDT In	9%	-3%	4%	-5%	3%	-1%
LW MDT Mid	12%	0%	3%	-3%	3%	1%
BW MDT In	8%	0%	5%	9%	4%	0%
B MDT HiZMid	11%	4%	4%	3%	-1%	-25%
B MDT HiZOut	11%	6%	6%	3%	8%	11%

Table 8.29 Effect of changing the thickness of the polyethylene layer.

The compilation of 18 simulations that is given in Table 8.29 can also be used to study the dependence of the rate on the JTT polyethylene thickness. Simulation 8, 9, 10 and 11 are made with respectively 7 cm P.E. in the first half + no P.E. in the second half, 7 cm P.E. in the first half + 2 cm P.E. in the second half, 2 cm P.E. everywhere and 4 cm of P.E. everywhere. The rates for the various simulations give the impression that simulation 9, 10 and 11 are not significantly different while simulation 8 with no P.E. in the second half is best. The table does not, however, give the rate for low energy neutrons which almost double when the P.E. is removed.

Increase the JTT tolerance gaps in the baseline to 2 cm

This study explores the effects of introducing large gaps in the JTT to accommodate mechanical tolerances. The current design assumes that the polyboron layer will be wrapped or laminated onto the JTT core copper shield without a gap, and that the tolerance gap between the polyboron and the JTT support tube is 1.0 cm. In this option, a 2.0 cm gap was introduced between the poly and copper, and the 1.0 cm gap was increased to 2.0 cm. The resulting 3.0 cm radial material loss of copper shows up as 5% to 15% increase in background in almost all regions and estimators, and should be avoided if possible, as illustrated in Table 8.30.

PERCENT CHANGE FOR: Jan03 JTTol2cm / Jan03 Baseline

	N<100keV	N>100keV	Photons	Had>20MeV	Counts	Triggers
SW CSC	4%	1%	4%	1%	5%	6%
SW TGC	5%	5%	5%	3%	6%	12%
LW MDT In	11%	10%	4%	13%	7%	21%
LW MDT Mid	13%	14%	7%	15%	9%	15%
BW MDT In	5%	8%	7%	0%	14%	38%
B MDT HiZMid	11%	11%	10%	9%	8%	2%
B MDT HiZOut	12%	12%	12%	13%	11%	9%

Table 8.30 Effect of the tolerance gaps in JTT.

8.4.2 Optimisation of Polyethylene Shielding located Directly on the Toroid, JTV

A number of simulations have been done to optimize shielding outside the support tube, and to vary the materials.

Thicken the JT front ring

The Jan03 Baseline has a polyboron ring on the front of the JT support tube with a Z thickness of 8 cm. In this option, the ring is thickened in Z to 22 cm, the value it had in the Jun02 Baseline. Thickening this ring reduces low energy fluxes in the Small Wheel region, and elsewhere, by a few percent, as shown in Table 8.31.

PERCENT CHANGE FOR: Jan03 JTV22cmFRing / Jan03 Baseline

	N<100keV	N>100keV	Photons	Had>20MeV	Counts	Triggers
SW CSC	-3%	-4%	-5%	0%	-5%	-7%
SW TGC	-2%	-4%	-4%	-1%	-4%	-6%
LW MDT In	-2%	-1%	-3%	0%	-3%	-8%
LW MDT Mid	-1%	-1%	-2%	0%	-3%	-7%
BW MDT In	0%	4%	-2%	-4%	-4%	-10%
B MDT HiZMid	-3%	-2%	-2%	0%	-2%	-2%
B MDT HiZOut	-2%	-2%	-2%	0%	0%	8%

Table 8.31 Effect of thickening the JT front ring.

Omit the 8 cm JT front ring

In this option, the front ring is omitted. This has the opposite effect of the option above, worsening the fluxes slightly, as shown in Table 8.32.

PERCENT CHANGE FOR: Jan03 JTVNoFRing / Jan03 Baseline

	N<100keV	N>100keV	Photons	Had>20MeV	Counts	Triggers
SW CSC	5%	3%	-1%	0%	-3%	-8%
SW TGC	4%	2%	1%	0%	0%	-3%
LW MDT In	3%	-4%	-2%	0%	-1%	2%
LW MDT Mid	3%	-4%	0%	-1%	0%	0%
BW MDT In	0%	0%	1%	-6%	4%	15%
B MDT HiZMid	2%	0%	1%	0%	0%	-1%
B MDT HiZOut	2%	-2%	0%	0%	0%	3%

Table 8.32 Effect of removing the JT front ring.

Omit the JT front moderator wall

The Jun02 Baseline was identical to the Jan03 Baseline except for two items:
(1) there was no 8cm thick moderator sheets inside the endcap toroid (the JT front wall) and
(2) the front ring was 22 cm thick.
As the studies above show, number (2) has little effect compared to the effects of (1) that we see below, so we use the Jun02 Baseline to study the impact of omitting the JT front moderator wall.

The primary purpose of this moderator is to reduce neutron background flux coming throught the JT bore tube. In the baseline, this moderator is polyboron. In the Small Wheel region, the front facing has the largest effect on reduction of rates in the TGC. This is because the wall begins at an inner radius of 1.5 m, and offers less protection to the CSC's. Table 8.33 summarizes the changes.

On the other hand, this moderator is intercepting the upstream surface of the large plume of radiation emerging from the JT bore, and its effects are seen well outside the JT region. Since the low energy neutron flux in the Large Wheel involves a "gaslike" flow of neutrons, the moderation of the front face affects neutron rates hitting the back face. As a result, the rates in the Large Wheel are reduced by more than 15%. Similarly, low energy neutron rates in the muon barrel region outside the JT are reduced by more than 20% by the front moderator.

Photon rates are more complex. In the Small Wheel, they are increased by 4% because of neutron capture gammas created in the front moderator, while in the Large Wheel they are reduced because of the reduced flow of neutrons hitting the JT rear face.

High energy directional fluxes, such as Had>20 MeV, are almost unchanged.

PERCENT CHANGE FOR: Jun02 Baseline / Jan03 Baseline

	N<100keV	N>100keV	Photons	Had>20MeV	Counts	Triggers
SW CSC	10%	5%	-4%	-1%	-2%	-1%
SW TGC	26%	15%	-4%	0%	-2%	-5%
LW MDT In	15%	-1%	0%	1%	-1%	-6%
LW MDT Mid	18%	0%	2%	0%	1%	-2%
BW MDT In	6%	-1%	3%	0%	2%	0%
B MDT HiZMid	23%	5%	10%	0%	12%	14%
B MDT HiZOut	23%	5%	11%	1%	13%	15%

Table 8.33 Effect of removing the JTV front moderator wall.

Omit front and back JTV walls

Here, the polyboron moderator inside the JT front face, and the polylithium moderator on the back of the JT back face are removed. There is a significant increase in backgrounds in all tabulated regions, with the Large Wheel being notable for its 250% increase in low energy neutrons. These facings are clearly essential to the reduction of backgrounds in the muon system.

PERCENT CHANGE FOR: Jan03 JTVNoFacings / Jan03 Baseline

	N<100keV	N>100keV	Photons	Had>20MeV	Counts	Triggers
SW CSC	13%	3%	-5%	0%	-2%	-1%
SW TGC	27%	15%	-4%	0%	-1%	-3%
LW MDT In	251%	89%	5%	11%	6%	1%
LW MDT Mid	101%	42%	14%	16%	15%	8%
BW MDT In	25%	4%	14%	0%	9%	-8%
B MDT HiZMid	30%	8%	16%	3%	13%	0%
B MDT HiZOut	30%	5%	16%	3%	16%	10%

Table 8.34 Effect of removing both back and front moderator walls.

Omit the JTV back polyethylene wall

An 8 cm thick polyethylene wall doped with Lithium has been added to the back wall of the toroid. Boron cannot be used as as dopant since it is not possible to install a photon filter in this region.The table below show the large increase in neutron rates which occur if this wall is removed from the baseline. The introduction of this wall clearly makes a significant improvement, as seen in Table 8.35.

PERCENT CHANGE FOR: Jun02 No JT BackCld / Jun02 Baseline

	N<100k	N>100k	Photons	Had>20M	Counts	Triggers
SW CSC	0%	-1%	-1%	0%	-1%	-1%
SW TGC	0%	-1%	-2%	0%	0%	-4%
LW MDT In	198%	94%	5%	11%	10%	23%
LW MDT Mid	64%	43%	13%	16%	15%	17%
BW MDT In	14%	12%	10%	-1%	11%	15%
B MDT HiZMid	1%	0%	2%	0%	0%	-8%
B MDT HiZOut	2%	0%	4%	1%	4%	4%

Table 8.35 Effect of JTV back wall.

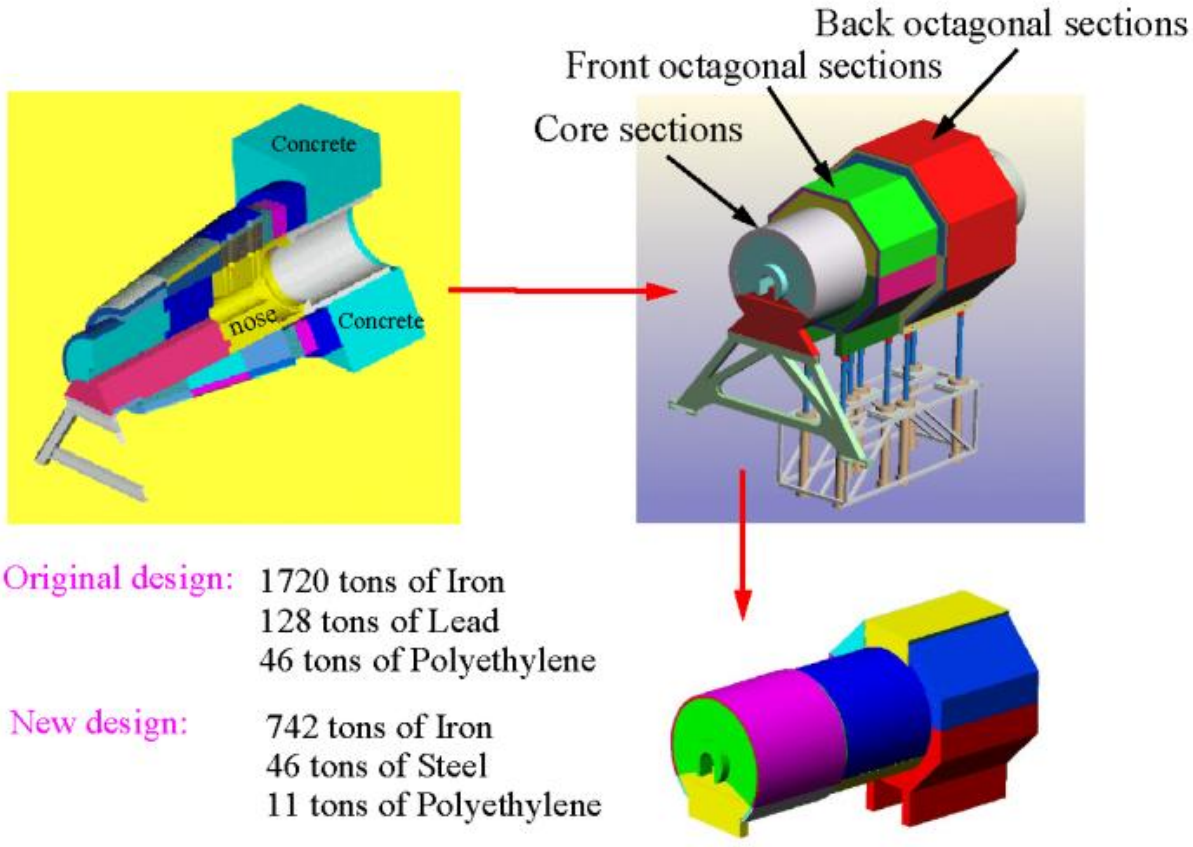

Figure 8.10 Evolution of the JF design.

8.5 Optimisation of JF

The massive forward shield between the back of the forward toroid and the front of the JN shield underwent major engineering revision beginning in mid-2001. The design concepts considered previously had filled the "maximum allowable envelope" of the muon acceptance; and were conical, with outer surfaces along the line $|\eta| = 2.7$. It had been known for some time that this region was over-shielded compared to the neighboring JT and JN regions. But it was not until mid-2001, in tandem with a new engineering design concept for the structure and assembly sequence of the JF, that systematic studies began to discover how much the mass of the JF could be reduced without raising the background rates appreciably in the muon system detectors. In the end it was possible to remove 1000 tons of material from the JF without increasing significantly the background rates. The reason for this is that the background rates in the large muon wheel are determined by the weakest point of the shielding (in this case the very front of the JF and the JT) and adding 1000 tons of iron to other parts of the shielding is useless. Figure 8.10 shows how the design has evolved from one with conical shape to one with a long cylindrical front and an octagonal shaped back section.

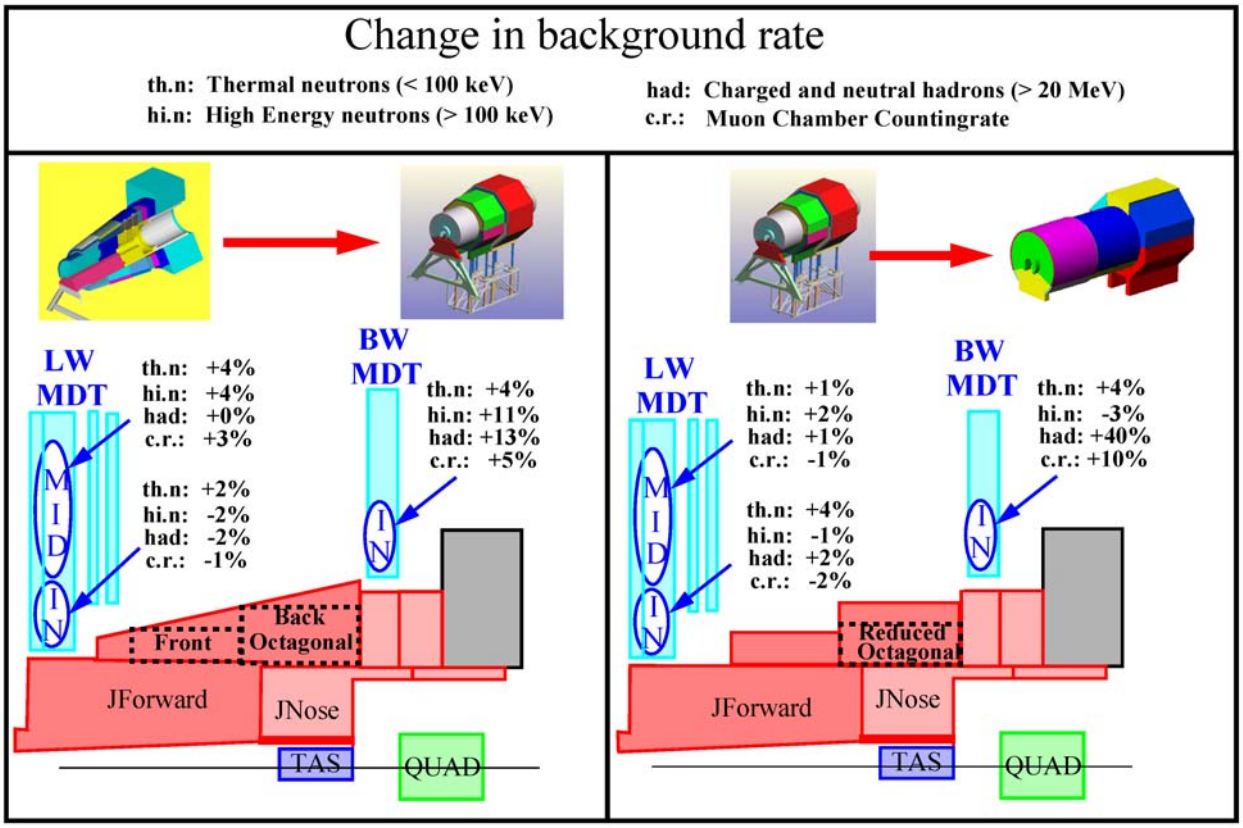

Figure 8.11 (Left) Change in particle rates when going from the original conical design to the Stage 2 design. (Right) Change in particle rates when going from the Stage 2 to the Stage 1 octagonal design.

The collaboration has decided to stage the installation of the forward shield. The June 2002 Baseline used as the reference geometry in this taskforce report corresponds to the "Stage 1" design for the ATLAS JF shield. "Stage 1" anticipates the need for additional shielding and cladding to be added to the outer surface of the JF (without altering the original pieces) to create "Stage 2". This allows for future increase in shielding power in the event that background rates

are higher than expected, or if detector subsystems are more susceptible to the effects of backgrounds than expected.

In Figure 8.10, the original conical shield is shown upper-left, the Stage 2 design upper-right, and the Stage 1 design, lower-right. Comparing the Stage 1 and conical designs, we see from the materials budget that the overall tonnage has been reduced by a factor of 2.5 through the removal of material at large radius. We also see that the Stage 1 design consists of the cylindrical core and an octagonal section (as detailed in the section on the ATLAS geometry). For Stage 2, the octagon has had 40 cm of steel plates added to its outer surface, and another octagon of 40 cm steel plates is created upstream of the first, on the surface of the cylindrical core.

The background rates in the new reduced forward shield.

With a more than a thousand ton reduction in weight in the new design it is not surprising if the expected background rates in the muon spectrometer increase. These increases are, however, not very large.

This can be seen in Figure 8.11 which shows the increase in rates when going from the original conical shield to the Stage 2 and Stage 1 designs. When going from the conical to the octagonal Stage 2 design there is no significant increase at all in the Large Muon Wall (LW MDT). A small increase of the high energy hadron rate is seen in the Back Muon Wall (BW MDT) but the absolute value of this rate is still much smaller than the one in the Large Muon Wall.

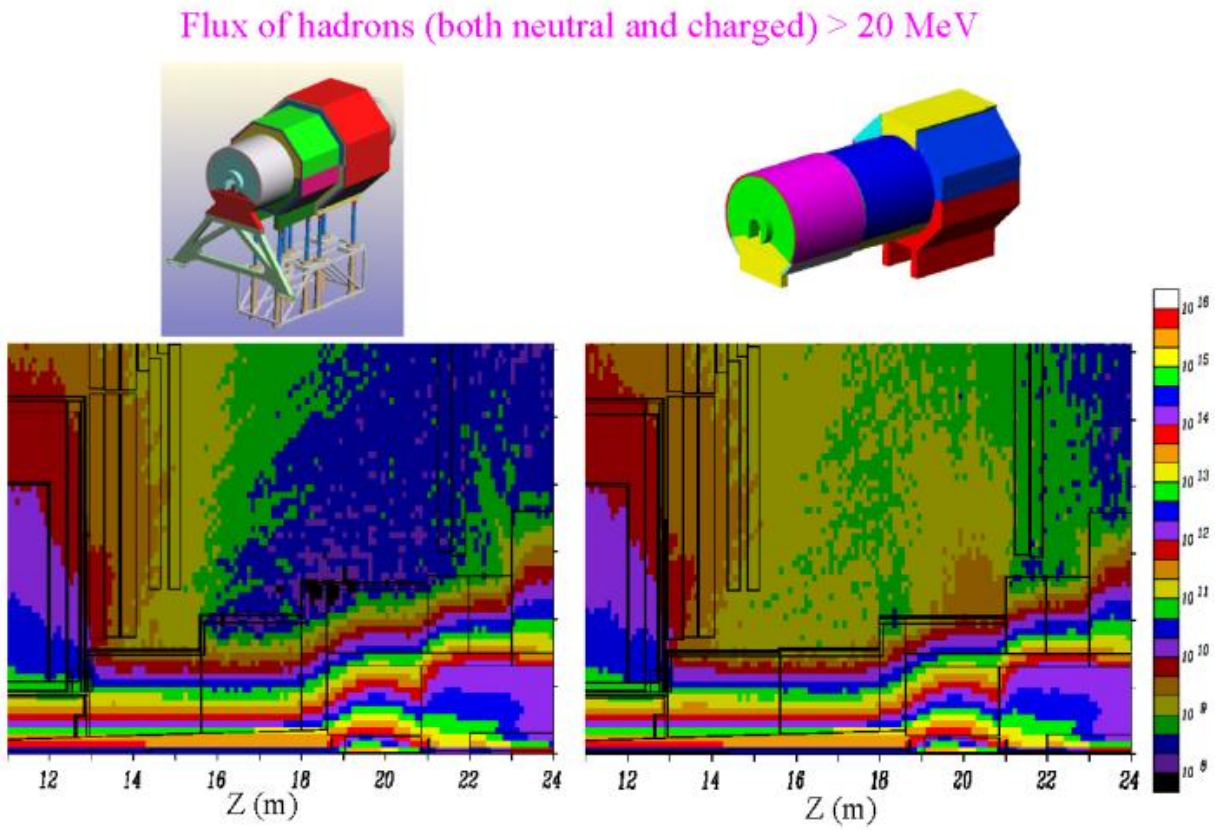

Figure 8.12 Flux of hadrons above 20 MeV for the Stage 2 (left), and the Stage 1 (right) JF design.

The reduction of the forward shield is even more significant in going from the Stage 2 to the Stage 1 design (see right-side plot in Figure 8.11). The rates in the Large Muon Wall are still unchanged while the hadronic rate increase with 40% in the back muon wall.

How is it possible to do these dramatic reductions of the JF without having the background rate exploding? The answer can be found in Figure 8.12 which shows the flux of hadrons above 20 MeV for Stage 2 (left), and the Stage 1 design (right). Notice that while there are minor differences in particle flow, the rates in detector regions—particularly the middle and back MDT's—are almost unchanged.

In Figure 8.12, Stage 2 is on the left and Stage 1 (the JAN03 baseline), is on the right. We see that the thinner shield of Stage 1 allows a flow of hadrons into the region between the middle and back MDT's, with a distinct plume escaping radially from the TAS collimator region, just upstream of the back MDT's, giving some increase in rates in this region. The rates in the middle MDT region is, however, unchanged since it depends only on the thickness of the JT shield and the front part of the JF which has not been changed.

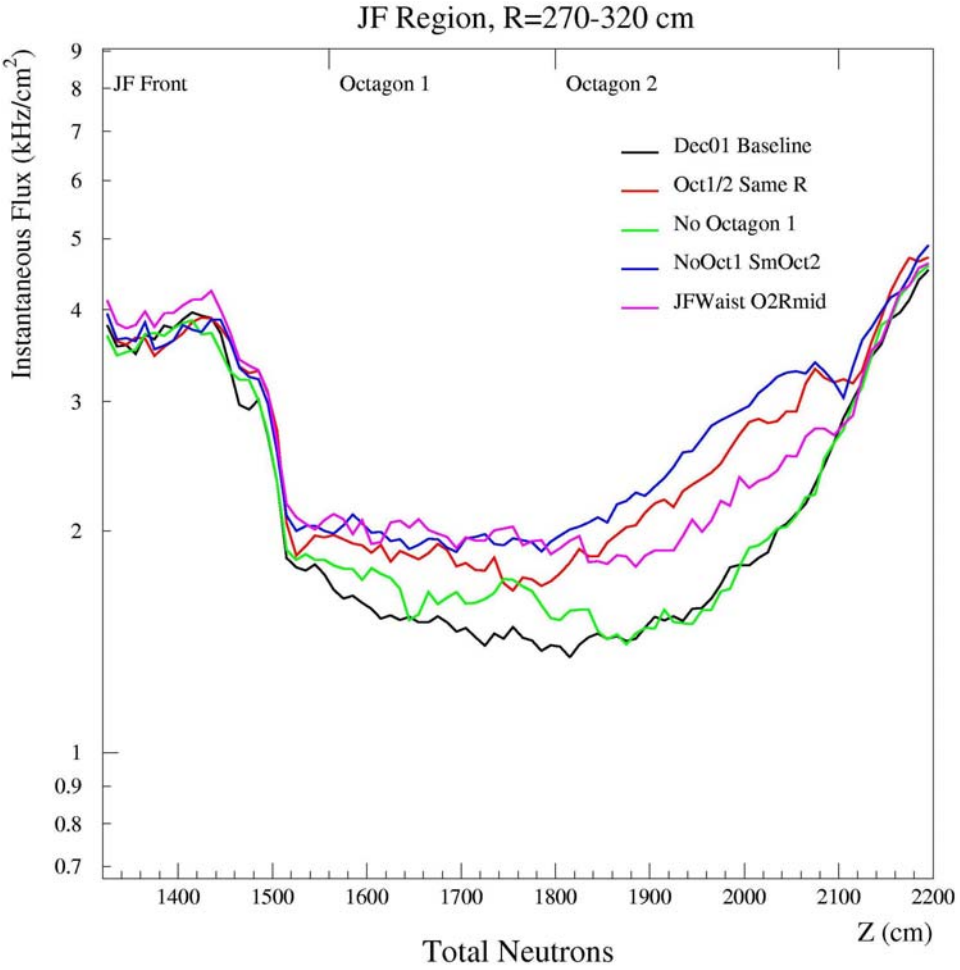

Figure 8.13 Total neutron rate in the JF region for five different JF designs

There is an overall pattern that appears in optimizing the JF region: For many background components, large changes can be made in the region between the middle and back MDT's, and because the flow is predominantly radial, little happens at the MDT's themselves. The comparison histogram in Figure 8.13 shows this behaviour for total neutrons with five different JF designs (the middle MDT's end at 1500 cm, and the back begin at 2100 cm).

Other design considerations.

It has been decided that the Stage 1 design is going to be used at the start-up of the LHC and that the Stage 2 design will be used at high luminosity running. Since the new design has saved ATLAS several MCHF it is natural that we have tried to reduce the size of the JF further in order to find even more savings. There have also been various options studied where the JF was simplified even if it was not reduced in size. Some of these studies are discussed below.

Option: Omit the octagonal JF shield, leaving only the central cylinder

Perhaps the octagonal sections can be removed altogether? As
Table 8.36 shows, the JF octagonal shielding section that begins at z = 18 m, 60 cm in front of the TAS monobloc, and ends at z = 23 m (where the JN begins), is critical to the attenuation of backgrounds from the hot secondary source in the TAS collimator. The Small Wheel region is isolated from this change, but all other muon system regions show dramatic increases of all backgrounds, with the Back Wheel region being most seriously affected. The increases are so severe that the rates without the octagonal shield would not be acceptable for even low luminosity running.

PERCENT CHANGE FOR: Nov Low Lum / Nov Baseline

	N<100keV	N>100keV	Photons	Had>20MeV	Counts	Triggers
SW CSC	2%	0%	2%	0%	0%	-2%
SW TGC	3%	0%	5%	-1%	4%	4%
LW MDT In	421%	66%	30%	1%	34%	32%
LW MDT Mid	326%	63%	92%	6%	96%	76%
BW MDT In	956%	524%	344%	861%	399%	454%
B MDT HiZMid	57%	7%	83%	1%	77%	72%
B MDT HiZOut	81%	18%	131%	10%	124%	132%

Table 8.36 Effect of removing the octagonal JF shield.

Option: Change outer cladding layer on JF from steel to Pb

By proximity, the large wheel MDT's would be most affected by changing the outer JF cladding from steel (the current baseline) to Pb. This change is an example of a trade-off, since it would increase the rates of N>100keV in the LW MDT's by 4-8% and decrease the photon rate by 6-7%, as seen in Table 8.37. The photon rate is more important to the counting rate in this region, which is lower by 6% with the current baseline. For this reason, the baseline choice of steel is preferred.

PERCENT CHANGE FOR: JF Clad Pb to Fe / Jul01 Baseline

	N<100keV	N>100keV	Photons	Had>20MeV	Counts	Triggers
SW CSC	-1%	0%	0%	1%	-1%	-5%
SW TGC	0%	0%	-1%	0%	-2%	-6%
LW MDT In	1%	-8%	7%	1%	6%	0%
LW MDT Mid	-1%	-4%	6%	-2%	6%	11%
BW MDT In	1%	-1%	0%	-5%	2%	10%
B MDT HiZMid	-1%	-3%	-1%	0%	1%	11%
B MDT HiZOut	-2%	-2%	0%	0%	-1%	-8%

Table 8.37 Effect of changing the JF photon filter from steel to lead.

Option: Change cladding layer on JF outer surface from polyboron and steel to only polylithium

The purpose of the steel layer is to stop photons created in the polyethylene. Since less photons are created in Lithium doped polyethylene one can imagine to change the boron doped polyethylene + steel layer to only polylithium. Again, as seen in Table 8.38, the LW MDT's are most affected**,** with noticeable increases in neutrons, photons, hadrons >20 MeV, and counting rates when going from boron to LiF as the dopant. Borated polyethylene is retained as the choice for the baseline.

PERCENT CHANGE FOR: JMDPB JFCladPLiF / Feb Baseline

	N<100keV	N>100keV	Photons	Had>20MeV	Counts	Triggers
SW CSC	-3%	-2%	0%	0%	0%	0%
SW TGC	-2%	-3%	-2%	-1%	-2%	-1%
LW MDT In	35%	5%	6%	18%	6%	6%
LW MDT Mid	8%	0%	6%	9%	4%	-3%
BW MDT In	4%	-4%	6%	3%	8%	14%
B MDT HiZMid	0%	0%	0%	0%	-2%	-10%
B MDT HiZOut	-2%	0%	1%	0%	2%	6%

Table 8.38 Effect of changing JF cladding from polyboron and steel to only polylithium.

Option: Change the radius of the cylindrical core sections

It has been stated previously that what determines the rates in the Large Wheel is the toroid shielding and the cylindrical front part of the JF, i.e. , the core sections. The radius of the core section is determined by the central hole in the Large Wheel since it has to move around the JF core during access. This central hole has been made smaller as the design of the Large Wheel support structure has evolved. The largest allowed JF radius is at present 155 cm and this value is what has been used in the baseline calculation. Even a small 5 cm reduction of this radius gives a significant increase of high energy neutron and hadron rates, as can be seen in Table 8.39:

PERCENT CHANGE FOR: Nov JF R=155cm / Nov Baseline R=150cm

	N<100keV	N>100keV	Photons	Had>20MeV	Counts	Triggers
SW CSC	-1%	0%	0%	0%	-2%	-8%
SW TGC	0%	0%	0%	0%	0%	-1%
LW MDT In	0%	-7%	-1%	-9%	-1%	-2%
LW MDT Mid	-2%	-6%	-1%	-4%	-2%	-6%
BW MDT In	1%	2%	0%	5%	4%	21%
B MDT HiZMid	0%	-2%	-1%	0%	2%	16%
B MDT HiZOut	-1%	-2%	0%	0%	0%	2%

Table 8.39 Sensitivity to the radius of the core section.

To optimise this region further we tried to reduce the thickness of the polyethylene layer on the core sections from 8 cm to 5 cm. It can be seen in Table 8.40 that the hadron rate improves as expected on the expense of the neutron rate. In the end the 5 cm thickness was chosen.

PERCENT CHANGE FOR: Nov R=155 P=5cm / Nov Baseline R=150cm P=8cm

	N<100keV	N>100keV	Photons	Had>20MeV	Counts	Triggers
SW CSC	3%	-5%	1%	0%	-2%	-9%
SW TGC	3%	-6%	0%	0%	-1%	-6%
LW MDT In	5%	-5%	-1%	-14%	-1%	-3%
LW MDT Mid	1%	-3%	-1%	-6%	-2%	-6%
BW MDT In	0%	-2%	0%	3%	1%	8%
B MDT HiZMid	0%	-4%	0%	0%	-1%	-4%
B MDT HiZOut	0%	-4%	0%	0%	0%	7%

Table 8.40 Effect of the reduction of the polyethylene layer in the core section.

In the section about the JT optimisation (Table 8.25 and Figure 8.9) are presented many more options with different JF designs used in the optimisation of the background rates in the Large Muon Wheel.

Option: Effects of increased tolerance gaps at the front of the JF

One problem under current consideration is the tolerance that must be allowed when installing the JF bridge behind the JT. The truck used to lift this bridge has a positioning tolerance of 5 cm at full extension. If this is added to the mechanical tolerance gap already at the JT/JF interface, one needs a gap of 8 cm during installation. In this simulation, the gap was set at 8 cm, with the result that rates increase at the inner rim of the Large Wheel: most notably, 20% for low energy neutrons and 15% for hadrons above 20 MeV.

PERCENT CHANGE FOR: Jan03 JF8cmFrntGap / Jan03 Baseline

	N<100keV	N>100keV	Photons	Had>20MeV	Counts	Triggers
SW CSC	0%	0%	1%	0%	1%	2%
SW TGC	-1%	0%	-1%	0%	-4%	-12%
LW MDT In	21%	9%	0%	15%	0%	-9%
LW MDT Mid	3%	1%	2%	7%	1%	-2%
BW MDT In	3%	-2%	-1%	-2%	1%	12%
B MDT HiZMid	0%	-1%	-1%	1%	-4%	-12%
B MDT HiZOut	0%	-1%	0%	0%	0%	7%

Table 8.41 Effect of increasing the tolerance gap in front of JF

8.6 Optimisation of the JN (TX1S)

The JN region is the domain of the LHC, and is being designed and constructed by engineers associated with the LHC project. The Radiation Taskforce has worked closely with this group during JN optimisation, with the primary contact person being Francois Butin. As outlined in the discussion of the baseline geometry, the JN, or "nose" region includes a large steel tube that supports the first quadrupole magnet. A large cast iron "monobloc" is bolted to the front of this tube, to support the TAS collimator, its carrier, and various beamline components (see Figure 8.14). The large tube itself is surrounded for much of its length by a large concrete block protruding from the end wall of the ATLAS cavern and held from below by large columns resting on the cavern floor. Roughly 2 meters of the large tube protrudes from this block, and it

is this two meter section that must be shielded independently, and which is the subject of optimization studies. The baseline design is to slide large cast iron "washers" (disks with center holes) onto the tube, to create a shield that blocks radiation from the back of the TAS and the front of the first quadrupole magnet.

The JN washers surround the large steel tube in the region z = 21 m to 23 m, and span the radius from the outside of the tube at 1.5 m, to an outer radius of 3.6 m. Their purpose is to stop radiation from the back of the TAS collimator and the front of the first quadrupole from entering the muon system through the wall of the tube.

Figure 8.14 shows the original and present design of the JN. The main difference is that the largest washers situated at the back has been reduced in size so that all washers except the first one now are identical. The shape has also been changed from a circular one to a 16-sided one. This makes it easier to increase the size of the washers or add a polyethylene cladding if that turns out to be necessary during high luminosity running.

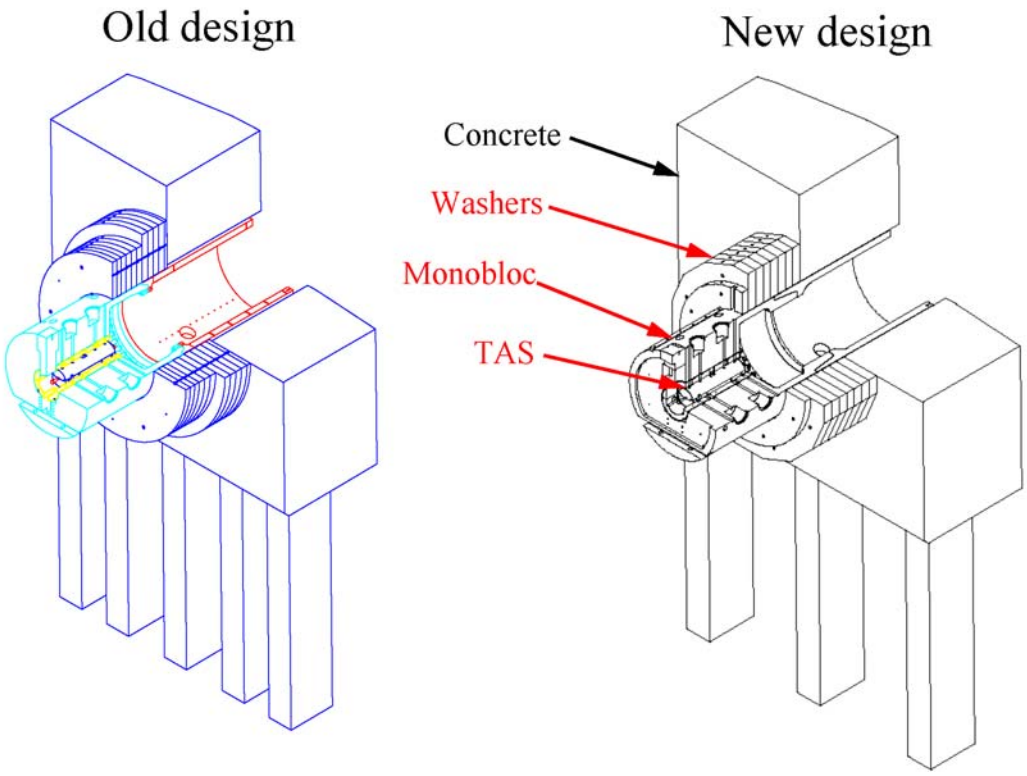

Figure 8.14 The old and the new designs of the nose shield.

Option: Reducing the size of the large JN cast iron washers

Table 8.42 shows that there is an increase of rates in the Back Wheel when the washers are reduced. The hadron rates increase by as much as 28% but the absolute rates are still small compared to other part of the muon spectrometer.

PERCENT CHANGE FOR: Oct Small Nose / Oct base (JT 4cm)

	N<100keV	N>100keV	Photons	Had>20MeV	Counts	Triggers
SW CSC	-1%	-3%	0%	-1%	2%	7%
SW TGC	+1%	-3%	-1%	-3%	-3%	-7%
LW MDT In	-3%	0%	0%	3%	-1%	-5%
LW MDT Mid	-1%	-1%	-1%	-1%	-1%	-2%
BW MDT In	5%	19%	7%	28%	6%	2%
B MDT HiZMid	0%	1%	-1%	-1%	3%	18%
B MDT HiZOut	0%	-1%	-1%	2%	-1%	-1%

Table 8.42 Effect of reducing the size of the large JN cast iron washers.

Option: Remove the washers

If these washers are completely omitted, radiation floods into the region of the back wheel, easily reaching the large wheel and barrel muon regions, as Table 8.43 illustrates.

PERCENT CHANGE FOR: Dec No JN / Dec01 Baseline

	N<100keV	N>100keV	Photons	Had>20MeV	Counts	Triggers
SW CSC	4%	0%	5%	0%	8%	14%
SW TGC	6%	0%	11%	0%	8%	3%
LW MDT In	737%	99%	78%	2%	84%	81%
LW MDT Mid	567%	113%	225%	3%	220%	162%
BW MDT In	7319%	13614%	3073%	10396%	3461%	3170%
B MDT HiZMid	126%	23%	236%	1%	193%	118%
B MDT HiZOut	187%	51%	354%	5%	319%	270%

Table 8.43 Effect of removing the washers.

Option: Change the monobloc from cast iron to steel

The monobloc support structure and shield surrounding the TAS collimator and its carrier is a complicated object most readily fabricated by casting. Cast iron is less dense than steel (7.2 g/cm^3 versus 7.8 g/cm^3), but with higher carbon content that helps in neutron moderation. Table 8.44 shows that both cast iron and cast steel are acceptable (the statistical errors in this comparison of trigger rates range from about 5% to about 20%, progressing down the column).

PERCENT CHANGE FOR: Steel Monobloc / Jul01 Baseline

	N<100keV	N>100keV	Photons	Had>20MeV	Counts	Triggers
SW CSC	-3%	-2%	-2%	0%	0%	3%
SW TGC	-2%	-1%	-3%	-1%	-3%	-4%
LW MDT In	0%	-4%	-1%	-1%	0%	10%
LW MDT Mid	0%	-1%	-1%	0%	-2%	-3%
BW MDT In	5%	0%	-1%	0%	4%	28%
B MDT HiZMid	-2%	-3%	-1%	-1%	0%	1%
B MDT HiZOut	0%	-2%	-2%	-1%	-3%	-6%

Table 8.44 The effect of changing the monobloc from cast iron to steel.

Option: Change the washers from cast iron to steel

Since steel seems to be a viable option for the monobloc it could also be considered for the washers. Table 8.45 shows, however, that steel washers are much less efficient in stopping neutron radiation. The reason is that steel does not contain enough carbon to moderate the neutrons. The monobloc is surrounded by the JF which is made of cast iron and which stops the neutrons but this is not the case for the washers and they can therefore only be made of iron.

PERCENT CHANGE FOR:	Oct Steel Nose / Oct base (JT 4cm)					
	N<100keV	N>100keV	Photons	Had>20MeV	Counts	Triggers
SW CSC	-1%	-4%	-1%	-1%	3%	10%
SW TGC	1%	-2%	0%	-1%	-1%	-2%
LW MDT In	5%	8%	-1%	1%	-3%	-8%
LW MDT Mid	7%	2%	1%	2%	1%	0%
BW MDT In	209%	250%	20%	-15%	32%	15%
B MDT HiZMid	2%	-1%	3%	0%	2%	-2%
B MDT HiZOut	4%	0%	4%	1%	3%	-2%

Table 8.45 Effect of changing the washers from cast iron to steel.

8.7 The beam pipe and related equipment

It has been known for some time that the ATLAS beam vacuum system is a secondary source contributing to background rates in the inner detector (especially near the endcap calorimeter) and in the muon system. The secondary particle production by the beamline is especially dramatic downstream of the forward calorimeter, and upstream of the TAS, and it is this flux that drives up backgrounds in the muon system. This effect was seen in early studies by Alfredo Ferrari, and has been mapped methodically in recent FLUKA and GCALOR simulations done by the Radiation Taskforce.

8.7.1 Studies with the beamline removed

To determine how much the beamline vacuum system contributes to background rates, FLUKA and GCALOR simulations have been done with the beamline removed entirely. (The Taskforce is, however, not proposing to operate the LHC in this mode.) We begin by presenting the FLUKA studies.

A zoom of the beampipe region ($r < 20$ cm) up to $z = 12$m, as described in the FLUKA geometry, is shown in Figure 8.15. The main results of this study are summarized in the following sections, the complete set of results can be found in [105].

Results in which the beamline equipment up to the TAS absorber was removed were compared to the default AV16 fluences with their ratios given in Table 8.46. Typically, the effect of the beamline and related equipment is to increase particles rates by factors of 2 to 4. However, inspection of fluences and currents in the *2nd-forward* region shows increases of factors up to 10. Background rates in the muon system are therefore dominated by interactions in the beampipe.

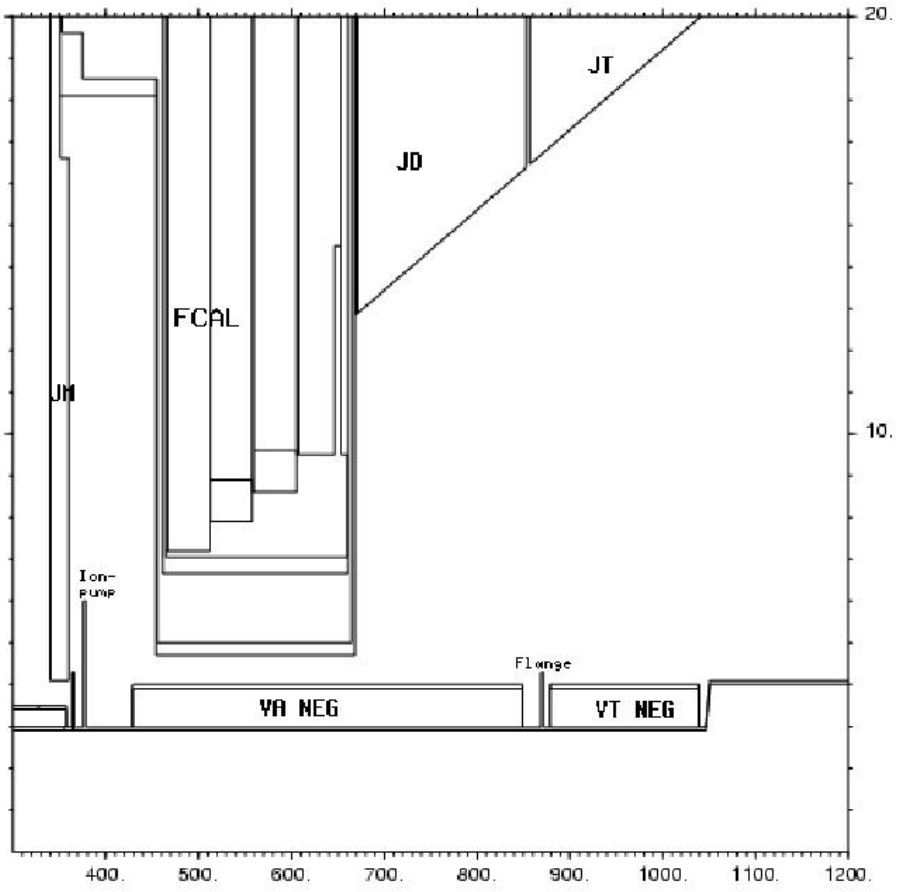

Figure 8.15 Radial zoom of the Fluka AV16 geometry.

Position	Ratios (with-beampipe/no-beampipe)							
	Neutrons			Photons	Ch.hads	Protons	μ^{+-}	e^{+-}
	Total	>100keV	>10MeV	>30keV	>10MeV	>10MeV	>10MeV	>0.5MeV
Barrel								
1st,low-z	2.02	1.61	1.36	2.13	1.45	1.57	1.02	1.58
1st,high-z	2.35	2.15	2.65	2.69	2.03	2.43	1.29	3.13
2nd,low-z	2.52	2.23	2.36	2.98	2.22	2.54	0.83	1.82
2nd,high-z	3.04	3.20	3.79	3.97	3.17	3.29	0.98	3.19
3rd,low-z	2.60	2.26	2.71	2.96	2.04	2.03	0.96	2.82
3rd,high-z	3.04	3.28	3.94	3.85	3.91	4.09	1.06	3.58
Forward								
1st,low-eta	2.61	2.57	2.82	2.97	3.64	3.77	1.14	3.42
1st,mid-eta	2.34	2.29	2.52	2.55	2.56	2.87	1.21	2.32
1st,high-eta	2.18	2.12	2.09	2.27	1.71	1.69	0.99	1.99
2nd,low-eta	3.57	4.59	3.98	4.10	4.24	4.31	1.27	4.87
2nd,mid-eta	4.19	5.23	5.03	4.29	4.80	5.04	0.94	3.55
2nd,high-eta	5.51	7.42	8.27	5.32	9.17	10.00	1.13	7.29
3rd,low-eta	3.28	3.69	3.11	3.51	4.04	4.13	1.08	2.89
3rd,mid-eta	3.31	3.20	2.08	3.36	3.02	3.29	0.84	2.21
3rd,high-eta	3.01	2.58	1.73	2.95	2.61	2.57	1.85	1.97

Table 8.46 Ratio of fluences and currents with and without beam pipe. The scoring regions used in this study are defined in Figure 5.14.

Colour plots of the radiation environment with and without the beamline equipment are show in Figure 8.16 to Figure 8.19. The effect of the beamline material in the region 365cm < z < 1100cm is very noticable (see individual particle fluence plots below). Comparison at r = 30cm and z = 1050 cm (mid-point in inner JT-shield) shows approximately an order of magnitude reduction in particle fluences. Inspection of the fluences in the NO beamline plot highlights the effect of the warm and cold cryostat vessels.

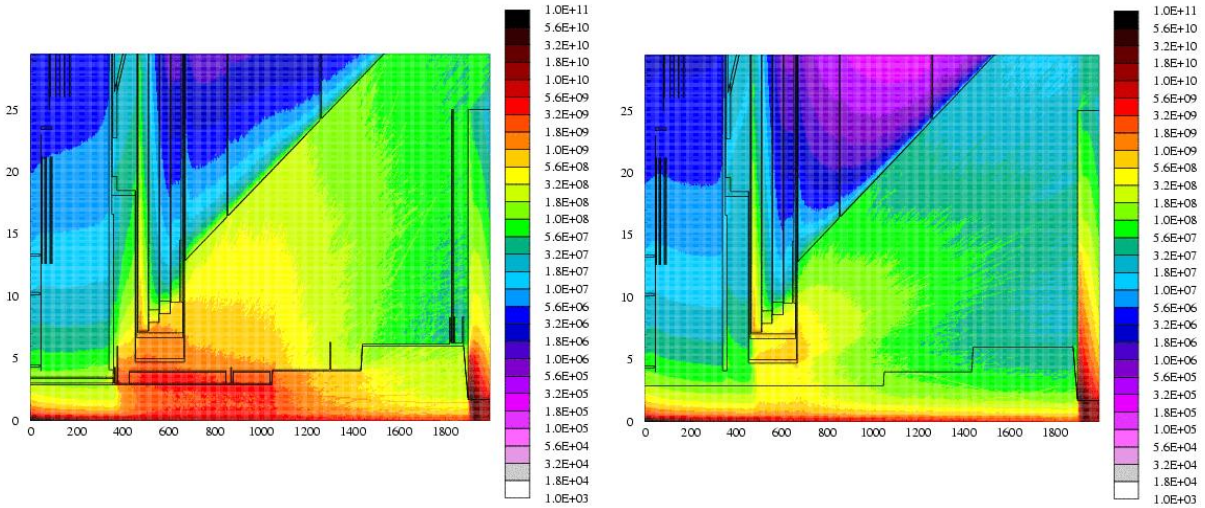

Figure 8.16 All particles > 10 MeV with beam equipment (left) and without (right).

Note the large increases and the directionality of the high energy neutron fields in Figure 8.17.

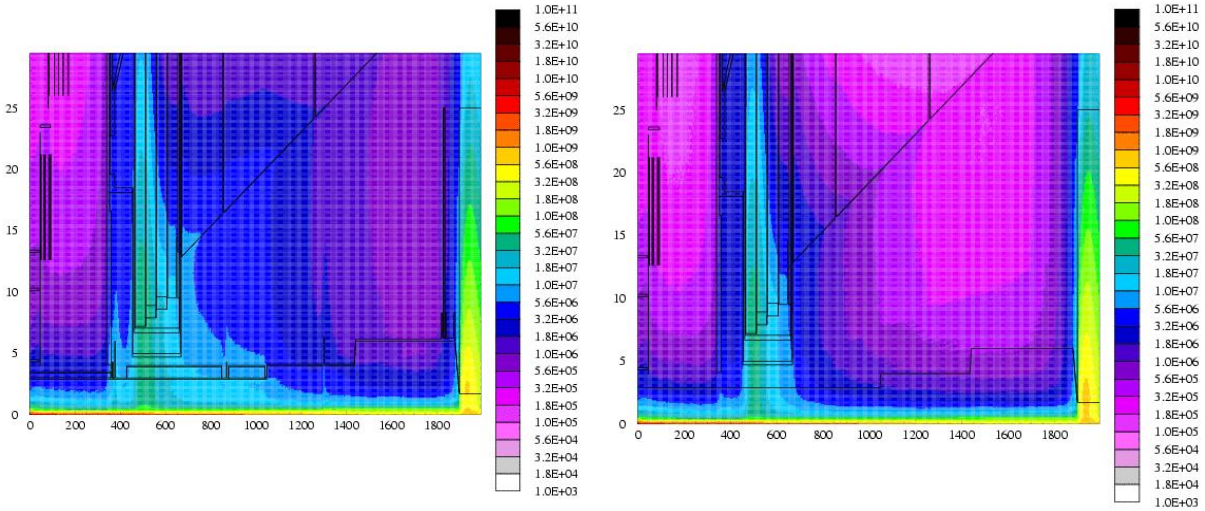

Figure 8.17. Neutron fluences above 10 MeV, with beam pipe (left) and without pipe and equipment (right).

It is photons and electrons that are responsible for the particle "cloud" around the beampipe, as can be seen in Figure 8.18.

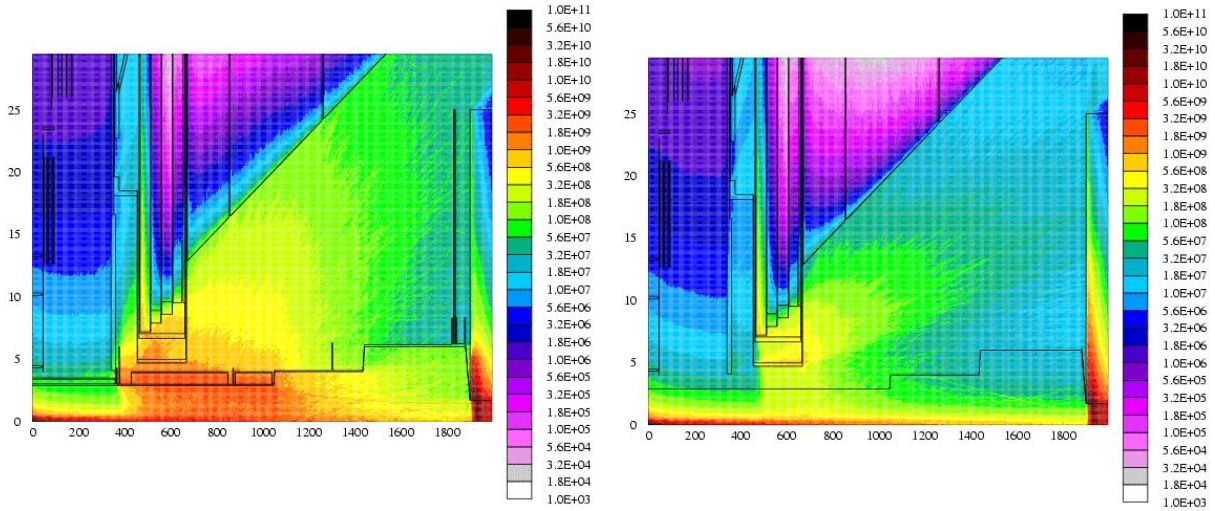

Figure 8.18 Photon fluences with beam line (left) and without beam line (right).

Table 8.46 shows that the beam pipe material does not have a strong influence on the muon rates. They mainly originate from punch-trough FCAL and subsequent decay in the cavity, as seen in Figure 8.19.

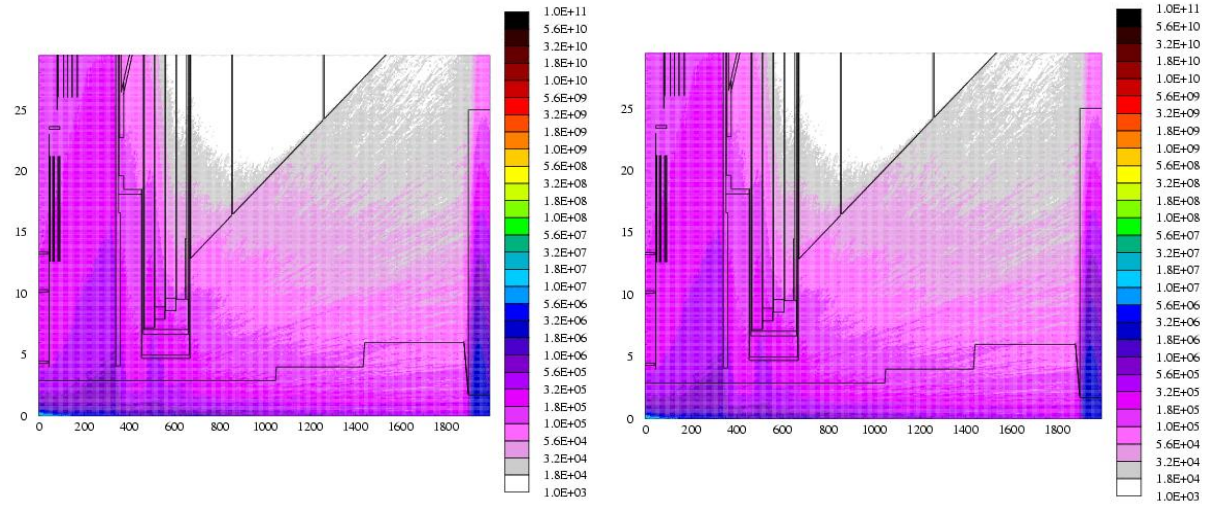

Figure 8.19 Muon fluences with beam line (left) and without beam line (right).

We now turn to the GCALOR simulations. Figure 8.20 shows a percentage difference map for the case where the beamline has been removed from the baseline geometry. The scoring regions used in this study are defined in Figure 5.13 with the SW TGC and MDT IN regions merged into one region.

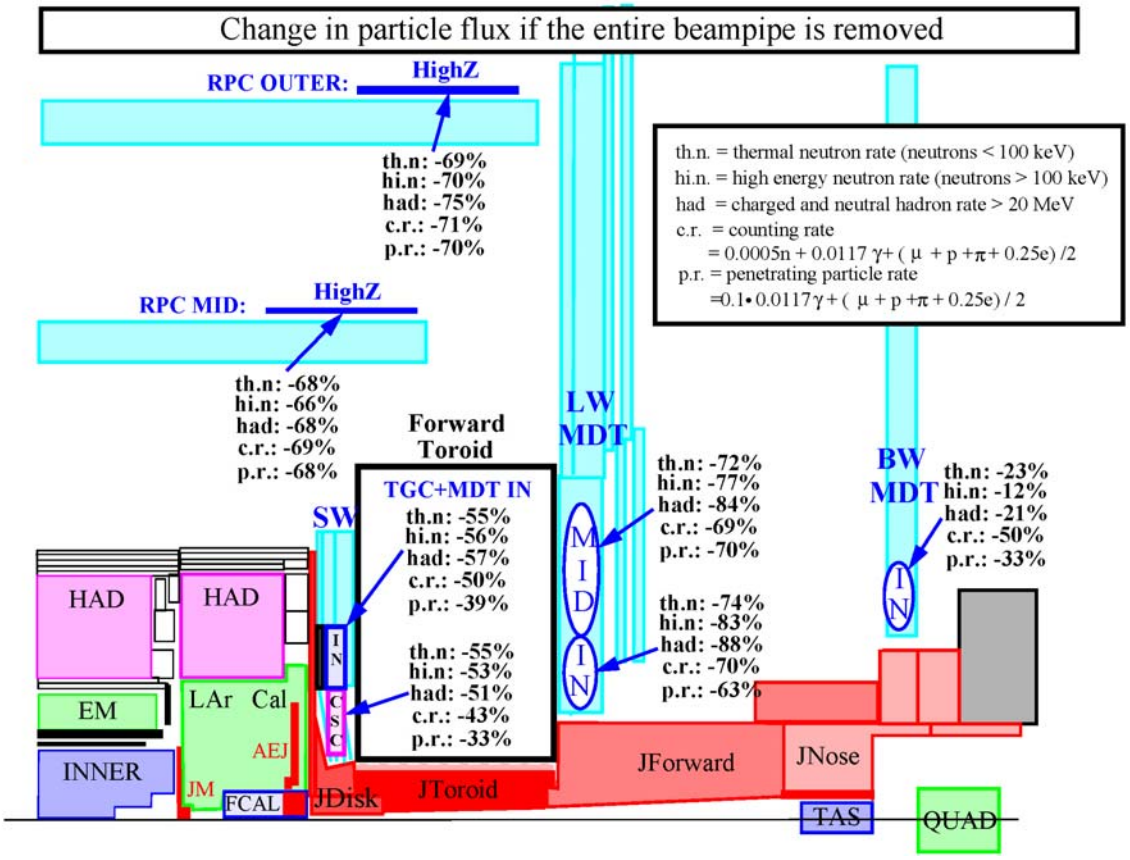

Figure 8.20 Change in particle flux if the entire beampipe is removed (GCALOR).

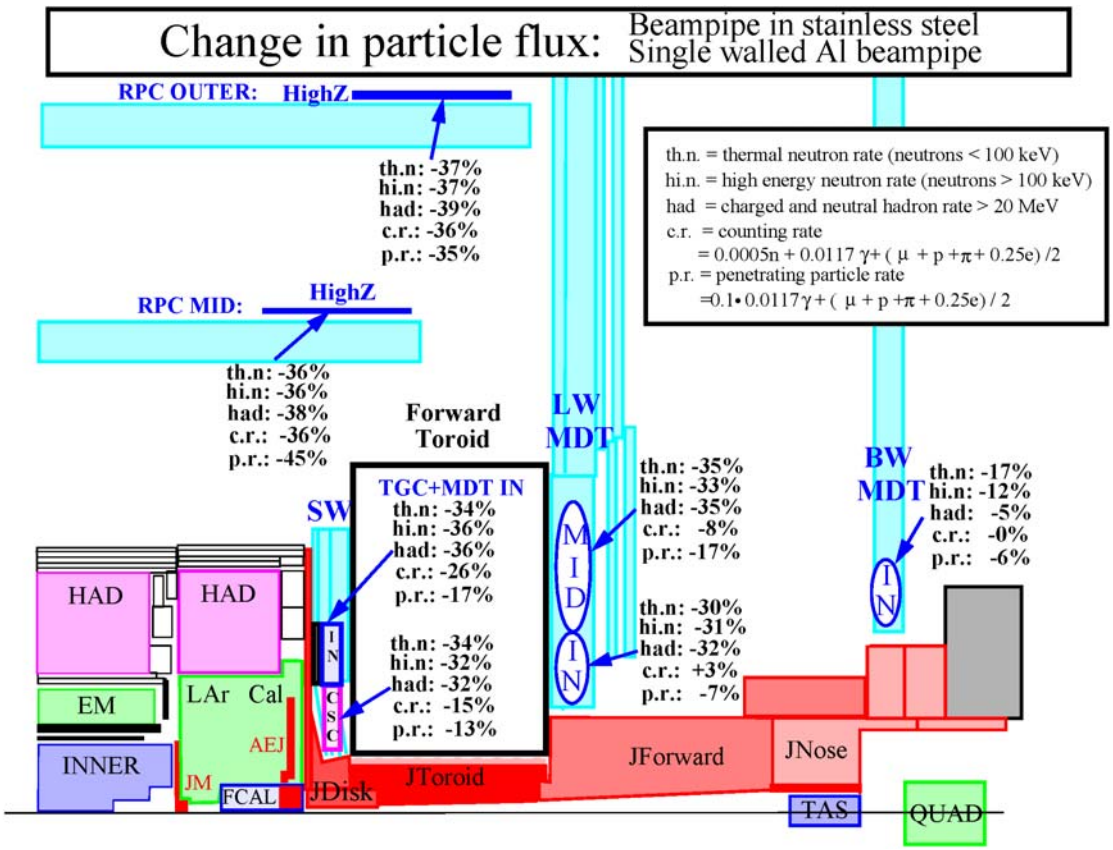

Figure 8.21 Change in particle flux when the stainless steel beampipe is changed to aluminium.

This graphic shows dramatically how uniform the reduction is across all types of background flux in a given region. In the Small Wheel (SW) region, rates are reduced by about a factor of 2, as also seen in the FLUKA simulations above. The reductions are even more dramatic in the Large Wheel (LW) region and in the barrel regions: factors of 3 to 4. The Back Wheel (BW) region shows the least reduction, because the TAS and Quadrupole secondary sources have a larger fractional contribution in this region.

This graphic shows an effect that is also seen in flux maps. The secondary particle production in the beamline walls inside the JD, JT, and JF regions is somewhat directional, flowing forward with much of the flux in the range 30 to 60 degrees from the beamline. This causes the LW region to be more seriously affected than the SW or BW regions. The barrel regions at large z are also affected because the JT shield is thin, and the secondary and tertiary particle flow penetrates to the outside.

8.7.2 Change the stainless steel beampipe to a single wall aluminium beampipe

Since removal of the beampipe is not a realistic option, we have investigated the advantages of replacing the stainless steel pipes and flanges with aluminum, beginning in front of the endcap calorimeter at z = 350 cm, and ending at the junction of the copper pipe through the TAS. In addition, the double-walled sections are made single-wall, and the walls are thickened slightly from 1 to 1.5 mm since aluminum is weaker than stainless steel. The improvements are dramatic by comparison with what can be achieved by much more expensive options, such as using tungsten in the core of the JD. This aluminum-pipe option has been calculated a number of times with GCALOR and FLUKA, and the results are consistent. Figure 8.21 shows the percentage changes relative to the February, 2002, baseline.

And this is the corresponding table for the June, 2002, baseline:

PERCENT CHANGE FOR: Jun02 Be1Al1Pipe / Jun02 Baseline

	N<100keV	N>100keV	Photons	Had>20MeV	Counts	Triggers
SW CSC	-33%	-32%	-16%	-30%	-17%	-15%
SW TGC	-32%	-34%	-29%	-34%	-26%	-14%
LW MDT In	-33%	-28%	5%	-34%	2%	-5%
LW MDT Mid	-35%	-33%	-3%	-35%	-8%	-22%
BW MDT In	-13%	-2%	0%	-1%	0%	0%
B MDT HiZMid	-37%	-36%	-36%	-38%	-37%	-39%
B MDT HiZOut	-37%	-37%	-36%	-38%	-36%	-34%

Table 8.47 Ratios of rates for an aluminium beampipe compared to stainless steel.

We note that the backgrounds are reduced typically by 30% for most critical rates in the muon system. The exceptions are understandable. The photons in the Large Wheel MDT's are little affected because the JD corner and JTT shield are thin, and EM punchthrough from hadronic showers is still reaching the middle MDT's. The back wheel MDT rates are almost unchanged because they are dominated by secondaries from the TAS and the first quadrupole.

8.7.3 The contribution of individual vacuum elements

The contribution of some of the individual elements has been studied with FLUKA:
1) The effect of removing the flange after the inner detector at ~365cm and the ion-pump at ~375cm. This did not reduce particle fluences drastically, indicating that the stainless-steel beampipe material is responsible for the bulk of the radiation.
2) The effect of removing the beampipe and associated equipment in the forward shield region (z > 1050cm) and comparing rates with the default av16 (see Table 8.48). Typically the differences are small, although a ~27% effect is seen in the 2nd, high-eta region.
3) Concerns over the high levels of induced radioactivity expected in the beam-line equipment have resulted in the request for simulations using aluminium instead of steel in certain regions. In the current study, the outer-layers of the VA and VT NEG pumps have been changed from Steel to Aluminium, along with the flange positioned in between these two NEG pumps. No changes have been made to any dimensions. Results are given shown in Table 8.49. There is typically a 10% to 30% reduction of all particles except muons in most regions.

8.7.4 Discussion

The importance of the beamline equipment on particle backgrounds in the muon system is clear and CMS came to the same conclusions in their beampipe studies [106], and choose a conical beampipe structure. With the cylindrical structure of the ATLAS beampipe, the studies have shown that the change to aluminum should be done, if all possible, because single backgrounds, counting rates, and penetrating particle rates are reduced dramatically in (1) the barrel muon system, (2) the LW muon system, and (3) to a lesser extent in the SW muon system.

Another reason to go to an aluminium beampipe is that the activation of the beamline is greatly reduced.

	Ratios							
	Neutrons			Photons	Ch.hads	Protons	μ^{+-}	e^{+-}
Position	Total	>100keV	>10MeV	>30keV	>10MeV	>10MeV	>10MeV	>0.5MeV
Barrel								
1st,low-z	1.04	1.06	1.03	1.06	1.02	1.04	0.96	–
1st,high-z	1.04	0.99	0.96	1.13	0.96	1.06	0.98	0.86
2nd,low-z	1.04	1.00	1.01	1.06	0.95	0.92	0.66	0.80
2nd,high-z	1.04	1.00	1.03	1.06	0.97	0.98	0.99	0.83
3rd,low-z	1.04	1.01	1.06	1.07	0.89	0.91	1.18	1.04
3rd,high-z	1.07	1.03	1.05	1.11	1.15	1.17	0.99	1.19
Forward								
1st,low-eta	1.02	1.01	1.13	1.07	1.07	1.08	0.99	0.95
1st,mid-eta	1.00	0.97	1.04	1.02	0.95	0.99	1.01	1.01
1st,high-eta	0.96	0.97	0.97	0.98	1.12	1.08	1.02	1.09
2nd,low-eta	1.13	1.16	1.08	1.08	1.08	1.08	0.92	1.28
2nd,mid-eta	1.17	1.17	1.09	1.09	0.95	0.96	1.09	1.14
2nd,high-eta	1.26	1.27	1.28	1.17	1.28	1.27	0.97	1.30
3rd,low-eta	1.08	1.08	1.13	1.08	1.12	1.13	1.19	1.02
3rd,mid-eta	1.08	1.03	1.07	1.10	1.01	1.02	1.09	1.05
3rd,high-eta	1.04	0.94	0.95	0.99	0.71	0.72	0.79	0.81

Table 8.48 Ratio of fluences with and without a beam pipe section at Z >1050 cm.

Position	Ratios							
	Neutrons			Photons	Ch.hads	Protons	μ^{+-}	e^{+-}
	Total	>100keV	>10MeV	>30keV	>10MeV	>10MeV	>10MeV	>0.5MeV
Barrel								
1st,low-z	0.88	0.92	1.02	0.82	0.98	0.93	1.05	–
1st,high-z	0.89	0.86	0.76	0.82	0.94	0.81	0.95	1.06
2nd,low-z	0.88	0.91	0.92	0.87	1.03	1.00	–	1.12
2nd,high-z	0.86	0.82	0.80	0.85	0.80	0.81	0.87	–
3rd,low-z	0.87	0.88	0.91	0.86	0.90	0.92	0.84	1.07
3rd,high-z	0.87	0.85	0.82	0.85	0.83	0.82	0.77	0.85
Forward								
1st,low-eta	0.83	0.79	0.83	0.83	0.77	0.75	1.00	0.80
1st,mid-eta	0.83	0.81	0.79	0.86	0.72	0.68	0.96	0.78
1st,high-eta	0.85	0.83	0.78	0.91	0.89	0.88	1.01	0.68
2nd,low-eta	0.86	0.87	0.83	0.83	0.85	0.83	0.75	0.76
2nd,mid-eta	0.88	0.87	0.89	0.85	0.92	0.92	1.11	0.72
2nd,high-eta	0.87	0.86	0.91	0.96	0.94	0.93	0.89	0.93
3rd,low-eta	0.86	0.86	0.88	0.88	0.85	0.86	1.16	0.77
3rd,mid-eta	0.86	0.88	0.97	0.89	0.71	0.69	–	1.06
3rd,high-eta	0.91	0.96	0.90	0.84	0.79	0.81	1.05	0.76

Table 8.49 Effect of replacing outer NEG jackets and flanges in VA and VT regions with aluminium. Ratios are not given if the statistical uncertainty is greater than 20%.

8.8 The Effects from Increasing the Barrel/Endcap Services Gap by 4 cm

In spring of 2001, the services gap between the barrel and endcap cryostats was increased by 4 cm to accommodate the more-realistic assessment of the space needed for inner detector services made during that period. This increase causes the endcap cryostat, the extended TileCal, and everything behind them to move away from the interaction point by 4 cm, as far as the front of the TAS monobloc, which remains fixed at 1860 cm. In effect, the increase is taken up in z by a decrease in the length of the JF massive shield, allowing the small wheel, forward toroid, and large wheel, to move back.

As usual, we use the baseline rates for reference, and give the percentage change if the gap were returned to its old value. From Table 8.50, we see that there is little change. The slight decrease is caused by relatively minor change in the beamline that accompanied this gap increase. The flange connecting the beryllium inner detector section to the stainless steel section was moved more than 4cm from the I.P., putting it further into the front end of the endcap calorimeter. This shields the services gap from some of the large angle secondary spray from the flange.

Why has widening the gap between the calorimeter, and then filling it with the additional services, not driven the background rates much higher? As noted before in the description of this area, the “thin material channel” in this region is actually more than 50 cm wide, since it includes cryostat aluminium, vacuum, liquid argon, and services—all of lower density than the calorimeter modules of the barrel and endcap.

PERCENT CHANGE FOR:	Old Gap / Jul01 Baseline					
	N<100keV	N>100keV	Photons	Had>20MeV	Counts	Triggers
SW CSC	-1%	0%	0%	0%	3%	10%
SW TGC	-2%	1%	0%	5%	0%	0%
LW MDT In	-4%	-4%	-3%	-5%	-2%	2%
LW MDT Mid	-4%	-1%	-5%	-2%	-5%	-7%
BW MDT In	-6%	-3%	0%	2%	14%	16%
Barrl LoZInr	-2%	-8%	-4%	-1%	0%	9%
B MDT LoZMid	-1%	-8%	-6%	-9%	0%	20%
B MDT LoZOtr	-2%	-4%	-3%	-8%	-1%	6%
Barrl MiZInr	-1%	-4%	-1%	1%	2%	13%
B MDT MiZMid	-2%	-5%	-3%	-1%	0%	9%
B MDT MiZOtr	-2%	-5%	-2%	0%	-2%	-4%
B MDT HiZMid	0%	-2%	-3%	0%	-1%	4%

Table 8.50 Effect of widening the gap by 4 cm.

8.9 The ATLAS Cavern: Modeling Effects and Wall Treatment

To speed up the simulation of radiation backgrounds, the geometry descriptions used in GCALOR and FLUKA are simplified compared to a full description, such as that in DICE. In most production simulations, the ATLAS cavern is a cylindrical solid of air, 12 m in radius and 24 m in half-length in the z direction. The real ATLAS cavern is an irregular solid, roughly rectangular in cross section, with vaulted ceiling and end walls. All real cavern surfaces are further from the beamline than the surface of the simulation cylinder. This means that all simulated background rates will be conservative over-estimates of the true rates, particularly in the muon region. At any given radius from the beamline, the flow coming from the beamline will be little affected. But albedo from the walls will be reduced since the real walls are further away. And, nearly isotropic fluxes, such as thermal neutrons, will be dispersed through a larger volume, leading to noticeably smaller rates in the real cavern.

Model the ATLAS cavern as a rectangular solid

To first approximation, these effects can be explored by describing the cavern as a rectangular solid of air, with a nearest distance to the floor, ceiling, and side walls of 12.5 m, and endwalls at $z = \pm 24$ m (as before). Table 8.51 shows that rates in this rectangular cavern are reduced for all particles and estimators, with the largest reductions in the outer regions of the muon system. We see that the most isotropic fluxes, N<100keV and Photons, are most reduced, followed by semi-directional fluxes such as N>100keV. The most energetic particles, Had>20MeV, are not affected. For photons and low energy photons, the reductions in the outer muon region are typically 15% with the more realistic cavern.

PERCENT CHANGE FOR:	Rect Cavern / Jul01 Baseline					
	N<100keV	N>100keV	Photons	Had>20MeV	Counts	Triggers
SW CSC	-1%	0%	-3%	0%	0%	5%
SW TGC	-3%	-1%	-3%	0%	-1%	1%
LW MDT In	-2%	-6%	-2%	-1%	-4%	-9%
LW MDT Mid	-5%	-4%	-5%	-1%	-3%	3%
BW MDT In	-2%	-6%	-4%	0%	0%	16%
Barrl LoZInr	-17%	-10%	-16%	1%	-9%	12%
B MDT LoZMid	-14%	-13%	-14%	0%	-11%	0%
B MDT LoZOtr	-17%	-13%	-17%	-1%	-17%	-18%
Barrl MiZInr	-13%	-6%	-13%	-1%	-8%	1%
B MDT MiZMid	-13%	-10%	-13%	0%	-13%	-11%
B MDT MiZOtr	-17%	-11%	-17%	0%	-16%	-12%
B MDT HiZMid	-11%	-7%	-12%	0%	-16%	-12%
B MDT HiZOut	-18%	-10%	-18%	0%	-15%	-4%

Table 8.51 Effect of changing the shape of the cavern wall.

Apply borated paint to rectangular walls

It appears that one possibly serious problem in the outer muon region would be damage to control electronics due to neutrons above 100 keV. In studies to reduce their rates, two simulations were done with borated "paint" (boron loaded concrete), applied to the walls of the rectangular cavern described above. The first is a minimal coating of 1 mm thickness loaded with 10% boron by weight, and the second, 2 mm thickness with 20% boron.

1 mm thickness with 10% boron by weight

PERCENT CHANGE FOR:	Paint 1mm 10% B / Jul01 Baseline					
	N<100keV	N>100keV	Photons	Had>20MeV	Counts	Triggers
SW CSC	-4%	0%	-3%	-1%	1%	11%
SW TGC	-2%	-1%	-5%	-1%	-3%	0%
LW MDT In	-9%	-5%	-3%	2%	-2%	5%
LW MDT Mid	-13%	-7%	-6%	2%	-9%	-19%
BW MDT In	-24%	0%	-8%	14%	-3%	20%
Barrl LoZInr	-39%	-11%	-23%	1%	-16%	7%
B MDT LoZMid	-43%	-10%	-15%	1%	-18%	-18%
B MDT LoZOtr	-49%	-11%	-7%	3%	-14%	-28%
Barrl MiZInr	-30%	-8%	-18%	0%	-23%	-33%
B MDT MiZMid	-38%	-9%	-12%	0%	-17%	-28%
B MDT MiZOtr	-46%	-12%	-12%	0%	-18%	-32%
B MDT HiZMid	-32%	-8%	-13%	0%	-13%	-10%
B MDT HiZOut	-40%	-10%	-13%	0%	-16%	-18%

Table 8.52 Effect of 1 mm thick paint loaded with boron (20% by weight).

In both cases, see respectively Table 8.52 and Table 8.53, the low energy neutrons are reduced considerably by capture in the boron, but the neutrons above 100 keV have reductions due mostly to the rectangular geometry (no reduction due to the paint). Since the low energy neutrons are not a problem in the outer muon region, where their rates absolute rates are small compared to the muon wheel regions, it was decided that the cost and fabrication time of borated paint make it undesirable compared to simpler shielding solutions being used nearer the beamline.

2 mm thickness with 20% boron by weight

PERCENT CHANGE FOR: Paint 2mm 20% B / Jul01 Baseline

	N<100keV	N>100keV	Photons	Had>20MeV	Counts	Triggers
SW CSC	-2%	0%	0%	0%	4%	15%
SW TGC	-1%	1%	0%	1%	0%	-3%
LW MDT In	-4%	-1%	-3%	-2%	-2%	0%
LW MDT Mid	-9%	-2%	-5%	0%	-7%	-15%
BW MDT In	-25%	-6%	-2%	-1%	-7%	-20%
Barrl LoZInr	-43%	-3%	-22%	0%	-19%	-6%
B MDT LoZMid	-48%	-8%	-15%	0%	-16%	-6%
B MDT LoZOtr	-55%	-5%	-7%	0%	-11%	-8%
Barrl MiZInr	-32%	-3%	-14%	-1%	-12%	-5%
B MDT MiZMid	-42%	-2%	-14%	-1%	-11%	7%
B MDT MiZOtr	-51%	-7%	-8%	0%	-13%	-16%
B MDT HiZMid	-34%	-1%	-13%	0%	-11%	1%
B MDT HiZOut	-44%	-6%	-10%	-2%	-14%	-15%

Table 8.53 Effect of 2 mm thick paint loaded with boron (20% by weight).

9 Activation

9.1 Introduction

It is well known that the amount of induced radioactivity that will be produced in the LHC experiments will be much larger than in most previous high-energy physics experiments and that one of the most serious radiation problems to be encountered in the operation of ATLAS will be radioactivity induced in the beamline and in detector structures nearby. Some of the induced radio-nuclides will be long-lived, and lead to dose rates that must be carefully planned for in the course of making accesses. This problem has been recognized for some time, and early studies of the ATLAS TAS region and beamline were performed by Ian Dawson and Graham Stevenson [20]. Activation of the ATLAS FCAL was studied separately by Laurie Waters at Los Alamos [21]. In the course of FLUKA and GCALOR studies, Ferrari and Shupe would periodically produce star density maps, which can be used as estimators of activation.

More recently activation of the ATLAS SCT was studied by Dawson et al., which also included the irradiation of SCT components [22]. The Prague group has also made some calculations of induced radioactivity [108].

The ATLAS activation calculations were put on a new footing with the arrival of Vincent Hedberg in 2001, as convenor of the Shielding Engineering Working Group. V. Hedberg developed a close collaboration with a group of physicist at the Moscow Engineering Physics Institute that had been contracted by ATLAS for the purpose of calculating the induced radioactivity in ATLAS. The induced radiation in many parts of the ATLAS experiment has now been calculated taking into account various access scenarios and more than 600 radiation maps for different regions, running times and cooling off times are now available on the ATLAS activation web-pages [109]. The work of M. Morev et al. has lead to a new understanding of the high dose levels due to radioactivity near the beamline, and its consequences for safety during accesses to ATLAS. The predictions made for the SCT are also in good agreement with the activation studies of Dawson et al. [22]. In this chapter some of the results from the Moscow group will be presented but for more detailed results the reader is refered to the tables posted on the activation web-site [109].

9.2 Methods and assumptions

Two methods were used to calculate the induced radiation in ATLAS. The first method uses the well-known relationship between the density of inelastic interactions (the so-called star density) and the dose-rate [110,111]. This approximative method, which is depicted in Figure 9.1, was used in an initial stage of the study to determine which of the massive shielding and detector elements were potential problem regions. The star-density was calculated by Mike Shupe using the GCALOR code [8] under the assumptions of 7x7 TeV collisions and a luminosity of 10^{34} cm^2/s giving a p-p interaction rate of 8×10^8 s^{-1} as predicted by the PHOJET program [33]. Inelastic hadronic interactions with energy above 50 MeV were counted as stars.

The second method [113,114] that was used by the MEPhI group was using the standard activation formula given in Figure 9.1. Particle flux maps were again produced by Mike Shupe using the PHOJET and GCALOR programs [8] and they were then used as inputs in the

calculations. The calculations were made separately for (n,γ) capture of low-energy thermal neutrons and high energy hadrons. In the latter case the lack of knowledge of the cross sections above 20 MeV for all possible types of interactions made it necessary to make the assumption that the cross section of all incident hadrons would be the same as that of protons [115]. The codes DOT-III [116] and MCNP [117] were used to calculate self-absorption and photon transport. Only gamma radiation was calculated. An LHC year was assumed to consist of 120 days of continuing running with a 245-day stop. In order to be conservative the results of the calculations are always given with the shortest possible cool-off time at which it is possible to reach a part of the experiment. In most cases the real cool-off times will be longer.

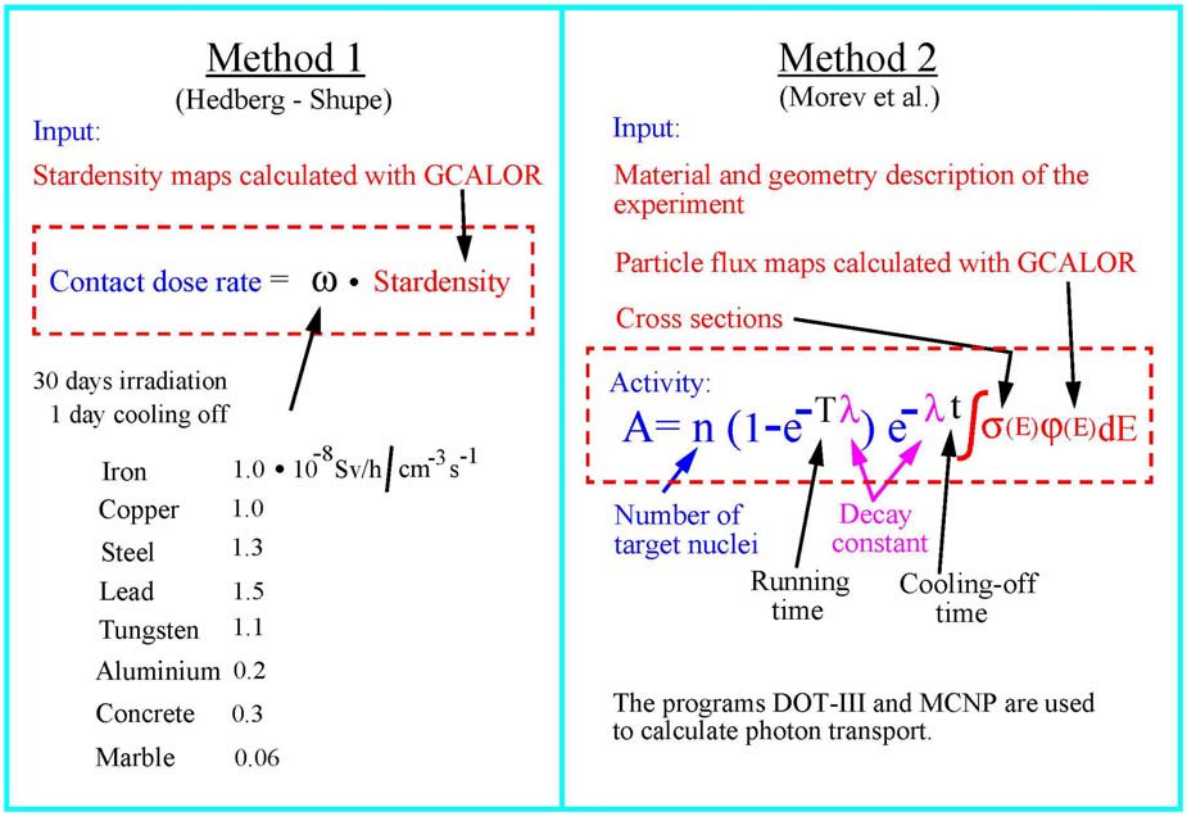

Figure 9.1 A summary of the two methods used to estimate the amount of induced radioactivity in the ATLAS experiment.

9.3 The Standard Access Scenario

It has been known for some time where in ATLAS the largest amount of induced radioactivity will be produced. It is, however, not necessarily the most radioactive areas that are the most troublesome for the experiment since these are not areas were maintenance work has to be carried out. It is the combination of radiation levels with the expected maintenance times which decides if an area is a potential problem for the experiment or not. As a general rule the radiation levels are the highest close to the beampipe and so the first thing to determine is what work will be needed to do around the beampipe. To understand this one has to understand the principle of the ATLAS access scenarios.

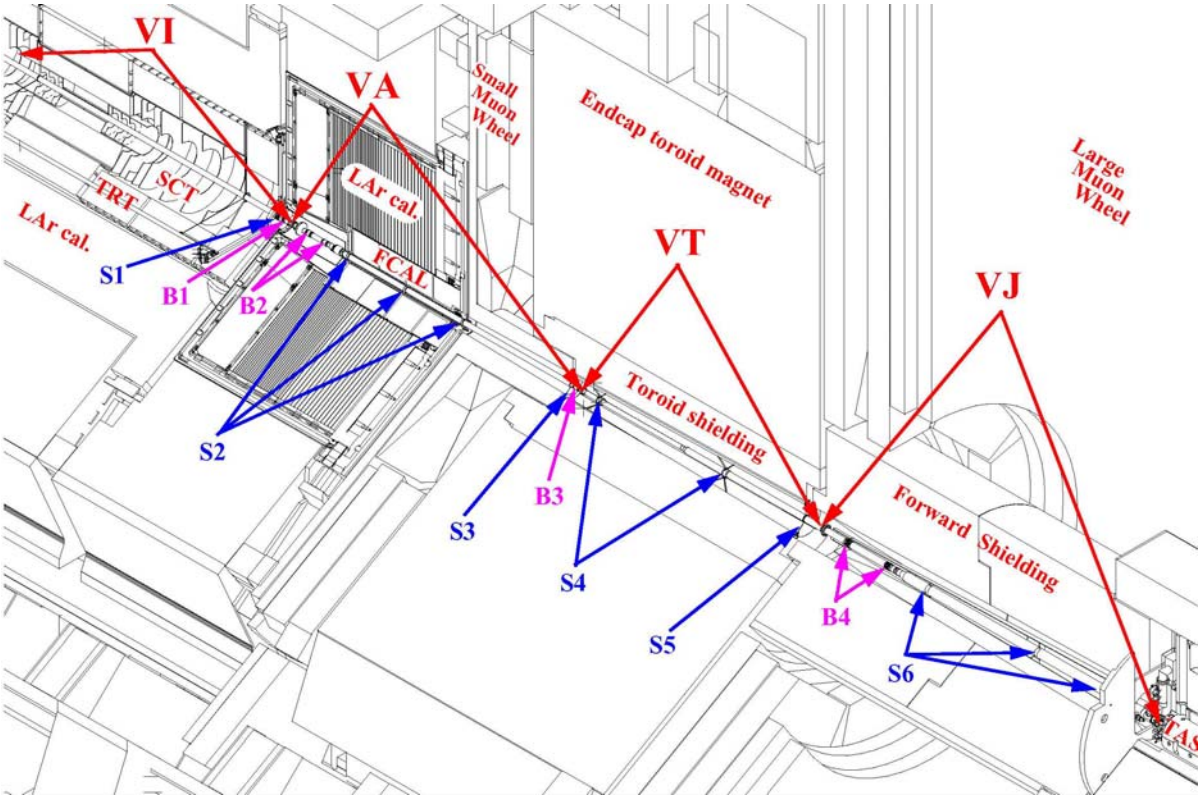

Figure 9.2 The drawing shows the beampipe sections in ATLAS and the detectors and shielding that surrounds it. S1-S6 indicates the position of beampipe supports and B1-B4 the position of bellows.

The ATLAS experiment has two main scenarios called the standard and inner detector access scenario. In the inner detector scenario the beampipe is removed which is not the case in the standard scenario.

Figure 9.2 shows the detectors and shielding surrounding the beampipe in one half of the ATLAS experiment (between the interaction point (IP) and the TAS collimator). In both the inner detector and the standard access the massive forward shielding is first brought to the surface and stored and the large muon wheel is moved forward to the z-position of the TAS collimator.

Figure 9.3 shows the region between the endcap toroid with its shielding (JT) and the nose shield (JN) after the forward shielding has been removed. The beampipe in this region (VJ) is supported off the nose shield by a conical support made of aluminium. This support prevents people to get too close to the beampipe itself and the very hot TAS collimator but dose rates in the 1-2 mSv/h range is still expected at the front of the VJ beampipe close to toroid and at the back close to the TAS. At the front, the beampipe support S5 has to be removed and S4 has to be undone (see Figure 9.2) and this work thus has to be done in a very radioactive environment.

The endcap toroid can then be moved into the place previously occupied by the forward shielding. In this way a gap opens up between the JD/SW and the endcap toroid as illustrated in Figure 9.4. The first part of the toroid beampipe (VT) was assumed to have double walls in the calculation of the activation and this more than doubles the radiation in this region to about 1 mSv/h at a distance of 6 cm from the beampipe. At 1 m from the beampipe the dose rate is less than 80 μSv/h. There is a beampipe support S3 that is situated inside the copper plug in the disk shield that has to be removed before the small muon wheel can be moved.

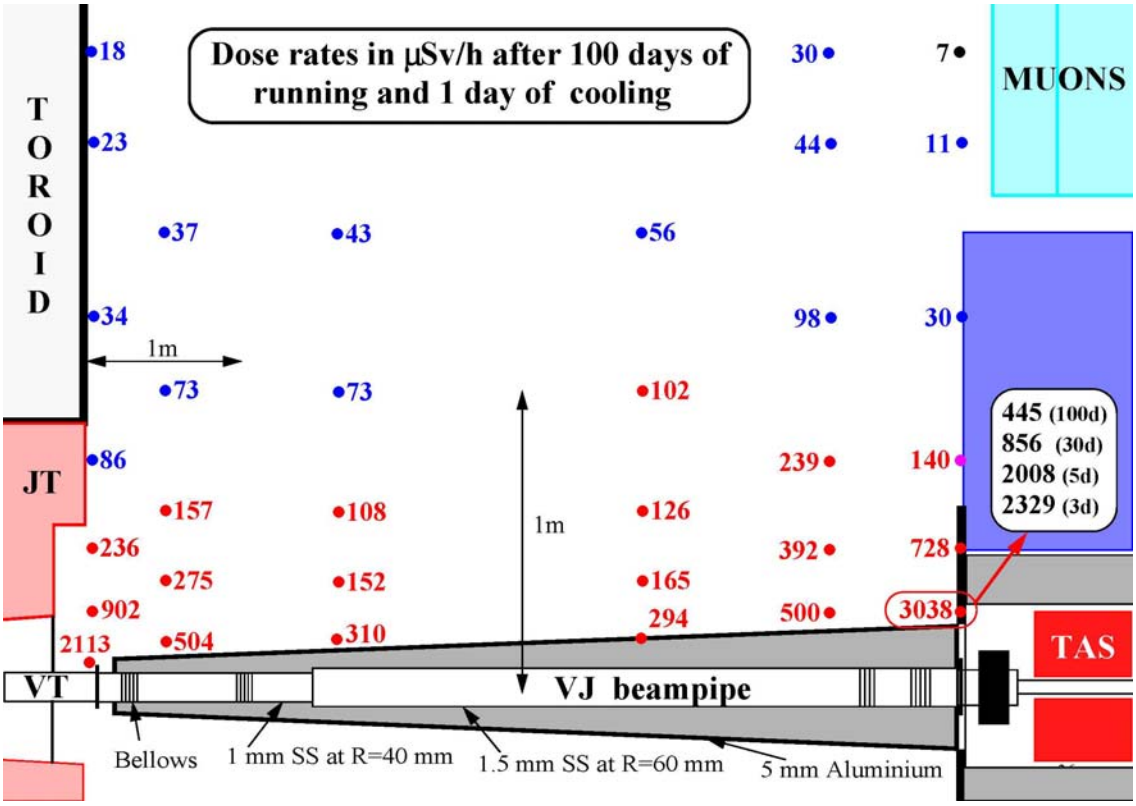

Figure 9.3 The dose rates between the endcap toroid and the nose shield after the forward shield has been removed. Note that the scale in r is not the same as in z. Calculation by Morev [119].

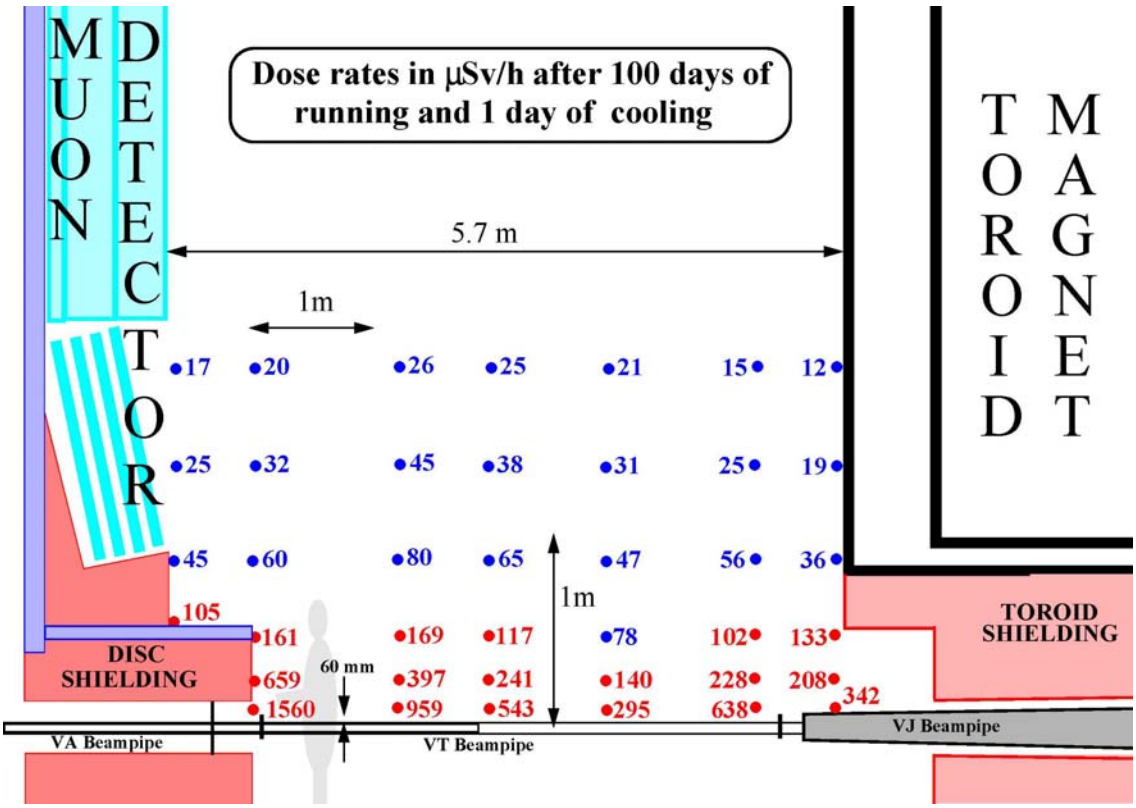

Figure 9.4 The dose rates between the small muon wheel and the endcap toroid. Note that the scale in r is not the same as in z. Calculation by Morev et al. [120].

Figure 9.5 depicts how the disk shield with the small muon wheel is moved into close contact with the endcap toroid and the expected dose rates in front of the shielding. It can be seen from the figure that there is a hot region directly in front of the JD plug. There is no reason to allow people access to this zone and as long as people stay 2 m away from the beampipe the dose rate should be below 10 μSv/h.

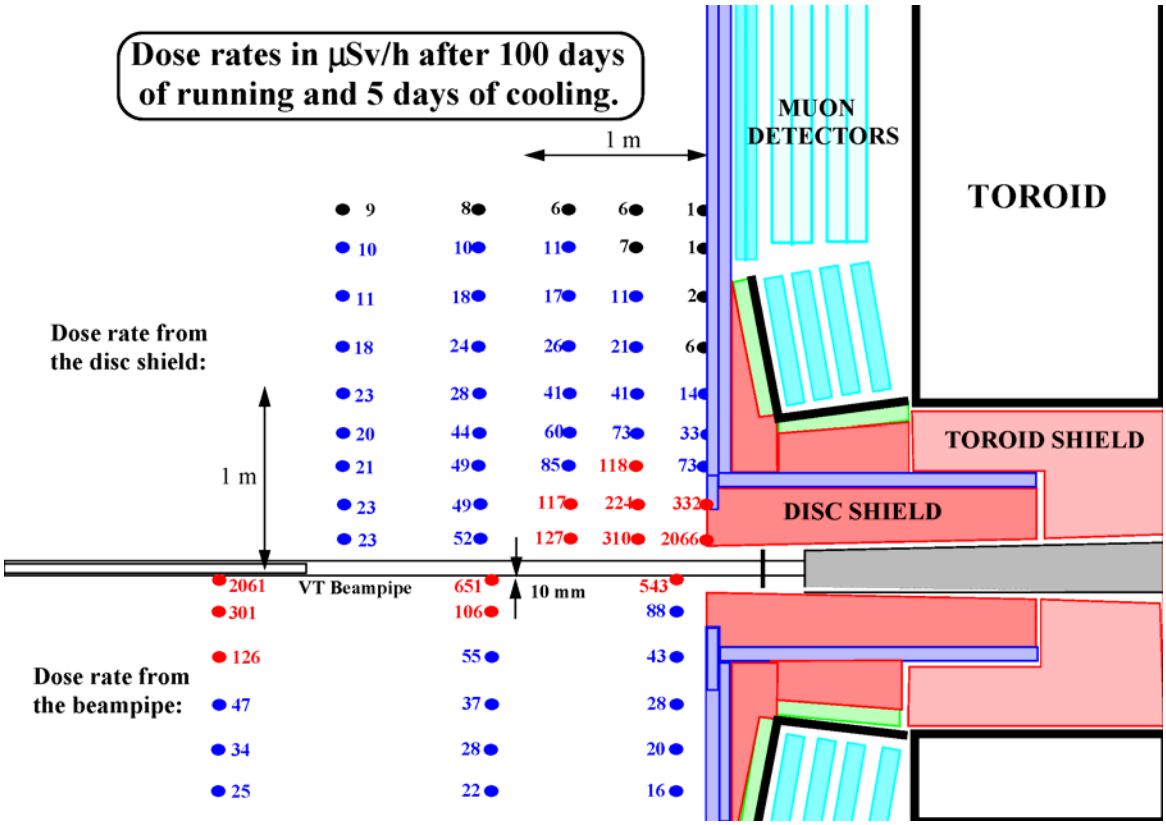

Figure 9.5 The dose rates in front of the disk shield (JD) after it has been moved into its garage position during the standard access. Dose rates caused by the activation of the JD shielding are given separately from the dose rates from activation of the beampipe. Calculation by Morev et al. [121].

On the other side of the access region is the endcap calorimeter at this stage of the opening scenario. Figure 9.6 show the dose rate behind the calorimeter. The radiation is mostly coming from the beampipe which has a small radius and which is double walled in this region in the calculation. The region closer than 1-2 m from the beampipe should be regarded as a "forbidden zone" so that people cannot get into regions with a dose rate exceeding 1 mSv/h. This is not a severe limitation since there is no maintenance work foreseen close to the beampipe at the back of the calorimeter anyway.

The last operation in the standard access scenario is to move the endcap calorimeter so that an access area opens up between the inner detector and the calorimeter (see Figure 9.7). The VA beampipe that is situated inside the FCAL during LHC running becomes very hot. Contact dose rates of more than 3 mSv/h can be expected from gamma radiation and at 1 m distance from the beampipe the dose rate still exceeds 100 μSv/h. The full body dose rate for someone working on the inner detector can be expected to be as much as 0.5 mSv/h. The situation is made worse by a vacuum pump situated just in front of the inner detector. Not much maintenance work on the inner detector is planned when the beampipe is in place and the region closer than 2 m to the beampipe should be fenced off and regarded as a restricted area due to the high radiation levels.

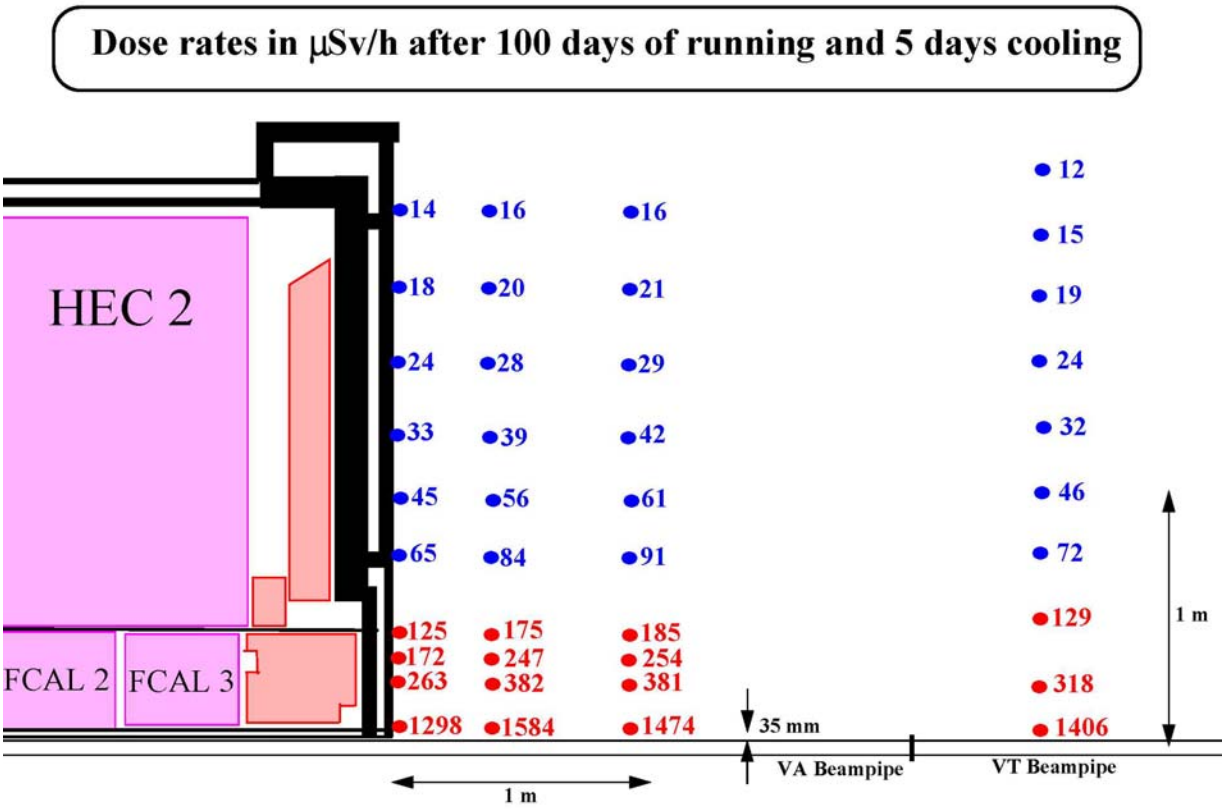

Figure 9.6 The dose rate behind the endcap calorimeter. Calculation by Morev et al. [121].

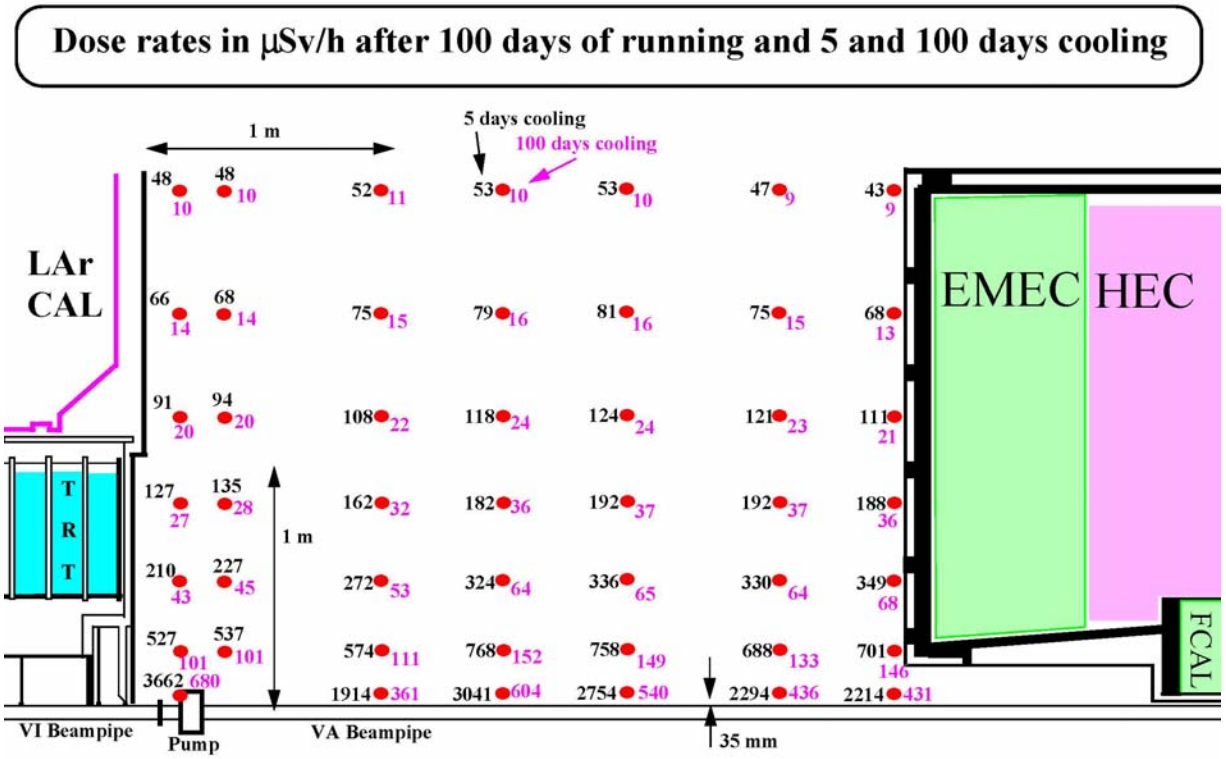

Figure 9.7 The doserate between the inner detector and the endcap calorimeter during the standard access scenario. Values are given for both 5 and 100 days of cooling-off. Calculation by Morev et al. [122].

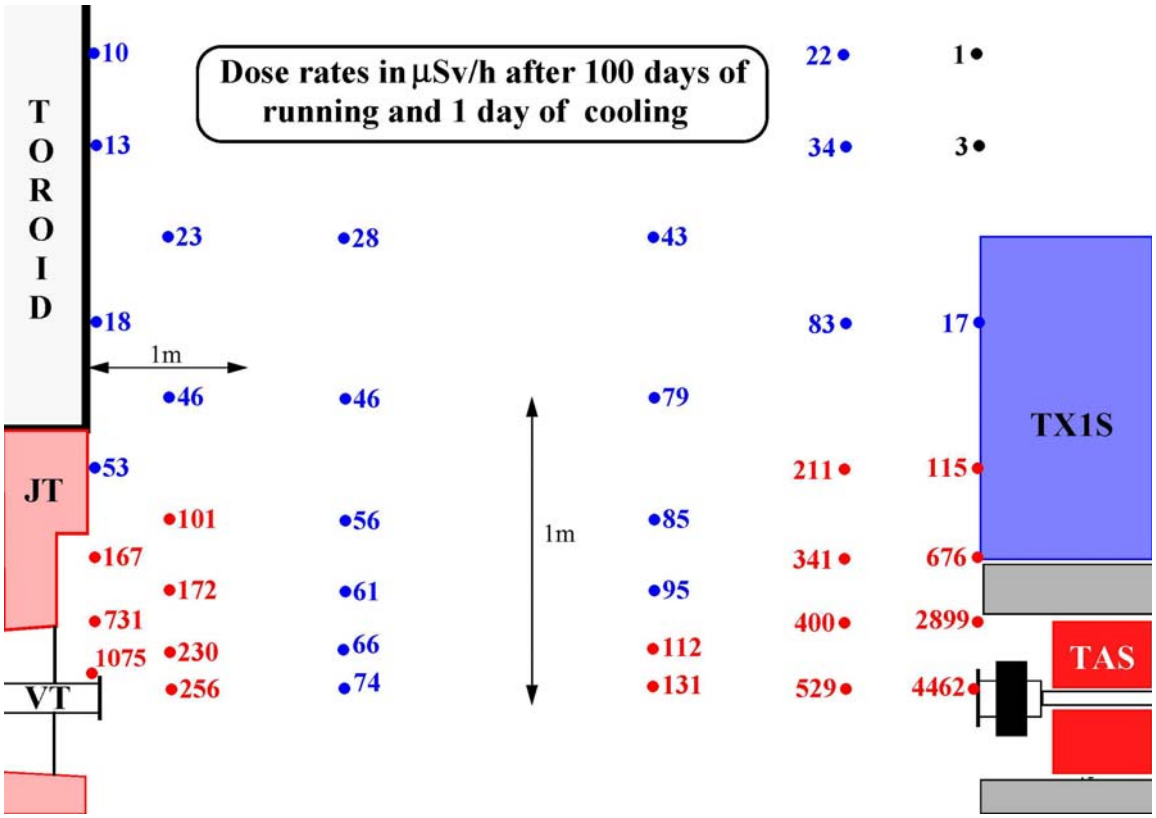

Figure 9.8 The expected dose rate in the region between the endcap toroid and the nose shield (TX1S) after the forward shielding and the VJ beampipe have been removed. Calculation by Morev et al. [119].

9.4 Inner detector access

In the inner detector access scenario the entire beampipe is removed with the possible exception of the beryllium beampipe inside the inner detector (VI). The removal starts with the VJ beampipe that has a remotely operated flange on the TAS side but a normal flange that has to be removed manually on the toroid side. Figure 9.8 shows the dose rate after both the forward shielding and the VJ beampipe have been removed. There is a hot zone around the TAS collimator on one side and the VT beampipe on the other. The TAS zone should not be made accessible. The VT region has to be visited by vacuum technicians who have to remove beampipe support S5 and undo the support S4 (see
Figure 9.2). A beampipe extension with a rolling support also has to be attached to the VT flange so that the beampipe can be supported when the endcap toroid is moved. During this work the full body dose rate to the vacuum technicians might exceed 0.5 mSv/h and the tooling has to be made such that the work can be done quickly and at the largest possible distance from the hot VT beampipe.

The next step in the inner detector access scenario is to move the endcap toroid onto the HF truck until it gets close to the nose shield (TX1S). The VT beampipe can then be removed. It is done by removing the bolts that holds the VA and VT flanges together and by removing the extension piece. This work has to be done in the radiation environment described by Figure 9.4. The beampipe support inside the hole in the JD plug has also to be removed in the same way as in the standard access scenario. The endcap toroid is then moved sideways out of the beamline and the

second HF truck is moved in. The JD/SW assembly is moved onto this HF truck and is lifted to the surface building. Before this can be done a transport frame has to be attached to the JD shielding. The radiation field around the JD is given in Figure 9.9. Full body dose rates of 200-300 μSv/h can be expected during this work.

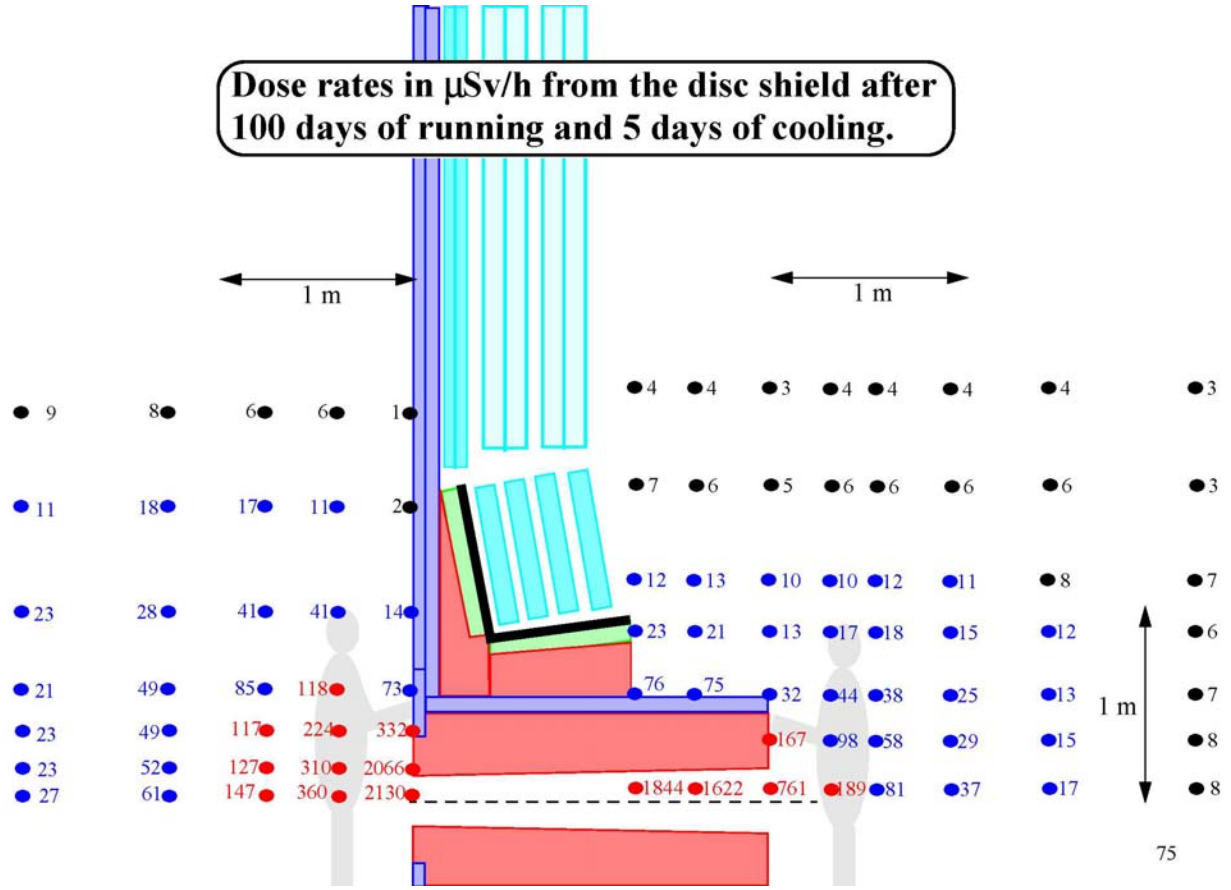

Figure 9.9 The dose rates around the JD disk shielding after the beampipe has been removed. Calculation by Morev et al. [121] [123].

After the endcap calorimeter has been moved enough away from the inner detector it is possible to remove the VA beampipe section. This has do be done in the high radiation field depicted in Figure 9.7 and therefore has to be done very fast. After the VA had been removed the endcap calorimeter can be move onto the HF truck. The FCAL region will, as can be seen in Figure 9.10, be hot but there is no reason for anybody to have access to this zone.

From the above description it is clear that the vacuum group has to work for a considerable amount of time in very close contact to the beampipe. It is also obvious that the standard access scenario will result in much shorter exposure to radiation of the vacuum technicians than the inner detector scenario in which the beampipe is removed.

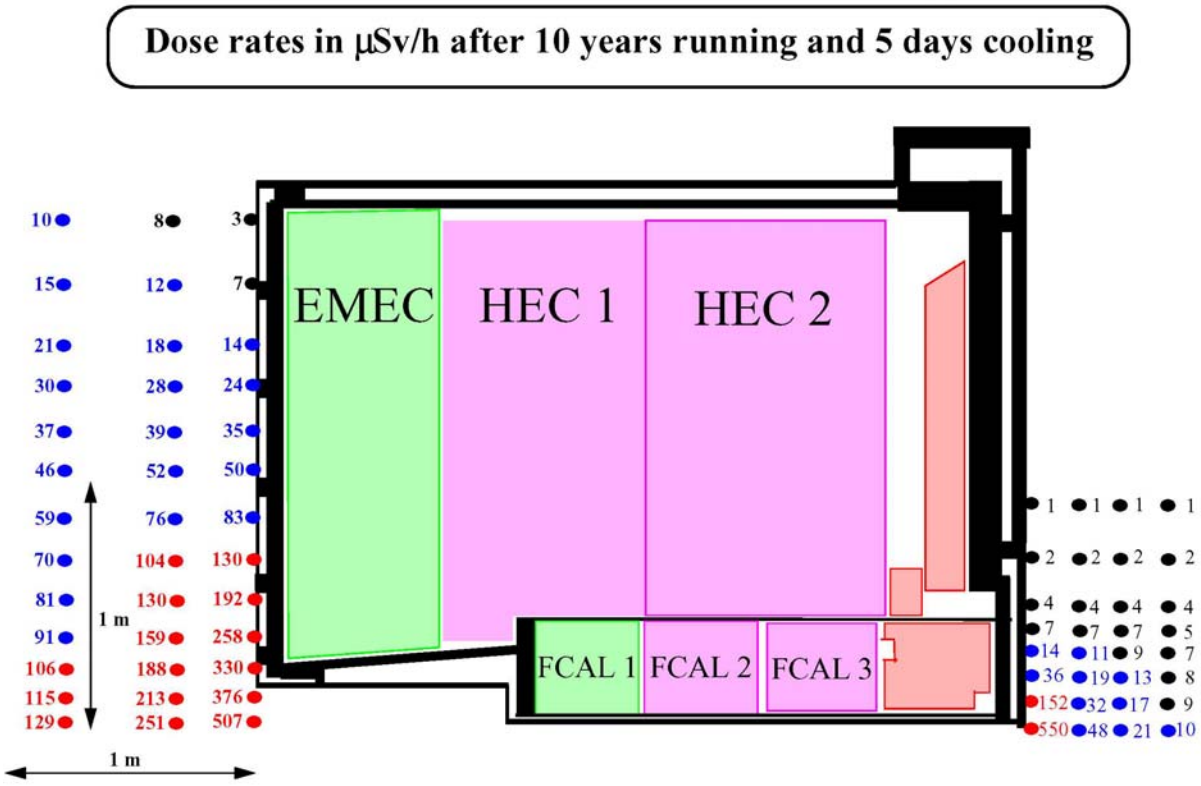

Figure 9.10 The dose rate at the front and back of the endcap calorimeter. Calculation by Morev et al. [121],[122].

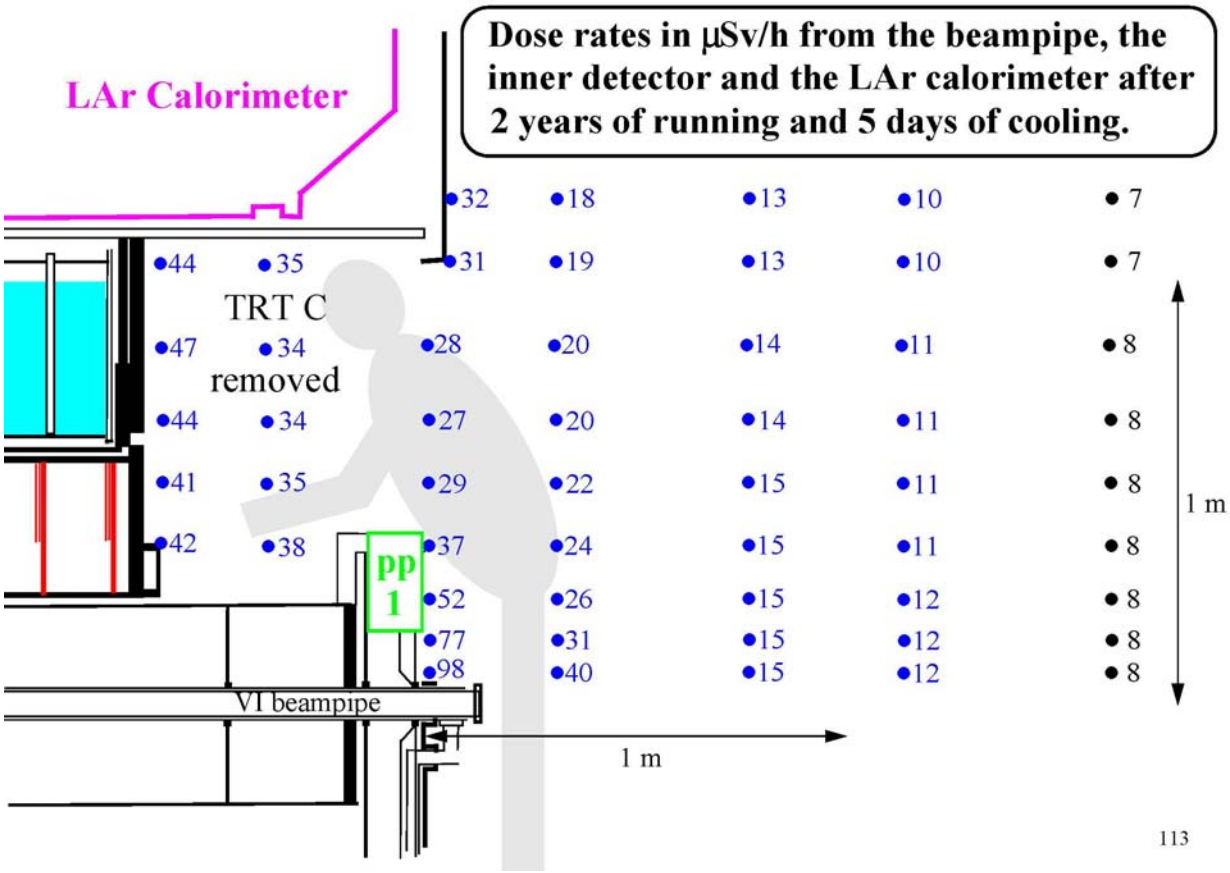

Figure 9.11 The doserate to a person working on the TRT. Calculation by Morev et al. [122].

When it comes to the maintenance of the ATLAS experiment it is mostly work at the inner detector that will require technical personnel to spend time close to the beamline. During the standard access scenario the high radiation levels prevents all but very short maintenance operations to the inner detector. But what is the situation after the VJ, VT and VA beampipes have been removed and only VI remains? Figure 9.11 shows the expected dose rates to a person working with maintenance or installation/removal of the TRT. The values are now much lower since the stainless steel beampipe (VA) has been removed. The hottest area is close to the end of the VI beampipe which is made of aluminium. Here the dose rate is 100 μSv/h but the full body dose rate to a person working on the TRT should be around 30 μSv/h.

The PIXEL detector might have to be removed for maintenance or repair. Figure 9.12 show the situation in the experiment after the PIXEL detector has been removed and Figure 9.13 the dose rate around the detector itself. In this scenario the remaining dose rate in the vicinity of the inner detector is around 20-30 μSv/h. The radiation field is quite uniform without any hotspots.

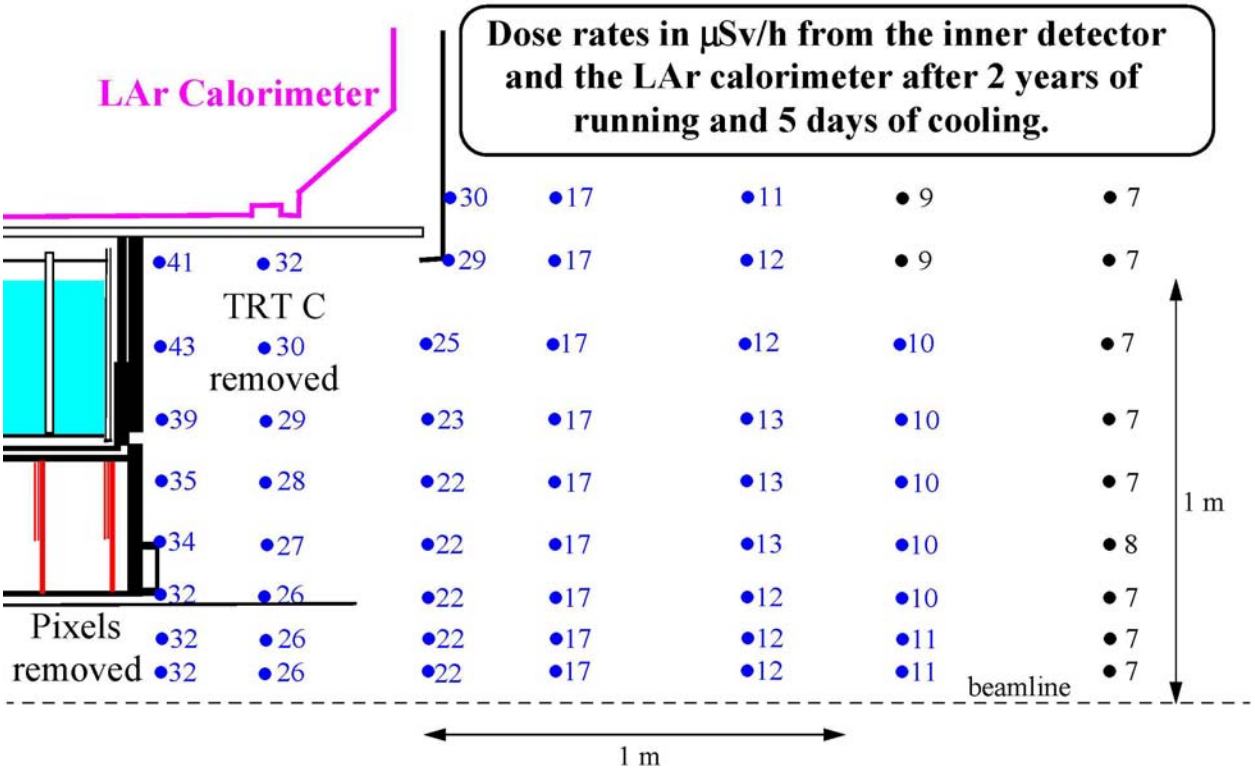

Figure 9.12 The dose rate after the TRT wheel C and the pixel detector have been removed. Calculation by Morev et al. [122].

Someone doing repair work on the activated pixel detector can expect to receive 10-30 μSv/h. The aluminium part on the VI beampipe is as mentioned earlier a hot region with contact dose rates up to 200 μSv/h and this part should be shielded during the work. The PIXEL detector it self can give contact dose rates of up to 100 μSv/h.

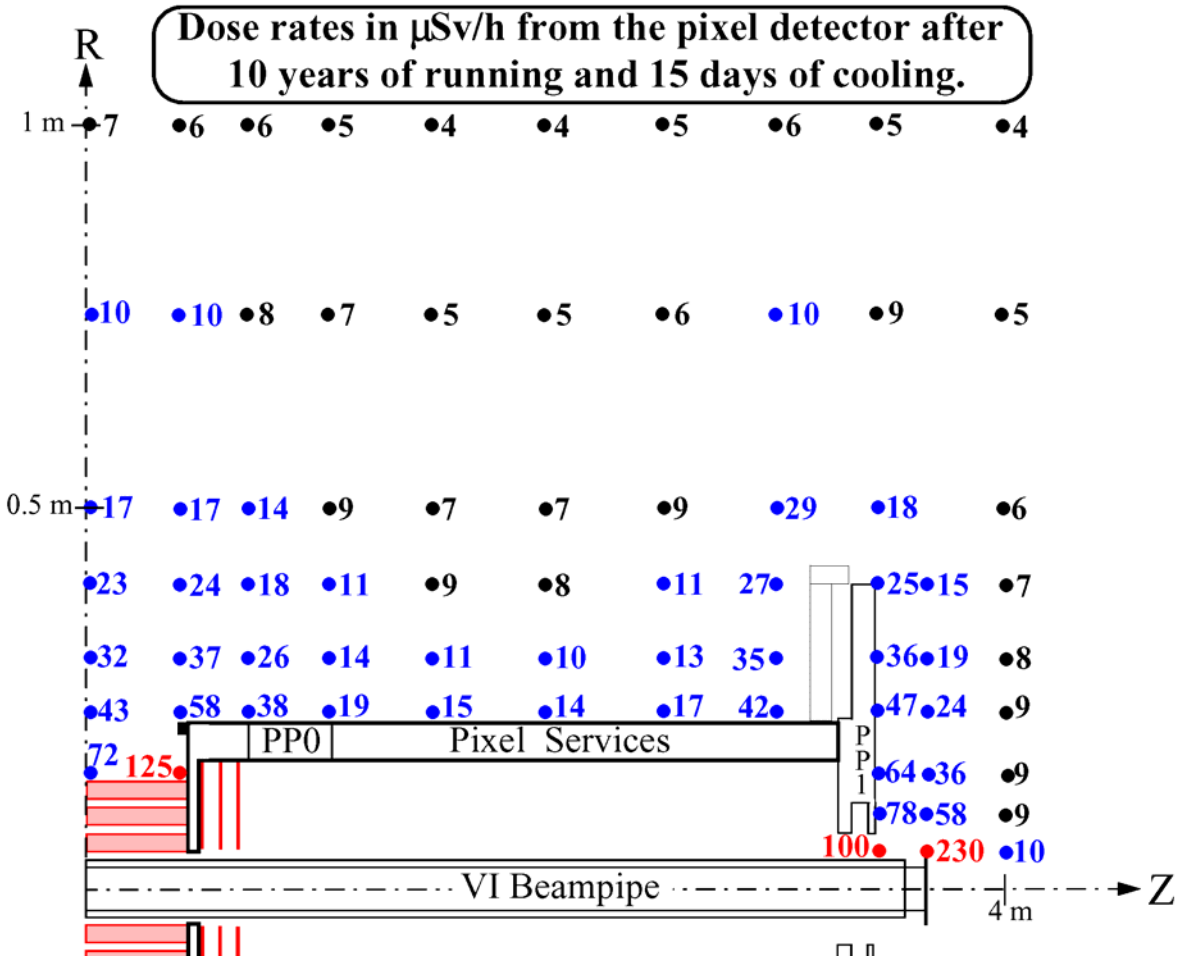

Figure 9.13 The dose rate around the pixel detector after it has been removed from the experiment. Note that the scale in R and Z are very different in this plot. Calculation by Morev et al. [122].

9.5 Considerations about the choice of material

The low-energy neutron activation is very much dependent on the material. The amount of radiation from silver can for example be 10000 times larger than that of the radiation from the same amount of lead due to differences in cross sections and half-lifes of the produced isotopes. As stated earlier it is, however, radiation from high energy hadron activation that dominates close to the beamline (<1-2 m) in ATLAS. Figure 9.14 shows how the activation by high energy hadrons is expected to vary with the atomic number for very long irradiation times i.e. when saturation is reached. Except for very light materials such as beryllium and carbon most materials give similar amounts of radiation. It can be noted that 1g of aluminium is predicted to give the same dose-rate as iron and only a factor 2 less than 1g of lead.

It can also be noted that the predicted values by Morev et al. are in a reasonable agreement with the ones calculated by Barbier back in 1969 [118].

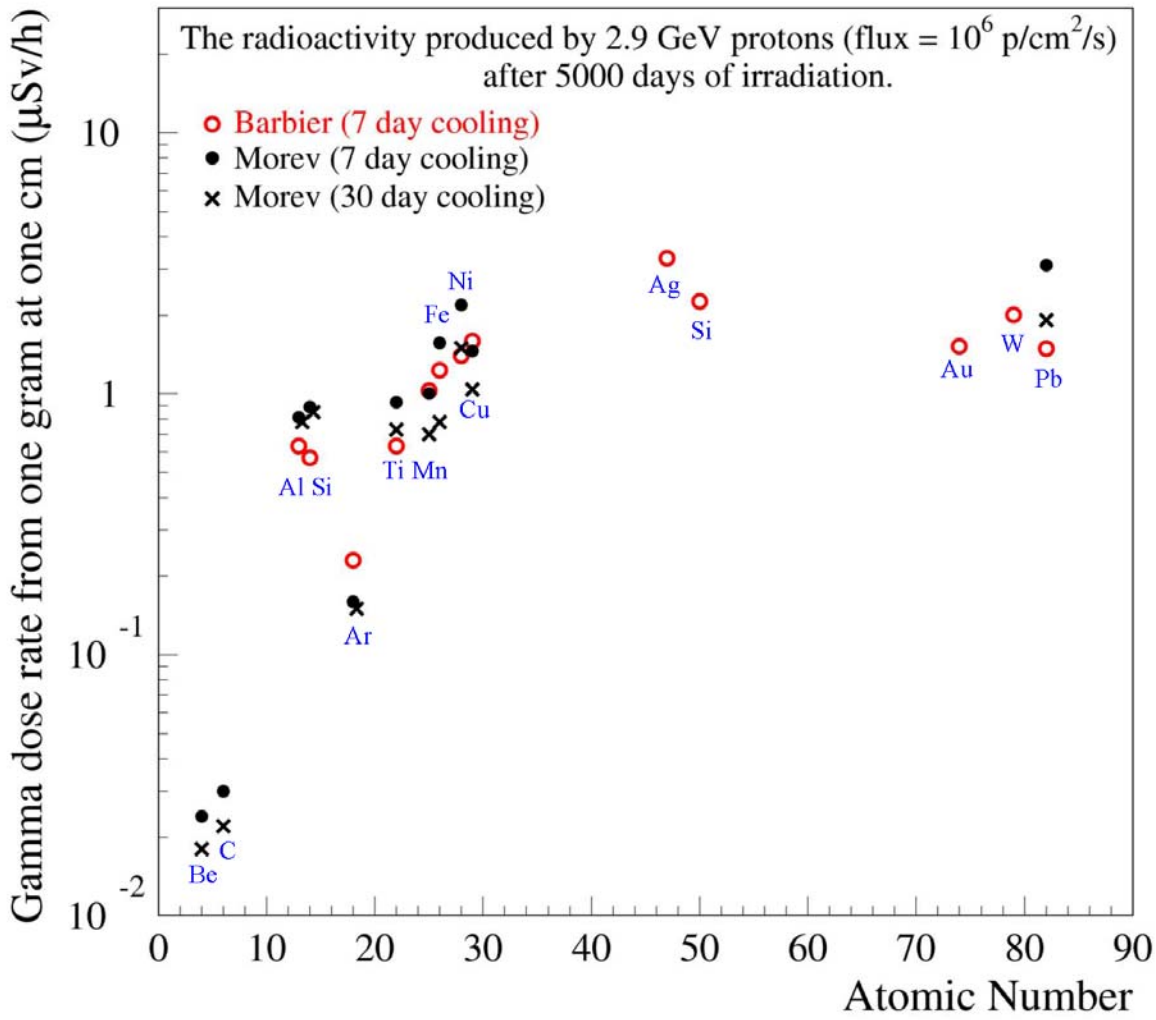

Figure 9.14 The calculated dose-rate from a point source of 1 g at a distance of 1 cm. The radioactivity was induced by 2.9 GeV protons (flux=10^6 p/cm^2). The dose-rate is after 5000 days of irradiation and 30 days of cooling-off.

To conclude from Figure 9.14 that the choice of material is irrelevant is not correct. Table 9.1 gives the ratio of the predicted dose-rate from the VA beampipe in ATLAS when it is made of stainless steel or aluminium. For long irradiation times the difference is small as noted previously but the shorter the irradiation time the larger the difference between aluminium and stainless steel. The reason for this is the different half-lifes of the most important activation products in steel (^{48}V τ=16 days, ^{52}Mn τ=5.6 days, ^{54}Mn τ=312 days, ^{46}Sc τ=84 days and ^{56}Co τ=77 days) and aluminium (^{22}Na τ =2.61 years and ^{24}Na τ =15 hours). Due to the long half-life of ^{22}Na, aluminium reaches saturation much later than steel. Figure 9.15 shows what dose rate to expect in front of the inner detector if the VA beampipe is made of stainless steel or aluminium. The difference is more than a factor of 10. The Radiation Taskforce therefore recommends that ATLAS change from a steel to an aluminium beampipe before high luminosity running.

The ratio of the doserate from a steel and an aluminium beampipe with the same thickness.

Cooling time	Running time 5000d	1000d	100d	30d
1 d:	9	13	23	23
5 d:	9	15	76	181
7 d:	8	14	68	164
30 d:	4	7	22	39

Table 9.1 The ratio of the expected dose-rate from a VA beam pipe in ATLAS made out of stainless steel compared to a beam pipe made out of aluminium. Calculation by Morev et al. [124].

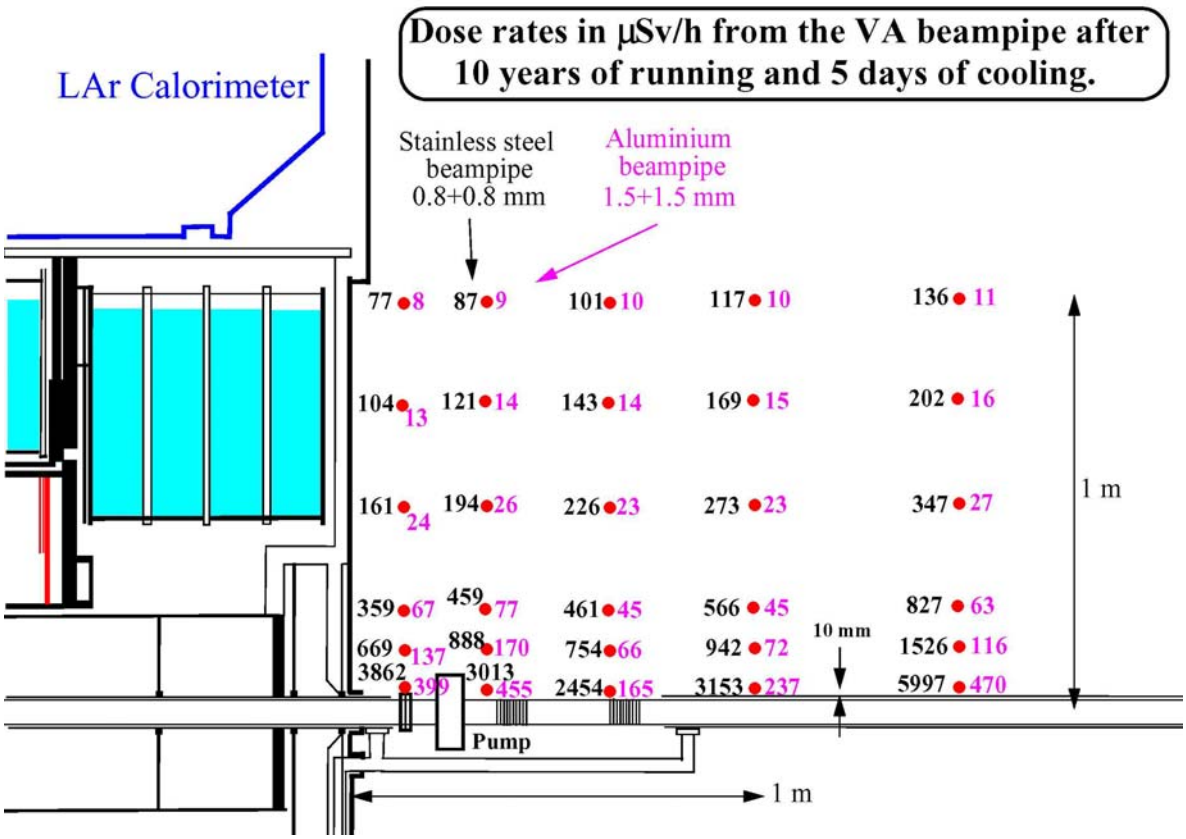

Figure 9.15 The predicted dose rate from the VA beampipe section when it is made of stainless steel and aluminium. The stainless steel pipe was assumed to be double walled with a thickness of 0.8+0.8 mm. The aluminium pipe was assumed to be 1.5+1.5 mm thick. Calculation by Morev et al. [124].

10 Conclusion

The task force has worked simultaneously on various fronts in order to predict with the best possible accuracy the levels of background in ATLAS and their impact on the detector. The geometry and material description has been updated to adjust to the final design of the detector elements. The latest layout of the vacuum equipment was introduced. Realistic material and engineering solutions have been implemented for the elements of the shielding under study. The simulation tools, event generators and transport programs, have been systematically reviewed and associated uncertainties estimated. Background rates of relevant particle species have been calculated. Their impact on the detector performance has been studied as well as the induced radioactivity. The task force carried out, in parallel, a systematic shielding optimization to minimize the effects that were identified as most critical.

A summary of the topics covered by this report is given in the beginning of this document and here we will only list some of the overall conclusions:

- The difference between the fluences calculated with different minimum bias event generators is small (typically 20%).
- The comparison of different transport codes (FLUKA2001, MARS14(2002) and GCALOR) showed a good agreement between the programs for energy-integrated neutron, photon and e^+e^- fluxes as well as energy-deposition (typically within 50%). The agreement for charged-hadrons was not as good, but differences are always within a factor 2.5. It can be concluded that the predictions of FLUKA, MARS and GCALOR are in good agreement for neutron and photon fluxes, especially for material environments dominated by iron. At large radii, or in outer-detector regions, neutrons and photons are usually the most important components of the radiation background and the consistency of the Monte Carlo predictions gives confidence in their predictions. In general, no discrepancies have been observed which exceed the safety-factor of 2.5 used by ATLAS as an estimate of transport-code uncertainties in the outer-detector regions with one exception, the very energetic photon fluence with energies above 10 MeV that shows differences of the order of a factor 10.
- From the benchmarking results given in [96] it can be concluded that FLUKA is accurate to ~20% in its predictions for neutrons and photons and this suggests that a lower safety-factor than 2.5 could be used for neutron and photons (at least when the main material is iron).
- The predicted particle flux in the Inner Detector for the latest ATLAS geometry is ~30% lower than what was predicted at the time of the Inner Detector Technical Design Report.
- The single plane muon counting rates have been calculated on the base of the new fluences and average chambers counting efficiencies. Predicted rates are the same or lower than what was predicted at the time of the Muon Spectrometer Technical Design Report with the exception of the region of the Large Muon Wheel where the rate has doubled since the TDR.
- In the study of the muon trigger rate a new significant process called "Double-Compton scattering" has been identified. The estimation of the low-p_T muon trigger rate in the

barrel is now about twice as high as at the time of the muon TDR due to this new process. However, even after applying a 5 safety factor the rates in the barrel are lower than that of the prompt muons. In the endcap, double Compton scattering dominates over accidentals and with the safety factor the rate is close to that of the prompt muons. This is however an upper limit because it was calculated with coincidence window sizes larger than the baseline. Both in the barrel and in the endcap, protons are potentially the most dangerous component. They require a dedicated detailed study.

- The expected high-p_T muon trigger rate in the barrel is low and at the same level as at the time of the muon TDR. The rate is acceptable even with a safety factor 10. An upper limit of 1-3 kHz has been calculated for the high-p_T muon trigger rate in the endcap. Most of the rate comes from photons with an energy larger than 100 MeV and the uncertainty on the predicted flux is large (a factor 5-10). It is recommended to make a more precise estimate of the trigger rate due to these energetic photons in the endcap.

- Of the many studies done in order to optimize the shielding design, the most important new insight was that the forward shielding was over-dimensioned and that 1000 tons of iron, polyethylene and lead could be removed from it without significantly increasing the background rates.

- The study of the radiation in USA15 has shown that one can expect an increase of the radiation levels during LHC running of at most 60% since the time of the design of USA15. The reason for this increase is not the holes in the USA15 wall for the trigger cables or other ducts and passageways but the increase of radiation levels in ATLAS due to the "plume" of neutron radiation coming out of the endcap toroid magnets. This increase would not be a problem if it was not for the fact that discussions are underway to lower the limit for a simple controlled area. Due to the uncertainties in the calculations it could be that the radiation levels at 10^{34} $cm^{-2}s^{-1}$ will exceed the limits allowed for a simple controlled area and if the luminosity is increased well past 10^{34} $cm^{-2}s^{-1}$ it is almost certain that USA15 cannot remain a simple controlled area.

- Induced radioactivity will limit the access to ATLAS. The beampipe will be the major source of induced radiation in ATLAS and the region surrounding it out to a radius of about one meter should be made off limit to the ATLAS personnel. This means that there will be virtually no maintenance of the Inner Detector possible during standard access. Work close to the one-meter limit will be allowed for 2-3 weeks per person and year. For time-consuming work on the Inner Detector it is necessary to remove the beampipe as foreseen in the Inner Detector access scenario. It will then be possible to work for at least 5 weeks per person and year in the close vicinity of the Inner Detector. Since the beampipe is such a large source of induced radiation the Radiation Task Force recommends that ATLAS upgrade its beampipe to an Aluminium or Beryllium beampipe before the high luminosity running starts.

- If the LHC will run at a luminosity much higher than the present design luminosity it will not be possible to keep the background rates in the muon spectrometer unchanged. A beryllium beampipe could reduce the background rate with up to a factor of 3 but increased shielding will not be able to decrease the rates with much in addition to that.

10.1 Remaining issues and follow-ups

In the course of Radiation Taskforce work, it has become apparent that there are a number of areas where future simulations and study would be useful, but which lie beyond the scope, and resources of the RTF group.

- AZIMUTHAL ASYMMETRY EFFECTS:
  GCALOR and FLUKA geometries used for ATLAS backgrounds simulations are simplified for computational speed by using phi-symmetric shapes whenever possible. However, in the forward toroid, the electronics gaps, and the TAS collimator regions the geometry models consists of lumped elements (boxes, wedges, etc) representing magnet coils, electronics crates, etc. It is expected that the radiation background rates will be phi-dependent and this could be done readily as part of future investigations.

- INNER DETECTOR MATERIAL DESCRIPTION:
  Study of inner detector material description with respect to isotopes with large neutron capture cross-sections, as described in Section 5.2.1. In some materials the details of the isotopic composition is not available, and sometimes the relevant (n,γ) cross sections are not known.

- HALL SHAPE EFFECTS AND USA15 RATES:
  Most of GCALOR and FLUKA simulations were performed with a simplified cylindrical hall giving conservative results, since it has been shown that the larger, more realistic hall gives low energy neutron and photon rates that are reduced by 10% to 15% in most of the muon system. However, future work could go further in this area, putting in a completely realistic experimental hall, and mapping the rates in this design.

- DICE/GCALOR SIMULATIONS:
  The ATLAS DICE geometry has been updated to contain all the ingredients needed for full simulation of radiation backgrounds. With these pieces now in place, DICE may be used to investigate the phi-dependence of radiation backgrounds, rates in the realistic description of the hall, and future issues, such as beamline upgrades (see below). In addition, radiation background can be superimposed to physics events and their effect on tracking efficiency can be studied.

- MUON SYSTEM EFFICIENCIES AND TRIGGER RATES:
  The detailed geometry simulations mentioned above can also be used to calculate directly muon chamber efficiencies and trigger rates. These results should be compared to the rate as calculated so far. The detailed simulation may give more precise information on local effects due to the presences of material. However, one has to consider the limitation due to the fact that the background sample may have poor statistics, especially for the hardest particles that represent a dangerous penetrating component. How to handle double counting is an issue in both approaches and comparing both predictions will be a useful cross-check.

- GEANT4:
  Detailed simulation is now done in ATLAS with GEANT4. Radiation background predictions should also be provided with GEANT4. Radiation calculations should be benchmarked in the same way as was done in this report with FLUKA, MARS and GCALOR.

- FERMILAB SHIELDING EXPERIENCE IN RUN II:
  As described in Chapter 7, much effort has been put into understanding the systematics involved in simulations using the available neutron transport codes: GCALOR, FLUKA, and MARS. However, simulations are best checked by experimental data, and retuned or modified as needed should discrepancies be found. The D0 and CDF experiments at the Fermilab Tevatron are in the midst of Run II data taking. Radiation shielding was added to both experiments prior to Run IIa, and simulations done in the course of shielding design. For D0, Vladimir Sirotenko-- also an ATLAS collaborator--used GCALOR to simulate the background rates. It should be possible to look at D0 forward muon detector rates in the pixel scintillators and MDT's to gain information both about the reliability of the transport code, and the muon detector response.

- BEAM PIPE UPGRADE STUDY:
  A number of studies reported in section 8.7 of this document and in [6] show that the beamline is an important source of secondary particle production leading to detector backgrounds, and that further beamline design optimisation can potentially yield large improvements in backgrounds. It is strongly suggested that over the next few years, the LHC vacuum group should continue to work in tandem with ATLAS to create an optimized beamline design that could be the installed as a future upgrade.

- BEAM GAS BACKGROUND:
  Simulating the beam gas background is not a trivial project. The LHC vacuum group has Z position profiles from its pumping programs of the densities of contaminant atomic and molecular gases along the beamline. This information must be used as input to what is essentially a fixed target collision simulation of primary beam protons interacting with the contaminant molecules. Most of the collisions are low p_T, and an event generator such as PHOJET must be used (in fixed target mode), to get the right distribution of collision products. Such a simulation is sufficiently different from standard backgrounds studies that it requires a dedicated effort. This work has started in ATLAS [125] and it is recommended to pursue it.

References

1. Radiation Task Force predicted radiation levels: http://atlas.web.cern.ch/Atlas/GROUPS/PHYSICS/RADIATION/Radiation_Levels.html
2. "Shielding for the ATLAS Experimental Region", A. Ferrari, K. Potter, and S. Rollet , LHC Project Note 6, http://atlas.web.cern.ch/Atlas/TCOORD/Activities/CommonSys/Shielding/Activation/act_USA15.html
3. "Radiation Calculations for the ATLAS Detector and Experimental Hall", A. Ferrari, K. Potter, S. Rollet and P.R. Sala, CERN-EST-96-001, http://atlas.web.cern.ch/Atlas/TCOORD/Activities/CommonSys/Shielding/Activation/act_USA15.html
4. "Attenuation of Radiation in the Access Labyrinths and Service Ducts between the ATLAS Experimental and Service Caverns", S. Rollet, K.M. Potter and G.R. Stevenson, CERN-EST-LEA/99-02, http://atlas.web.cern.ch/Atlas/TCOORD/Activities/CommonSys/Shielding/Activation/act_USA15.html
5. "Radiation in the USA15 cavern in ATLAS",I. Dawson and V. Hedberg, ATLAS note ATL-TECH-2004-001, http://doc.cern.ch//archive/electronic/cern/others/atlnot/Note/tech/tech-2004-001.pdf
6. "Radiation and induced activation at high luminosity", V. Hedberg and M. Shupe, ATLAS note ATL-TECH-2004-002, http://doc.cern.ch//archive/electronic/cern/others/atlnot/Note/tech/tech-2004-002.pdf
7. FLUKA: "Status and Prospective for Hadronic Applications", A. Fasso, A. Ferrari, J. Ranft, P.R. Sala, "Electron-photon transport in FLUKA: status" in the Proceedings of the MonteCarlo 2000 Conference, Lisbon, October 23-26 2000, Springer-Verlag Berlin, p. 955-960 (2001).
   Web page: http://www.fluka.org
8. C.Zeitnitz and T.A.Gabriel, The GEANT-CALOR Interface and Benchmark Calculations for Zeus Calorimeters, Nucl. Instrum. Methods Phys. Res., A 349 (1994) 106-111
   Web page: http://www.physik.uni-mainz.de/zeitnitz/gcalor/gcalor.html
9. Summary of the activity of the RADIATION and SHIELDING working group, reported by M.Cobal, ATL-TECH-98-034.
10. The ATLAS activation studies, V.Hedberg. http://atlas.web.cern.ch/Atlas/TCOORD/Activities/CommonSys/Shielding/Activation/activation.html
11. Background calculations for the ATLAS detector and hall, G.Battistoni et al., ATL-GEN-94-010 and addendum.
12. ATLAS Muon Region Background Fluxes in Four Forward Configurations, M.Shupe, ATL-GEN-94-011.
13. Task Force initial membership: M. Bosman (chair), W. Witzeling, P. Norton, M. Shupe, I. Dawson, I. Štekl, S. Willis, S. Lloyd, G. Stevenson (consultant), M. Huhtinen (consultant), ATLAS management (ex-officio), Physics coordinator (ex-officio). Additional members: S. Baranov, V. Hedberg, A. Nisati, S. Pospišil.
14. A.I.Drozhdin et al., Nucl. Instrum. Methods Phys. Res., A 381, (1996) 531.
15. ATLAS Collaboration, Technical Proposal for a General Purpose pp Experiment at the Large Hadron Collider at CERN, CERN/LHCC/94-43,LHCC/P2,1994

16. ATLAS Collaboration, series of detector Technical Design Report, CERN/LHCC/97
17. ATLAS Inner Detector TDR, CERN/LHCC/97-16.
18. Conceptual design and performance of the CMS forward shielding, CMS note CMS-IN-2000/051, M.Huhtinen et al.
19. On the Lifetime of Proportional Counters, Ph.D. thesis, M.Spegel, CERN 1997.
20. Radiation Studies in the Collimator regions of the ATLAS experimental area, I. Dawson and G.R. Stevenson, CERN/TIS-RP/IR/98-01.
21. Lahet TM/ MCNP TM/ Cinder'90 activation calculations for the ATLAS integrated forward calorimeter concept, Waters, L; Wilson, W.B, ATL-CAL-94-047; ATL-AC-PN-47.
22. Dawson et al., "Radioactivation of silicon tracker modules in high-luminosity hadron collider radiation environments", Nucl. Instrum. Methods Phys. Res., A 515 (2003) 422-438.
23. Radiation Safety Manual: http://edms.cern.ch/file/335729/LAST_RELEASED/F_E.pdf Available from the TIS division at CERN: http://tis.cern.ch/
24. Radiation Hard Electronics web page http://atlas.web.cern.ch/Atlas/GROUPS/FRONTEND/radhard.htm
25. Computational method to estimate single event upset rates in an accelerator environment, Huhtinen, M; Faccio, F, Nucl. Instrum. Methods Phys. Res., A 450 (2000) 155-72.
26. Monte-Carlo Simulations of Neutron Shielding for the ATLAS Forward Region**,** Stekl, I et al., CERN-OPEN-2000-128 and Nucl. Instrum. Methods Phys. Res., A 452 (2000) 458-69; Monte-Carlo simulations of different concepts for shielding in the ATLAS experiment forward region, Stekl, I et al., ATL-TECH-2001-002.
27. Experimental Tests of Neutron Shielding for the ATLAS Forward Region, S.Pospišil et al., CERN-OPEN-1998-025 and Nucl. Instrum. Methods Phys. Res., A 440 (1999) 249-258.
28. Study of neutrons and gamma backgrounds in ATLAS, Y.Fisiak, ATL-CAL-94-039.
29. Radiation Calculations for the ATLAS Detector and Experimental Hall, A.Ferrari, S Rollet, et al., CERN/TIS/RP/97-05 report, presented at the 2nd workshop on Simulating Accelerator Radiation Environment (SARE-2)
30. Ambient Dose and Ambient Dose Equivalent Conversion Factors for High Energy Neutrons, A.V.Sannikov and E.N.Savitskaya, CERN Int.Report CERN/TIS-RP/93-14 (1993).
31. Radiological Safety Aspects of the Operation of Proton Accelerators, R.Thomas and G.R.Stevenson, Technical Report Series No 283, IAEA Vienna (1988).
32. R. Engel, J. Ranft and S. Roesler, Hard diffraction in hadron-hadron interactions and in photoproduction Phys. Rev. D52 (1995) 1459
33. R. Engel, Photoproduction within the two component dual parton model: Amplitudes and cross-sections, Z.Phys.C66:203-214,1995; R. Engel and J. Ranft, Hadronic photon-photon interactions at high-energies, Phys.Rev.D54:4244-4262,1996: http://lepton.bartol.udel.edu/~eng/phojet.html
34. Grenoble "Hybrid Nuclear Reactors" web site http://isnwww.in2p3.fr/reacteurs-hybrides/PPNPport/node1.html
35. T.Sjostrand et al., *PYTHIA 6.1*, Comput. Phys. Commun. 135 (2001) 238 (LU TP 00-30, hep-ph/0010017): http://www.thep.lu.se/~torbjorn/Pythia.html
36. A.Capella et al., Dual Parton Model, Phys.Rep.236 (1994) 225--329.
37. F.Paige and S.Protopopescu, Supercollider Physics, p.41, ed. D Soper, World Scientific, (1986).
38. G. Corcella et al., HERWIG 6.4, JHEP 0101 (2001) 010 [hep-ph/0011363]; hep-ph/0201201.
39. "DTUJET93", P. Aurenche, et al., Comput. Phys. Commun., 83, p. 107, 1994.
40. The First-Level Trigger Technical Design Report, CERN/LHCC/98-14.
41. ATLAS Physics and Detector Performance Technical Design Report, CERN/LHCC/99-15.
42. Radiation Task Force Summary page: http://atlas.web.cern.ch/Atlas/GROUPS/PHYSICS/RADIATION/RTF_SummaryPage.htm

43. M.B. Emmett, The MORSE Monte Carlo radiation transport system, Oak Ridge National Laboratory report ORNL-4972 (1975)
44. ALIFE: http://aliweb.cern.ch/offline/fluka/Welcome.html#ALIFE, author A.Morsh.
45. R.Brun, F.Carminati, GEANT Detector Description and Simulation Tool, CERN Program Library Long Writeup W5013, September, 1993. (web address:)
46. H.W. Bertini. Phys. Rev. 188 (1969), p. 1711; H.W. Bertini. Phys. Rev. C 6 (1972), p. 631.
47. H. Fesefeldt, GHEISHA, The simulation of hadronic showers, Technical Report PITHA 85-02, Aachen, 1985.
48. The modified version of the FLDIST subroutine is available at the the following link: http://atlas.web.cern.ch/Atlas/GROUPS/PHYSICS/RADIATION/jan03_baseline/GCALOR_FLDIST.txt
49. T.A.Gabriel et al., CALOR89: A Monte Carlo Program Package for the Design and Analysis of Calorimeter Systems, ORNL/TM-11185.
50. N.V.Mokhov, "The MARS Code System User's Guide", Fermilab-FN-628 (1995); N.V.Mokhov and O.E.Krivosheev, "MARS Code Status", Proc. Monte Carlo 2000 Conf., p.943, Lisbon, October 23-26, 2000; Fermilab-Conf-00/181 (2000); http://www-ap.fnal.gov/MARS/Lisbon, October 23-26, 2000 ; Fermilab-Conf-00/181 (2000); http://www-ap.fnal.gov/MARS/
51. International Commission on Radiation Units and Measurements, Inc., ICRU: http://www.icru.org/
52. I.Dawson, Craig Buttar, The radiation environment in the inner detector, Nucl. Inst. and Meth. A 453 (2000) 461--467. I.Dawson, "Review of the radiation environment in the inner detector" , Atlas Internal note, ATL-INDET-2000-006
53. Radiation Environment Simulations for the CMS Detector, M. Huhtinen, CERN CMS TN/95-198
54. The ATLAS Radiation Hard Electronics web page: http://atlas.web.cern.ch/Atlas/GROUPS/FRONTEND/radhard.htm
55. The ATLAS Muon Spectrometer Technical Design Report, CERN/LHCC/97-22.
56. Muon Chamber Sensitivity to Neutron and Photon Background in the ATLAS Hall, G.Battistoni et al., ATL-MUON-94-05, and P.Sala, private communication.
57. Investigation of spectral efficiency of pressurized drift tubes for detection of neutrons in the energy range between 5 eV and 200 keV, Chelkov, G.A; Fadeev, V.A; Ignatenko, M.A; Kotov, S.A; Kravchenko, I.V; Krumstein, Z.V; Samosvat, G; Shvetsov, V.N; Strelkov, A.V., ATL-MUON-93-031; ATL-M-PN-31.- 15 Nov 1993. Response of the MDT filled with Ar+5%CO2+3%CH4 to thermal neutrons. Borzakov, S; Boyko, I; Chelkov, G; Dodonov, V; Ignatenko, M; Nikolenko, M; Nozdrin, A; Pisarev, I, ATL-MUON-96-116; ATL-M-PN-116.- 09 May 1996
58. Evaluation of ionization produced by fast neutrons in Atlas muon detectors. P.N., V.P., V.T. BNL, August 2001.
59. A proposal to use Cathode Strip Chambers (CSC) for the Atlas forward muon system. V. Polychronakos. ATL-MUON-1994-038.
60. Differential sensitivity of cathode strip chambers to neutrons and photons, A.S.Denisov et al., ATL-MUON-1994-033.
61. TGC response to neutrons, H.Nanjo, presentation at the ATLAS Muon Instrumentation meeting 17th January 2002, http://agenda.cern.ch/askArchive.php?base=agenda&categ=a02910&id=a02910s1t3/transparencies
62. Gamma sensitivity of Pressurized Drift Tubes, Baranov, S.A; Boyko, I.R; Chelkov, G.A; Ignatenko, M.A, ATL-MUON-94-036; ATL-M-PN-36.- 14 Feb 1994
63. Gamma-ray sensitivity of a thin gap chamber, S.Tsuno, T.Kobayashi and B.Ye, Nucl. Instrum. Methods Phys. Res., A 482, (2002) 667.

64. Background studies in the muon spectrometer: summary of GCALOR studies http://atlas.web.cern.ch/Atlas/TCOORD/Activities/CommonSys/Shielding/Activation/back/background.html
65. Calculation of the low PT trigger probability for protons, by S.Robins (A. Nisati private communication).
66. Improvement to the Level-1 muon trigger giving increased robustness against backgrounds, ATLAS Levl-1 muon trigger group, ATL-DAQ-99-008
67. Induced Radioactivity in the Active Gas System of ATLAS ID – TRT, S. A. Cetin and A.Romaniouk, ATL-INDET-2002-001.
68. Induced Radioactivity in the Inner Detector – TRT, S. A. Cetin and A. Romaniouk, ATL-INDET-2000-013.
69. ATLAS Inner Detector TDR, CERN/LHCC/97-17.
70. TRT Module Irradiation Test with High Intensity Neutron Fluxes by P. Gagnon, V. V. Golikov, N. Grigalashvili, G. Kekelidze, H. Ogren, V. Pechekhonov, D. Rust, M. Shafranov to be published.
71. Radiation Hardness: Design Approach and Measurements of the ASDBLR ASIC for the ATLAS TRT by N. Dressnandt, F.M. Newcomer, O. Rohne and S.Passmore. Published in an IEEE proceeding.
72. Irradiation qualification of the DSM DTMROC by M. S. Passmore and R. Ryjov http://agenda.cern.ch/askArchive.php?base=agenda&categ=a022145&id=a022145s1t5/document
73. TRT straw counting rate from photon background at LHC by A. Romaniouk, ATL-INDET-96-149.
74. L.Johansen et al., Radiation studies of silicon microstrip detectors for use in ATLAS Accepted for publication in the IEEE Transactions on Nuclear Science, NSREC Conference issue (December 2002)
75. I.Mandic et al., Radiation effects in the readout chip for the ATLAS SCT, Accepted for publication in the IEEE Transactions on Nuclear Science, NSREC Conference issue (December 2002)
76. M.Lee et al., Radiation hardness studies for the ATLAS SCT optical links, Accepted for publication in the IEEE Transactions on Nuclear Science, NSREC Conference issue (December 2002).
77. ATLAS Pixel Collaboration, ATLAS Pixel Detector Technical Design Report, CERN/LHCC/98-13 (1998).
78. The ATLAS Pixel Detector, presented by M. Garcia-Sciveres on behalf of the Pixel collaboration, Proceedings of the International Workshop on Semiconductor Pixel Detectors for Particles and X-Rays (PIXEL2002), Carmel, California, USA September 9-12, 2002, http://www.slac.stanford.edu/econf/C020909/
79. C.Buttar et al., ATLAS internal note, ATL-INDET-2002-013.
80. The ROSE Collaboration web page: http://rd48.web.cern.ch/RD48/
81. A. Vasilescu (INPE Bucharest) and G. Lindstroem (University of Hamburg): Notes on the fluence normalisation based on NIEL scaling hypothesis, ROSE/TN/2000-02; Displacement damage in silicon, on-line compilation, http://sesam.desy.de/members/gunnar/Si-dfuncs.html http://rd48.web.cern.ch/RD48/Default.htm and references therein.
82. G.P.Summers, IEEE Trans. Nucl. Sci. 34 (1987) 1134
83. M.Huhtinen and P.A.Aarnio, Nucl. Instrum. Methods Phys. Res., A 335 (1993) 580
84. M.Huhtinen, CMS COTS workshop, November 1999
85. D.Bisello et al, ROSE/TN/2000-08, http://rd48.web.cern.ch/RD48/Default.htm
86. M.Huhtinen, ROSE/TN/2001-02, http://rd48.web.cern.ch/RD48/Default.htm
87. Study of the effect of the radiation on the TILECAL Barrel Hadron calorimeter to be used in ATLAS, A. Amorim et al, ATLAS internal note, TILECAL-93-021; Study of molded

scintillator radiation hardness, A. Karyukhin et al, ATLAS internal note, TILECAL-94-025, 1994; ATLAS Technical Proposal, section 2.5, "Hadronic Scintillator Calorimeter", 1994; Low Dose rate effects in scintillating and WLS fibers by ionizing radiation, M.David et al, ATLAS internal note, TILECAL-96-078; Radiation Damage in WLS Fibers, M.-David et al, ATLAS internal note, TILECAL-98-151.

88. HV Distributor Radiation Qualification Part One: SEE Tests, R. Chadelas et al, ATLAS internal note, TILECAL-2002-005; About SEEs in the HV Distributor System of the TILECAL, R. Chadelas et al, ATLAS internal note, TILECAL-2002-006; HV Distributor Radiation Qualification Part Two: TID Tests, R. Chadelas et al, ATLAS internal note, TILECAL-2002-007; HV Distributor Radiation Qualification Part Three: NIEL Tests, R. Chadelas et al, ATLAS internal note, TILECAL-2002-008.
89. Study of neutron induced outgassing from tungsten alloy for ATLAS FCAL, C.-Leroy et al, ATLAS internal note, LARG-99-020.
90. Irradiation test of readout chain components of the ATLAS liguid argon calorimeters, C. Cheplakov et al, ATLAS internal note, LARG-99-018; Irradiation tests of ATLAS liquid argon forward calorimeter (FCAL) electronics components, C.Leroy, ATLAS internal note, LARG-2002-003; Radiation Hardness Tests of the ATLAS Liquid Argon Calorimeter Materials and Equipment at the IBR-2 Reactor in Dubna, C. Leroy et al, submitted to Nucl. Instrum. Methods, Sept. 2003.
91. Pollution of liquid Argon due to neutron radiation, P.Martin, ATLAS internal note, LARG-96-052; Signal loss extrapolation from pollution measurements done at SARA using an alpha cell to the case of the barrel EM calorimeter, J.Collot et al, ATLAS internal note, ATL-LARG-96-056; Pollution of liquid argon after neutron irradiation measured at SARA: summary of raw data, M.L.Andrieux et al, ATLAS internal note, LARG-98-105; Pollution of liquid argon after neutron irradiation, M.L.-Andrieux et al, Nucl. Instrum. Methods Phys. Res., B 183 (2001).
92. Signal Degradation due to Charge Build-up in Noble Liquid Ionization Chambers, J. Rutherfoord . Nucl. Instrum. Methods Phys. Res., A 482(2002) 156 (also ATL-COM-PHYS-2001-02).
93. Radiation Hardness of GaAs Preamplifiers for Liquid Argon Calorimetery at LHC, A. Cheplakov et al, ATLAS internal note, LARG-96-054; Neutron irradiation of HF BJT and 0-T hybrids, G. Battistoni et al, ATLAS internal note, LARG-NO-083; The LARG Calorimeter Calibration Board, J.Colas et al, ATLAS internal note, AL-EN-0005, Dec 27. 1999; Radiation Qualification of the SCA Controller Preselection, (LArg front end boards), D.M. Gingrich et al, ATLAS internal note.
94. http://atlasinfo.cern.ch/ATLAS/internal/Welcome.html
95. Remarks on a concept of the ATLAS forward region shielding, C.Leroy et al., ATL-TECH-NO-032,1998.
96. E.Gschwendtner et al., Benchmarking the Particle Background in the Large Hadron Collider Experiments, ATL-MUON-2002-002.
97. Reliability of Monte Carlo predictions: I.Dawson's web page with complete set of data : http://dawson.home.cern.ch/dawson/fluka/MCstudies/MCstudies.html
98. FLUKA 2001, official Fluka web site: http://pcfluka.mi.infn.it/
99. MARS 14.02, official Mars web site: http://www-ap.fnal.gov/MARS/
100. A Cross-comparison of MARS and FLUKA Simulation Codes, M.Huhtinen and N.V. Mokhov, http://fnalpubs.fnal.gov/archive/2000/fn/FN-697.html
101. GEANT Hadronic Event Generators: a comparison at the single interaction level, A. Ferrari and P.Sala, ATL-PHYS-96-086.
102. P.A.Arnio, A.Fasso, A.Ferrari et al., A new model for hadronic interactions at intermediate energies for the FLUKA code. International conference on Monte-Carlo simulation in high-energy physics, Tallahassee, Florida, 22-26 February 1993, Publ. In:

MC93: proceedings P-Dragovitsch, S.L.Linn and M.Burbank World Sci., Singapore, 1994(88-99).
103. J.O.Johnson and T.A.Gabriel, A user's guide to MICAP: A Monte Carlo Ionization Chamber Analysis Package. Technical Report TM-10340, ORNL, 1988.
104. GAMLIB library, developed in CENBG Bordeaux in the framework of the NEMO experiment, LAL preprint 94-29 (1994).
105. http://dawson.home.cern.ch/dawson/fluka/BPstudy/BPstudy.html
106. Impact of beam-pipe geometry on radiation background in CMS, M.Huhtinen, CMS-NOTE-2000-069.
107. Background rates in the muon system results and the effect of the tungsten plug, A.Ferrari and P.Sala, ATL-MUON-95-090.
108. The induced radioactivity in the Forward Shielding and Semiconductor Tracker of the Atlas detector, I. Bedajanek et al., Submitted to the Tenth International Conference on Radiation Shielding (ICRS-10) and the Thirteen Topical Meeting on Radiation Protection and Shielding (RPS-2004), Funchal, Portugal, May 2004.
109. *The ATLAS activation studies* http://atlasinfo.cern.ch/Atlas/TCOORD/Activities/CommonSys/Shielding/Activation/activation.html
110. G.R. Stevenson, Activation at accelerators, CERN/TIS-RP/90-10/CF
111. M. Hoefert and A. Bonifas, Measurement of radiation parameters for the prediction of dose rates from induced radioactivity, CERN Internal report HP-75-148 (1975)
112. R. Engel and J. Ranft, Hadronic photon-photon interactions at high-energies, Phys. Rev. D54(1996)424.
113. V.A. Klimanov, E.I. Kulakova, M.N. Morev and V.K. Sakharov, *Activation study of the ATLAS detector*, ISTC Project #1800, April-June 2001, Moscow Engineering Physics Institute;http://atlasinfo.cern.ch/Atlas/TCOORD/Activities/CommonSys/Shielding/Activation/report_1_2_new.pdf
114. V.A. Klimanov, E.I. Kulakova, M.N. Morev and V.K. Sakharov, *Activation dose rate in access scenarios to the area between the disk shield and the toroid*, ISTC Project #1800, July-September 2001, Moscow Engineering Physics Institute; http://atlasinfo.cern.ch/Atlas/TCOORD/Activities/CommonSys/Shielding/Activation/text_tab_1_4.pdf
115. V.G. Semenov and N.M. Sobolevsky, Approximation of Radionuclide Production Cross section in Proton Induced Nuclear Reactions. Report on the ISTC project #187, Moscow, 1998
116. F. Mynat et al., The DOT-III Two-Dimensional Discrete Ordinates Transport Code, ORNL-TM-4280, Oak Ridge, 1973.
117. J.F. Briesmeister, *MCNP - A general Monte Carlo N-Particle Transport Code*, *Version 4A*, Los Alamos National Laboratory Report, LA-12625, 1995.
118. M. Barbier, *Induced Radioactivity*, North Holland, Amsterdam, 1969.
119. M.N. Morev, *Dose rates between the JT and JN*, ISTC Project #1800, Moscow Engineering Physics Institute. http://atlasinfo.cern.ch/Atlas/TCOORD/Activities/CommonSys/Shielding/Activation/nose_fields.pdf
120. M.N. Morev, *Dose rates between the JD and the JT with beampipe*, ISTC Project #1800, Moscow Engineering Physics Institute. http://atlasinfo.cern.ch/Atlas/TCOORD/Activities/CommonSys/Shielding/Activation/JD_fields.pdf
121. M.N. Morev, *Dose rates between the LAr endcap calorimeter and the JD*, ISTC Project #1800, Moscow Engineering Physics Institute.

http://atlasinfo.cern.ch/Atlas/TCOORD/Activities/CommonSys/Shielding/Activation/larback_fields.pdf
122. V.A. Klimanov, E.I. Kulakova, M.N. Morev and V.K. Sakharov, *Activation doserate during access to the inner detector*, ISTC Project #1800, Moscow Engineering Physics Institute. http://atlasinfo.cern.ch/Atlas/TCOORD/Activities/CommonSys/Shielding/Activation/id_report_updated_may_2004.pdf
123. M.N. Morev, *Dose rates behind the JD*, ISTC Project #1800, Moscow Engineering Physics Institute. http://atlasinfo.cern.ch/Atlas/TCOORD/Activities/CommonSys/Shielding/Activation/JD_fields_backside.pdf
124. M.N. Morev, *Doses with the LAr (VA) beampipe made in 1.5 mm thick aluminium*, ISTC Project #1800, Moscow Engineering Physics Institute. http://atlasinfo.cern.ch/Atlas/TCOORD/Activities/CommonSys/Shielding/Activation/va_beampipe_15_real_al.pdf
125. Cosmic Ray, Beam-Halo and Beam-Gas Rate Studies for ATLAS Commissioning, M. Boonekamp et al., ATL-GEN-2004-001.

Index of Tables

Index of Figures

Appendix I: RTF Mandate

Radiation background taskforce Mandate

T. Åkesson

Introduction

A large effort is made to evaluate the radiation background in the different areas of ATLAS. These levels have a major impact on performance and equipment, and also significant resource implications. If the levels in reality are significantly different from the estimates made today it could result in scientific failure and loss of millions in resources. To reduce this risk ATLAS will organize a taskforce to evaluate our understanding of the radiation levels. The taskforce should start immediately and come forward with an estimated date for its report.

Charge

The taskforce is asked to look into both the geometry and material input, and the physics models and analysis methodologies used for evaluating the radiation background. It should also evaluate the most critical areas, i.e. where small variations in physics, geometry and material have the strongest impact on the radiation levels. The membership of the taskforce is listed in the next section. Part of the charge of the taskforce is to request colleagues responsible for different (geographical) regions of the apparatus to formally sign-off that the corresponding geometry modeling in the background calculations corresponds to the set-up they are preparing. The taskforce should analyze the levels predicted and their impact on ATLAS.

Appendix II: Fluences and Currents

In radiation background calculations, the rates of particles in given detector regions are quantified in terms of flux (or fluence rate), and current. These two quantities have the dimensions of number/unit-time/unit-area, but they do not have the same meaning. "Flux" counts the rate of arrivals per unit area independent of particle direction, whereas "current" counts the rate crossing through a given plane, referred to area elements in the surface of the plane. The definition of flux from Van Nostrand's Scientific Encyclopedia under "Neutron" is easy to visualize: "Neutron flux density is the number of neutrons that enter a sphere of unit cross-sectional area per unit of time."

Under the same conditions, the current will always be less than or equal to the flux because, for current, the rate per unit area depends on the cosine of the particle direction relative to the surface normal vector. For example, if all particle flow is normal to a plane, the flux and current are identical. On the other hand, if the plane is rotated so that the flow is parallel, the flux remains the same but no particles cross the plane, so the current is zero. For current, the cosine of the angle relative to the plane's normal vector will account for the change in the projected area element in the surface of the plane as the surface is rotated from perpendicular to parallel. Each area element in the surface intercepts less flow as the angle is increased.

For the special case where particle flow in a given region is isotropic, there is a simple ratio between the flux and the current incident on a planar surface. One can find this by integrating the arrival directions over a sphere, finding the average value of the magnitude of the cosine; or by integrating over a hemisphere and finding the average value of the cosine. In the latter case, the phi integration is 2π radians, the solid angle integral in the denominator is 2π steradians (to normalize the result), and the remaining integral in the numerator is over $\cos\theta \times d(\cos\theta)$, or $u \times du$, integrated from 0 to 1, which gives 0.5. So for isotropic flow, the value of the flux is exactly a factor of 2 larger than the magnitude of the current.

The calculation of flux and current in simulation programs (such as FLUKA and GCALOR), is perhaps more involved than one might expect. The current calculation is the easier of the two. For a given scoring surface, one simply finds the rate of particles crossing the surface in either direction and divides by the area of the surface. Components of the flow near normal will contribute with larger weight per unit area than those near parallel because of the area projection effect discussed above.

The flux calculation is more complicated. It begins by dividing the experimental volume into a regular array of computational volumes-- usually in subdivisions $dR \times dZ$, spanning all phi. One typical binning is 10 cm by 10 cm for dR by dZ. As particles of a given type are tracked in the simulation, their total tracklength in each subdivision is accumulated. Tracks may be created or stopped within the subdivision, or may be passing through it; but all track length for each type is added. In post-run processing, the flux in each subdivision is found by dividing the summed track length by the volume of the subdivision and by the experimental running time corresponding to the number of simulated events.

A simple example shows how the current and flux found in this way would be equal for normal incidence. Imagine a cube S cm on a side, with the particle flow normal to a face, and all particles passing through the cube. Each particle will leave a track S cm long passing face to face through the cube. If N particles pass through the cube in T seconds, the current through the incoming face is $I = N/T/(S^2)$ [number per unit time per unit area]. The flux calculation will find an accumulated track length of $N \times S$ during this time, and the flux calculation will give $F = (N \times S)/V/T = (N \times S)/(S^3)/T$, where the S's cancel so as to give the same I. If the cube is rotated,

the current through the chosen face goes to zero as the flow becomes parallel to it, while flux value does not change.

The second part of the last statement is a bit subtle (and assumes the flow is uniform over the region sampled by the cube). As the cube is rotated, some tracklengths will grow longer and some shorter, and the area intercepted by the cube will change. But the summed tracklength is invariant, because after thousands of tracks have passed through the cube, this quantity has sampled the volume of the cube as V = Sum_i(N_i×S_i)/F/T. This argument applies to volumes of any shape, and in any orientation.

As a cross check, in the course of backgrounds calculations, a number of simulations have been done where flux is calculated in two ways for the same region: (1) by the standard method of accumulating track length in small subdivisions, and (2) during the summing for current from crossings of scoring surfaces, by forming an additional accumulation of 1/cosθ for each hit. In the latter accumulation, the area projection effect is compensated for, hit by hit, and the resulting value should be the same as the flux found by method (1). These two methods give the same number for the flux, confirming the calculations.

The central question is: for which investigations is flux the relevant quantity, and for which should one use current instead? The simple answer is: use flux for physical processes that are independent of particle direction, and current for those that depend on particle direction. That question was also discussed by A.Ferrari and P.Sala in [107].

But it is not always easy to know if some processes are independent of particle direction; and, if not, whether the dependence is cosθ or something else One case to consider is damage effects caused by minimum ionizing particles passing through an object, such as a thin or thick detector, any electronics component, or a structural element. Assume that the particles interact only by dE/dX energy loss due to ionization. The damage will depend on accumulated track length, even in the case of very thin detectors, and the damage scales with the flux, since the accumulated track length does not depend on orientation. In practice, dose due to ionization energy loss is found by summing over the dE/dX given in each tracking step by the simulation (GCALOR or FLUKA), so the particles are not assumed to be minimum ionizing, and the results are reported in Gray or Sieverts. But dose, like flux, is independent of direction, since it depends on track length.

The situation is similar for phenomena associated with nuclear interactions, such as activation, silicon damage by non-ionizing energy loss (NIEL), single event electronics upsets, and other single event effects such as those leading to power supply damage. Most often these are independent of direction because the activity or damage is associated with a target volume that is equally sensitive from all directions. So flux (or a similar non-directional quantity such as 1 MeV Equivalent Neutron dose) is the best measure of these rates or doses. However, situations are possible where direction becomes important. For example, if there is a thin layer of material with a large nuclear cross section in some energy range (such as Ag), a detector layer on the downstream side of this “target” may be more heavily bombarded by nuclear fragments than one upstream of the material. As one can see, this depends on the specific energies and size scales involved, and could only be investigated by detailed simulation of the device. So it should be remembered that backgrounds of the type reported in flux maps or tables produced for general use do not take such directional effects into account.

There are interesting cases where a given physical quantity will scale neither as the flux nor the current, but in some intermediate way. For example, the ATLAS experiment has many planes of MDT chambers consisting of individual tubes stacked into layers. If one asks for the rate of particles crossing through the front and back surfaces of the chamber, the current gives the correct number. However, individual MDT tubes will count at a rate which is roughly independent of the rotation angle, phi, around their symmetry axis (the wire). For circular MDT's this would be exactly true, and for square or rectangular MDT's it is approximately correct because as the cross sectional area increases with phi, so does the fraction of short tracks

in the corners whose ionization will not be efficiently collected (and pass threshold). But considering the angle, theta, (the complement of the usual polar angle) the counting rate will scale as the cosine of this angle because of the variation of projected length of the tube with particle direction. One can get the ratio between the current and flux by calculating the average value of the cosine between 0 and $\pi/2$. In contrast to the earlier calculation, the integrand is now $\cos\theta \times d\theta$ since we are averaging in angle rather than solid angle. The resulting average is now 0.637 instead of 0.5, so the counting rate scales more closely to the current than the flux for this type of detector, but not precisely as either. Note that all these arguments are geometrical, and do not take into account the many physical processes that will cause a given flux to induce counts in a given chamber; such as delta ray production, Compton scattering, recoil hadrons, etc. In the end, detailed modeling is required to determine realistic counting rates.

Appendix III: GCALOR Jan03 geometry definition

ATLAS January 2003 Baseline Geometry in GCALOR:
http://atlas.web.cern.ch/Atlas/GROUPS/PHYSICS/RADIATION/jan03_baseline/dimn_report_jan03_base.txt

Appendix IV: GCALOR Jan03 material definition

ATLAS January 2003 Baseline Geometry Materials List in GCALOR:
http://atlas.web.cern.ch/Atlas/GROUPS/PHYSICS/RADIATION/jan03_baseline/material_jan03_base.txt

Appendix V: GCALOR Jan03 complete set of results

Jan03 GCALOR Fluxmaps:
http://atlas.web.cern.ch/Atlas/GROUPS/PHYSICS/RADIATION/Radiation_maps_jan03.html

Jan03 GCALOR Tables:
http://atlas.web.cern.ch/Atlas/GROUPS/PHYSICS/RADIATION/Radiation_tables_jan03.html

http://atlas.web.cern.ch/Atlas/GROUPS/PHYSICS/RADIATION/electronics_jan03.htm

http://atlas.web.cern.ch/Atlas/GROUPS/PHYSICS/RADIATION/muonchambers_jan03.htm

Jan03 GCALOR Histograms (given in form of tables)
http://atlas.web.cern.ch/Atlas/GROUPS/PHYSICS/RADIATION/muonchambers_jan03.htm

Appendix VI: FLUKA AV16 complete set of results

FLUKA AV16 results are available via the following links:
http://dawson.home.cern.ch/dawson/fluka/av16results/av16results.html

http://atlas.web.cern.ch/Atlas/GROUPS/PHYSICS/RADIATION/AV16_thermal_neutrons_ID.pdf

http://atlas.web.cern.ch/Atlas/GROUPS/PHYSICS/RADIATION/AV16_thermal_neutrons_Muon.pdf